

**Soft Matter between Soft Solids.
Sorption-Induced Pore Deformation and
Fluid Phase Behaviour**

vorgelegt von
Dipl.-Chem. Gerrit Günther
aus Berlin

Von der Fakultät II – Mathematik und Naturwissenschaften
der Technischen Universität Berlin
zur Erlangung des akademischen Grades
Doktor der Naturwissenschaften
Dr. rer. nat.
genehmigte Dissertation

Promotionsausschuss:

Vorsitzender: Prof. Dr. Peter Strasser
Berichter: Prof. Dr. Martin Schoen
Berichterin: Prof. Dr. Sabine Klapp
Berichter: Prof. Dr. Reinhard Lipowsky

Tag der wissenschaftlichen Aussprache: 25.01.2011

Berlin 2011

D 83

Abstract

Monte Carlo simulations in the semi-grand canonical ensemble are employed to investigate the sorption strain of mesoporous materials and their influence on the phase behaviour of the confined fluid. For this purpose, a simple fluid is considered which is confined between two parallel plane walls consisting of single wall particles. The wall and fluid particles are of the same type and interacting via Lennard–Jones(12,6) potentials. The wall particles are not fixed to their lattice sites but bound to them by harmonic potentials. By changing the force constant of this harmonic potential, we are able to control the softness of the wall from an almost rigid structure to more flexible walls. Flexible means that the wall particles can move farther from their equilibrium positions to react to the fluid to a greater extent.

The pore strain is calculated as an ensemble average of the positions of the wall particles and may indicate either a contraction or an expansion of the pore, depending on the interaction between the fluid and the wall particles. By tuning the parameters of the model system, a strain isotherm is obtained which is in semi-quantitative agreement with the data of small-angle X-ray diffraction experiments. Strain isotherms over a wide temperature regime and thermodynamic conditions are computed to investigate the origin of sorption strain: if the confined fluid is in the gas-like phase, the strain is dominated by the wetting characteristics of the fluid whereas at capillary condensation the pore shrinks on account of the attractive fluid–wall interaction. Confining a liquid-like phase, the strain behaviour becomes independent of the fluid characteristics and exhibits a nanomechanical property of the confining medium. In this regime, the course of the strain isotherm is explained by a simple thermodynamic analysis.

On the other hand, the deformability of mesopores has an impact on the phase behaviour of the confined fluid. The phase diagram for a fluid in a rigid pore and one in a deformable pore are computed. By using finite-size scaling concepts the location of the critical point is determined accurately for the fluid both in confinement and in bulk. Compared with rigid pores, deformable pores affect the phase boundaries of the confined fluid and have an impact on the critical density of the fluid.

Publications

- G. Günther, J. Prass, O. Paris and M. Schoen. *Novel Insights into Nanopore Deformation Caused by Capillary Condensation*. PRL **101**: 086104 (2008).
- G. Günther and M. Schoen. *Sorption Strain and their Consequences for Capillary Condensation in Nanoconfinement*. Mol. Simul. **35**(1-2): 138–150 (2009).
- G. Günther and M. Schoen. *Sorption Strain as a Packing Phenomenon*. Phys. Chem. Chem. Phys. **11**: 9082–9092 (2009).
- M. Schoen, O. Paris, G. Günther, D. Mütter, J. Prass and P. Fratzl. *Pore-Lattice Deformations in Ordered Mesoporous Matrices: Experimental Studies and Theoretical Analysis*. Phys. Chem. Chem. Phys. **12**(37): 11267–11279 (2010).
- G. Günther and M. Schoen. *Capillary Condensation in Deformable Mesopores: Wetting versus Nanomechanics*. Molecular Physics **12**: 11267–11279 (2010).
- M. Schoen and G. Günther. *Phase Transitions in Nanoconfined Fluids: Synergistic Coupling between Soft and Hard Matter*. Soft Matter **6**: 5832–5838 (2010).

Content

1	Introduction	9
2	Theory	13
2.1	Phenomenological Thermodynamics	13
2.2	Ensemble Average	18
2.3	Grand Canonical Ensemble	20
2.4	Pair Correlation	24
2.5	Monte Carlo Method	26
2.6	Markov Process	28
3	A Model of Flexible Walls	31
3.1	Pore Filling in Ordered Mesoporous Materials	31
3.2	Degree of Confinement	32
3.3	Harmonic Approximation	36
3.4	Model of Thermally Coupled Walls	37
3.5	Semi-Grand Canonical Ensemble	41
3.6	Simulation Details	44
4	Phase Behaviour	49
4.1	Sorption in Experiment and Theory	49
4.2	Bulk Phase Transition	52
4.3	Perturbation Theory	56
4.3.1	Reference Model of Smooth Walls	57
4.3.2	λ -Expansion	59
4.3.3	Calculation of the Semi-Grand Potential Density	60
4.4	Capillary Condensation Between Flexible Walls	64
4.4.1	Contact with Sorption Experiments	68
4.4.2	Comparison with Rough Pore Models	69
4.4.3	Comparison with Another Model of Deformable Pores	70
4.5	Coexisting Phases	70

4.5.1	Improved SGCMC Algorithm to Explore Phase Coexistence	74
4.5.2	Universality	74
4.5.3	Finite Size Effects	76
4.5.4	Finite Size Scaling	77
4.5.5	Phase Diagram of a Fluid in Flexible Confinement	85
4.6	Fluid Structure between Flexible Walls	87
4.6.1	Local Density	87
4.6.2	In-Plane Pair Correlation	89
5	Pore Deformation	93
5.1	Strain of Ideal Pores	94
5.2	Sorption Strain	96
5.2.1	Strain Distributions	99
5.2.2	Strain Upon Pore Filling	101
5.3	Pentane in MCM-41: Theory and Experiment	108
5.3.1	Small-Angle X-Ray Diffraction	108
5.3.2	Lattice Strain vs. Pore Strain	112
5.4	Comparison With Other Studies	114
5.5	Stress–Strain Relation	117
5.5.1	Force and Virial Expression of Stress	118
5.5.2	Strain as a Packing Phenomenon	119
5.6	Strain Caused by Gas-like Phases	122
5.7	Strain Caused by Liquid-like Phases	125
5.7.1	Quasi-Kelvin Equation	125
5.7.2	Nanomechanical Substrate Properties	129
5.7.3	Comparison with Experiment	132
6	Summary	133
	Bibliography	137
A	Substrate Details	155
A.1	Choice of Unit Cell in a 2-Dimensional Lattice	155
A.2	Mobility of Wall Particles	156
A.3	Substrate Structure	157
A.3.1	Solid vs. Liquid	158
A.3.2	Lindemann Criterion	159
B	Stress in Deformable Pores	163

Content

B.1	Stress via the Force Route	165
B.2	Stress via the Virial Route	166
C	Kelvin Equation	171

1

Introduction

Every substance changes its properties upon changing thermodynamic conditions such as temperature, pressure or volume. The properties of a substance are therefore determined by thermodynamic conditions, the so-called thermodynamic state. Upon changing the thermodynamic state successively (such as increasing the temperature while keeping pressure and volume constant) we find regions in which properties of a substance change only slightly and continuously. Thus, states of such a region share similar properties and they are collectively subsumed under the term *phase*. But there are thermodynamic conditions at which a substance reacts to minor perturbations of the thermodynamic state with a sharp, discontinuous change of a property. We denote the latter phenomenon as *phase transition* (of first order according to Ehrenfest's classification [1]) which separates different phases. For example, by increasing the temperature water is transformed from a liquid to a gaseous phase, characterised by a discontinuous, sharp drop of density at the liquid–gas phase transition. This phase transition separates two regions in which the density changes only continuously and thus both phases basically differ in density.

In general, a phase is a state of organisation of matter characterised by a specific molecular interaction and degree of symmetry. The interaction of particles is observable through, e.g., the pair correlation function or structure factor [2] and increases in the sequence gas–liquid–solid. On the other hand, the degree of symmetry, specified by, e.g., an order parameter [3], may lead to an additional distinction of phases

such as smectic or nematic phases of liquid crystals [4, 5] as well as cubic or hexagonal packed solids [6]. Thus, phases resemble preferred organisations of matter in the sense of interaction and symmetry under the given thermodynamic conditions, whereas phase transitions mark the reorganisation of matter from one preferred form of organisation into another. However, with regard to ordinary (single-component bulk) matter the concept of phases and phase transitions leads to the basic classification according to three aggregation states, namely solid, liquid and gas.

In a liquid–solid phase transition of infinitely large bulk systems there is a clear distinction between both phases, because the transition is always associated with a discontinuous increase of molecular order. Even so-called hard sphere systems, i.e. systems of impenetrable spheres that cannot overlap in space, show this first-order behaviour. In this context computer simulations proved that a discontinuous drop of pressure marks solidification when an ordered arrangement prohibits particles from passing each other for sheer lack of space. [7–10] Thus, solidification is clearly driven by repulsive forces, because this is the only interaction between a pair of hard spheres. As soon as additional attraction between particles is present, the liquid–solid phase transition is accompanied by the release of latent heat.

The presence of intermolecular attraction leads to another phase transition that separates gas and liquid phases, characterised by a significant change in density. The difference between the gas–liquid and liquid–solid phase transition reflects the atomic structure of substances which consists of a negative electron cloud surrounding a positive core. If one atom comes closer to another one, their electron clouds mutually induce temporary dipoles that result in attractive forces, decaying with r^{-6} (r is the distance between atoms). [11] When molecules approach each other so closely that their electron clouds overlap, electrons shield the positively charged cores less well. The resulting repulsion of cores is often assumed to fall off exponentially and overwhelms the attraction at closer distances. As a result, contrary to repulsion, the effective attraction between a pair of particles is always of finite strength, overwhelmed by repulsion at close distances and vanishing at larger ones. This finite nature of attraction is reflected by the critical temperature of the gas–liquid phase transition, a maximum temperature, which marks the upper limit of first-order behaviour and which has no counterpart at the liquid–solid transition (for reasons discussed in §83 of [12]). At temperatures above the critical one, the density changes continuously because now any attraction is negligible compared to the kinetic energy of particles. This offers the possibility of circumventing the gas–liquid phase transition at high temperatures which leaves the distinction between gas and liquid meaningful only in the presence of a phase boundary. For this reason both non-solid phases are referred

to collectively as *fluid*, in cases where a more detailed distinction is not important or not possible.

On account of their physical nature, fluid phases always need a container to confine them to a specific volume. Consequently, we have always an interaction of the fluid with the walls of the container which in general is expected to have an influence on fluid properties. Usually the range of molecular interactions is of a microscopic length scale and can be neglected as long as the dimensions of the container are of macroscopic size, so that the portion of the fluid that interacts with the container's wall is negligible related to the remaining (non-interacting) part. This is the typical situation encountered in the *bulk*: properties of the fluid are not affected by the presence of the surrounding walls of the container.

However, if the dimensions of the container become comparable to the range of molecular interactions, the fluid–wall interaction becomes important. In this study mesopores, i.e. pores of 2–50 nm pore width, will serve as the container. To date a wide variety of mesoporous materials has been synthesised ranging from carbons [13, 14] to silicas [15], ceramics [16] and metals [17, 18]. Some exhibit a more amorphous structure such as controlled-pore glasses (CPG) which consist of an irregular network of different pores, varying both in shape and width, while others, such as MCM- or SBA-type silicas consist of individual, disconnected pores of nearly the same shape and width. In addition, pores of these latter materials are arranged in a regular array. [19–25]

If a fluid fills such structure, its properties are modified due to the interaction with the mesoporous material depending on (i) the strength of the fluid–wall interaction, (ii) its amount (i.e., the volume–wall ratio), and (iii) the available space (i.e., the pore geometry). This situation differs from bulk and is referred to as *confined* because fluid properties are affected by the surrounding media. Up to now a broad spectrum of confined fluids ranging from classical polar and nonpolar fluids [26–28] to quantum fluids [29, 30] has been investigated. Confinement generally causes the fluid's phase boundaries to shift relatively to their location in bulk. This applies to both phases and affects the gas–liquid as well as the liquid–solid phase transition. The former is referred to as ‘capillary condensation’ [31, 32] and the latter as ‘capillary freezing’. [33–35] As an example, bulk water freezes and forms well-ordered structures while its solid-like phases in MCM-41 are highly disordered as a result of its interaction with the substrates and the specific pore geometry. [34] The confining walls impose their structure on the confined fluid via a *template effect* and therefore confined water remains liquid at a temperature up to 45 K below the freezing point of its bulk counterpart. [36] This template effect is predicted to cause even novel phases

which have no counterpart in bulk. [37, 38]

Today there are applications of confining systems which employ their huge surface area such as adsorbants (e.g., to clean fuel from sulphur) [39, 40], drug delivery systems [41] or nanoreactors in catalysis [42–45]. Also structures with narrow pore size distribution (such as MCM-41 or SBA-15) are already in use as molecular sieves. [46–48] These applications are the result of a continuously increasing interest reflected by the increase of publications regarding nanoconfinement. [49] In the overwhelming number of theoretical studies the confining medium is basically treated as an external field which acts on the confined fluid and induces a change of its properties. Thus, characteristic features of a confined fluid come about by superimposing the external field on the intermolecular interactions of the fluid. Conventionally, this external field may be anisotropic and perhaps inhomogeneous but otherwise static, that is, it does not change with the fluid's thermodynamic state. In other words, the confining substrate does not respond to any changes that occur in a confined fluid, no matter whether they are of thermodynamic or mechanical origin. [31, 32, 50]

Since the synthesis of ordered materials as well as experimental techniques has advanced significantly in recent years, new and highly accurate experimental data have become available showing that even rigid materials, such as silicas or metals, deform during a fluid's ad- or desorption (subsequently subsumed under the term *sorption* throughout this work). [26, 28, 51–53] Thus, the substrate cannot be considered to be completely rigid and, therefore, cannot be treated as a static field in the above sense. This novel property of rigid substrates, their deformability, may be interesting for the use of mesoporous materials as actuators or nanosensors. [51, 52] The potential applications are a consequence of fairly large forces exerted by the confined fluid on the walls as, for example, it is the strength of these forces that keeps sand castles together. [54] The high stiffness of silicas, which allows only reversible deformations, will be particularly suitable in this context. To optimise their usage the interaction of confined fluids and the confining substrate needs to be understood more comprehensively. Here we present a novel approach to gain deeper insight into the sorption process by considering nanoporous materials that are to a certain extent deformable at the molecular level.

2

Theory

This chapter introduces the general concepts concerning the treatment of confined fluids and deals with the basic assumptions about the system under consideration.

2.1 Phenomenological Thermodynamics

Since we are interested in the relationship between fluid properties and thermodynamic conditions, phenomenological thermodynamics provides an appropriate framework from a macroscopic perspective because it relies on a sparse set of empirical rules (i.e. the laws of thermodynamics) and their rigorous mathematical treatment. Within this framework we must differentiate between the *system* that we are interested in, and its environment or *surroundings*. As a consequence of this classification both parts share the same boundary through which they are able to interact. This boundary may be simply the surface of the system (e.g. as with a drop of liquid) or a solid container and its exact nature determines the kind of interaction. In isolated systems the boundary is impermeable to energy and matter, while in closed systems energy may be transmitted but no matter. However, this work deals with *open* systems, in which the boundary allows an exchange of energy and matter, as for example in sorption, where the pores of a confining medium (i.e. the system) are in open contact with a bulk reservoir of the fluid (i.e. the surroundings). [28, 55]

As we already emphasised in Chapter 1, nanoconfined phases are generally highly inhomogeneous and anisotropic. To account for the anisotropy properly the pressure P of the (homogeneous and isotropic) bulk needs to be generalised to the pressure tensor \mathbf{P} . Consequently, situations of thermodynamic equilibrium, that is a combination of thermal, mechanical and chemical equilibrium, are characterised by

$$T = T_{sur} \quad (\text{thermal equilibrium}) \quad (2.1)$$

$$\mathbf{P} = \mathbf{P}_{sur} \quad (\text{mechanical equilibrium}) \quad (2.2)$$

$$\mu = \mu_{sur} \quad (\text{chemical equilibrium}) \quad (2.3)$$

where T is the temperature, \mathbf{P} is the pressure tensor, and μ is the chemical potential. In Eqs. (2.1)–(2.3) only properties of the surroundings are labelled with the subscript ‘*sur*’ according to the convention that system properties are considered if not otherwise mentioned. We restrict ourselves to situations of thermodynamic equilibrium and therefore the open system reacts to any changes of its surrounding to restore these equilibrium conditions. For example, an increase of temperature ($T_{sur} > T$) results in the flow of heat to restore thermal equilibrium, while a change of the (anisotropic) pressure tensor ($\mathbf{P}_{sur} \neq \mathbf{P}$) may cause the deformation of the system’s boundaries. The latter process is connected with the mechanical work $W_{mech} = -V_0 \text{Tr}(\mathbf{P}d\boldsymbol{\sigma})$ where $d\boldsymbol{\sigma}$ denotes the (infinitesimal) strain (or deformation) tensor, V_0 is the volume of the unstrained state and ‘Tr’ represents the trace of the matrix $\mathbf{P}d\boldsymbol{\sigma}$. This treatment is usually adopted in the thermodynamic analysis of solids which can be highly anisotropic media depending on the direction of the lattice vector considered. [56] In some applications it appears to be somewhat more convenient to formulate the mechanical work contribution in terms of the stress tensor $\boldsymbol{\tau}$ rather than the pressure tensor \mathbf{P} . However, the two are trivially related through $\boldsymbol{\tau} = -\mathbf{P}$. To get a more physical feel for $\boldsymbol{\tau}$ it is useful to think of its elements $\tau_{\alpha\beta}$ as the α -components of a force exerted on the β -directed face of a parallelepiped.

According to the parallelepiped, stresses acting on opposite sites have to cancel each other, because the system should not move through space. As a result it is sufficient to consider the stress on three rather than on all six sites of the parallelepiped. Using one stress vector for each site, the stress of the system can be written as a 3×3 matrix of the form

$$\boldsymbol{\tau} = \begin{pmatrix} \tau_{xx} & \tau_{xy} & \tau_{xz} \\ \tau_{yx} & \tau_{yy} & \tau_{yz} \\ \tau_{zx} & \tau_{zy} & \tau_{zz} \end{pmatrix} \quad (2.4)$$

which is illustrated in Fig. 2.1a. In fact this matrix describes a second-rank tensor as was shown by Schoen et al. [32] in detail.

2.1 | Phenomenological Thermodynamics

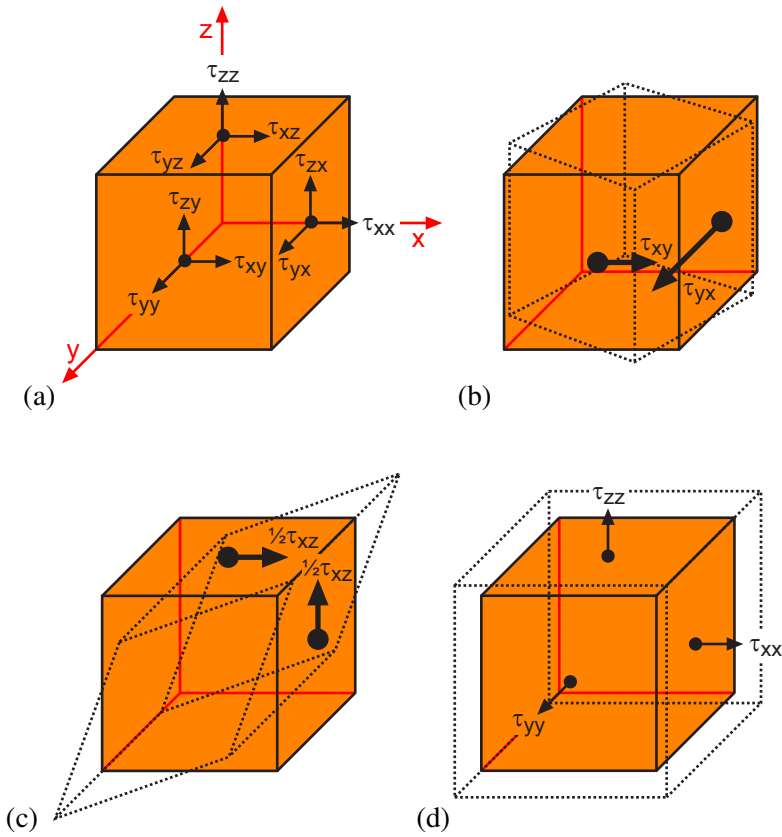


FIG. 2.1: (a) Illustration of stress tensor elements given in Eq. (2.4) which define the stress of a system without translational movement. (b) To prevent rotation of the entire system around the z -axis, the tensor element τ_{xy} must be equal to τ_{yx} . (c) Off-diagonal shear stress elements such as τ_{xz} affect a system's shape while (d) diagonal stress tensor elements τ_{xx} , τ_{yy} and τ_{zz} determine its volume, that means they produce an expansion (shown here) or contraction of the system without changing its shape.

However, the stress tensor must fulfil one more constraint to describe a system at rest. To prevent a rotation of the entire system, the stress tensor elements must satisfy the symmetry relation

$$\tau_{\alpha\beta} = \tau_{\beta\alpha} \quad \forall \alpha \neq \beta \quad (2.5)$$

sketched in Fig. 2.1b. This leads to a symmetric stress tensor that may be written as

$$\boldsymbol{\tau} = \begin{pmatrix} \tau_{xx} & \frac{1}{2}\tau_{xy} & \frac{1}{2}\tau_{xz} \\ \frac{1}{2}\tau_{xy} & \tau_{yy} & \frac{1}{2}\tau_{yz} \\ \frac{1}{2}\tau_{xz} & \frac{1}{2}\tau_{yz} & \tau_{zz} \end{pmatrix} \quad (2.6)$$

where the factor $\frac{1}{2}$ arises for off-diagonal elements because they appear twice using the Cartesian tensor description. In general, we distinguish between diagonal and off-diagonal elements because they lead to different kinds of deformations. The latter refer to shear forces acting on the system which lead to a change in the system's shape as sketched in Fig. 2.1c. In this work we limit ourselves to the special case in which the geometry of the system remains fixed. Under these conditions off-diagonal stress tensor elements must vanish and Eq. (2.6) reduces to

$$\boldsymbol{\tau} = \begin{pmatrix} \tau_{xx} & 0 & 0 \\ 0 & \tau_{yy} & 0 \\ 0 & 0 & \tau_{zz} \end{pmatrix} \quad (2.7)$$

which is illustrated in Fig. 2.1d. This stress tensor describes anisotropic stresses which may result in a contraction or expansion of the system while keeping its rectangular shape.

Because the compressional stresses are acting on faces of the parallelepiped one may envision changes in the system size that can be accounted for quantitatively via strain tensor $\boldsymbol{\sigma}$ represented by the 3×3 matrix

$$\begin{aligned} \boldsymbol{\sigma} &= \begin{pmatrix} \sigma_{xx} & 0 & 0 \\ 0 & \sigma_{yy} & 0 \\ 0 & 0 & \sigma_{zz} \end{pmatrix} \\ &= \begin{pmatrix} (s_x - s_{x0})/s_{x0} & 0 & 0 \\ 0 & (s_y - s_{y0})/s_{y0} & 0 \\ 0 & 0 & (s_z - s_{z0})/s_{z0} \end{pmatrix} \end{aligned} \quad (2.8)$$

where the subscript '0' refers to some unspecified unstrained state. An element of the strain (or deformation) tensor expresses the deviation of the side s_α in a strained state relative to the unstrained one (i.e. $s_{\alpha 0}$). In terms of stress and strain the mechanical (compressional) work can be expressed as

$$dW_{mech} = V_0 \text{Tr}(\boldsymbol{\tau} d\boldsymbol{\sigma}) \quad (2.9)$$

where $V_0 = s_{x0}s_{y0}s_{z0}$ and, as we already explained, 'Tr' is a shorthand notation for the trace of a matrix.

Beside the mechanical kind, another kind of work may arise if the system reacts to a perturbation of chemical equilibrium ($\mu \neq \mu_{sur}$). The associated intrusion or extrusion of matter is connected with chemical work dW_{chem} given by

$$dW_{chem} = \mu dN \quad (2.10)$$

2.1 | Phenomenological Thermodynamics

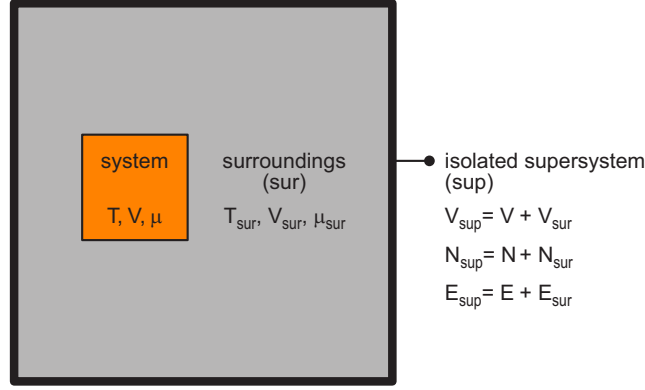


FIG. 2.2: Sketch of an open system and its surroundings (sur) as subsystems of an isolated supersystem (sup) characterised by total volume V_{sup} , total particle number N_{sup} and total internal energy E_{sup} . Since system and surroundings mutually exchange heat and matter, the surroundings also represent an open system.

depending on the chemical potential μ and the change in the number of particles dN . From the last equation it becomes apparent that the chemical potential μ is the work that must be done to change the particle number N at constant volume (i.e. the density) by dN .

We exclude types of work other than the chemical or mechanical ones, so that the total work W of our system consists of

$$dW = dW_{chem} + dW_{mech} \quad (2.11)$$

Consequently, the Gibbs fundamental equation [32] may be written as

$$dE = TdS + dW \quad (2.12)$$

where E is the internal energy, T is the temperature, S is the entropy and dW is given in Eq. (2.11). Using Eqs. (2.9), (2.10) and (2.11) we can rewrite Eq. (2.12) more explicitly as

$$dE = TdS + \mu dN + V_0 \text{Tr}(\tau d\sigma) \quad (2.13)$$

The first law of thermodynamics states that the internal energy is a *state function*, which means it depends on the thermodynamic state, defined by state variables such as S , N and σ , but not on the path taken to reach this condition. In other words, the internal energy must obey the relation

$$\int_A^B dE = E_B - E_A \quad (2.14)$$

where A and B mark arbitrary thermodynamic states. If we consider the open system *plus* its surrounding as an isolated supersystem (see Fig. 2.2), the subsystems are connected with each other through

$$dN = -dN_{sur} \quad (2.15)$$

$$dE = -dE_{sur} \quad (2.16)$$

The first and second laws of thermodynamics state that a spontaneous process of an isolated system, which leads from state A to state B , results in neither a decrease of entropy nor an increase of internal energy. Since states of thermodynamic equilibrium are achieved as results of spontaneous processes, they are characterised by a minimum of internal energy of the supersystem because any (infinitesimal) transformation δ that takes the supersystem (*sup*) from thermodynamic equilibrium would be connected with $\delta E_{sup} = \delta(E + E_{sur}) \geq 0$.

Consider now a situation of thermodynamic equilibrium with fixed compressional strain $\boldsymbol{\sigma} = \boldsymbol{\sigma}_{sur} = \mathbf{0}$ ($\mathbf{0}$ is the zero tensor) so that an (infinitesimal) transformation δ of this state can be written as

$$\begin{aligned} \delta E_{sup} &= \delta(E + E_{sur}) \\ &= \delta E + T_{sur} \delta S_{sur} + \mu_{sur} \delta N_{sur} \\ &= \delta(E - TS - \mu N) \equiv \delta \Omega \geq 0 \end{aligned} \quad (2.17)$$

where Ω is the grand potential and we use Eqs. (2.1), (2.3), (2.15), (2.16) as well as (2.13) which is adapted for the surroundings. Thus, in open systems the grand potential marks states of thermodynamic equilibrium through a minimum at conditions of fixed strain, temperature and chemical potential. Combining Eqs. (2.13) and (2.17) the exact differential of the grand potential can be expressed as

$$d\Omega = -S dT - N d\mu + V_0 \text{Tr}(\boldsymbol{\tau} d\boldsymbol{\sigma}) \quad (2.18)$$

Although we find a way to identify states of thermodynamic equilibrium, we cannot go any further because phenomenological thermodynamics does not provide a route to calculate the value of the grand potential (or any other property). We need additional assumptions about the system, that is why we leave this approach now in favour of a microscopic model.

2.2 Ensemble Average

The treatment summarised in the preceding section has the great advantage that it is general because it is independent of the molecular details of a specific system un-

2.2 | Ensemble Average

der consideration. The price to pay for this generality is, however, that none of its properties can be calculated. One way to overcome this difficulty is to connect thermodynamic properties with molecular expressions based upon the notion of particles and their interaction.

While from a *macroscopic* point of view the state of a system is defined by three state variables such as T , V and μ , these macroscopic properties are clearly connected to molecular properties of the system, the so-called *microstate*. For example, the pressure of the system is considered as the force per area imposed by its molecules while temperature reflects their kinetic energy.

Since now we are dealing with objects of molecular dimensions, quantum mechanics provide the theoretical framework. Within this theory, the wavelength associated to the linear dimension of a (free) quantum mechanical particle is given by the so-called de Broglie wavelength Λ given by [32]

$$\Lambda = \frac{h}{\sqrt{2\pi mk_B T}} \quad (2.19)$$

which depends on the mass m of the particle and the temperature T , aside from Planck's constant h and the Boltzmann constant k_B . In this work we restrict ourselves to fluids at sufficiently high temperatures above and below the gas–liquid critical temperature. In this temperature regime the mean distance between particles $\propto 1/\sqrt[3]{\rho}$ (ρ is density) is larger than Λ . For most fluids Λ is of the order of $\mathcal{O}(10^{-1}\sigma)$ or smaller, where σ is the particle diameter, and thus the classical description becomes exact. For example, the associated de Broglie wavelength of n-pentane ($m \simeq 72u$ where u is the atomic mass unit) at standard temperature may be estimated as $\Lambda \approx 10^{-2}\sigma$ (where $\sigma \simeq 0.4$ nm of Eq. (3.4) is utilised) suggesting that its physics are governed by classical laws.

According to the classical treatment, a single particle is characterised by six generalised coordinates such as three spatial coordinates and three momenta. While a particle is represented by a point in a six dimensional space, the microstate of a system containing N particles is defined as a point $\Gamma(\mathbf{p}, \mathbf{q})$ in a $6N$ dimensional phase space where momenta $\mathbf{p} = \{p_1, p_2, p_3 \dots p_{3N}\}$ and spatial coordinates $\mathbf{q} = \{q_1, q_2, q_3 \dots q_{3N}\}$ are of dimension $3N$, respectively. If spatial coordinates or momenta of particles change, the microstate of the system changes, that is it evolves in phase space. The motion of phase point given by $\Gamma(\mathbf{p}, \mathbf{q})$ along a phase trajectory is determined by classical Hamiltonian dynamics through

$$\dot{q}_j = \frac{\partial H}{\partial p_j} \quad (2.20)$$

$$\dot{p}_j = -\frac{\partial H}{\partial q_j} \quad (2.21)$$

for $j = 1 \dots 3N$ where the Hamiltonian function H relates to the internal energy E via

$$H(\mathbf{p}, \mathbf{q}) = E \quad (2.22)$$

For example, consider that the system is at fixed T, V, μ : From a microscopic perspective a macroscopic property M of the system (e.g. the pressure) depends on the microstate $\Gamma(\mathbf{p}, \mathbf{q})$ which evolves along its phase trajectory through phase space under the macroscopic constraints T, V, μ . Since the number of particles is typically of the order of Avogadro's number $N_A \approx 10^{23}$, the number of possible microstates which match the macroscopic criteria T, V, μ is overwhelmingly large. The discrepancy in information between the micro- and macroscopic perspective (i.e. more than 10^{23} versus 3) suggests that the macroscopic treatment should be independent of a particular microstate and its evolution through phase space but rather involve all microstates, or at least a representative part of phase space. A virtual collection of all possible microstates, each constructed to be a replica of the macroscopic thermodynamic system, is called an *ensemble*. [57] If the ensemble realises the thermodynamic conditions T, V and μ , it is referred to as a *grand canonical ensemble*.

According to the ensemble concept, a thermodynamic property M can be considered as a so-called ensemble average $\langle M \rangle$, that is the average of property M_Γ , belonging to microstate $\Gamma(\mathbf{p}, \mathbf{q})$, over phase space given by

$$\langle M \rangle = \sum_N \iint M_\Gamma P(\mathbf{p}, \mathbf{q}, N) d^{3N} \mathbf{p} d^{3N} \mathbf{q} \equiv M \quad (2.23)$$

where $P(\mathbf{p}, \mathbf{q}, N)$ is the probability that the system is in microstate $\Gamma(\mathbf{p}, \mathbf{q})$ with particle number N . This probability is normalised such that

$$\sum_N \iint P(\mathbf{p}, \mathbf{q}, N) d^{3N} \mathbf{p} d^{3N} \mathbf{q} = 1 \quad (2.24)$$

The first relation in Eq. (2.23) is reasonable but the second one which establishes a connection between the ensemble average of a property $\langle M \rangle$ and a thermodynamic property M , although reasonable too, is a postulate. In other words, we assume that thermodynamic properties of the system arise from a representative part of the phase space.

2.3 Grand Canonical Ensemble

Microstates of the grand canonical ensemble are subject to the constraints of fixed thermodynamic conditions specified by T, V and μ but may differ in other properties

2.3 | Grand Canonical Ensemble

such as internal energy E or particle number N . These fluctuations of E and N are the result of a system's interaction with its surroundings. Following the spirit of Section 2.1 we consider an isolated supersystem (sup) composed of a system *plus* its surroundings (sur) which is illustrated in Fig. 2.2 (p. 17), so that the internal energy and particle number of the supersystem remain fixed and are composed of the two subsystems given by

$$E_{sup} = E + E_{sur} \quad (2.25)$$

$$N_{sup} = N + N_{sur} \quad (2.26)$$

As opposed to its subsystems, the supersystem represents an isolated system of fixed internal energy E_{sup} , particle number N_{sup} and volume V_{sup} . An isolated system is studied via the microcanonical ensemble, which contains all possible microstates that realise the same thermodynamic conditions of E , N and V on the microscopic level. The associated microcanonical partition function $Q_{sup}(E_{sup}, N_{sup})$ can be expressed in terms of its subsystems as [58]

$$Q_{sup}(E_{sup}, N_{sup}) = \sum_N \int Q(E, N) Q_{sur}(E_{sup} - E, N_{sup} - N) dE \quad (2.27)$$

where both partition functions of the subsystems are formulated to depend on the internal energy E and particle number N of the system. The microcanonical partition function Q is connected to entropy S through the famous equation [58, 59]

$$S = k_B \ln Q \quad (2.28)$$

This equation relates the macroscopic quantity S with the microscopic quantity Q and therefore establishes a connection between the macroscopic and microscopic treatment, here introduced in the form of a definition. To derive Eq. (2.28), the entropy needs further identification such as being an extensive quantity and $1/k_B T$ being an integrating factor, discussed in more detail in [59] or in Sections 2.3.1 and 2.3.2 of [32].

According to Eq. (2.27), the probability $P(E, N)$ that the system has energy E and particle number N can be written as

$$P(E, N) = \frac{Q(E, N) Q_{sur}(E_{sup} - E, N_{sup} - N)}{\sum_N \int Q(E, N) Q_{sur}(E_{sup} - E, N_{sup} - N) dE} \quad (2.29)$$

where we assume the *principle of equal a priori probabilities* which states that all microstates of the isolated supersystem of fixed E_{sup} occur with the same probability. We assume that the supersystem is large ($N_{sup} \rightarrow \infty$) and that the size of the surroundings exceeds the system size by so much that $E_{sur} \gg E$ and $N_{sur} \gg N$. Since Q

is expected to increase monotonically with particle number and internal energy, for all practical purposes the system's influence is negligible because of [60]

$$\frac{E}{E_{sup}} = 1 - \frac{E_{sur}}{E_{sup}} \ll 1 \quad \text{and} \quad \frac{N}{N_{sup}} = 1 - \frac{N_{sur}}{N_{sup}} \ll 1, \quad (2.30)$$

so the surroundings approximately corresponds to the supersystem. With regard to Eq. (2.28) the microcanonical partition function of the surroundings is related to its entropy through

$$Q_{sur}(E_{sup} - E, N_{sup} - N) = e^{S_{sur}(E_{sup}-E, N_{sup}-N)/k_B} \quad (2.31)$$

while changes of entropy at constant strain σ are given by Eq. (2.13), which we rewrite as

$$dS = \frac{1}{T}dE - \frac{\mu}{T}dN \quad (2.32)$$

Because of $E_{sup} \gg E$ and $N_{sup} \gg N$, we can expand S_{sur} around E at constant N in a Taylor series

$$S_{sur}(E_{sup}, E) = S(E_{sup}) - E \left(\frac{\partial S}{\partial E} \right)_{N,V} + \dots \quad (2.33)$$

and also around N at constant E

$$S_{sur}(N_{sup}, N) = S(N_{sup}) - N \left(\frac{\partial S}{\partial N} \right)_{E,V} + \dots \quad (2.34)$$

where we can use Eq. (2.32) to establish the relations given by

$$\left(\frac{\partial S}{\partial E} \right)_{N,V} = \frac{1}{T} \quad (2.35)$$

$$\left(\frac{\partial S}{\partial N} \right)_{E,V} = -\frac{\mu}{T} \quad (2.36)$$

Combining Eqs. (2.33)–(2.36) the entropy of the surroundings can be expressed in terms of system properties as

$$S_{sur}(E, N) = \text{const.} - \frac{E}{T} + \frac{\mu N}{T} \quad (2.37)$$

which can be used to write Eq. (2.29) with regard to Eq. (2.31) as

$$P(E, N) = \frac{e^{\gamma N} e^{-\beta E}}{\sum_N \int e^{\gamma N} e^{-\beta E} dE} \quad (2.38)$$

2.3 | Grand Canonical Ensemble

where $\beta = 1/k_B T$, $\gamma = \mu/k_B T$ and \mathbf{Q} is neglected in Eq. (2.29) on account of Eq. (2.30). The transformation of variables $E \rightarrow \mathbf{p}\mathbf{q}$ under consideration of Eq. (2.22) leads to another expression of Eq. (2.38) in the form of

$$P(\mathbf{p}, \mathbf{q}, N) = \frac{1}{\Xi} e^{\gamma N} e^{-\beta H(\mathbf{p}, \mathbf{q})} \quad (2.39)$$

where Ξ is the grand partition function given by

$$\Xi = \sum_N \frac{1}{N! h^{3N}} \iint e^{\gamma N} e^{-\beta H(\mathbf{p}, \mathbf{q})} d^{3N} \mathbf{p} d^{3N} \mathbf{q} \quad (2.40)$$

which is connected to the grand potential Ω through [32, 59]

$$\Omega = -k_B T \ln \Xi \quad (2.41)$$

given as a definition in analogy to Eq. (2.28).

The factor in front of the integral in Eq. (2.40) which arises as a result of the transformation $E \rightarrow \mathbf{p}\mathbf{q}$ requires some comment. Since we are dealing with N indistinguishable particles, the term ‘ $1/N!$ ’ ensures that situations of the same internal energy E in which two or more particles just change their sets of variables (i.e. positions and momenta) are counted only once. Moreover, the factor of ‘ $1/h^{3N}$ ’ is included to make the classical treatment compatible with quantum mechanics where Heisenberg’s Uncertainty Principle precludes the *simultaneous exact* knowledge of a particle’s position in space and its momentum. [61] As a consequence, the classical phase space spanned by \mathbf{p} and \mathbf{q} is coarse-grained in terms of hypervolumes $\propto h^3$.

If we restrict ourselves to point-like fluid particles with only three translational degrees of freedom, the Hamiltonian H is given by

$$H(\mathbf{p}, \mathbf{q}) = \sum_{j=1}^{3N} \frac{p_j^2}{2m} + U(\mathbf{q}) \quad (2.42)$$

where $U(\mathbf{q})$ is the potential energy. Thus, Eq. (2.40) can be written as

$$\Xi = \sum_N e^{\gamma N} \frac{1}{N! h^{3N}} \int e^{-\beta p^2/2m} d^{3N} \mathbf{p} \int e^{-\beta U(\mathbf{q})} d^{3N} \mathbf{q} \quad (2.43)$$

whose phase space can be reduced from $6N$ to $3N$ dimensions by integration over momenta \mathbf{p} that leads to

$$\Xi = \sum_N e^{\gamma N} \frac{Z(\mathbf{q})}{N! \Lambda^{3N}} \quad (2.44)$$

where Λ is the thermal de Broglie wavelength given by Eq. (2.19) and $Z(\mathbf{q})$ is the so-called configuration integral defined as

$$Z(\mathbf{q}) = \int e^{-\beta U(\mathbf{q})} d^{3N} \mathbf{q} \quad (2.45)$$

of dimension $3N$, depending only on spatial coordinates \mathbf{q} .

According to Eqs. (2.44) and (2.45) the probability that the system is in configuration \mathbf{q} with potential energy U and particle number N can be expressed as

$$P(N, \mathbf{q}) = \frac{1}{\Xi} e^{\gamma N} e^{-\beta U(\mathbf{q})} \quad (2.46)$$

while the ensemble average of a property $\langle M \rangle$ that only depends on the spatial coordinates of N particles can be written as

$$\langle M \rangle = \sum_N \int M_{\Gamma} P(N, \mathbf{q}) d^{3N} \mathbf{q} \quad (2.47)$$

with probability $P(N, \mathbf{q})$ given by Eq. (2.46).

2.4 Pair Correlation

The grand partition function of Eq. (2.44) defines equilibrium states of the system via Eqs. (2.17), (2.41) on the basis of spatial coordinates \mathbf{q} of the particles and, therefore, exhibits information about the distribution of particles within the system: The probability $\rho^{(n)}$ of finding a certain particle configuration can be written as [59]

$$\rho^{(n)} = \sum_{N \geq n} \rho_N^{(n)} \quad (2.48)$$

where $\rho_N^{(n)}$ is the probability that a configuration with N particles occurs and that $n \leq N$ of these particles show a certain distribution. In other words, $\rho_N^{(n)}$ can be considered as the probability that particle 1 is located somewhere in the range $d\mathbf{q}_1$ at position \mathbf{q}_1 , particle 2 in $d\mathbf{q}_2$ at \mathbf{q}_2 and so on, up to particle n which is located in $d\mathbf{q}_n$ at \mathbf{q}_n . In this context \mathbf{q}_n denotes a set of three spatial coordinates, required to define the location of particle n , e.g. in Cartesian coordinates $\mathbf{q}_n \equiv \{x_n, y_n, z_n\}$. For a certain number of particles N , this probability can be obtained from Eq. (2.46) as

$$P(N, \mathbf{q}) d\mathbf{q}_1 \dots d\mathbf{q}_n = \frac{1}{\Xi} e^{\gamma N} e^{-\beta U(\mathbf{q})} d\mathbf{q}_1 \dots d\mathbf{q}_n \quad (2.49)$$

2.4 | Pair Correlation

By integrating this equation over the possible coordinates of the particles $n+1$ through N , one obtains the probability of finding a certain distribution *irrespective* of the configuration of the remaining particles, written as

$$\left[\int \cdots \int P(N, \mathbf{q}) d\mathbf{q}_{n+1} \cdots d\mathbf{q}_N \right] d\mathbf{q}_1 \cdots d\mathbf{q}_n \quad (2.50)$$

Because particles are indistinguishable, *any* particle may be particle 1, 2 ... n and, thus, the probability that we are looking for is [59]

$$\tilde{\rho}_N^{(n)} d\mathbf{q}_1 \cdots d\mathbf{q}_n = \frac{N!}{(N-n)!} \left[\int \cdots \int P(N, \mathbf{q}) d\mathbf{q}_{n+1} \cdots d\mathbf{q}_N \right] d\mathbf{q}_1 \cdots d\mathbf{q}_n \quad (2.51)$$

If the particles do not prefer regions of the volume V as in bulk, the probability of observing n particles in $d\mathbf{q}_1 \cdots d\mathbf{q}_n$ is given by integrating the last equation over $d\mathbf{q}_1 \cdots d\mathbf{q}_n$ according to

$$\begin{aligned} \rho_N^{(n)} &= \frac{1}{V} \int \cdots \int \tilde{\rho}_N^{(n)} d\mathbf{q}_1 \cdots d\mathbf{q}_n \\ &= \frac{1}{V} \int \frac{N!}{(N-n)!} P(N, \mathbf{q}) d^{3N} \mathbf{q} \end{aligned} \quad (2.52)$$

The simplest distribution is $\rho^{(1)}$ which denotes the probability of finding any particle within the volume $d\mathbf{q}_1$, written as

$$\rho^{(1)} = \frac{1}{V} \sum_N \int NP(N, \mathbf{q}) d\mathbf{q} = \frac{\langle N \rangle}{V} = \rho \quad (2.53)$$

where Eqs. (2.47), (2.48) and (2.52) are used. In Eq. (2.53) brackets $\langle \dots \rangle$ denote ensemble averages and ρ is the (average) density of the fluid. It is convenient to define a correlation function $g^{(n)}(\mathbf{q})$ in the form of

$$\rho^{(n)} = \rho^n g^{(n)}(\mathbf{q}) \quad (2.54)$$

where $g^{(n)}(\mathbf{q})$ accounts for the correlations of particles and, thus, becomes 1 if the particles are independent of each other, so that in this case $\rho^{(n)} = \rho^n$. In other words, $g^{(n)}(\mathbf{q})$ measures the extent to which a structure deviates from complete randomness. [59]

The so-called pair correlation function $g^{(2)}(r)$ which is associated with the distribution probability $\rho^{(2)}$ plays a central role because it serves as a connection between theory and experiment. The function $g^{(2)}(r)$ can be considered as the probability of finding another particle 2 at distance $r = |\mathbf{q}_1 - \mathbf{q}_2|$ if a reference particle 1 is located at $r = 0$. Because of its significance, it is referred to as simply $g(r)$ by convention. On the one hand, $g(r)$ provides an alternative route to calculating the thermodynamic

properties of fluids through integral equations. [59, 62] On the other hand, $g(r)$ is related to the static structure factor $S(k)$ through a Fourier transformation by [32, 63]

$$S(k) = 1 + \rho \int g(r) e^{-i\mathbf{k}\cdot\mathbf{r}} d^3\mathbf{r} \quad (2.55)$$

where \mathbf{k} is the wavevector and $i \equiv \sqrt{-1}$. Conversely, $g(r)$ can be expressed as the Fourier transform of the static structure factor given by [59]

$$g(r) = \frac{1}{(2\pi)^3} \int [S(\mathbf{k}) - 1] e^{i\mathbf{k}\cdot\mathbf{r}} d^3\mathbf{k} \quad (2.56)$$

Since the angle-averaged $S(k)$ is experimentally accessible through, e.g., X-ray or neutron scattering data, the pair correlation function is of great interest for comparing theory and experiment. [64]

2.5 Monte Carlo Method

Apart from integral equations, there are different other ways to study the huge configuration integral of Eq. (2.45) which involves integrations of the order of the Avogadro constant $N_A \approx 10^{23}$ with the Boltzmann factor as integrand. In principle, we can make further assumptions to reduce this integral severely but additional basic assumptions run the risk of oversimplifying the model and depart from realism and experimental conditions. For example, Z can be exactly solved for the one-dimensional Ising model [63, 65] or if intermolecular interactions are neglected (i.e. $U = 0$) which leads to the ideal gas law [66], but both models lack the phenomenon of phase transition which we are interested in.

Another way, the mean-field approach, simplifies the integrand by the assumption that correlations between particles are negligible and that every particle ‘feels’ the same field caused by the other particles which implies their homogeneous distribution over space. In this case the integral factors, which can be used for example to achieve the van der Waals equation, the first mathematical description of the gas–liquid phase transition. [67]

A more refined approach, which incorporates the possibility that matter may be inhomogeneously distributed in space, is density functional theory but here the inhomogeneity is restricted to a local density function. [68] If we search for a solution that accounts for the position and correlation of particles in an explicit manner, we have to turn to computer aided molecular simulation techniques to explore the phase space. A prominent example is molecular dynamics, where the time dependent phase

2.5 | Monte Carlo Method

space of dimension $6N$ is approximated to yield time dependent properties such as the diffusion coefficient. [69] Since we are not interested in dynamic properties of fluids but in their static behaviour, such as sorption phenomena, the solution of the configuration integral of dimension $3N$ would be advantageous.

In this work we use a method to numerically approximate the still tremendous configuration integral of Eq. (2.45). In general this can be done by choosing some points, called nodes \mathbf{r}_n , compute the values $Z(\mathbf{r}_n)$, fit a function $\tilde{Z}(\mathbf{r}_n)$ through these points and calculate $\int \tilde{Z}(\mathbf{r}_n) d\mathbf{r}_n$. A simple approach is that we choose equidistant nodes to cover the function homogeneously. Since a function must be bounded to deliver a finite value, values near its limits must vanish or at least converge to zero. In case of a one-dimensional function there would be only two nodes at the upper and lower limit which make no contribution to the integral but this holds also for every additional dimension of the integral. So the ratio of inner nodes to nodes at the border can be approximated as [32]

$$\left(\frac{p-2}{p}\right)^d \simeq e^{-\frac{2d}{p}} \quad (2.57)$$

where p is the number of nodes per dimension d . Since the configuration integral has dimension $d = 3N_A \approx 10^{23}$, nearly all nodes would be at the surface of this hyperspace if we arrange them in an equidistant fashion.

If we use a so-called *importance sampling technique* first used by Metropolis et al. [70] to generate configurations \mathbf{q} according to their probability $P(N, \mathbf{q})$, then we evaluate just such parts of the integral which make significant contributions. In this way our system evolves along particular, physically likely tracks through phase space. Additionally all values of quantity M are also generated according to their probability and Eq. (2.47) can be estimated in a finite number of trials τ as

$$\langle M \rangle = \frac{\sum_N \int M \mathcal{P}(N, \mathbf{q}) d^{3N} \mathbf{q}}{\sum_N \xi \int \mathcal{P}(N, \mathbf{q}) d^{3N} \mathbf{q}} \approx \frac{1}{\tau} \sum_{\tau} M_{\tau} \quad \text{with } \xi = 1/(N! \Lambda^{3N}) \quad (2.58)$$

because in most cases the integrand $M\mathcal{P}(N, \mathbf{q})$ is significant where $\mathcal{P}(N, \mathbf{q})$ of the denominator is significant. [69] In Eq. (2.58) we use the unnormalised probability $\mathcal{P}(N, \mathbf{q}) = e^{\gamma N} e^{-\beta U(\mathbf{q})}$ to emphasise the relation between numerator and denominator.

The advantage of Eq. (2.58) is that the average of a quantity reduces to an arithmetic mean. Moreover the calculation becomes independent of initial conditions after a couple of trials. Even from an improbable configuration as a starting point this technique directs the system to the most likely path through phase space and henceforward takes only important contributions into account.

The *Monte Carlo method* implements the above ideas [70–72] and is used throughout this work to calculate properties of the system under consideration.

2.6 Markov Process

It is of great relevance for the Monte Carlo method that configurations \mathbf{q} are generated according to their corresponding probability $P(N, \mathbf{q})$. Only when the system evolves with the correct probability in phase space is the approximation in Eq. (2.58) valid. In this connection Markov asserted in 1913 that such a process must generate a future state from the present state alone but must not depend on any past ones. [73] Every process with a one-step memory in which a state emanates just from the previous state is called a Markov process, or, in the case of a finite state-space, a Markov chain. Here, we restrict ourselves to Markov chains with finite phase space. The probability $P_j \equiv P(N_j, \mathbf{q}_j)$ that configuration \mathbf{q}_j is generated from a configuration \mathbf{q}_i is specified through the transition matrix π_{ij} which is of the same dimension as the phase space

$$P_j = \sum_i P_i \pi_{ij} \quad \text{for } i \neq j \quad (2.59)$$

Single elements of this transition matrix π_{ij} determine the probability of reaching the configuration \mathbf{q}_j from another configuration \mathbf{q}_i . Because the other configurations \mathbf{q}_i occur with the probability P_i , in Eq. (2.59) the transition probabilities π_{ij} are weighted by the probability P_i that the respective (other) configuration occurs. Since we are talking about probabilities it makes sense that rows of the transition matrix add to one

$$\sum_j \pi_{ij} = 1 \quad (2.60)$$

and π_{ij} is termed a stochastic matrix.

To follow the evolution of the system through configuration space we need an initial state \mathbf{q}_i which is not known but given by probability, somehow related to elements of π_{ij} . We denote this initial state by a vector \mathbf{v}_i where its elements v_i are the probabilities that the system is in state i . The following state \mathbf{v}_j is also known with a certain probability determined by

$$\mathbf{v}_j = \mathbf{v}_i \pi_{ij} \quad (2.61)$$

Provided that the transition matrix obeys the *principle of detailed balance* (see Section E.1.2 of [32], or [74]) such that $\mathbf{v}_i \pi_{ij} = \mathbf{v}_j \pi_{ji}$, any further application of π results

in the convergence of \boldsymbol{v} which therefore must obey the *eigenvalue* equation

$$\boldsymbol{\pi}\boldsymbol{v} = \tilde{\boldsymbol{v}} \quad (2.62)$$

$$\begin{pmatrix} \pi_{11} & \pi_{12} & \pi_{13} & \dots \\ \pi_{21} & \pi_{22} & \pi_{23} & \dots \\ \pi_{31} & \pi_{32} & \pi_{33} & \dots \\ \vdots & \vdots & \vdots & \ddots \end{pmatrix} \begin{pmatrix} v_{11} \\ v_{21} \\ v_{31} \\ \vdots \end{pmatrix} = \begin{pmatrix} \tilde{v}_{11} \\ \tilde{v}_{21} \\ \tilde{v}_{31} \\ \vdots \end{pmatrix} \quad (2.63)$$

where \boldsymbol{v} is the *eigenvector* and $\tilde{\boldsymbol{v}}$ the converged state of the system. An illustrative example of this convergence is given in Chapter 4.3 of [69]. Consequently, a system property M converges towards its exact value and becomes independent of the initial condition which therefore can be chosen arbitrarily.

Since we are dealing with a transition matrix whose elements represent the probability of reaching one configuration from another one, we have to determine in which way configurations of the grand canonical ensemble differ. In principle there are two kinds of changes that can occur: the configuration \mathbf{q} changes because a particle moves or the particle number N changes due to a particle exchange with the surroundings.

First we consider that a particle changes its spatial position and follow Metropolis et al. [70]. Since the particle number remains constant, the transition probability of generating configuration \mathbf{q}_j out of configuration \mathbf{q}_i is given by

$$\pi_{ij}^c = \frac{P_j}{P_i} = e^{-\beta\Delta U_{ij}} \quad \text{with } \Delta U_{ij} = U_j - U_i \quad (2.64)$$

where we use Eq. (2.46) with $N_i = N_j$ and the shorthand notation $U_i \equiv U(\mathbf{q}_i)$. According to one's physical intuition the probability of reaching one configuration from another depends on the energy of both configurations. While the probability of configurations P_i and P_j actually has to be normalised by the grand partition function Ξ , fortunately their ratio (i.e. the transition probability) results in a normalised probability. Since the transition probability π_{ij} reaches unphysical values greater than 1 for $\Delta U < 0$, these transitions are always accepted with a probability of 1. To summarise this, the probability π_{ij}^c that configuration \mathbf{q}_j is accepted if the system is actually in configuration \mathbf{q}_i is

$$\pi_{ij}^c = \begin{cases} 1 & \Delta U_{ij} \leq 0, \quad i \neq j \\ e^{-\beta\Delta U_{ij}} & \Delta U_{ij} > 0, \quad i \neq j \end{cases} \quad (2.65)$$

so there is a chance that the system remains in configuration \mathbf{q}_i given by

$$\pi_{ii}^c = 1 - \sum_{i \neq j} \pi_{ij} \quad (2.66)$$

Next, we consider the case when the particle number N changes which can be simulated by the destruction of random particles and the creation of particles at random positions. The transition probability from configuration \mathbf{q}_i to another configuration \mathbf{q}_j which differ in the creation of one particle $N_j = N_i + 1$ is given by

$$\pi_{ij}^+ = \frac{P_j}{VP_i} = \frac{N_j! \Lambda^{3N_j}}{VN_i! \Lambda^{3N_i}} \frac{e^{\beta\mu N_i} e^{-\beta U_i}}{e^{\beta\mu N_j} e^{-\beta U_j}} \quad (2.67)$$

$$= \frac{N_j \Lambda^3}{V} e^{\beta\mu} e^{-\beta\Delta U_{ij}} \quad (2.68)$$

where we use Eqs. (2.46) with the factor $1/V$ as a result of the discrepancy in the dimension of phase space between initial and final state. Thus, the creation of one particle can be expressed as [75]

$$\pi_{ij}^+ = e^{B - \ln N_j - \beta\Delta U_{ij}} \quad (2.69)$$

while the destruction of one particle that results in configuration \mathbf{q}_j with $N_j = N_i - 1$ is related to

$$\pi_{ij}^- = e^{-B + \ln N_i + \beta\Delta U_{ij}} \quad (2.70)$$

The particle numbers N_i and N_j belong to configurations before and after the particle number changes, whereas B is related to the de Broglie wavelength Λ of Eq. (2.19) and the chemical potential μ through [75]

$$B = \beta\mu - \ln(\Lambda^3/V) = \beta\mu_{ex} + \ln \langle N \rangle \quad (2.71)$$

where $\langle N \rangle$ denotes the ensemble average of the fluid particle number and μ_{ex} is the excess chemical potential. The latter quantity is a measure for the difference of the chemical potential from the chemical potential of an ideal gas and, thus, we imply that the (virtual) fluid reservoir is ideal in character. [76]

If π_{ij}^\pm results in probabilities greater than 1 they are counted as 1. Thus, we get the following probabilities of creating or destroying one particle

$$\pi_{ij}^{gc} = \begin{cases} 1 & \pi_{ij}^\pm \geq 1, \quad i \neq j \\ \pi_{ij}^\pm & \pi_{ij}^\pm < 1, \quad i \neq j \end{cases} \quad (2.72)$$

The use of Eqs. (2.65) and (2.72) is a very useful technique [75, 77] to explore grand canonical systems with the Monte Carlo method unless there is a *bottleneck*, that is, an unlikely transition probability between two significant regions of phase space. [78] For example, bottlenecks occur often in the two phase region near phase transitions and in this case we would have to look for another transition matrix or at least for some modifications of the existing one.

3

A Model of Flexible Walls

The treatment of fluids developed in the preceding chapter is now applied to a particular model. It is suitable to base the model on an experimental setup of interest that, of course, must be simplified to be computationally efficient.

In this study MCM-type silica matrices provide an easy to model system because of their disconnected, regular arranged pores of almost uniform width and shape [19] which allows experiments of high accuracy. [53] Individual pores of this type are of hexagonal to nearly cylindrical shape [79] where the length can be considered as infinite compared to the (average) pore diameter which is typically in the range of 2-10 nm. The pores are well ordered in a two-dimensional hexagonal array, sketched in Fig. 3.1a.

3.1 Pore Filling in Ordered Mesoporous Materials

According to sorption experiments a confined fluid condenses if the pressure in the bulk reservoir exceeds the pressure at which capillary condensation sets in (afterwards discussed in detail in Section 4.1). One may assume that the condensation pressure in MCM-41 depends on the width of an *individual* pore because pores are regular and disconnected. Consequently, all pores up to a particular width condense at certain pressure and the now-filled pores should be distributed at random across the

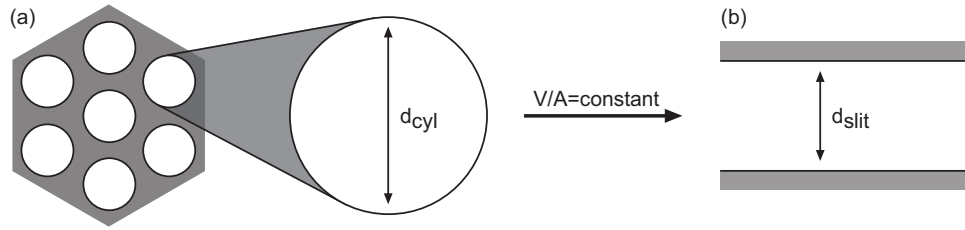


FIG. 3.1: (a) Sketch of a two-dimensional hexagonal array of cylindrical pores representing the structure of MCM-41. To maintain the degree of confinement while pore geometry is changed from a cylinder of diameter d_{cyl} to a (b) slit of width d_{slit} , we assume that the ratio of pore volume V to wall area A must remain constant.

confining media because pores of (slightly) different widths are randomly distributed throughout the mesoporous material. [19]

On the other hand, it has been suggested [80–83] that the filling process of an ordered mesoporous material proceeds via the formation of clusters of liquid filled pores. This suggestion is based on the belief that an individual pore affects a neighbouring pore through the associated deformation of the pore wall which both share. Thus, the filling of a pore would induce the filling of its neighbours and would result in clusters of liquid filled pores during the sorption process. In other words, pores would be affected through a long-range interaction mechanism of local deformations which are transmitted throughout the mesoporous material. However, this assumption is based on a detailed analysis of Nitrogen sorption isotherms in SBA-15 [81] (whose structure almost resembles that of MCM-41) where the correlation of pores can only be extracted *indirectly*.

Contrary to this indirect analysis, neutron scattering data of perfluoropentane in SBA-15 from recent experiments [84] are fully consistent with the assumption that the spatial distribution of pores remains random during the sorption process, which confirms the assumption that individual pores are unaffected by their neighbours. With regard to this *direct* experimental finding, we base the description of such ordered mesoporous materials on a *single* isolated pore.

3.2 Degree of Confinement

In this work we make contact to the experimental system of n-pentane (hereafter simply referred to as pentane) confined in MCM-41(16) [34] whose pore geometry is nearly cylindrical [79], see Fig. 3.1a. In general, the exact pore geometry is subdominant to the fact that matter is confined as, for example, capillary condensations occurs

3.2 | Degree of Confinement

in cylindrical as well as in slit pores. [31] According to this argument, we choose a model of slit pore geometry, that is, the fluid is confined between two parallel plane walls which are separated by a particular distance (i.e. the slit pore width). To establish a connection between the slit pore model and the experimental (cylindrical) system, we estimate the size of a pentane molecule and then adjust the slit pore size to resemble the confining situation of its experimental counterpart.

The space which is occupied by a pentane molecule (C_5H_{12}) is estimated as follows: At temperature $T \approx 273$ K the bulk density of pentane is $\rho_{C_5H_{12}} = 0.63$ g cm⁻³. With regard to the molar mass $M_{C_5H_{12}} = 72$ g mol⁻¹ the molar volume $V_{C_5H_{12}}^{mol}$ is given by

$$V_{C_5H_{12}}^{mol} = \frac{M_{C_5H_{12}}}{\rho_{C_5H_{12}}} \approx 10^{-4} \text{ m}^3 \text{ mol}^{-1} \quad (3.1)$$

and the volume $V_{C_5H_{12}}$ of a single pentane molecule can be approximated as

$$V_{C_5H_{12}} = \frac{V_{C_5H_{12}}^{mol}}{N_A} \approx 1.7 \times 10^{-28} \text{ m}^3 \quad (3.2)$$

where we imply a packing fraction of $\phi = 1$ which means that all available space is occupied by pentane molecules, a physically impossible situation. The packing fraction ϕ is the occupied space by N particles related to the volume V written as

$$\phi = \frac{NV_{sphere}}{V} = \rho \frac{1}{6} \pi \sigma_{sphere}^3 \quad (3.3)$$

where $\rho = N/V$ is the density and we assume spherical particles of volume V_{sphere} and diameter σ_{sphere} . The packing fraction is experimentally accessible *in principle*, e.g. through X-ray scattering, and is determined for liquid pentane as $\phi_{exp} = 0.49$. [85] From Eq. (3.3) it is obvious that ϕ depends on density ρ and particle diameter σ_{sphere} whose value is sensitive to the measurement method and conditions such as temperature. [86] Even in computer simulations the size of a particle is only well-defined in case of hard sphere systems and otherwise usually relies on convention.

To make contact with the used simulation method, we have to interpret ϕ on the basis of Monte Carlo simulations, that is, on usual values for ρ and σ_{sphere} . It turns out that comparable bulk systems with $\sigma_{sphere} \equiv 1$ exhibit a critical density $\rho_c \approx 0.3$ which can be regarded as the lower limit of ρ in liquid phases (afterwards discussed in Section 4.5.4). Since the lower limit of ρ is shifted to larger values with decreasing temperature, we assume that a comparable bulk simulation exhibit a density $\rho \approx 0.4$ for a liquid phase near the gas–liquid phase transition which is the case for pentane with boiling temperature $T_b \approx 308$ K $\approx T$. Assuming pentane to be a sphere, we

estimate the diameter $\sigma_{C_5H_{12}}$ of a pentane molecule as

$$\begin{aligned}\phi V_{C_5H_{12}} &= \frac{1}{6}\pi\sigma_{C_5H_{12}}^3 \\ \sigma_{C_5H_{12}} &= \sqrt[3]{\frac{6V_{C_5H_{12}}}{\phi}} \approx 0.408 \text{ nm}\end{aligned}\quad (3.4)$$

where we use Eqs. (3.2) and (3.3) with $\rho = 0.4$.

With regard to the experimental system of pentane in a MCM-type silica matrix, the fluid-wall interaction is considered to be short-ranged. Thus, the wall affects only fluid particles in its immediate vicinity while the wall's influence on fluid particles at larger distances can be neglected. According to this consideration, we assume that the ratio of pore volume to wall area is the crucial factor of a confined system and therefore determines the *degree of confinement* ψ of a system.

In cylindrical geometry (*cyl*) the degree of confinement ψ_{cyl} can be written as

$$\psi_{cyl} = \frac{V_{cyl}}{A_{cyl}} = \frac{\pi(d_{cyl}/2)^2}{\pi d_{cyl}} = \frac{d_{cyl}}{4}\quad (3.5)$$

where V_{cyl} is the volume, A_{cyl} is the wall area and d_{cyl} is the diameter of the cylindrical pore. On the other hand, in slit pore geometry (*slit*) this ratio is given by

$$\psi_{slit} = \frac{V_{slit}}{A_{slit}} = \frac{d_{slit}a^2}{2a^2} = \frac{d_{slit}}{2}\quad (3.6)$$

with the slit pore width d_{slit} and a as the considered length in x - and y -direction of the pore (i.e. the area of upper and lower wall). To keep the same degree of confinement while geometry is changed from a cylinder to a slit (see Fig. 3.1a,b), one obtains

$$\psi_{cyl} = \psi_{slit} \Leftrightarrow d_{slit} = \frac{1}{2}d_{cyl}\quad (3.7)$$

where we use Eqs. (3.5) and (3.6). The pore diameter d_{cyl} is accessible from experimental data through, e.g., the improved Kruk-Jaroniec-Sayari method (KJS) [87, 88], the method of Barrett, Joyner and Halenda (BJH) [89] or Density Functional Theory (DFT) [90].

In general, DFT establishes a connection between a thermodynamic potential such as the grand potential and the local density in form of a functional. Applied to a confined system, the global minimum of the thermodynamic potential is determined by adjusting the local density of the fluid within the pore from which the total amount of adsorbed fluid matter is obtained. Thus, DFT yields an adsorption isotherm which is further fitted to experimental data by adjusting the pore diameter of the confined model system, resulting in d_{cyl} .

Other approaches are basing on the Kelvin equation (see appendix C) which establishes a relationship between the radius of a (macroscopic) cylinder and the bulk

3.2 | Degree of Confinement

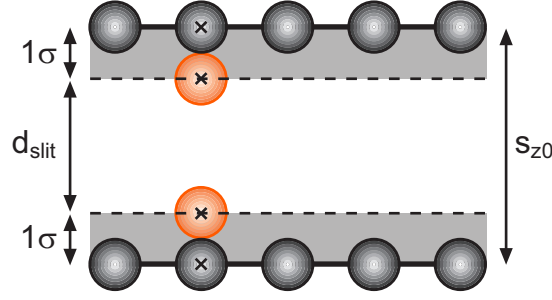


FIG. 3.2: In the model system fluid particles (orange) can only approach wall particles (dark grey) up to the distance of 1σ (grey area) on account of repulsive forces of fluid and wall particles and the fact that both share the same size. Thus, the total of 2σ of the pore width s_{z0} is inaccessible to fluid particles.

fluid pressure of a connected reservoir, at which the fluid inside the cylinder condenses. Since MCM-type silicas consist of uniform pores of nearly cylindrical shape, the Kelvin equation can be used to calculate the pore radius from the experimentally determined bulk pressure at which capillary condensation occurs. On this basis the BJH method takes into account the reduced pore radius as a result of preadsorbed fluid layers at the pore wall, whereas the improved KJS method makes further modifications to improve this macroscopic relation according to mesoporous materials with pore widths smaller than 10 nm.

In general, the pore diameter is always determined from experimental data by assuming an underlying model that may take into account a repulsive fluid–wall interaction, as in some DFT calculations, or that ignores the repulsion of walls such as the BJH and KJS methods which are basing on the Kelvin equation. Thus, we have to consider the discrepancy between the model of the present study and the one that has been used to determine the pore size of the experimental system.

The walls of the model system used throughout this work consist of discrete wall particles which are of the same size as the fluid, that is both share the diameter σ . To make contact to the pore diameter determined through the KJS method, d_{cyl}^{KJS} , we must account for the distance of (approximately) 1σ at each substrate which is inaccessible to fluid particles according to repulsive forces of fluid and wall particles, illustrated in Fig. 3.2. If s_{z0} denotes the distance between wall particles of opposite walls, then Eq. (3.7) can be used to express s_{z0} as

$$s_{z0} \simeq d_{slit} + 2\sigma = \frac{1}{2}d_{cyl}^{KJS} + 2\sigma \quad (3.8)$$

The (average) pore diameter of MCM-41(16) was determined according to the KJS method as $d_{cyl}^{KJS} = 3.91$ nm [34] or expressed in units of pentane diameters as $d_{cyl}^{KJS} =$

$9.6\sigma_{C_5H_{12}}$ using Eq. (3.4). Finally, Eq. (3.8) can be written as

$$s_{z0} = \frac{1}{2}d_{cyl}^{KJS} + 2\sigma \approx 6.8\sigma \quad (3.9)$$

where we omit the subscript ' C_5H_{12} ' from now on. Thus, the slit pore width of $s_{z0} = 6.8\sigma$ should reflect the confining conditions of the experimental system.

3.3 Harmonic Approximation

With regard to the discrete structure of the confining wall, in a first approach the wall particles are fixed at lattice sites according to the arrangement of an ideal crystal. Following a more refined treatment the wall particles are allowed to move from their lattice sites to some extent on account of their thermal energy. Since ideal crystals resemble configurations which minimise the potential energy, the movement of a wall particle from its ideal position must be connected with an increase of potential energy. Thus, the potential energy of a wall particle is minimum at its lattice site $\mathbf{r}_0 = \{r_{1,0}, r_{2,0}, r_{3,0}\}$. With respect to small deviations $\mathbf{r} - \mathbf{r}_0$ from this equilibrium position, a Taylor expansion around \mathbf{r}_0 approximates its potential energy $u(\mathbf{r})$ through

$$u(\mathbf{r}) = u(\mathbf{r}_0) + (\mathbf{r} - \mathbf{r}_0) u^{(1)}(\mathbf{r}_0) + \frac{1}{2} (\mathbf{r} - \mathbf{r}_0)^2 u^{(2)}(\mathbf{r}_0) + \xi (\mathbf{r} - \mathbf{r}_0)^3 + \dots \quad (3.10)$$

where $\mathbf{r} = \{r_1, r_2, r_3\}$ is the position of the wall particle and terms of the form $u^{(m)}(\mathbf{r}_0)$ denote the m -th derivative of $u(\mathbf{r})$ with respect to \mathbf{r} at $\mathbf{r} = \mathbf{r}_0$, expressed as

$$u^{(m)}(\mathbf{r}_0) \equiv \left. \frac{d^m u(\mathbf{r})}{d\mathbf{r}^m} \right|_{\mathbf{r}=\mathbf{r}_0} \quad (3.11)$$

Since energy is minimum at \mathbf{r}_0 the linear term in Eq. (3.10) vanishes. Further, we set $u(\mathbf{r}_0) \equiv 0$ and disregard all terms of third or higher order, therefore we approximate

$$u(\mathbf{r}) \approx \frac{1}{2} (\mathbf{r} - \mathbf{r}_0)^2 u^{(2)}(\mathbf{r}_0) \quad (3.12)$$

With the transformation of the variables $\Delta r = |\mathbf{r} - \mathbf{r}_0|$ we obtain the potential of the harmonic oscillator as a first approximation through

$$u(\mathbf{r}) = \frac{1}{2} \Delta r^2 u^{(2)}(0) = \kappa \Delta r^2 \quad (3.13)$$

where $\kappa \equiv u^{(2)}(0)/2 \geq 0$ is (one-half) the harmonic force constant. Regarding the one dimensional movement along the Cartesian principal z -axis, the mean square displacement $\langle \Delta z^2 \rangle$ of a single wall particle is given by

$$\langle \Delta z^2 \rangle = \frac{\int \Delta z^2 e^{-\beta U(\Delta z)} dz}{\int e^{-\beta U(\Delta z)} dz} \quad (3.14)$$

3.4 | Model of Thermally Coupled Walls

where we use Eqs. (2.46) and (2.47) with particle number $N = 1$. The numerator leads with Eq. (3.13) and integration by parts to

$$\int \Delta z^2 e^{-\beta U(\Delta z)} dz = \frac{1}{2\beta\kappa} \int e^{-\beta U(\Delta z)} dz \quad (3.15)$$

which simplifies Eq. (3.14) to result in

$$\langle \Delta z^2 \rangle = \frac{k_B T}{2\kappa} \quad (3.16)$$

As expected the mean square displacement of a wall particle is proportional to temperature T and that is why we term a wall *thermally coupled* if its particles are bound by harmonic potentials of Eq. (3.13). The larger force constant κ the lesser is the mean square displacement of wall particles, thus, κ resembles a substance specific property of the confining media which determines its rigidity. Moreover, for $T\kappa^{-1} > 0$ we can only fix the lattice site of a wall particle, i.e. the position where $u(\mathbf{r}) = 0$, but not the wall particle because of its mobility.

3.4 Model of Thermally Coupled Walls

From a simple perspective the fluid of interest, i.e. pentane, consists of an outer shell of hydrogen atoms which encloses an inner carbon core. Consequently, the interaction of a pentane molecule with its surroundings can be reduced to the interaction of one species, i.e. hydrogen, while the other species can be neglected because of steric considerations. In this treatment we disregard the fact that pentane bears actually two types of hydrogen where one is part of a methylene group whereas the other belongs to a methyl group. Both types of hydrogen differ only slightly in their interaction [91] (compared with the discrepancy between elements) and, thus, we introduce an average potential for both types of hydrogen.

Since pentane bear no long-range forces [85], we can use an explicitly short ranged potential of the form

$$u(r) = \begin{cases} u_{sh}(r), & r \leq r_c \\ 0, & r > r_c \end{cases} \quad (3.17)$$

where r_c is the cut-off distance at which $u_{sh}(r)$ vanishes. Explicitly short-ranged potentials are advantageous in Monte Carlo simulations (see Section 3.6) and therefore a cut-off distance $r_c = 3.5\sigma$ is used throughout this work.

To simulate the gas–liquid phase behaviour of pentane, the potential $u_{sh}(r)$ of Eq.

(3.17) must involve an attractive component, as already mentioned in chapter 1. Here, the shifted 12-6 Lennard–Jones (LJ) potential is used, written as [69]

$$u_{sh}(r) = u_{LJ}(r) - u_{LJ}(r_c) - \left. \frac{du_{LJ}(r)}{dr} \right|_{r=r_c} (r - r_c) \quad (3.18)$$

that vanishes continuously with its first derivative (i.e. the intermolecular force) at r_c unlike the full Lennard–Jones potential [92, 93] defined as

$$u_{LJ}(r) = 4\epsilon \left[\left(\frac{\sigma}{r} \right)^{12} - \left(\frac{\sigma}{r} \right)^6 \right] \quad (3.19)$$

where σ resembles the diameter of particles and ϵ is the strength of intermolecular interactions, i.e. the well depth of the potential. The Lennard–Jones potential accounts for the attractive and repulsive components of (nonpolar, spherical) particles consisting of a negatively charged electron cloud around a positively charged core, discussed before in Chapter 1. The attractive term of the LJ potential decays with r^{-6} as a result of temporary dipoles mutually induced by nearby electron clouds and is overwhelmed at short distances by a repulsive term reflecting the repulsion of cores. The decay of repulsion is chosen to be $r^{-12} = r^{-6}r^{-6}$ for reasons of computational efficiency. [69] The shifted version of Eq. (3.18) preserves the features of the full LJ potential but transforms the latter into an explicitly short-ranged potential, disregarding the slow, monotonic decay at distances larger than a few particle diameters.

Since the Lennard–Jones potential reflects the basic interaction of (ordinary, non-polar) matter, it has been used to simulate a wide variety of particles ranging from noble gases [94, 95] and other atomic species [69] to small (nearly) spherical particles like methane or CF_4 [96] and to functional groups of organic molecules [91, 97, 98]. In principle, the parameters ϵ and σ of the LJ potential are accessible through *ab initio* calculations [99, 100] or by fitting simulation results to empirical data [101].

On account of the typical low density of fluid systems, we consider only a pairwise additive interaction of particles and neglect interactions between three or more particles. This treatment reflects the salient features of fluids in general. [69] Using the above argument, the potential energy U_{ff} of N fluid particles can be written as

$$U_{ff}(\mathbf{R}) = \sum_{i=1}^N \sum_{j>i}^N u(r_{ij}) \quad \text{with } r_{ij} = |\mathbf{r}_i - \mathbf{r}_j| \quad (3.20)$$

where $u(r)$ is the potential given in Eq. (3.17), $\mathbf{R} \equiv (\mathbf{r}_1, \mathbf{r}_2, \dots, \mathbf{r}_N)$ is a short-hand notation for the configuration of fluid particles and \mathbf{r}_i respectively \mathbf{r}_j denotes the position of the fluid particle i respectively j .

When a fluid is confined by surfaces, the outer molecular layer of the wall dominates the fluid–wall interaction. It is the surface layer where adsorption or desorption

3.4 | Model of Thermally Coupled Walls

of fluids takes place and which prevents the fluid from leaving the system, whereas inner wall layers have lesser influence as long as short-ranged interactions are considered: a fact that can be used e.g. to tune the wetting behaviour of surfaces through monolayer coatings. [102–104]

Following this idea, we build a wall of a single layer of N_s wall particles which are of the same type as the fluid, i.e. they have the same size σ and interact in the same manner. The lattice sites \mathbf{r}_{i0} of a wall are arranged to resemble the (100) plane of a face centred cubic (fcc) lattice¹, shown in Fig. 3.3a. To achieve slit pore geometry we put two parallel walls, denoted by k , at a distance s_{z0} from each other where one wall is located at the bottom ($k=1$) and the other at the top ($k=2$) of the simulation cell, see Fig. 3.3b. Thus, the lattice points of wall particles are fixed at $z = \pm s_{z0}/2$, with ‘-’ corresponding to $k=1$ and ‘+’ corresponding to $k=2$. Moreover, for every lattice point in one wall, there exists an opposite lattice point in the other wall with the same equilibrium position with respect to x - and y -direction. This means that there are always two lattice points in the simulation box which differ only in their z -coordinates. According to this arrangement any shear stress is omitted *on average* and the condition to use Eq. (2.9) is fulfilled.

Regarding the discrete structure of the wall there is a contribution to the potential energy which originates from the interaction between fluid and wall particles given by

$$U_{fs}(\mathbf{R}, \mathbf{R}_s) = \epsilon_{fs} \sum_{k=1}^2 \sum_{i=1}^N \sum_{j=1}^{N_s} u(r_{ij}^{[k]}) \quad \text{with } r_{ij}^{[k]} = |\mathbf{r}_i - \mathbf{r}_j^{[k]}| \quad (3.21)$$

where ϵ_{fs} is used to tune the strength of the fluid–wall interaction in terms of the fluid–fluid interaction ϵ . In Eq. (3.21) \mathbf{r}_i denotes the position of the i -th fluid particle and $\mathbf{r}_j^{[k]}$ denotes the position of the j -th wall particle of wall k . Moreover, $\mathbf{R}_s \equiv (\mathbf{r}_1^{[1]}, \mathbf{r}_2^{[1]}, \dots, \mathbf{r}_{N_s}^{[1]}, \mathbf{r}_1^{[2]}, \mathbf{r}_2^{[2]}, \dots, \mathbf{r}_{N_s}^{[2]})$ is a short-hand notation for the configuration of wall particles.

At the beginning of a simulation we place one wall particle at each lattice site and bound it with the harmonic potential of Eq. (3.13) to this position. The potential energy $U_h^{[k]}$ of wall k which originates from deviations of these equilibrium positions (i.e. the potential minimum) is given by

$$U_h^{[k]}(\mathbf{R}_s, \kappa) = \kappa \sum_{i=1}^{N_s} (\Delta r_i^{[k]})^2 \quad \text{with } \Delta r_i^{[k]} = |\mathbf{r}_i^{[k]} - \mathbf{r}_{i0}^{[k]}| \quad (3.22)$$

¹This notation is based on the original model of Diestler and Schoen [105], discussed in more detail in A.1 (p. 155). Since we consider only the surface layer of a lattice, in fact any cubic lattice corresponds to this two-dimensional arrangement.

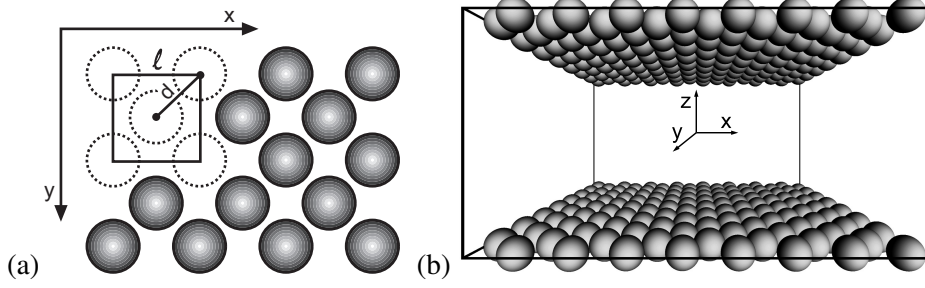


FIG. 3.3: (a) Sketch of (100) plane of the fcc lattice with unit cell and lattice parameter ℓ . The nearest neighbour distance $d = 2^{1/6}\sigma$ between wall particles of diameter σ corresponds to the minimum of LJ interaction. (b) Simulation box of slit pore with fcc (100) walls at top and bottom (without fluid). Wall particles are located at their lattice sites, thus, resembling an ideal fcc (100) structure.

where $\mathbf{r}_i^{[k]}$ is the position of the i -th wall particle of wall k and $\Delta r_i^{[k]}$ determines the absolute departure from its lattice site $\mathbf{r}_{i0}^{[k]}$.

To prevent that wall particles come unrealistically close to one another², they interact through an additional potential $u(r)$ according to Eq. (3.17) which give rise to a potential energy contribution $U_w^{[k]}(\mathbf{R}_s)$ written as

$$U_w^{[k]}(\mathbf{R}_s) = \epsilon_{ss} \sum_{i=1}^{N_s} \sum_{j>i}^{N_s} u(r_{ij}^{[k]}) \quad (3.23)$$

with the distance $r_{ij}^{[k]} = |\mathbf{r}_i^{[k]} - \mathbf{r}_j^{[k]}|$ of two wall particles i and j as well as the strength ϵ_{ss} of the wall particle interaction. Note that ϵ_{ss} and ϵ_{fs} , cf. Eq. (3.21), are not independent of each other but connected using Berthelot's combining rule [99, 106] to yield

$$\epsilon_{fs} = \sqrt{\epsilon\epsilon_{ss}} \quad (3.24)$$

Thus, changing ϵ_{fs} implies a change of ϵ_{ss} as well and Eq. (3.23) can be rewritten as

$$U_w^{[k]}(\mathbf{R}_s) = \frac{\epsilon_{fs}^2}{\epsilon} \sum_{i=1}^{N_s} \sum_{j>i}^{N_s} u(r_{ij}^{[k]}) \quad (3.25)$$

We choose the nearest neighbour distance of the fcc structure to match the minimum of the wall particle interaction which corresponds to $2^{1/6}\sigma$ in case of the LJ potential, illustrated in Fig. 3.3a. This implies a lattice parameter $\ell = \sqrt[3]{4}\sigma$ and the areal wall

²The need for an additional potential at smaller values of κ is discussed in the Appendix A.2 (p. 156).

3.5 | Semi-Grand Canonical Ensemble

particle density $\rho_s = 2\sigma^2/\ell^2$.

The potential energy of both walls is given by Eqs. (3.22) and (3.25) as

$$U_{ss}(\mathbf{R}_s, \kappa) = \sum_{k=1}^2 U_w^{[k]} + U_h^{[k]} = \sum_{k=1}^2 \left[\frac{\epsilon_{fs}^2}{\epsilon} \sum_{i=1}^{N_s} \sum_{j>i}^{N_s} u(r_{ij}^{[k]}) + \kappa \sum_{i=1}^{N_s} (\Delta r_i^{[k]})^2 \right] \quad (3.26)$$

where N_s is the number of wall particles in wall k . According to this potential energy contribution and those of Eqs. (3.20) and (3.21) the total potential energy of the system is written as

$$U(\mathbf{R}, \mathbf{R}_s, \kappa) = U_{ff}(\mathbf{R}) + U_{fs}(\mathbf{R}, \mathbf{R}_s) + U_{ss}(\mathbf{R}_s, \kappa) \quad (3.27)$$

Apart from the interaction between wall particles, this model was already used by Diestler and Schoen to couple a fluid phase to thermally coupled walls. [105] Here it is invoked to investigate, on the one hand, the thermodynamic behaviour of the fluid in dependence on the wall rigidity and, on the other hand, the mechanical wall properties in reaction to the fluid's thermodynamic state. In this context the force constant κ plays a key role since it determines the flexibility of the wall and with it we are able to tune the wall deformability. With large κ the wall resembles an almost rigid structure where wall particles are located virtually at their lattice sites, i.e. every displacement is associated with a high energy penalty through the binding potential, see Fig. 3.4a. By lowering κ , the wall particles move farther from their lattice points and are able to respond to the fluid to a greater extent. This can lead to an average pore size s_z which may differ from the distance s_{z0} that lattice sites of opposite walls are apart, sketched in Fig. 3.4b. In other words, s_{z0} is an input parameter of the Monte Carlo simulation contrary to s_z which is a result of the simulation.

Please note that wall particles of the present model system do not resemble the wall at the atomic scale but rather can be considered as portions of the confining medium which are *coarse-grained* to the same degree as the fluid (see Section 3.2). Except for the explicitly treated wall layer, remote substrate layers are accounted for in an average manner through the harmonic force constant κ of Eq. (3.22) representing the stiffness of a macroscopically thick body. Thus, we are *effectively* dealing with a multilayered substrate which is resolved at the molecular level of the fluid.

3.5 Semi-Grand Canonical Ensemble

The present model system is slightly unconventional and needs some comment because we deal with two types of particles which are treated in different ways. At first

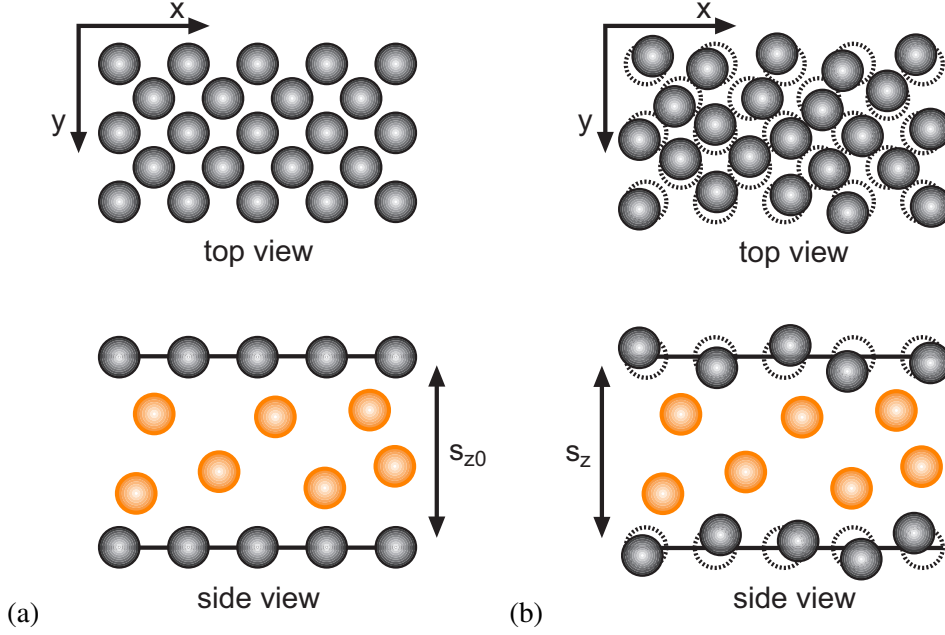


FIG. 3.4: Schematic representation of the model system. Side views show spherical fluid particles (orange) confined between two planar solid substrates, while top views exhibit the arrangement of wall particles (grey) across the plane of the substrate. **(a)** The limiting case of a rigid substrate also corresponds to the initial configuration of wall particles which are arranged according to the (100) plane of the fcc lattice. **(b)** Sketch of a deformable solid substrate where dashed circles represent the position of particles exactly at their fcc (100) lattice sites. Due to its deformability s_z may differ from the ideal or initial s_{z0} of situation (a).

sight fluid and wall particles seem to be of the same type, since they are of the same size and interact through the same type of potential. Nevertheless we must distinguish between fluid and wall particles because wall particles resemble a solid body due to their spatial binding via the harmonic potential, unlike the fluid. We would rather treat the system as a mixture of two types of particles, even though one is arranged in a more ordered fashion.

Since the system contains two types of particles, the chemical work of Eq. (2.10) can be expressed as

$$dW_{chem} = \mu dN + 2\mu_s dN_s \quad (3.28)$$

where μ and μ_s are the chemical potential of the fluid and wall particles, respectively, N is the fluid particle number and N_s is the wall particle number of one wall. Combining the last equation with Eqs. (2.9), (2.11), (2.12) and (2.17), we can express the

3.5 | Semi-Grand Canonical Ensemble

exact differential of Ω as

$$d\Omega(T, \mu, N_s, \sigma) = -SdT - Nd\mu + 2\mu_s dN_s + V_0 \text{Tr}(\tau d\sigma) \quad (3.29)$$

where Ω is referred to as the *semi-grand potential* because it depends on two different types of particles where the number of one species is fixed. Thus, for a specific system under consideration the expression ‘ $2\mu_s dN_s$ ’ may be treated as an external (dynamic) field, but in its general form $d\Omega$ depends explicitly on the number of wall particles N_s and therefore the system is referred to as a semi-grand canonical ensemble.

The thermodynamic analysis is similar to that of e.g. macromolecules dispersed in a solution in which the number of macromolecules is fixed while the solution is considered to be at constant chemical potential and may exchange matter through a membrane with a reservoir (see Section 2.3 of Ref. [107]). Also the situation of a confined fluid in the presence of a fixed number of preadsorbed fluid molecules may be related. [108]

In the model system only the number of fluid particles is allowed to change, whereas the wall particle number remains fixed because wall particles resemble the boundary of the system. Using Eqs. (2.46), (2.47) and (3.27), a property M in the semi-grand canonical ensemble of our model system is given by

$$\langle M \rangle = \frac{1}{\Xi} \sum_N e^{\gamma N} \int \int M e^{-\beta U(\mathbf{R}, \mathbf{R}_s, \kappa)} d^{3N} \mathbf{R} d^{6N_s} \mathbf{R}_s \quad (3.30)$$

where we adapt Eqs. (2.44) and (2.45) to give the semi-grand partition function Ξ written as

$$\Xi(T, s_{x0}, s_{y0}, s_{z0}, \mu, \kappa) = \sum_N e^{\gamma N} \frac{Z}{N! \Lambda^{3(N+2N_s)}} \quad (3.31)$$

with the configuration integral Z given by

$$Z(T, s_{x0}, s_{y0}, s_{z0}, \kappa) = \int \int e^{-\beta U(\mathbf{R}, \mathbf{R}_s, \kappa)} d^{3N} \mathbf{R} d^{6N_s} \mathbf{R}_s \quad (3.32)$$

using the spatial notation of the model system $\{\mathbf{R}, \mathbf{R}_s\} = \mathbf{q}$. Please note that in Eq. (3.31) the factor $1/N!$ arises only for indistinguishable fluid particles but not for wall particles since the latter ones are distinguishable through their lattice sites.

The situation described by Eqs. (3.30)–(3.32) is similar to that of quenched annealed systems (see for example Section 7.2 of [32]) which mimics the creation process of mesoporous materials. As an example, the synthesis of MCM-type silicas is based on the self-assembly of cationic tensides, i.e. amphiphilic molecules, dissolved in a liquid phase. [109] After a silica precursor such as tetraethoxysilan is

added, under certain conditions the tensides arrange themselves in cylindrical form where the lipophilic ends are directed inward and the hydrophilic ends are pointed outward. Here, the alkyl chain length of the tenside determines the (average) pore width of the mesoporous product, e.g. in case of MCM-41(16) the ‘16’ signifies that the (lipophilic) alkyl chain used contains 16 carbon atoms. [34] The silica precursor separates the cylindrical tenside structures and reacts to form the silica walls of the mesoporous material. Thus, self-assembled tensides dissolved in a liquid phase act as a template for the silica matrix and therefore the pores of the matrix differ (slightly) in size and shape.

Quenched annealed systems take into account the synthesis of the confining structure within a liquid medium and allow the confining matrix to vary. This is usually realised through a separate simulation (without fluid particles), e.g. in a canonical molecular dynamic simulation, where wall particles may start from an (ideal) configuration and then interact via appropriate potentials to rearrange themselves to some extent. When the simulation ends, the confining wall is quenched, that is, the configuration of wall particles is fixed and the simulation with the fluid is carried out. Thus, the confining matrix may differ in size and shape for different simulation runs and enters the configuration integral of the system similar to Eqs. (3.30)–(3.32) of the present model. In this way the disordered morphology of interconnected pores such as controlled pore glasses [32, 110] or aerogels [111] as well as the slight variety of more ordered structures such as MCM-41 [112–114] has been investigated.

Although both treatments take the substrate ‘roughness’ into account, the roughness of the present model system may react to the fluid and its thermodynamic state, unlike the case of quenched annealed systems.

3.6 Simulation Details

We apply *periodic boundary conditions* to the simulation cell in the usual manner [69] to mimic the infinity of the slit pore in the x - and y -directions. Thus, if a particle leaves the system in the x - or y -direction, it enters the system from the opposite site, while the walls prevent fluid particles from leaving the system in the z -direction. Since wall particles can move from their lattice sites to some extent depending on κ , the wall must be stiff enough (i.e., κ must be large enough) to prevent fluid particles from penetrating them, which was checked during every simulation run. That our choice of κ throughout the simulations corresponds to a realistic situation is discussed in Appendix A.3 on p. 157.

3.6 | Simulation Details

As a natural consequence of the periodic boundary conditions, all interactions are considered according to the *minimum image convention*. [69] This convention is based on the assumption that the simulation box is surrounded by exact copies (so-called images) of the simulation box in each direction at which periodic boundary conditions are applied (i.e., in the present case the x - and y -directions). Consequently, by calculating the potential energy of a central particle with a neighbouring one, also images of the neighbouring particle must be considered. Among the original and its images we choose only that (maybe virtual) particle which is closest to the central one and take only its interaction into account. To make sure that there is only one (virtual or original) particle within the cut-off radius of a central particle, the cut-off radius must not be greater than half the (shortest) system length at which periodic boundary conditions are applied.

According to the explicitly short-ranged potential of Eq. (3.17), only neighboring particles within a sphere with cut-off radius $r_c = 3.5$ around a central particle make significant contributions to its potential energy. These neighboring particles do not change in every new configuration, especially not during the time-consuming simulation of liquid-like phases. Since the computational effort increases with N^2 , cf. e.g. the sums of Eq. (3.20), it is obvious how to improve the simulation technique of dense phases: a Verlet neighbour-list combined with a link-cell list is used for fluid particles as well as for wall particles to save computer time. [69] Such a neighbour-list contains all neighboring particles around a central particle up to the radius $r_c + \Delta$ where Δ is an additional length which is chosen to be of the order of 1σ . Only if a particle of the system departs from its original position by Δ , which is a rare event in liquid phases according to the random (Brownian) displacements of particles, neighbour-lists of all particles are updated.

To realise the transition probabilities of the Markov process (see Section 2.6), we perform ‘trial’ transitions from a configuration where the new configuration is accepted or rejected in favour of the original configuration. Regarding the functional form of the phase space represented by Eqs. (3.31) and (3.32), configurations are generated through a sequence of three consecutive and independent processes, i.e. (i) moving of fluid particles, (ii) moving of wall particles and (iii) creation or destruction of fluid particles. Consequently, to calculate properties according to Eq. (3.30) an iteration cycle of the semi-grand canonical Monte Carlo (SGCMC) simulation consists of the following steps:

1. Try to move each of the N fluid particles using the probability of Eq. (2.65).
2. Try to move each of the $2N_s$ wall particles using the probability of Eq. (2.65).

3. Make N attempts to create or destroy fluid particles with respect to the probabilities of Eq. (2.72) where creation and destruction occur with the same probability of 0.5.
4. If desired, compute the system properties and start the next iteration cycle by returning to step 1.

In steps 1 and 2, a particle i is displaced at random according to

$$\mathbf{r}_i^{(n)} = \mathbf{r}_i^{(o)} + \delta_r(\mathbf{1} - 2\boldsymbol{\xi}) \quad (3.33)$$

where $\mathbf{r}_i^{(n)}$ is the new position of particle i , $\mathbf{r}_i^{(o)}$ is its original position, δ_r denotes the side length of a small cube centred at $\mathbf{r}_i^{(o)}$, $\mathbf{1} \equiv (1, 1, 1)$ and $\boldsymbol{\xi}$ is a three-dimensional vector whose components are (pseudo-) random numbers generated uniformly in the interval $[0, 1]$. Since the transition probability associated with the moving of a particle depends on the temperature and density of the system, the acceptance ratio for displacement steps generally depends on δ_r . To improve the efficiency of movement attempts, δ_r is adjusted during the simulation run to keep the overall acceptance ratio between 40% and 70%. Further, we use independent values of δ_r for fluid particles and wall particles.

As usual in computer simulations, all quantities will hereafter be expressed in suitable dimensionless ('reduced') units of the fluid, i.e. $\epsilon \equiv 1$ and $\sigma \equiv 1$. For example, energies are given in units of ϵ , temperature in units of ϵ/k_B and lengths in units of σ . Other derived quantities like stress, density, or binding parameter are expressed in terms of combinations of these 'basic' units such as ϵ/σ^3 , σ^3 , or ϵ/σ^2 , respectively.

We list in Table 3.1 all the properties of the simulations used if not otherwise mentioned. In essence both walls consist of 256 wall particles at temperature $T = 1.0$ while the dimensions in x - and y -directions are $s_{x0} = s_{y0} = 12.7$ respectively and the pore width corresponds to $s_{z0} = 6.8$ with regard to Eq. (3.9). Depending on the thermodynamic state, we simulate up to 700 fluid particles. In bulk-simulations a system size of $s_{x0} = s_{y0} = s_{z0} = 12.7$ and temperature $T = 1.0$ are used if not otherwise mentioned and, of course, we apply periodic boundary conditions in all three principal directions.

3.6 | Simulation Details

Total number of MC cycles	$3-10 \times 10^5$
Starting configuration	random
Number of equilibration cycles	10^3
Number of cycles between averaging	10
Side length s_{x0}, s_{y0}	12.7
Pore width s_{z0}	6.8
Number of wall particles N_s	128
Force constant κ	$30 - 10^4$
Lattice parameter ℓ	1.59
Areal wall particle density ρ_s	0.79
Temperature T	1.0
Potential cut-off r_c (fluid and wall particles)	3.5
Radius of neighbour list $r_c + \Delta$	4.5
Fluid-wall interaction ϵ_{fs}	1.0
Thickness of local density layer δs_z	0.01

TABLE 3.1: Common simulation parameters of the model system used throughout this work if not otherwise mentioned. One Monte Carlo (MC) cycle consists of $N + 2N_s$ movement and N creation/destruction attempts, explained on page 45. Values of ℓ and ρ_s are rounded.

4

Phase Behaviour

After the previous three more theoretically/technically oriented chapters, we now turn to a discussion of the phase behaviour of fluids, especially to the thermodynamic conditions at which the gas–liquid phase transition sets in and the impact of the wall’s flexibility on this phenomenon. Or, from a more fluid-oriented perspective, we are interested in the thermodynamic conditions at which one kind of organisation of matter is abandoned in favour of another one and how these conditions change if the confining walls become deformable.

4.1 Sorption in Experiment and Theory

From an experimental perspective, gas sorption experiments provide a basis to investigate the phase behaviour of confined fluids. As mentioned in Section 2.1, the experimental setup consists of a mesoporous material which is in open contact with a bulk fluid reservoir of pressure P at fixed temperature T . [26, 28] Assuming porous material and bulk reservoir restores thermodynamic equilibrium, the amount of fluid matter inside the pores changes if P of the reservoir changes. As an example, upon changing the pressure of the reservoir successively (at fixed V, T) from $P = 0$ to P_0 , at which bulk condensation sets in, adsorption takes place so that fluid matter enters the porous material. In the reverse process of desorption fluid matter leaves the meso-

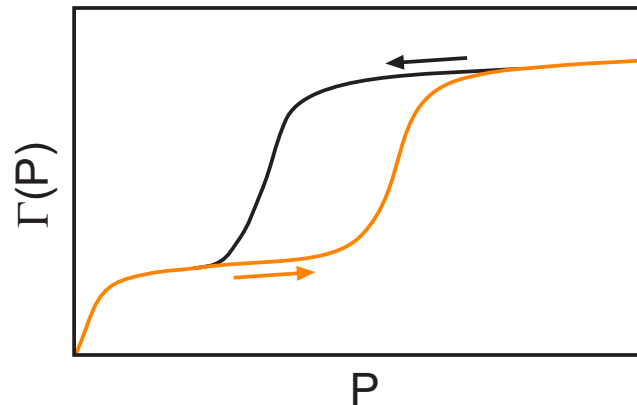


FIG. 4.1: Sketch of a sorption isotherm $\Gamma(P)$ of type IV according to the IUPAC classification as a function of the fluid pressure P of the bulk reservoir. The sorption isotherm shows hysteresis of type H1 with respect to the IUPAC classification. Thus, pressures at which capillary condensation sets in differ for adsorption (\rightarrow) and desorption (\leftarrow), i.e., the point of phase transition depends on the direction of sorption as indicated by arrows.

porous material as a reaction to the decrease of the bulk fluid pressure according to $P_0 \rightarrow P = 0$.

The adsorbed amount of fluid Γ inside the porous material in dependence of the bulk fluid pressure P is graphically represented by the *sorption isotherm* $\Gamma(P)$. Traditionally, there are two methods to measure the amount of adsorbed fluid: the gravimetric and the volumetric technique. [115] The volumetric measurement detects pressure changes between calibrated volumes and therefore is an indirect measurement, while the gravimetric method directly measures the weight of the mesoporous probe. Normally a sharp increase of $\Gamma(P)$ marks capillary condensation as the density inside the mesoporous material abruptly increases, while the reverse process, the transition from a liquid-like to a gas-like phase, is connected with a sharp drop of $\Gamma(P)$.

Fig. 4.1 shows the general course of a type IV sorption isotherm (according to the IUPAC classification [116]) which reflects a common sorption behaviour of fluids in ordered mesoporous materials, such as that of perfluoropentane in SBA-15 [27] or nitrogen in MCM-41 [19]. Type IV isotherms reflect a layer-wise sorption of the sorbate at the walls of non-interconnected pores [90] through physisorption, that is, sorbate molecules are bound by weak van der Waals forces, as distinct from chemisorption, where the forces are significantly stronger. With regard to the adsorption process, the sorption isotherm rises quickly at low pressures as a consequence of a strong fluid–wall interaction and a preferred arrangement of fluid matter along the pore walls. Once the first layer is build, sorption increases only gently due to a lower

4.1 | Sorption in Experiment and Theory

fluid–fluid interaction which retards the creation of additional fluid layers. Thus, the change in slope from mono-layer to multi-layer adsorption reflects the discrepancy between the fluid–wall and the fluid–fluid interactions. Upon capillary condensation, the fluid inside the pores condenses and therefore the sorption isotherm sharply increases where the width of the condensation region (i.e. the slope) reflects the pore size distribution of the mesoporous material. The filling process of ordered mesoporous materials has already been discussed in Section 3.1. In the liquid-like phase the sorption isotherm increases only slightly up to the bulk condensation pressure at which the experiment is stopped because condensation of the bulk fluid results in a further increase of fluid matter inside the sorption cell which occurs independently of the adsorbing material.

Type IV sorption isotherms show *sorption hysteresis* of the H1 type (according to the IUPAC classification [19]), that is, the pressure at which the phase transition sets in differ for the adsorption and desorption process, i.e. it depends on the direction of sorption. [117] It is assumed that sorption hysteresis is caused by metastable states that are states in which the grand potential Ω is not (the global) minimum, such as in the case of oversaturated gas or undersaturated liquid. However, since $\Gamma(P)$ depends on the direction (i.e. the history of the system), non-equilibrium states must be involved. As a consequence of sorption hysteresis, the equilibrium conditions at which a confined fluid undergoes a phase transition are often experimentally inaccessible.

In simulations we use the density ρ of the system rather than the adsorbed mass because the particle mass m is irrelevant in the Monte Carlo method and both are simply related. Moreover, in SGCMC simulations the bulk fluid reservoir is not explicitly considered but implicitly through the chemical potential μ of the system. For this reason, in simulations the density as a function of the chemical potential, $\rho(\mu)$, corresponds to the experimental sorption isotherm $\Gamma(P)$. According to the direction of sorption process, $\rho(\mu)$ is determined in a sequence of separate calculations where the chemical potential is successively increased or decreased. The first calculation of the sequence starts from a random configuration but every subsequent calculation for a different chemical potential starts from the last configuration of the previous calculation. For example, to calculate the adsorption isotherm one starts at a given chemical potential and successively increases μ by $\Delta\mu$ in a sequence of calculations while the desorption isotherm represents the reverse process, starting at given μ which is successively decreased by $\Delta\mu$ for each calculation.

It should be noted that the sorption isotherm is inaccessible at very small chemical potentials μ because of the finite size of the simulation cell. The smaller is μ , the smaller is the fluid particle number density of the system. Consequently, there is a

limiting chemical potential where no or an insufficient number of fluid particles prohibits a statistical treatment of the model system through the Monte Carlo method.

However, in analogy with experiments, calculated sorption isotherms $\rho(\mu)$ also show hysteresis. It is a general phenomena that occurs in confinement as in bulk, shown for the latter situation in Fig. 4.2a. The phenomena of hysteresis in Monte Carlo simulations was proved by Schoen et al. to depend on the size of the simulation cell rather than on the physical parameters of the system (i.e., it is a finite size effect which vanishes by enlarging the simulation box). [118] Thus, it is an artifact without physical meaning. Consequently, the calculated sorption isotherm $\rho(\mu)$ is unsuitable for indicating phase transitions and that is why we leave this observable in favour of the grand potential.

4.2 Bulk Phase Transition

As explained in the previous section, the sorption process in confinement is a reaction to a pressure change of a connected bulk fluid reservoir. According to sorption experiments where the bulk phase transition serves as a reference for the confined fluid, we investigate the phase behaviour of the bulk fluid before we turn to confined situations.

A bulk fluid phase is homogeneous with respect to each direction, that is, $\tau_b \equiv \tau_{xx} = \tau_{yy} = \tau_{zz}$ [see Eq. (2.7)]. Consequently, the mechanical work of Eq. (2.9) can be expressed as

$$dW_{mech}^b = \tau_b dV \quad (4.1)$$

which reflects the isotropy of bulk systems. A way to control the bulk fluid pressure in experiment is through another, larger *super-reservoir* where both are connected via a valve (see Fig. 5.9a on p. 109). [27] Upon closing or opening the valve, the pressure of the bulk fluid reservoir is changed as a result of an exchange of matter and energy with the super-reservoir. According to the experimental setup, the bulk fluid of the sorption cell belongs to a grand canonical ensemble and therefore the grand potential is the relevant thermodynamic potential. Combining Eqs. (2.10), (2.11), (2.12), (2.17) and (4.1) yields

$$d\Omega = -S dT - Nd\mu + \tau_b dV \quad (4.2)$$

which at fixed T and μ reduces to

$$d\Omega(V) = \tau_b dV \quad (4.3)$$

4.2 | Bulk Phase Transition

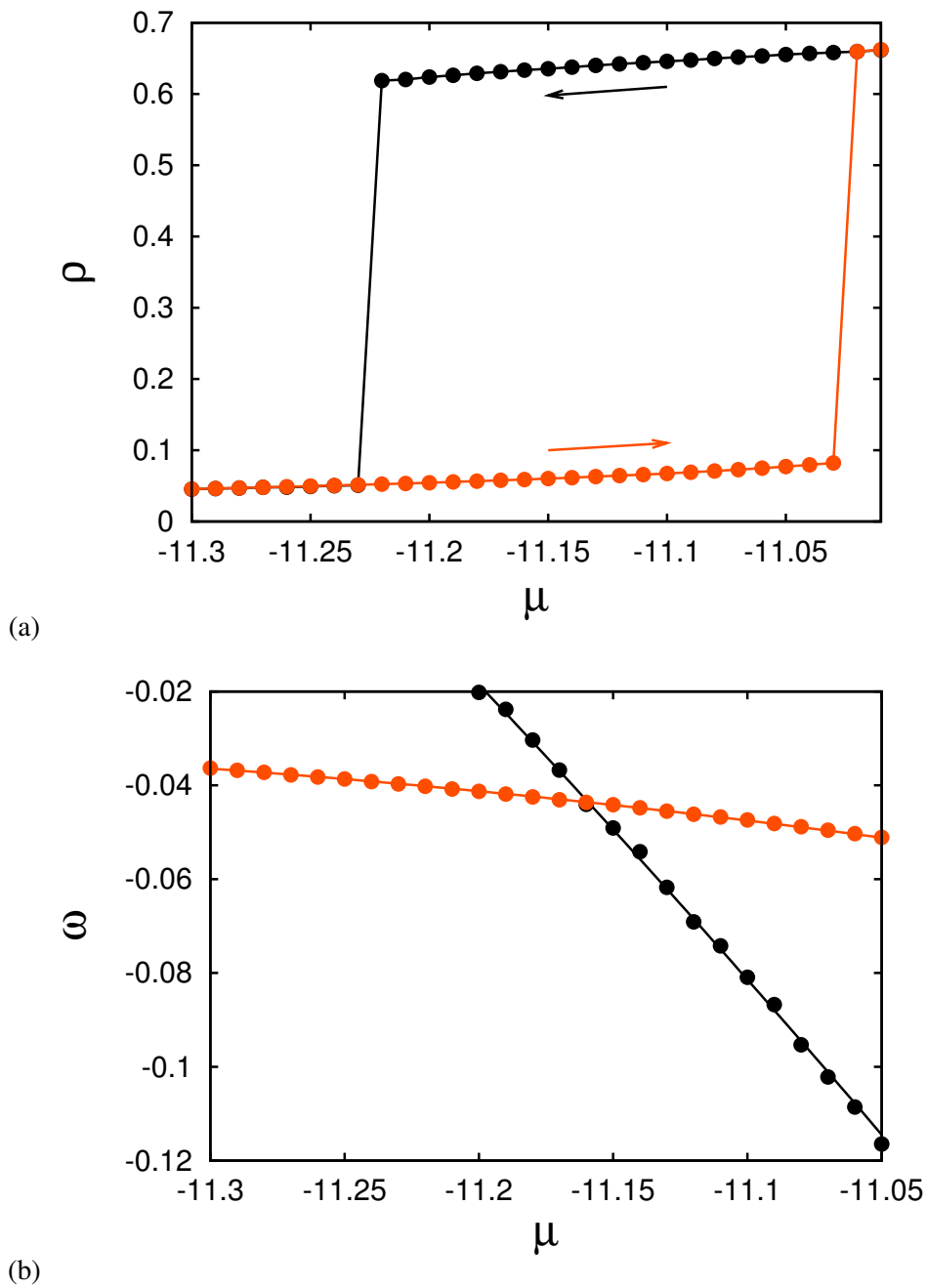


FIG. 4.2: (a) Density ρ as a function of the chemical potential μ for bulk fluid at $T = 1.0$. The point of phase transition depends on the direction of the calculation sequence, i.e. whether μ was successively increased (●) or decreased (●) as indicated by the arrows. (b) Same data as (a), but the grand potential density $\omega(\mu)$ is shown for the gas branch (●) and the liquid branch (●). The intersection of both branches at $\mu_x \approx -11.16$ marks the equilibrium gas–liquid phase transition.

Regarding Ω to be an extensive quantity in connection with the homogeneity of bulk phases, a change of the volume V by factor α (under the given conditions of fixed T and μ) results in a change of Ω by α as well, expressed as

$$\Omega(T, \mu, \alpha V) = \alpha \Omega(T, \mu, V) \quad (4.4)$$

which identifies Ω as a homogeneous function of degree 1 in V . In general, according to Euler's Theorem, a homogeneous function f of degree 1 in $\{x_1, x_2, x_3, \dots, x_n\}$ obeys the relation (see Section A.3 of [32])

$$\sum_{i=1}^n x_i \left(\frac{\partial f}{\partial (\alpha x_i)} \right)_{\{\cdot\} \setminus x_i} = f(x_1, x_2, x_3, \dots, x_n) \quad (4.5)$$

where ' $\{\cdot\} \setminus x_i$ ' is a shorthand notation to indicate that all variables are held fixed but x_i . With the transformation of the variables $V \rightarrow \alpha V$, we can rewrite Eq. (4.3) as

$$\left(\frac{\partial \Omega}{\partial (\alpha V)} \right)_{T, \mu} = \tau_b \quad (4.6)$$

and the last equation combined with Eq. (4.5), where we set $i = 1$, substitute $x_1 \rightarrow V$ and $f \rightarrow \Omega$, results in the expression for the grand potential in form of

$$\Omega(T, \mu, V) = V \left(\frac{\partial \Omega}{\partial (\alpha V)} \right)_{T, \mu} = V \tau_b \quad (4.7)$$

which is referred to as a 'mechanical' expression of Ω because it depends on the (mechanical) stress. The stress in bulk systems can be computed in Monte Carlo simulations through [32]

$$\tau_b = -\frac{\langle N \rangle k_B T}{V} + \frac{1}{6V} \left\langle \sum_{i=1}^N \sum_{j=1 \neq i}^N u'(r_{ij}) r_{ij} \right\rangle \quad (4.8)$$

where r_{ij} is the distance between two fluid particles, $u'(r)$ is the first derivative of the interaction potential $u(r)$ with respect to r (i.e., the intermolecular force) and brackets $\langle \dots \rangle$ refer to ensemble averages.

Instead of the extensive grand potential, it is often more suitable to deal with the grand potential density ω defined by

$$\omega = \frac{\Omega}{V_0} = \tau_b \quad (4.9)$$

because the latter is an intensive quantity which is independent from the system size. In Eq. (4.9), V_0 refers to the volume of an unstrained state. At fixed T and V , Eqs. (4.2) and (4.9) can be combined to give

$$\left(\frac{\partial \omega}{\partial \mu} \right)_{T, V} = -\rho \leq 0 \quad (4.10)$$

4.2 | Bulk Phase Transition

where $\rho = N/V_0$ is the density of an unstrained reference system. Since $\rho \geq 0$, the grand potential density is a monotonically decaying function of μ . Furthermore, the gas–liquid phase transition is characterised by a significant change in density and so we expect that $\omega(\mu)$ is steeper in the liquid phase than in the gas phase. We can identify another property of $\omega(\mu)$, written [32]

$$\left(\frac{\partial^2 \omega}{\partial \mu^2}\right)_{T,V} = -\left(\frac{\partial \rho}{\partial \mu}\right)_{T,V} = -\rho^2 K_T \leq 0 \quad (4.11)$$

where K_T is the isothermal compressibility. Since $\rho, K_T > 0$, the grand potential density is a concave function.

Fig. 4.2b shows the grand potential density depending on the chemical potential for a bulk fluid at temperature $T = 1.0$. The graph consists of two branches, one belongs to the gas phase (●) and the other to the liquid phase (●). According to Eq. (4.10) the branch of the liquid is steeper than the branch of the gas and both branches are concave, reflecting Eq. (4.11). The intersection of both branches at $\mu_x \simeq -11.16$ marks the gas–liquid phase transition at which both organisations of matter share the same grand potential density, written

$$\omega_{gx} = \omega_{lx} \quad (4.12)$$

where ‘g’ denotes the gas phase, ‘l’ denotes the liquid phase and ‘x’ indicates that both phases have the same ω . Following the course of the smallest ω , that is the course of thermodynamic equilibrium [see Eq. (2.17)], its slope changes discontinuously at μ_x because the densities of the coexisting phases $\rho_{gx} \simeq 0.059$ and $\rho_{lx} \simeq 0.634$ differ. To make a connection with sorption experiments, we determine the pressure P_0 at which the gas–liquid phase transition of the bulk fluid occurs as

$$P_0 = -\tau_{bx} = -\omega_x = 0.043 \quad (4.13)$$

which is taken from Fig. 4.2b according to Eq. (4.9).

As explained in Section 4.1, the calculation of a branch consists of a sequence of individual simulations with increasing or decreasing μ where each subsequent simulation starts from the last configuration of the preceding simulation. According to experimental sorption, the calculation sequence mimics a process with history and, thus, it may pass the point of phase transition, as in Fig. 4.2b, because the transition from one phase to another is inhibited by (unlikely) intermediate configurations between those of gas and liquid. This can lead to metastable states such that

$$\omega_i > \omega_j \quad (4.14)$$

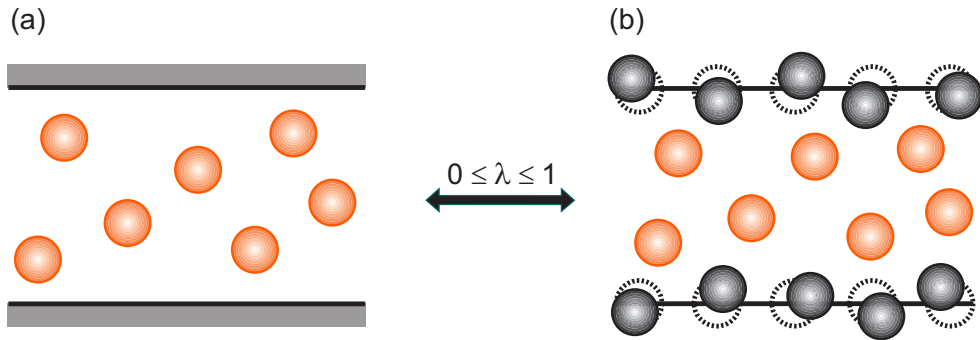


FIG. 4.3: Upon changing the parameter λ we switch between **(a)** the reference model with smooth walls ($\lambda = 0$) and **(b)** the model of thermally coupled walls ($\lambda = 1$). Other values of λ correspond to situations in-between where the fluid is affected to some extent by the walls of both systems.

where ‘ i ’ belongs to the metastable state and ‘ j ’ to the state of thermodynamic equilibrium. The metastability of states causes the hysteresis-like phenomena in simulations which becomes apparent from a comparison of Figs. 4.2a and 4.2b.

4.3 Perturbation Theory

Unfortunately, a mechanical expression of Ω as in bulk [see Eq. (4.7)] does not exist for the model of thermally coupled walls, which is a consequence of the inhomogeneity of the system. In the z -direction the system is confined by walls, that is, the potential energy of a fluid particle depends on z , whereas the discrete structure of the walls induce an inhomogeneous (periodic) field along the x - and y -directions. Since the displacement of a fluid particle causes a change in potential energy, regardless of the direction of displacement, system properties are not translational invariant. Thus, Ω is not a homogeneous function of degree 1 in any direction which is a prerequisite to derive a mechanical expression for Ω . [32]

Since direct calculation of Ω through a mechanical expression is inaccessible, we take an *indirect* route as suggested by Zwanzig. [119] According to this, we calculate the grand potential of a reference model, in which a mechanical expression of Ω exists. Then we establish a connection between the reference model and the model of interest, that is the model of thermally coupled walls, through a so-called λ -expansion. Here λ acts as a (continuous) ‘switch’ between the reference model ($\lambda = 0$), the model of interest ($\lambda = 1$) and situations in between ($0 < \lambda < 1$), see Fig. 4.3. Thus, the λ -expansion provides a thermodynamic route to the (semi-) grand potential of the system of interest. [120]

4.3.1 Reference Model of Smooth Walls

To introduce a homogeneity into the model of thermally coupled walls, we smear the wall particles homogeneously over the wall area along the x - and y -directions. Thus, the interaction of a fluid particle at fixed position $\mathbf{r}_i = \{x_i, y_i, z_i\}$ with the (now) smeared wall particles is averaged in the x - y -plane parallel to the wall. This idea results in the so-called *smooth* wall, i.e. a structureless barrier whose potential only depends on the z -direction while the x - and y -direction are translational invariant [32], sketched in Fig. 4.3a.

According to the model of thermally coupled walls, two (parallel plane) smooth walls labelled by $k = 1, 2$ are located at $z = \pm s_{z0}/2$ in the reference model system, where ‘-’ corresponds to $k=1$ and ‘+’ corresponds to $k=2$. Confining N fluid particles between the smooth walls, a fluid–wall contribution to the potential energy of the system arises, written

$$U_{fs}^{ref}(z) = \sum_{k=1}^2 \sum_{i=1}^N u_{sm}^{[k]}(z_i) \quad (4.15)$$

where z_i is the z -coordinate of the i th fluid particle and $u_{sm}^{[k]}(z)$ is the interaction potential between a fluid particle and a smooth wall given by [32, 121]

$$u_{sm}^{[k]}(z) = 2\pi\epsilon\rho_s\sigma^2 \left[\frac{2}{5} \left(\frac{\sigma}{z \pm s_{z0}/2} \right)^{10} - \left(\frac{\sigma}{z \pm s_{z0}/2} \right)^4 \right] \quad (4.16)$$

Here, $\rho_s \approx 0.79$ is the areal wall particle density of the system of thermally coupled walls, see Table 3.1. Because of the isotropy of smooth walls in the x - y -plane, the stress tensor of Eq. (2.7) can be written as

$$\boldsymbol{\tau}^{ref} = \begin{pmatrix} \tau_{\parallel}^{ref} & 0 & 0 \\ 0 & \tau_{\parallel}^{ref} & 0 \\ 0 & 0 & \tau_{zz}^{ref} \end{pmatrix} \quad (4.17)$$

where we use $\tau_{\parallel}^{ref} \equiv \tau_{xx}^{ref} = \tau_{yy}^{ref}$. Moreover, deformation tensor elements of Eq. (2.8) can be written

$$\frac{\sigma_{\parallel}^{ref}}{2} \equiv \sigma_{xx}^{ref} = \sigma_{yy}^{ref} \quad (4.18)$$

while the volume of the unstrained system is expressed as

$$V_0 = s_{x0}s_{y0}s_{z0} = A_0s_{z0} \quad (4.19)$$

where A_0 is the z -directed face of the system in the unstrained reference state. Consequently, the mechanical work of Eq. (2.9) can be written for the reference model system in the form

$$dW_{mech} = s_{z0}\tau_{\parallel}^{ref} dA + A_0\tau_{zz}^{ref} ds_z \quad (4.20)$$

Combining the last equation with Eqs. (2.11), (2.12), (2.17) and (3.28), the exact differential of Ω^{ref} for the reference model system can be written

$$d\Omega^{ref}(T, \mu, N_s, A, s_z) = -S dT - Nd\mu + 2\mu_s dN_s + s_{z0}\tau_{\parallel}^{ref} dA + A_0\tau_{zz}^{ref} ds_z \quad (4.21)$$

At fixed T , μ , N_s and s_z , changes of Ω^{ref} given in Eq. (4.21) reduce to

$$d\Omega^{ref}(A) = s_{z0}\tau_{\parallel}^{ref} dA \quad (4.22)$$

On account of the isotropy in the x - y -plane of the reference model system, we have that Ω^{ref} is a homogeneous function of degree 1 in A and we follow the argument of Section 4.2, cf. Eqs. (4.3)–(4.7) and (4.9), to derive the following mechanical expression of the semi grand potential density ω^{ref} ,

$$\omega^{ref} = \frac{\Omega^{ref}}{A_0 s_{z0}} = \tau_{\parallel}^{ref} \quad (4.23)$$

where the stress parallel to the pore walls τ_{\parallel}^{ref} can be computed using [32]

$$\begin{aligned} \tau_{\parallel}^{ref} &= \frac{1}{s_{z0}} \left(\frac{\partial \Omega^{ref}}{\partial A} \right)_{\{\cdot\} \setminus A} = -\frac{k_B T}{s_{z0}} \left(\frac{\partial \ln \Xi^{ref}}{\partial A} \right)_{\{\cdot\} \setminus A} \\ &= -\frac{\langle N \rangle k_B T}{V} + \frac{1}{4V} \left\langle \sum_{i=1}^N \sum_{j=1 \neq i}^N u'(r_{ij}) r_{ij} [(\hat{\mathbf{r}}_{ij} \cdot \hat{\mathbf{e}}_x)^2 + (\hat{\mathbf{r}}_{ij} \cdot \hat{\mathbf{e}}_y)^2] \right\rangle \end{aligned} \quad (4.24)$$

where $\mathbf{r}_{ij} = r_{ij}\hat{\mathbf{r}}$ and $\hat{\mathbf{e}}_\alpha$ is a unit vector along the α -axis of the Cartesian coordinate system. As before, we use the shorthand notation ' $\{\cdot\} \setminus A$ ' to indicate that all variables are held fixed but A . Eq. (4.24) can be verified from Eqs. (2.41), (3.31), (4.21) and the configuration integral of Eq. (3.32) which simplifies for the reference model system to

$$Z^{ref}(T, N, A, s_z) = \int e^{-\beta(U_{ff} + U_{fs}^{ref})} d^{3N}\mathbf{R} \quad (4.25)$$

where U_{ff} is given by Eq. (3.20) and U_{fs}^{ref} is defined as in Eq. (4.15).

4.3.2 λ -Expansion

The reference model system with smooth walls almost resembles the system of interest with thermally coupled walls except for the discrete structure of the walls. In fact, a smooth wall can be considered as a first approximation to the fcc structured wall. [122, 123] Thus, thermally coupled walls can be treated as a perturbation of smooth walls where the λ -expansion establishes a connection between both model systems. [119, 124] Within the λ -expansion theory, the coupling parameter λ serves as a continuous switch to control the degree of perturbation, i.e. in this case the extent to which the fluid is affected by the thermally coupled walls.

Consider a model system that incorporates both models, that is, the smooth walls of the reference system and the thermally coupled walls of the system of interest. Thus, the fluid is affected by walls of both systems to some extent, where the situation with $\lambda = 0$ corresponds to the (unperturbed) reference model system with smooth walls while at $\lambda = 1$ the fluid is only influenced by thermally coupled walls, i.e. the system of interest (see Fig. 4.3a,b). Upon increasing the coupling parameter λ from 0 to 1 continuously the influence of the perturbation (i.e., the thermally coupled walls) increases by the same amount λ by which the influence of the reference model system (i.e., the smooth walls) decreases. Consequently, the total configurational energy of the (composite) model system depends on λ and can be written

$$U(\lambda) = U_{ff} + (1 - \lambda)U_{fs}^{ref} + \lambda(U_{fs} + U_{ss}) \quad (4.26)$$

$$\equiv U_{ff} + U_{fs}^{ref} + \lambda\Phi \quad (4.27)$$

where $\lambda \in [0, 1]$ and the function Φ is introduced merely for notational convenience as

$$\Phi(\mathbf{R}, \mathbf{R}_s, \kappa) \equiv U_{fs}(\mathbf{R}, \mathbf{R}_s) + U_{ss}(\mathbf{R}_s, \kappa) - U_{fs}^{ref}(\mathbf{R}) \quad (4.28)$$

In Eq. (4.26)–(4.28), the contributions to the configurational energy are given by Eqs. (3.20), (3.21), (3.26) and (4.15). Since U is a function of λ , the configuration integral Z , the (semi-) grand partition function Ξ and the (semi-) grand potential Ω depend on λ as well. According to Eqs. (2.41) and (3.31), the dependence of Ω on λ can be written

$$\frac{d\Omega}{d\lambda} = -\frac{k_B T}{\Xi(\lambda)} \frac{d\Xi}{d\lambda} = -\frac{k_B T}{\Xi(\lambda)} \sum_N \frac{e^{\gamma N}}{N! \Lambda^{3(N+2N_s)}} \frac{dZ(\lambda)}{d\lambda} \quad (4.29)$$

where

$$\frac{dZ}{d\lambda} = -\beta \iint \Phi(\mathbf{R}, \mathbf{R}_s, \kappa) e^{-\beta U(\lambda)} d^{3N} \mathbf{R} d^{6N_s} \mathbf{R}_s \quad (4.30)$$

and combining the last two equations yields

$$\begin{aligned}\frac{d\Omega}{d\lambda} &= \frac{1}{\Xi(\lambda)} \sum_N \frac{e^{\gamma N}}{N! \Lambda^{3(N+2N_s)}} \iint \Phi(\mathbf{R}, \mathbf{R}_s, \kappa) e^{-\beta U(\lambda)} d^{3N} \mathbf{R} d^{6N_s} \mathbf{R}_s \\ &= \langle \Phi(\mathbf{R}, \mathbf{R}_s, \kappa) \rangle\end{aligned}\quad (4.31)$$

By integrating Eq. (4.31) formally with respect to λ we can express the (semi-) grand potential density ω with regard to Eq. (4.9) as

$$\begin{aligned}\omega(\lambda) &= \omega(0) + \frac{1}{V_0} \int_0^\lambda \langle \Phi \rangle_{\lambda'} d\lambda' \\ &= \tau_{\parallel}^{ref} + \frac{1}{V_0} \int_0^\lambda \langle \Phi \rangle_{\lambda'} d\lambda'\end{aligned}\quad (4.32)$$

The last equation uses the relation $\omega(0) = \tau_{\parallel}^{ref}$ of Eq. (4.23) which holds at $\lambda = 0$ because the system corresponds to the (unperturbed) reference system of smooth walls. Eq. (4.32) provides a route to the (semi-) grand potential density of the model of thermally coupled walls because τ_{\parallel}^{ref} and $\langle \Phi \rangle$ can be obtained from a Monte Carlo simulation while V_0 is an input parameter.

4.3.3 Calculation of the Semi-Grand Potential Density

The perturbational procedure described in the previous section permits us to compute $\omega(\lambda = 1)$ for the model of thermally coupled walls at fixed temperature T and chemical potential μ . According to the two branches of ω whose intersection marks the phase transition (cf. Fig. 4.2b) we choose two initial chemical potentials $\mu^{(in)}$ which are sufficiently far from the point of phase transition. Consequently, at one chemical potential $\mu_g^{(in)}$, the fluid corresponds to the one phase region of the gas-like state while at the other one, i.e. $\mu_l^{(in)}$, the fluid is in a (pure) liquid-like state. These values of $\mu^{(in)}$ are not known *a priori* so that one needs some trial and error at this point.

For both $\mu^{(in)}$, we compute $\langle \Phi(\mathbf{R}, \mathbf{R}_s, \kappa) \rangle$ in a sequence of 10–20 individual simulations for discrete values of $0 \leq \lambda \leq 1$ while τ_{\parallel}^{ref} is taken from the simulation at $\lambda = 0$ according to Eq. (4.24). The calculated values of Φ and its contributions as in Eq. (4.28) are plotted in Fig. 4.4a as a function of λ for $\mu^{(in)} = -11.3$, $T = 1.0$ and $\kappa = 10^4$. Thus, the system of interest at $\lambda = 1$ corresponds to a slit pore with almost rigid fcc walls. At $\lambda = 0$ the interaction between the fluid and the smooth wall, U_{fs}^{ref} (●), is smallest because the fluid is only affected by the smooth wall. On the other hand, the interaction between the fluid and the fcc wall U_{fs} (●) is largest

4.3 | Perturbation Theory

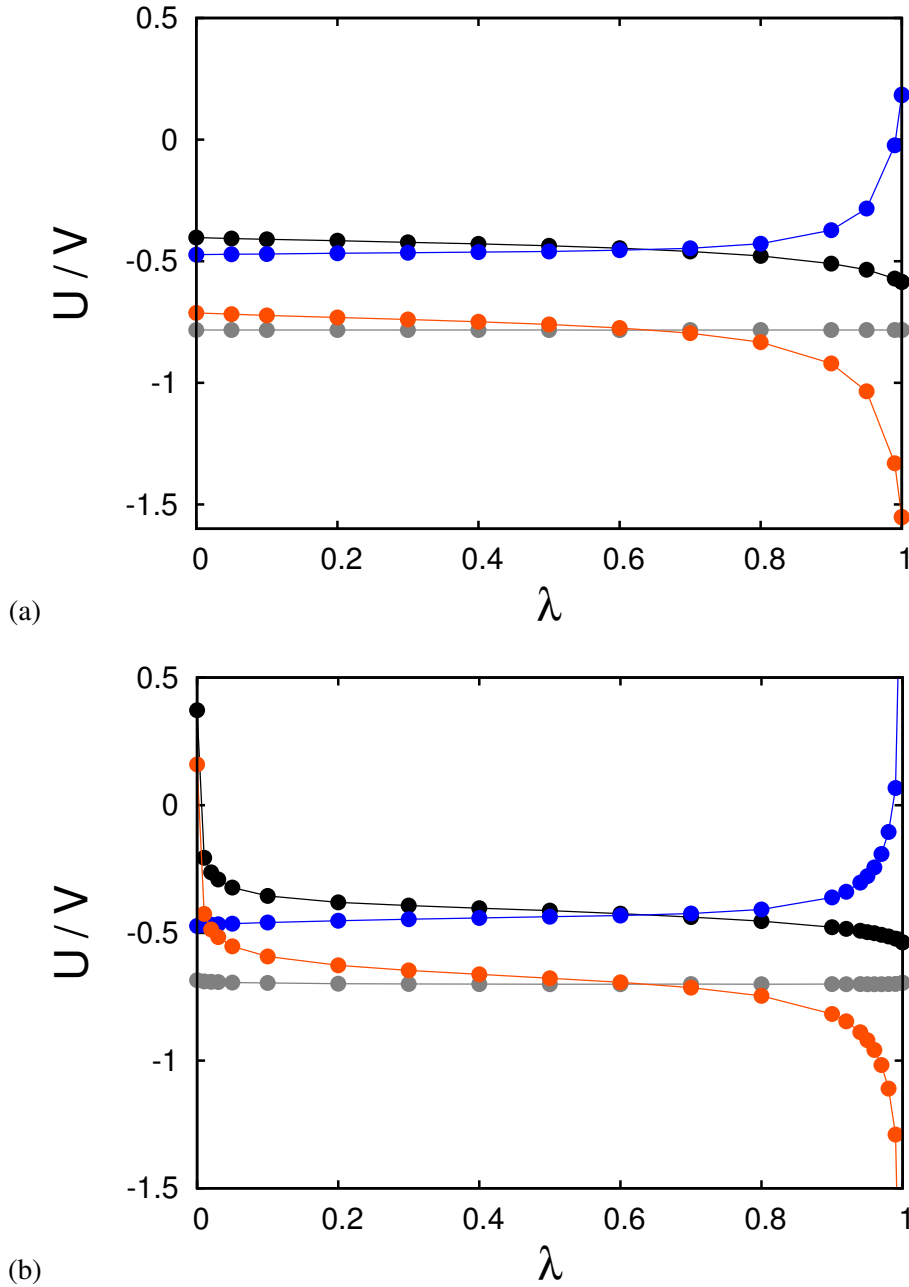


FIG. 4.4: Energy contributions U_{fs}^{ref} (●), U_{fs} (●), U_{ss} (●) and Φ (●) per volume as a function of the coupling parameter λ for **(a)** a (quasi-) rigid fcc wall ($\kappa = 10^4$) and **(b)** a deformable wall with $\kappa = 30$. In the system with deformable walls the energy contributions of U_{fs}^{ref} and Φ exceed the scaling of the y-axis and reach at $\lambda = 1$ the values $U_{fs}^{ref}(\lambda = 1) \simeq 4.2$ and $\Phi(\lambda = 1) \simeq -5.5$. Both simulation sequences are carried out at $\mu = -11.3$, $s_{z0} = 6.8$ and $T = 1.0$.

because this potential is not considered when configurations of fluid particles are chosen. Upon increasing λ , i.e. increasing the influence of the rigid wall, U_{fs} decreases monotonically while U_{fs}^{ref} increases monotonically. Finally, at $\lambda = 1$ the reverse situation is reached because the fluid particles arrange themselves only with regard to the structured fcc wall and therefore U_{fs} is smallest while U_{fs}^{ref} is largest. U_{fs}^{ref} becomes even positive because fluid particles adsorb along the fcc structured wall in a manner that continues the fcc wall structure (see Appendix A.1) where fluid particles ‘fill’ the holes between the wall particles. Since U_{fs} vanishes with z^{-12} (z is the distance between the fluid and the wall particles in the z -direction) but U_{fs}^{ref} decreases with z^{-10} , the interaction between the fluid and the smooth wall becomes repulsive at $\lambda = 1$. Moreover, the plot shows that the transition from a smooth wall to an fcc structured wall is connected with a decrease of the effective fluid–wall interaction since $U_{fs}^{ref}(\lambda = 0) > U_{fs}(\lambda = 1)$. The contribution of U_{ss} (●) is unaffected by changing λ and remains constant in relation to the contributions U_{fs}^{ref} and U_{fs} .

If one reduces the binding strength ($\kappa = 30$) of the wall particles to make the walls of the system of interest deformable, as shown in Fig. 4.4b, the behaviour of the potential energy contributions is similar to that of the (quasi-) rigid wall. Only the discrepancy between U_{fs}^{ref} (●) and U_{fs} (●) is more pronounced in regions where the influence of one of the two walls vanishes, i.e. $\lambda \lesssim 0.1$ and $\lambda \gtrsim 0.9$. This discrepancy reflects the fact that the deformable wall differs more from the smooth wall than the (quasi-) rigid wall does. The fluid–wall interaction of the system with deformable walls is a dynamically changing potential where wall particles may depart from the x - y -plane of the smooth wall. On the other hand, the fluid–wall interaction of the system with (quasi-) rigid walls resembles a static field because the wall particles are fixed in the plane of the smooth wall. In the regions of $\lambda \lesssim 0.1$ and $\lambda \gtrsim 0.9$, the fluid particles almost ignore or ‘follow’ the departed wall particles of the deformable walls which results in higher values of either U_{fs} or U_{fs}^{ref} compared with the static field of the (quasi-) rigid wall.

However, the integral in Eq. (4.32) is evaluated numerically by a standard quadrature algorithm. [125] As a result of the monotonic behaviour of U_{fs} and U_{fs}^{ref} , Φ (●) is a monotonically decreasing function of λ so that the integration leads to a monotonic decrease of $\omega(\lambda)$ for the deformable wall (⊙) as well as for the rigid fcc wall (●), shown in Fig. 4.5a. The monotonicity of $\omega(\lambda)$ is a prerequisite for the perturbational approach of the preceding section because it implies that no first-order phase transition occurs whose discontinuity would mean that the integration as in Eq. (4.32) was invalid. That is why we mentioned in the beginning of this section that we choose $\mu^{(in)}$ ‘sufficiently far’ from the point of phase transition so that the changes in the

4.3 | Perturbation Theory

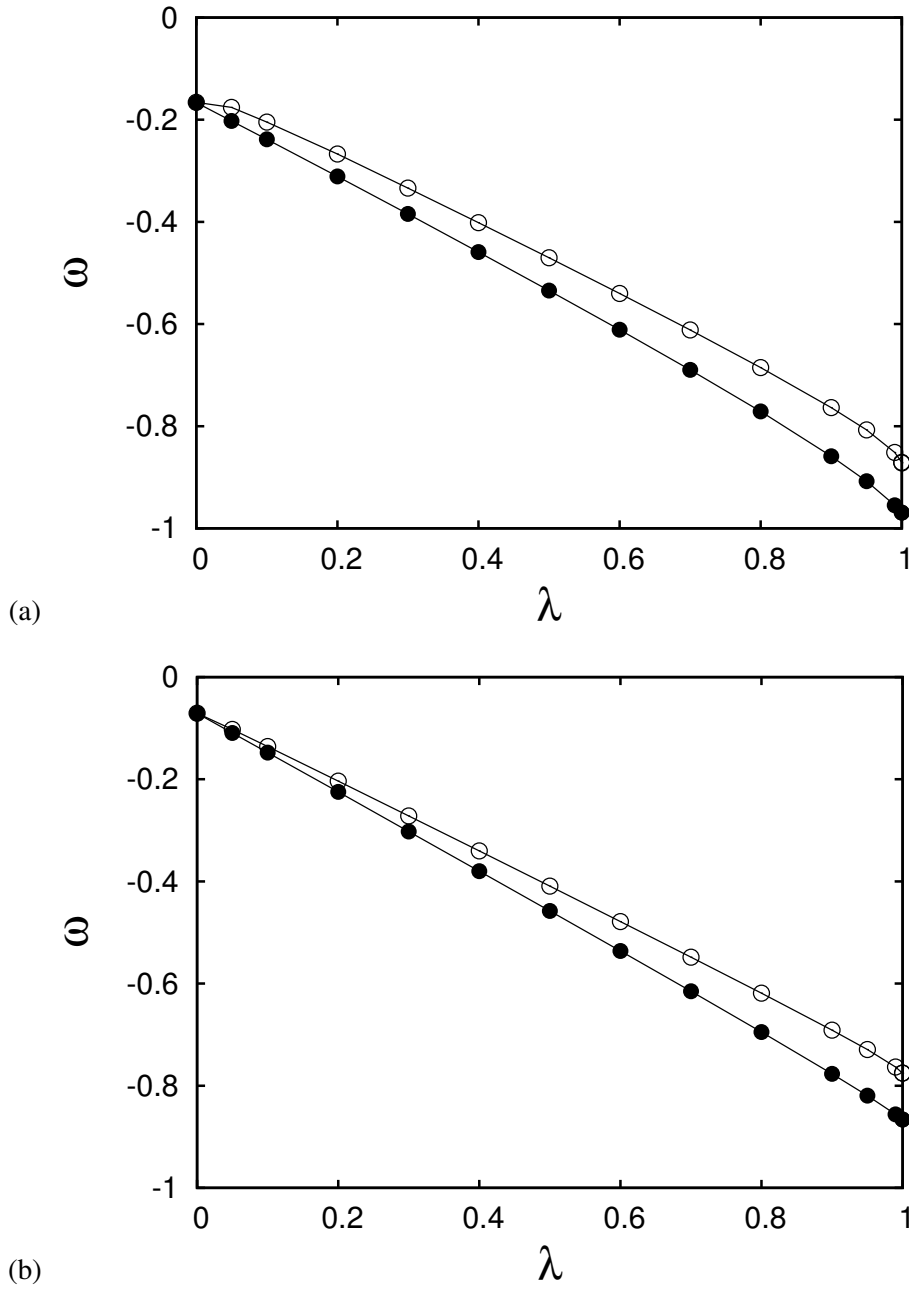


FIG. 4.5: Plots of the (semi-) grand potential density ω as a function of λ [see Eq. (4.32)] at $T = 1.0$ and $s_{z0} = 6.8$ for $\kappa = 10^4$ (●) and $\kappa = 30$ (○). Plot (a) corresponds to a fluid in a liquid-like phase at $\mu = -11.3$ while the fluid of (b) is in a gas-like phase at $\mu = -11.6$.

fluid–wall interaction associated with changing λ do not induce a phase transition.

From the plots in Fig. 4.5a, we recognise that both systems, the one with deformable walls as well as the one with (quasi-) rigid fcc walls, start with the same $\omega(0) = \tau_{\parallel}^{ref}$ as they must because both simulations correspond to the unperturbed system with smooth walls. Upon increasing λ , ω decreases regardless of κ although the decrease is faster the larger is κ . Thus, the final $\omega(1)$ of the system with (quasi-) rigid walls ($\kappa = 10^4$) is smaller than the $\omega(1)$ of the system with deformable walls ($\kappa = 30$).

The situation described so far belongs to an initial point $\mu_l^{(in)} = -11.3$ of the liquid-like phase but as mentioned before we apply the same procedure to determine a second initial point for the gas-like phase at $\mu_g^{(in)} = -11.6$. The plots in Fig. 4.5b show a similar behaviour of $\omega(\lambda)$ in the gas-like phase for the system with deformable walls (\odot) as well as for the system with (quasi-) rigid walls (\bullet).

Once two initial points $\omega(\mu^{(in)})$ are obtained for the system of interest, other values of $\omega(\mu)$ in between are calculated through

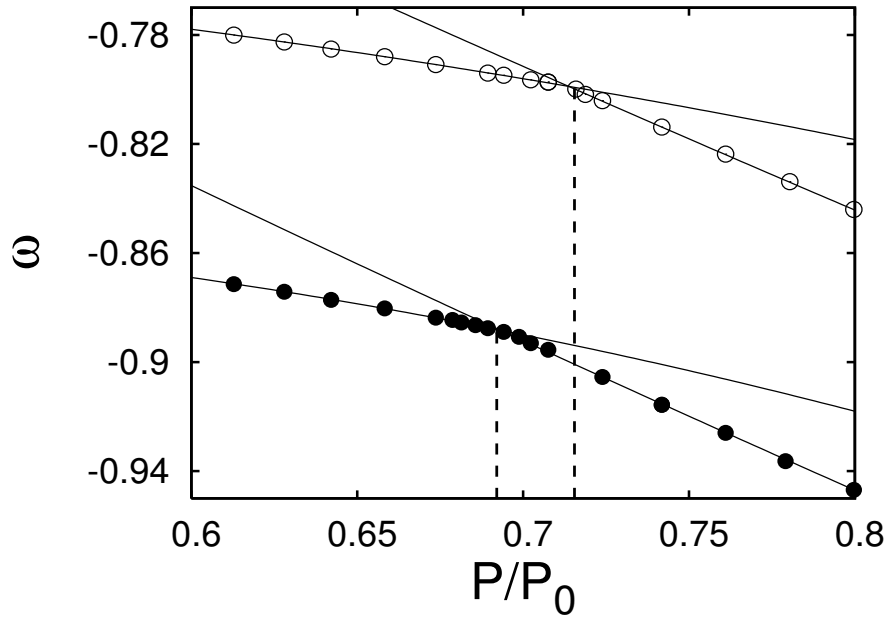
$$\omega(\mu) = \omega(\mu^{(in)}) - \int_{\mu^{(in)}}^{\mu} \rho(\mu') d\mu' \quad (4.33)$$

where we use Eq. (4.10) in its integrated form at $T = \text{const}$. The integrand in Eq. (4.33), i.e. the mean (number) density ρ , is computed as an ensemble average in SGCMC simulations and therefore can be derived from the calculated sorption isotherms of the system of interest.

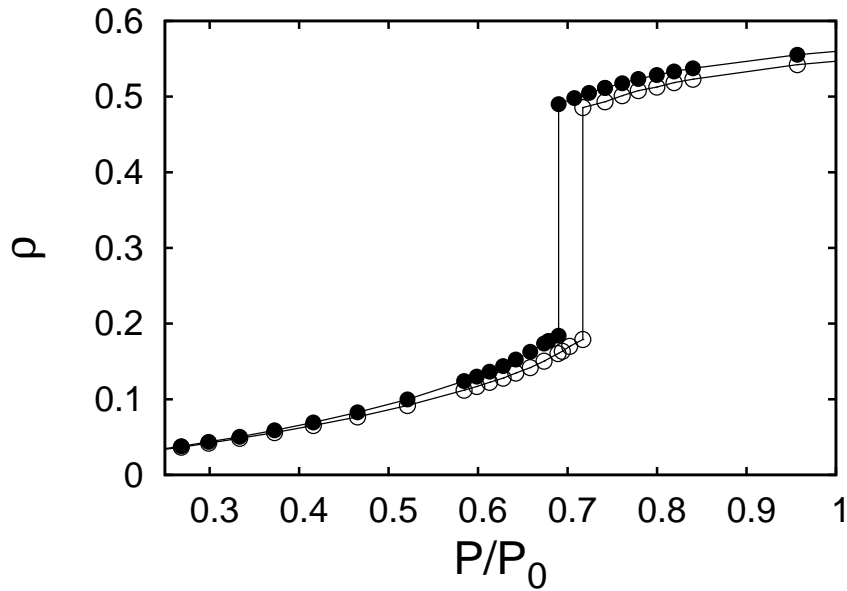
4.4 Capillary Condensation Between Flexible Walls

By confining a fluid between substrates of separation $s_{z0} = 6.8$ one expects a shift of the gas–liquid phase transition to smaller pressures than the pressure P_0 at which the bulk fluid condenses. The reason for this behaviour is that a part of the fluid–fluid interaction is replaced by the more attractive fluid–substrate interaction as a result of the denser structure of the solid substrate. Thus, it is suitable to analyse confinement effects by comparing the confined fluid with the bulk fluid as convenient in sorption experiments. To implement the (virtual) bulk fluid reservoir in SGCMC simulations, a separate bulk simulation is run for each μ of the confined system to compute the bulk pressure $P(\mu)$ [$= -\tau_b$, see Eq. (4.8)] at same μ and T . In the following discussion the chemical potential μ is expressed in terms of the bulk fluid pressure $P(\mu)$ which is normalised to the bulk condensation pressure P_0 given by Eq. (4.13).

4.4 | Capillary Condensation Between Flexible Walls



(a)



(b)

FIG. 4.6: (a) Semi-grand potential densities ω as a function of the (reduced) bulk fluid pressure P/P_0 for a fluid between deformable walls with $\kappa = 30$ (\odot) and between (quasi-) rigid walls with $\kappa = 10^4$ (\bullet) at $s_{z0} = 6.8$ and $T = 1.0$. The vertical dashed lines demarcate phase transitions. (b) As before, but sorption isotherms $\rho(P/P_0)$ of both systems are plotted where data from Section 4.5 have been utilised to achieve coexistence densities at capillary condensation. Values of $\rho(P/P_0)$ are inaccessible in the pressure range $P/P_0 \lesssim 0.25$ for reasons discussed in Section 4.1.

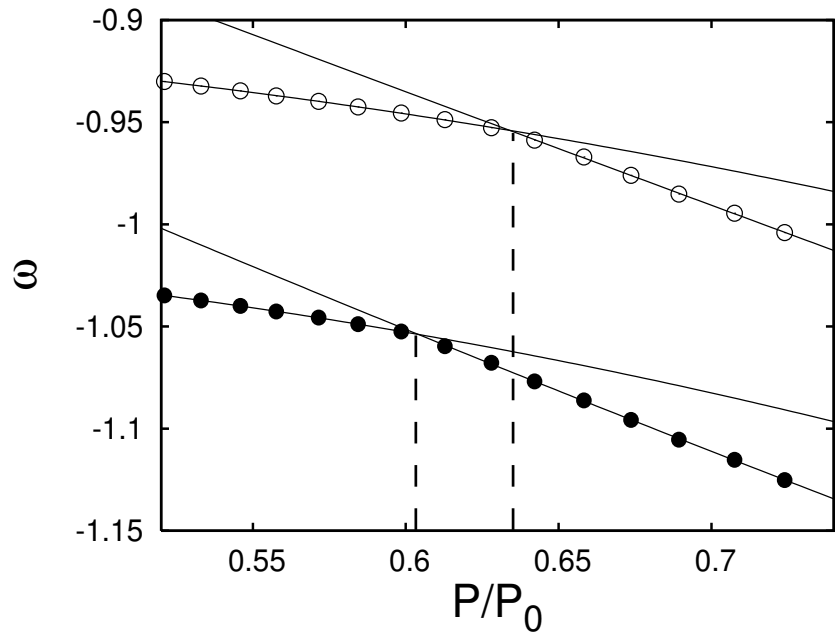
In Fig. 4.6a, the semi-grand potential density ω is plotted as a function of the (reduced) bulk fluid pressure P/P_0 for a system with almost rigid fcc walls ($\kappa = 10^4$, ●) at $T = 1.0$. Here, the initial chemical potentials $\mu^{(in)}$ of Fig. 4.5 correspond to situations slightly outside the plot at $P(\mu = -11.6)/P_0 \simeq 0.55$ and $P(\mu = -11.3)/P_0 \simeq 0.85$, respectively. It becomes apparent that the properties discussed in Section 4.2, in particular Eqs. (4.10) and (4.11), that is ω is a monotonically decreasing and concave function, also holds for a fluid in confinement and for the dependence on P/P_0 . The gas–liquid phase transition at $P/P_0 \simeq 0.69$, demarcated by a vertical dashed line, shows indeed the shift to lower pressures than the fluid bulk condensation pressure at $P/P_0 = 1$ which is outside the range of (reduced) pressures in Fig. 4.6a.

A decrease of the harmonic force constant to $\kappa = 30$ (⊙) makes the walls deformable, so that their wall particles are able to depart from their lattice sites to some extent. The wall flexibility causes a shift of the gas–liquid phase transition toward larger pressures $P/P_0 \simeq 0.72$ compared to the (quasi) rigid fcc walls. This means that the liquid phase is destabilised through the deformability of the substrate and that a (slightly) larger bulk fluid pressure is needed to induce the gas–liquid phase transition. A look at the adsorption isotherms $\rho(P/P_0)$ in Fig. 4.6b for a fluid between deformable walls (⊙) and (quasi-) rigid fcc walls (●) reveals a smaller fluid adsorption in pores with deformable walls. The discrepancy in adsorption increases in the gas-like phase with increasing pressure P/P_0 and remains almost constant for the liquid-like phase. As a result, the adsorption isotherm $\rho(P/P_0)$ for the fluid confined by deformable walls is shifted with respect to P/P_0 and ρ in relation to the fluid between rigid fcc walls, as long as pressures above capillary condensation are considered. The congruence of phase transitions indicated in Fig. 4.6a and 4.6b shows that no sorption hysteresis is involved and that the adsorption isotherms represent equilibrium processes. In fact, data from Section 4.5 is used to achieve coexistence densities exactly at the point of capillary condensation, that is, at $P/P_0 \simeq 0.69$ for the (quasi-) rigid pore with $\kappa = 10^4$ and at $P/P_0 \simeq 0.72$ for the flexible pore with $\kappa = 30$.

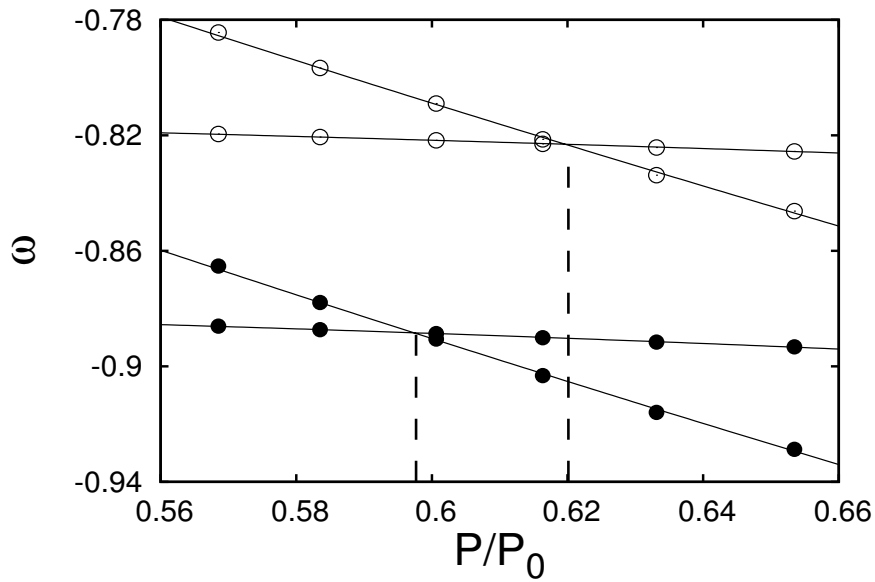
If one reduces the distance between the confining substrates to $s_{z0} = 5.6$, a similar situation arises which is shown in Fig. 4.7a. On account of the increased degree of confinement [cf. Eq. (3.6)] capillary condensation occurs at smaller bulk pressures but the shift of phase transition remains. While the fluid in the (quasi-) rigid pore with $\kappa = 10^4$ (●) condenses at $P/P_0 \simeq 0.61$, the fluid exposed to the dynamically changing field of the deformable pore with $\kappa = 30$ undergoes capillary condensation at $P/P_0 \simeq 0.63$.

Fig. 4.7b belongs to the reverse situation where the pore width of $s_{z0} = 6.8$ is maintained but the temperature is reduced to $T = 0.8$. According to one's physical

4.4 | Capillary Condensation Between Flexible Walls



(a)



(b)

FIG. 4.7: Semi-grand potential density ω as a function of the (reduced) bulk pressure P/P_0 for a fluid between deformable walls with $\kappa = 30$ (\circ) and between (quasi-) rigid fcc walls with $\kappa = 10^4$ (\bullet) at **(a)** $s_{20} = 5.6$, $T = 1.0$ and **(b)** $s_{20} = 6.8$, $T = 0.8$. The vertical dashed lines demarcate phase transitions.

intuition, the phase transition occurs at lower pressures P/P_0 because with decreasing temperature liquid-like phases are stabilised. The gas–liquid phase transition for the fluid between (quasi-) rigid fcc walls ($\kappa = 10^4$, ●) occurs at $P/P_0 \approx 0.6$, unlike the system with deformable walls ($\kappa = 30$, ⊙), where capillary condensation sets in at $P/P_0 \approx 0.62$.

The different conditions of Fig. 4.6a and 4.7a,b shows that the shift in capillary condensation due to the deformability of the wall is independent of the pore width s_{z0} and temperature T . Thus, it is a generic effect which is independent of the specific thermodynamic conditions of the system under consideration.

4.4.1 Contact with Sorption Experiments

Since the shift of phase transition toward bulk condensation pressure due to the wall's deformability is of a few percent, it should be experimentally observable in principle. However, an experimental verification of this effect is very demanding because it is nearly impossible to change the substrate deformability without changing other parameters.

For example, a way to tune the deformability of a pore wall is to modify its thickness. The wall thickness has been controlled during the synthesis of MCM-41 [126] and SBA-15 [20] but such modifications were always accompanied by other structural changes such as the pore size, i.e., the degree of confinement (cf. Section 3.2). Since the degree of confinement has a significant impact on a fluid's phase behaviour, the effect of substrate softness on capillary condensation cannot be separated in these systems. Moreover, in [126] and [20] the pore size is determined by using the BJH or KJS method (see Section 3.2) which are calculated from the pressure at which capillary condensation sets in and, thus, a shift due to the walls deformability would be buried in an erroneous determination of the (average) pore size.

At the moment there is only one experimental result by Grosmann et al. [127] that may show the shift of phase transition due to the wall's flexibility. Grosman et al. were able to synthesise mesoporous silicon and use it as a template for further synthesis of a silicon membrane which resembles its template in every sense but the wall thickness. [82, 127] Thus, template and membrane seem to be an experimental realisation of two systems which differ only in wall deformability.

The nitrogen adsorption isotherms in Figs. 1 and 2 of [127] show a shift in capillary condensation for the (more deformable) silicon membrane compared to the (more rigid) silicon template in analogy to the shift described in the preceding section. The shift applies to the adsorption as well as to the desorption process and therefore the

4.4 | Capillary Condensation Between Flexible Walls

whole hysteresis region is shifted for the membrane by a few percent as in the present computer experiment. The lesser fluid adsorption in the more deformable membrane in the gas-like phase is consistent with the simulation data, but the experiment shows nearly no discrepancy in adsorption in the liquid-like phase, contrary to the computed results of Fig. 4.6b.

Experimentally the sorption process often exhibits hysteresis, that is $\Gamma(P)$ is double-valued over a certain pressure range (see Fig. 4.1). The pressure at which the thermodynamic phase transition should occur is therefore buried somewhere in the hysteresis loop and normally not known precisely. As a result some of the states within the hysteresis loop cannot be true equilibrium states but must be metastable as discussed before in Section 4.1. Because of this lack of information as far as the location of the thermodynamic phase transition in the experimental system is concerned a direct comparison between experiment and theory is inhibited.

4.4.2 Comparison with Rough Pore Models

In Section 3.5 we already emphasised the similarity between the present model and the treatment of quenched annealed model systems which mimic the synthesis process and the resulting (static) roughness of pore walls. A study presented in [112] investigates the impact of such a rough structured pore wall on the sorption process in comparison to that of a regular structured wall. The computed sorption isotherms in Fig. 6 of [112] show a shift of capillary condensation to lower pressures for the rough pore compared to the regular pore, contrary to the findings in Section 4.4. This shift to lower pressures applies for the adsorption as well as for the desorption process. Additionally, a larger adsorption is observed for rough pores where the discrepancy is more pronounced in the gas-like phase than in the liquid-like phase. These results can be explained as follows: Although rough and regular pore share the same (average) pore diameter, the wall area is larger for the rough pore on account of bulges and bumps than for regular pores. Thus, the degree of confinement (see Section 3.2) is larger in the case of rough pore which explains the larger adsorption and the shift of capillary condensation to lower pressures. In general, one expects a more complex sorption behaviour for rough pores because of their irregularity and the associated fluctuations in the local pore size which may even lead to a step-wise sorption process. [128]

However, the situation in the present model is the opposite to that of the (static) rough pore of [112] because the thermal roughness of walls prevents fluid adsorption and results in a shift of capillary condensation to larger pressures compared to a reg-

ular (quasi-rigid) pore (see Fig. 4.6b). The discrepancy between static and thermal roughness can be explained if one perceives that the thermal rough pore bears no roughness *on average*, that is, the wall is homogeneous in direction to the pore axis, contrary to the static rough pore. Thus, even though static and thermal roughness seem to be related, their impact on sorption is directly opposed to one another.

4.4.3 Comparison with Another Model of Deformable Pores

In [129] Ustinov and Do present density functional calculations modelling nitrogen adsorption in deformable slit-like graphitic pores. According to the experimental system, their work deals with very narrow pores of width of one or two fluid diameters. Pore deformation is accounted for through an additional energy contribution which arises from the deformation of the wall as well as by a modified energy contribution from the interaction of opposite walls on account of their deformability.

The calculated adsorption isotherms in Fig. 3 of [129] demonstrate the effect of deformable pore walls on the bulk fluid pressure at which capillary condensation occurs. Nearly all systems exhibit a shift of capillary condensation to lower bulk fluid pressures due to wall deformability, where the shift is more pronounced the smaller the pore width. Thus, the findings of [129] are contrary to the results of the present model system.

4.5 Coexisting Phases

To gain further insight into the conditions under which a fluid undergoes a reorganisation of matter, i.e. a phase transition, we investigate the situation where neither of the phases is preferred, that is, both share the same probability of occurring. In Chapter 1 we emphasised that gas and liquid phases basically differ in density, that is the fluid particle number N of the system under consideration. Comparing Eqs. (2.47) and (3.30), the probability $P(N)$ of finding N fluid particles in a system at fixed temperature T and volume V can be written

$$P(N) = \frac{1}{\Xi} e^{\beta\mu N} e^{-\beta U} = \frac{1}{\Xi} \mathcal{P}(N) \quad (4.34)$$

where the (semi-) grand partition function Ξ is given by Eq. (3.31) and $\mathcal{P}(N)$ is the (unnormalised) probability of realising particle number N in the system of interest. According to Eq. (2.24) we can sum over the particle number on the left and right

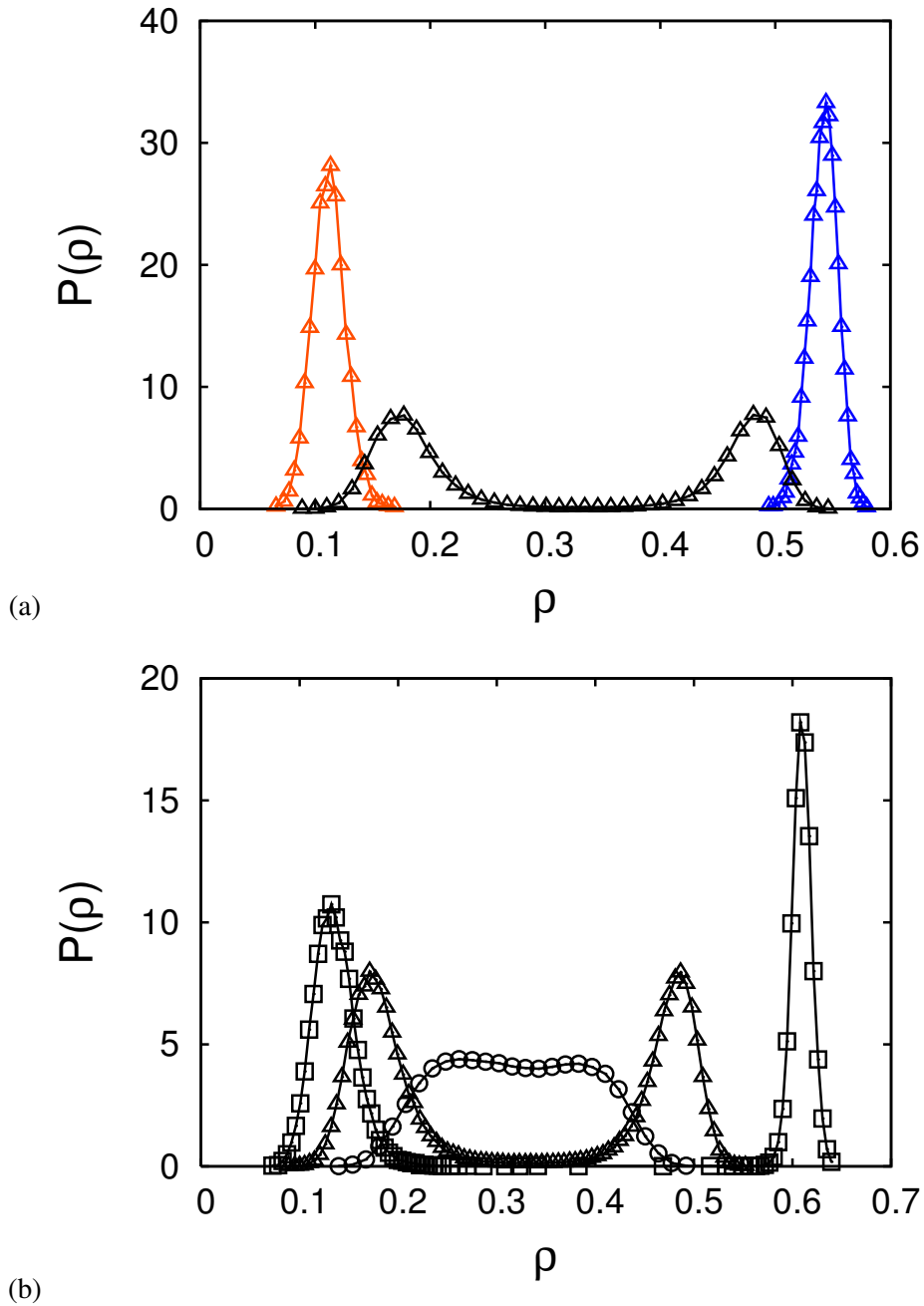


FIG. 4.8: Probability $P(\rho)$ as a function of density ρ for a fluid between flexible walls with $\kappa = 30$ and $s_{z0} = 6.8$: **(a)** For three chemical potentials μ at $T = 1.0$ where the fluid is (i) in the one-phase region of a gas-like state (Δ , $\mu = -11.438$), (ii) in the two-phase region at phase coexistence (Δ , $\mu_x = -11.431$) and (iii) in the one-phase region of a liquid-like state (Δ , $\mu = -11.2$). **(b)** For three temperatures $T = 0.85$ (\square , $\mu_x = -10.151$), $T = 1.0$ (Δ , $\mu_x = -11.431$), and $T = 1.06 \approx T_c$ (\circ , $\mu_x = -11.918$) at which fluid-like and gas-like phases are in coexistence.

side of Eq. (4.34) to yield

$$\sum_N P(N) = 1 = \frac{1}{\Xi} \sum_N \mathcal{P}(N) \quad (4.35)$$

Further, we can rewrite the latter equation through the transformation of variables $N \rightarrow \rho = N/V_0$ where ρ is approximated to be continuous in a (macroscopic) system of $V_0 \rightarrow \infty$ and, therefore, the sums become integrals

$$\int_0^\infty P(\rho) d\rho = 1 = \frac{1}{\Xi} \int_0^\infty \mathcal{P}(\rho) d\rho \quad (4.36)$$

where $P(\rho)$ is the normalised probability, unlike $\mathcal{P}(\rho)$ which is the unnormalised probability, of realising density ρ in the system of interest. Using Eqs. (2.41) and (4.36) $\mathcal{P}(\rho)$ can be identified as a property of a phase α in the system under consideration because of

$$\int_0^\infty \mathcal{P}_\alpha(\rho) d\rho = \Xi_\alpha = e^{-\beta\Omega_\alpha} \quad (4.37)$$

where $\mathcal{P}_\alpha(\rho)$ is the probability of phase α to realise density ρ . This conclusion is based upon the fact that phases are characterised by the grand potential which may be different as in the case of metastable states or that may be the same if the phases are coexistent, as discussed before in Section 4.2.

The probability distribution $P(\rho)$, given by the left side of Eq. (4.36), can be computed as a histogram in semi-grand canonical Monte Carlo simulations. As long as the system is in a one-phase region of a given isotherm, $P(\rho)$ resembles a nearly symmetric distribution with a maximum that approximately corresponds to the average density of the phase, shown in Fig. 4.8a for a fluid between flexible walls ($\kappa = 30$) in a gas-like phase (Δ) and in a liquid-like phase (Δ). But in the two-phase region, i.e. near capillary condensation, $P(\rho)$ shows a two-peaked structure (Δ) where an individual peak resembles $\mathcal{P}_\alpha(\rho)$ of phase α according to Eq. (4.37). It is obvious that the computed average density (and other averaged properties) of a simulation run in the two-phase region corresponds to neither of the two phases. In fact, the data must be analysed separately according to each individual peak to obtain the properties of a phase. For example, averaging the densities of each individual peak results in the (average) density of each phase.

To derive the condition for phase coexistence in terms of density distributions, we invoke Eq. (4.12) in the form of

$$\omega_\alpha(\mu_x) = \omega_\beta(\mu_x) \quad T, V = \text{const.} \quad (4.38)$$

4.5 | Coexisting Phases

where α and β denote two phases which are in coexistence at μ_x . Since the phase-containing volume V_0 is the same for a given system under consideration, $\omega = \Omega/V_0$ of Eq. (4.38) can be rewritten as

$$\Omega_\alpha(\mu_x) = \Omega_\beta(\mu_x) \quad (4.39)$$

$$\Xi_\alpha(\mu_x) = \Xi_\beta(\mu_x) \quad (4.40)$$

$$\int_0^\infty \mathcal{P}_\alpha[\rho(\mu_x)]d\rho = \int_0^\infty \mathcal{P}_\beta[\rho(\mu_x)]d\rho \quad (4.41)$$

where Eq. (4.37) is used to derive the latter two equations. In other words, for given T and V the areas under the individual peaks of $\mathcal{P}_{\alpha,\beta}$ has to be equal at μ_x . Since probability is normalised to 1, the area under an individual peak of a two peaked structure is 1/2 at phase coexistence.

Taking Eq. (4.41) into account, one identifies the probability distribution of the two-phase region given in Fig. 4.8a (Δ) to resemble coexisting states because the areas under both peaks correspond to one another. The peak at lower densities ($\rho \approx 0.18$) relates to the gas-like phase in confinement, while the peak associated to the liquid-like phase arises at higher densities ($\rho \approx 0.49$). Both phases are clearly separated through a region in which the probability drops to zero because the corresponding states relate to organisations of matter which are rejected at the given temperature $T = 1.0$. The gap between both peaks of $P(\rho)$ characterises a first-order gas–liquid phase transition.

In Fig. 4.8b the probability distribution at phase coexistence $P[\rho(\mu_x)]$ from Fig. 4.8a (Δ , $T=1.0$) is plotted in combination with $P[\rho(\mu_x)]$ at lower temperature (\square , $T=0.85$) and at higher, near-critical temperature (\odot , $T=1.06 \approx T_c$). It becomes apparent that the peaks are the more separated the lower the temperature because coexisting phases differ more in density as temperature decreases, a known feature of the gas–liquid phase transition. [58, 130] The relation of height and distance of the peaks is a measure of the potential energy barrier [131, 132] that separates preferred organisations of matter and, thus, may represent a bottleneck. This is a consequence of the Monte Carlo algorithm used (see p. 45) which changes the particle number only by one and therefore a sequence of unlikely configurations must be passed to ‘tunnel’ from one phase to the other. In general, the lower the temperature the more unlikely is a phase transition during the simulation run. Thus, there is a lower temperature limit at which bottlenecks arise which prevent the Monte Carlo method from exploring the whole phase space, mentioned before in Section 2.6. This temperature limit can be decreased by slight modifications of the Monte Carlo algorithm which are subject of the following section.

4.5.1 Improved SGCMC Algorithm to Explore Phase Coexistence

To improve the computational efficiency of the Monte Carlo algorithm in the two phase region, displacement attempts of fluid particles are omitted as suggested by Wilding. [131] According to this modification, only creation and destruction of fluid particles are implemented, these being the crucial steps to simulate the transition between gas-like and liquid-like phases. Consequently, the ‘tunnelling frequency’, i.e. the frequency of phase transitions, is increased whereas fluid particles are only indirectly displaced as combinations of destruction and creation processes.

The Monte Carlo algorithm of Section 3.6 is modified to give an improved algorithm which consists of the following steps:

1. Try to move each of the $2N_s$ wall particles using the probability of Eq. (2.65).
2. Make N attempts to create or destroy fluid particles with respect to the probabilities of Eq. (2.72) where creation and destruction occur with the same probability of 0.5.
3. If desired, compute the system properties and start the next iteration cycle by returning to step 1.

However, exploring the phase space near phase coexistence is still computationally intensive and needs $1 - 5 \times 10^6$ iteration cycles. Moreover, the interval in which the average system properties are computed is increased to 50 to ensure that averaged configurations are independent of one another.

4.5.2 Universality

With regard to the modifications described in the preceding section, phase coexistence in the temperature regime down to $T/T_c \approx 0.7$ is explored where T_c is the critical temperature. Since the chemical potential μ_x of phase coexistence is not known *a priori* for a given temperature, some trial and error is required. Once μ_x is determined which is characterised through a two peaked density histogram that satisfies Eq. (4.41), such as the ones shown in Fig. 4.8b, the average density $\rho_{\alpha x}$ of

4.5 | Coexisting Phases

each individual peak $\mathcal{P}_\alpha[\rho(\mu_x)]$ is computed according to

$$\rho_{\alpha x} = \frac{\int_0^\infty \rho \mathcal{P}_\alpha[\rho(\mu_x)] d\rho}{\int_0^\infty \mathcal{P}_\alpha[\rho(\mu_x)] d\rho} = \frac{2}{\Omega} \int_0^\infty \rho \mathcal{P}_\alpha[\rho(\mu_x)] d\rho \quad (4.42)$$

where Eqs. (4.37) and (4.40) are used. This procedure results in the coexistence densities of the gas-like phase ρ_{gx} and the liquid-like phase ρ_{lx} . The difference of both coexistence densities $\Delta\rho_x$ characterises the gas–liquid phase transition and serves as the *order parameter* which vanishes as [60]

$$\Delta\rho_x = \rho_{lx} - \rho_{gx} \propto (T_c - T)^\beta \quad \text{for } T \leq T_c \quad (4.43)$$

as the temperature T approaches the critical temperature T_c . The last equation holds only in the near critical regime and (of course) for subcritical temperatures. Unlike ρ_{gx} , ρ_{lx} and T_c which depend on the exact nature of the fluid system, the critical exponent β is *universal*, that is, it has the same value for a broad range of systems, belonging to the same so-called universality class. [60, 133] For example, β is 1/2 in mean-field models such as the van der Waals fluid [32], and is typically 1/8 in two-dimensional systems [134–136]. It turns out that many factors are irrelevant to decide the universality class of a system under consideration whereas (i) the dimension of the system, (ii) the range of molecular interactions, and (iii) the symmetry of the ordered phase are significant. [60] The last criterion is quite complex and may involve, e.g., the number of fluid components or the confining disordered matrix of quenched annealed systems [137].

It is a prediction of *renormalisation group* calculations that a (single-component) three-dimensional Lennard–Jones fluid belongs to the universal class of the 3D Ising model with $\beta = 1/3$. [131, 138] The identity of β for gas–liquid phase transitions and for magnetic (Ising-like) transitions is confirmed by experiments of high precision. [60]

According to Eq. (4.43) a plot of ρ_{lx} respectively ρ_{gx} versus T , a so-called ρ - T -phase diagram, is suitable to discuss the gas–liquid phase transition, e.g. as shown in Fig. 4.9. With regard to the ρ - T -plane the critical point is characterised by the critical density ρ_c and the critical temperature T_c at which Eq. (4.43) satisfies $\Delta\rho_x = 0$. Contrary to the 3D Ising model which shows a symmetry with respect to the critical point, the gas–liquid phase transition of the Lennard–Jones fluid is antisymmetric, that is, the way in which coexistence densities approach the critical point differ for the gas phase and the liquid phase. [60] Consequently, gas–liquid coexistence lines

which signify coexistence densities in phase diagrams can be described through

$$\rho_{\pm} - \rho_c = a|T - T_c| \pm b|T - T_c|^{\beta} \quad (4.44)$$

where ‘+’ corresponds to the liquid-like phase and ‘-’ denotes the gas-like phase. The parameters a and b are substance specific properties and therefore depend on the exact nature of the system, i.e., they are *not* universal. [139]

4.5.3 Finite Size Effects

Concerning a sufficiently subcritical temperature, such as $T = 0.85$ (\square) of Fig. 4.8b, individual peaks $\mathcal{P}[\rho(\mu)]$ differ in width at phase coexistence. The width of $\mathcal{P}[\rho(\mu)]$ reflects the fluctuations in particle number $N = \rho V$ which relate to the isothermal compressibility K_T of the fluid through [58]

$$K_T = \frac{(\Delta N)^2}{\rho k_B T \langle N \rangle} \quad (4.45)$$

where $(\Delta N)^2 = \langle (N - \langle N \rangle)^2 \rangle$ is the mean-square particle number fluctuation and $\langle N \rangle$ is the average fluid particle number within a phase. Since the compressibility of a fluid is larger in the gas-like phase than in the liquid-like phase, the peak appearing at lower densities is broader than the one arising at larger densities. The discrepancy in width vanishes as the critical regime is reached because upon increasing temperature gas-like and liquid-like phases become more alike until both are indistinguishable at T_c . Simultaneously, fluctuations in particle number (and therefore K_T) increase substantially in the near-critical regime which is reflected by the plots ($\square \rightarrow \Delta \rightarrow \odot$) in Fig. 4.8b.

However, density distributions $P[\rho(\mu)]$ of Fig. 4.8b correspond to systems of finite linear dimension L defined as

$$L \equiv \begin{cases} \frac{1}{3}(s_{x0} + s_{y0} + s_{z0}), & \text{bulk} \\ \frac{1}{2}(s_{x0} + s_{y0}), & \text{slit-pore} \end{cases} \quad (4.46)$$

In contrast, an experimental system is (usually) of macroscopic size and can be considered to consist of a huge number of such finite systems. Thus, density distributions of macroscopic systems with $L \rightarrow \infty$ vanish on account of the statistical behaviour of their subsystems. In general, the associated fluctuation in density, or in particle number ΔN , vanishes with $\langle N \rangle$ as [32, 58]

$$\frac{\Delta N}{\langle N \rangle} = \frac{1}{\sqrt{\langle N \rangle}} \quad (4.47)$$

4.5 | Coexisting Phases

and, thus, density fluctuations are (mostly) local phenomena.

The length scale of density fluctuations is described at the microscopic level through the so-called *correlation length* ξ at which the pair correlation function $g(r)$ (see Section 2.4) converges to 1. In the critical regime the *Ornstein-Zernike* approximation predicts that in the three-dimensional case $g(r)$ obeys the relation [1]

$$g(r) \propto \frac{\exp(-r/\xi(T))}{r^{1+\eta}} \quad (4.48)$$

where the correlation length $\xi(T)$ is a function of temperature and $\eta \approx 0.03$ [1] for the 3D Ising model. In the vicinity of T_c , $\xi(T)$ varies according to [130]

$$\xi(T) \propto t^{-\nu} \quad (4.49)$$

where ν is a (positive) universal parameter and $t = |1 - T/T_c|$ is the reduced temperature. Thus, ξ may become macroscopically large and $g(r)$ long-ranged [see Eq. (4.48)] at the critical temperature. This feature is visible to the unaided eye in form of *critical opalescence* when ξ is comparable to the wave length of light. [60]

According to the above consideration, the finite size of the simulation cell should lead to erroneous results if ξ exceeds L . In fact, finite size effects are always present in MC simulations and manifest themselves in, e.g., sorption hysteresis [118] (mentioned before in Section 4.1) or the (slight) asymmetry of peaks in the density histograms of Fig. 4.8b which should represent (symmetric) Gaussian distributions in the limit of an infinitely large system [135]. The plots in Fig. 4.9 confirm that finite size effects influence also the phase behaviour of fluids because coexistence densities as well as the critical point differ for systems of different size. Upon changing the system size from $L = 12.7$ (\odot) to $L = 15.875$ (Δ) the critical temperature decreases while the critical density increases slightly. The discrepancy on account of the system size is restricted to the near critical regime whereas at sufficiently low temperatures, coexistence densities are independent of the size of the simulation cell.

4.5.4 Finite Size Scaling

From Eq. (4.49) one may see that the critical temperature T_c is a function of the correlation length ξ written

$$T_c \sim \xi^{-1/\nu} \quad (4.50)$$

as long as $\xi < L$. However, if $L < \xi$, the finite size of the simulation cell cuts ξ off at the distance L so that $\xi = L$. Consequently, the cut-off affects the critical temperature

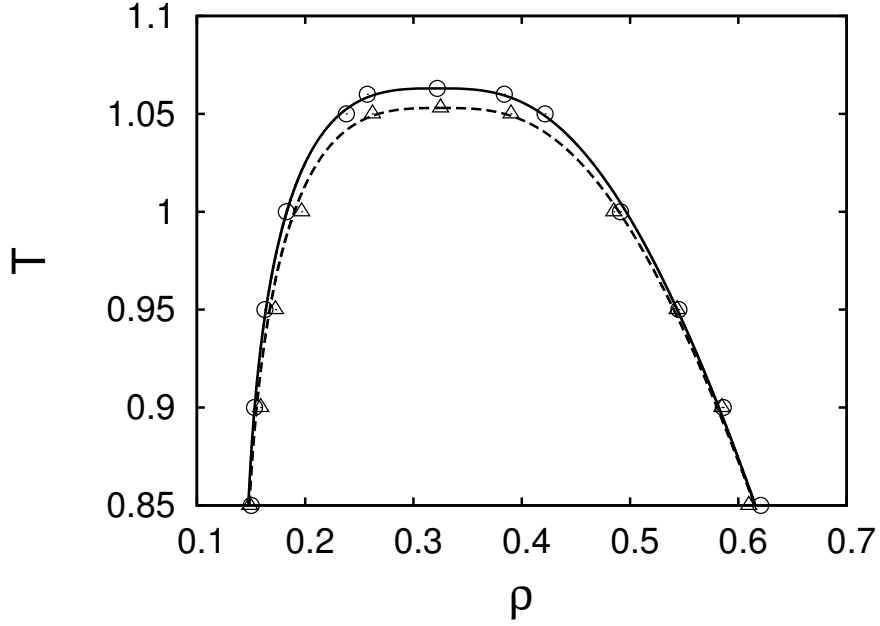


FIG. 4.9: Phase diagram (temperature T versus density ρ) of a fluid between (quasi-) rigid walls with $\kappa = 10^4$ and $s_{z0} = 6.8$ for two different system sizes $L = 12.7$ (\odot) and $L = 15.875$ (\triangle). The lines represent fits according to Eq. (4.44) with $T_c=1.063$, $\rho_c=0.322$, $a=0.28$, $b=0.39$ for $L = 12.7$ (\odot) and $T_c=1.053$, $\rho_c=0.325$, $a=0.28$, $b=0.395$ for $L = 15.875$ (\triangle). In both cases $\beta=0.33$ is utilised. The discrepancy of both curves is more pronounced in the critical regime whereas the system size becomes inconsequential at lower temperatures.

$T_c(L)$ which is shifted in relation to $T_c(\infty)$ of the infinite system according to [130]

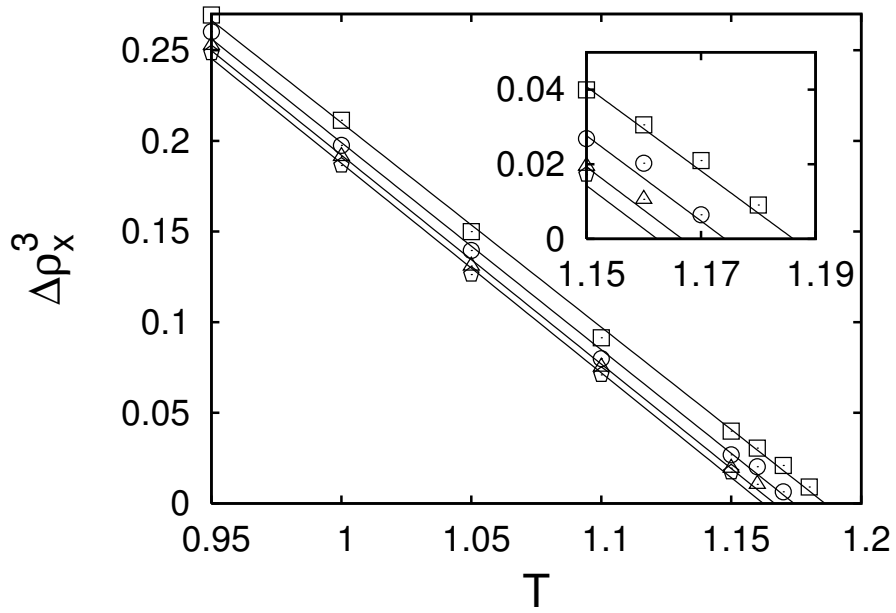
$$T_c(L) - T_c(\infty) \propto L^{-1/\nu}(1 + L^{-w}) \quad (4.51)$$

where Eq. (4.50) is adapted with $\xi = L$ and with an additional correction term L^{-w} . The correction is universal and arises as a consequence of ξ 's rigorous cut-off at distance L disregarding long-ranged correlations larger than L . The *mixed-field* finite size scaling theory identifies the correction term and therefore the exact scaling behaviour as [140]

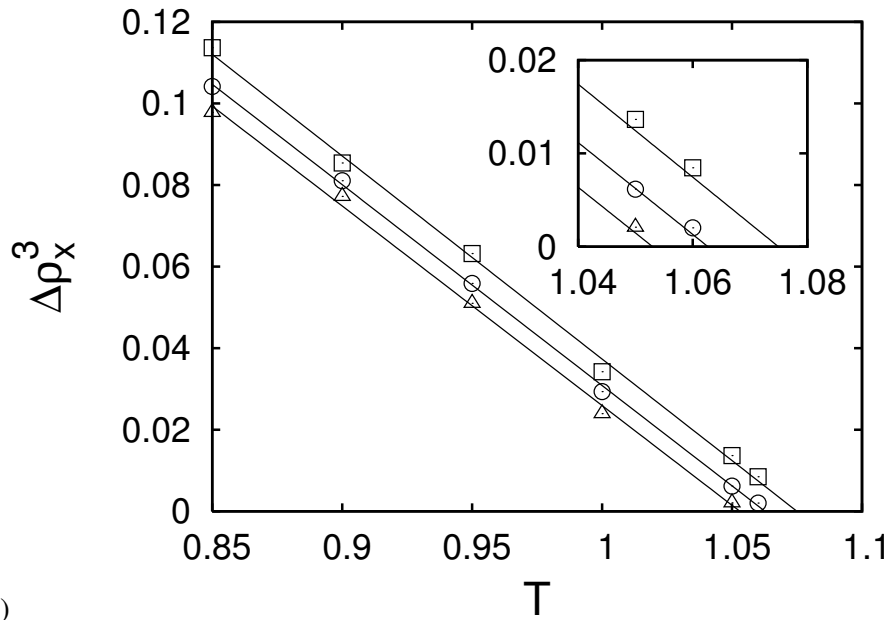
$$T_c(L) - T_c(\infty) \propto L^{-(\theta+1)/\nu} \quad (4.52)$$

where the universal parameters θ and ν for the three-dimensional Lennard–Jones fluid are $\theta = 0.54$ and $\nu = 0.629$. [131, 140]

In Fig. 4.10a the order parameter $\Delta\rho_x^3$, cf. Eq. (4.43), is plotted as a function of temperature for bulk systems of different size L . Analogous plots are shown for the fluid confined between (quasi-) rigid walls in Fig. 4.10b and between deformable



(a)



(b)

FIG. 4.10: Order parameter $\Delta\rho_x^3$ as a function of temperature T for different system sizes L . **(a)** For a bulk fluid of dimension $L = 7$ (\square), $L = 10$ (\odot), $L = 14$ (\triangle), and $L = 17.5$ (\diamond). **(b)** For a fluid in a (quasi-) rigid pore ($\kappa = 10^4$) of system size $L = 9.525$ (\square), $L = 12.7$ (\odot), and $L = 15.875$ (\triangle).

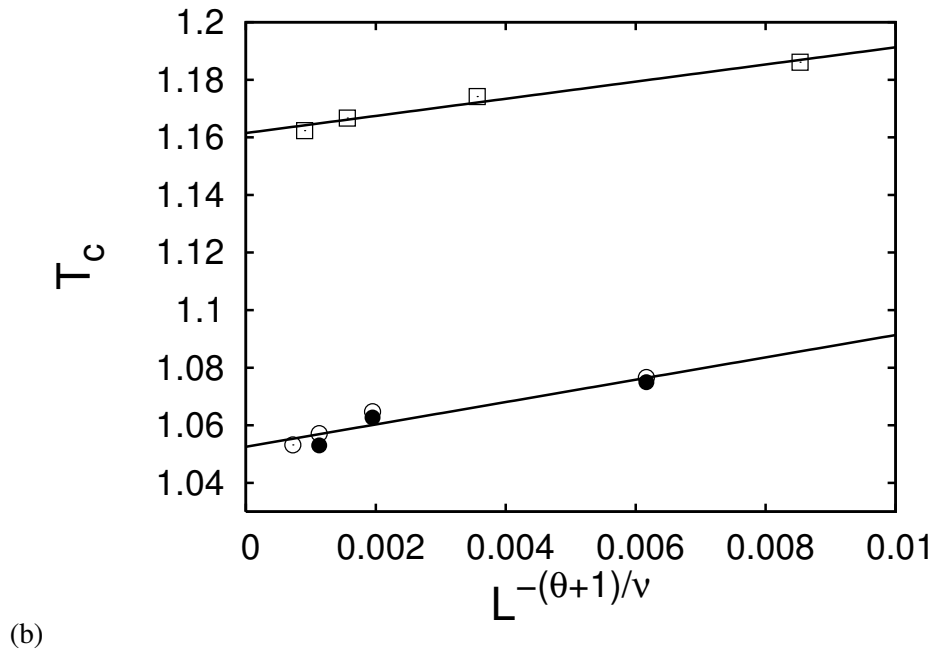
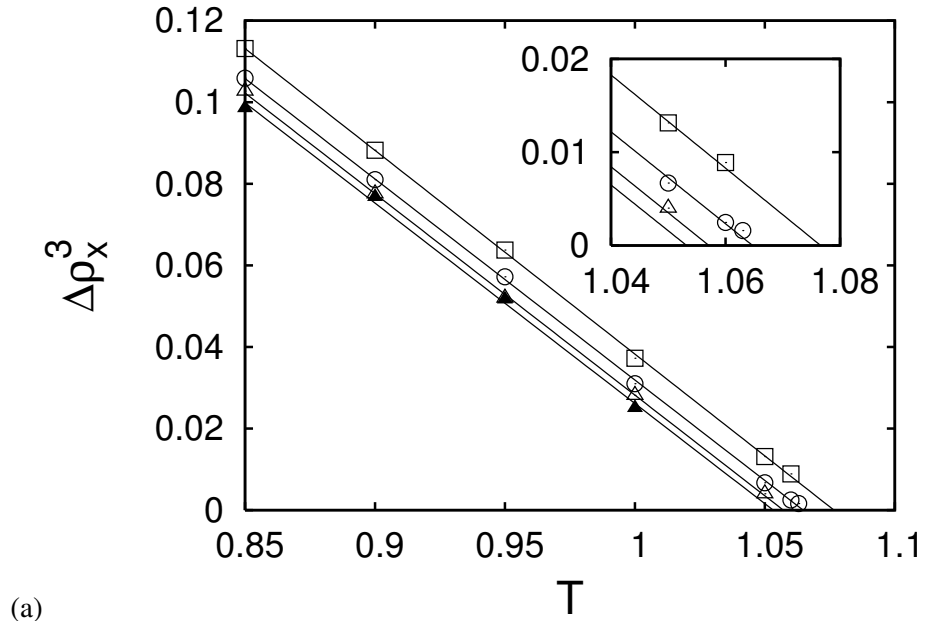


FIG. 4.11: (a) Order parameter $\Delta\rho_x^3$ as a function of temperature T for a fluid between flexible walls of $\kappa = 30$ and dimension $L = 9.525$ (\square), $L = 12.7$ (\circ), $L = 15.875$ (\triangle), and $L = 19.05$ (\blacktriangle). (b) The critical temperature T_c as a function of $L^{-(\theta+1)/\nu}$ for a bulk fluid (\square) and a fluid confined in a (quasi-) rigid pore (\bullet , $\kappa = 10^4$) as well as for a fluid in a flexible pore (\circ , $\kappa = 30$). According to Wilding $\theta = 0.54$ and $\nu = 0.629$ have been utilised. [131]

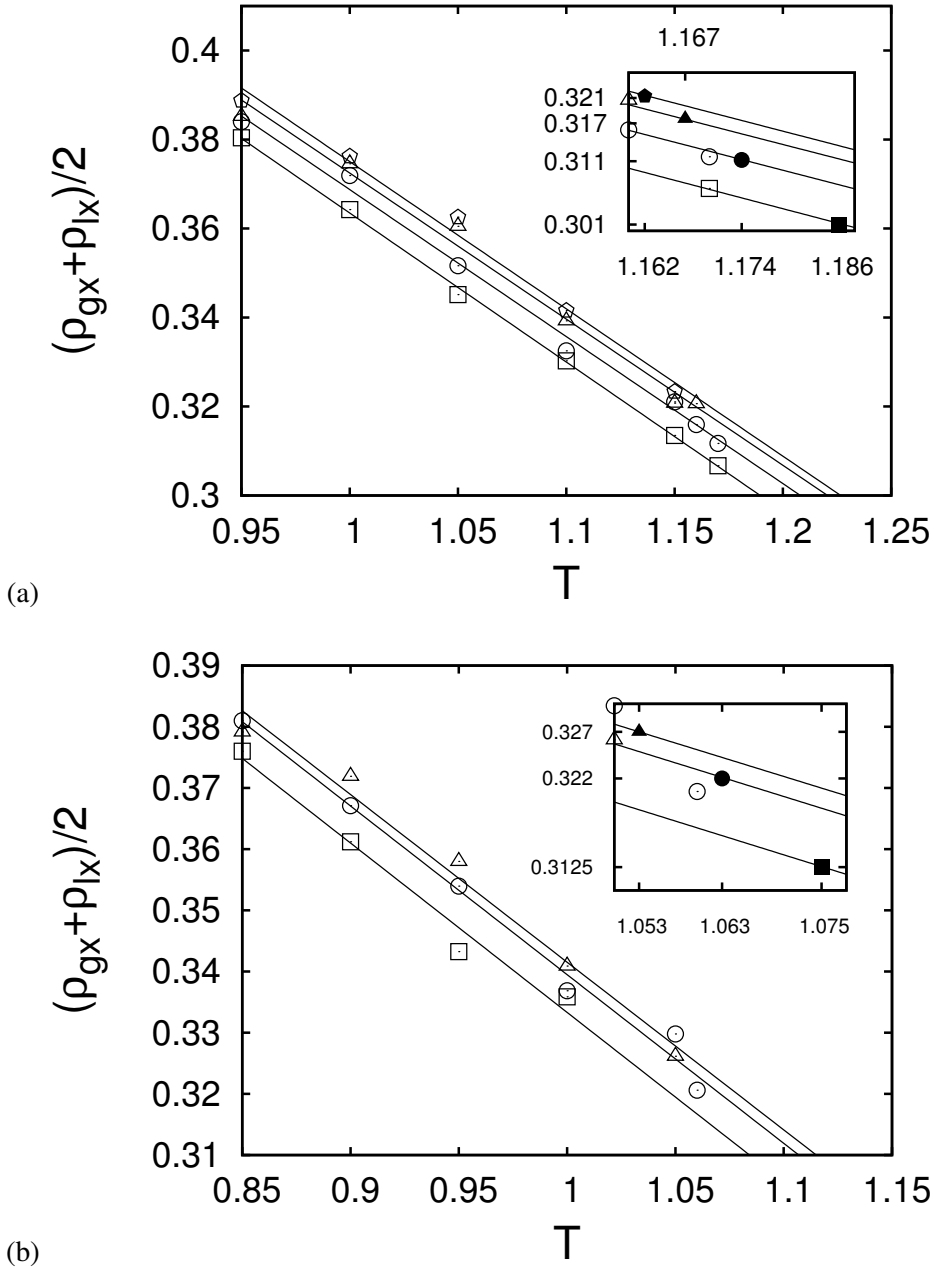


FIG. 4.12: Binodal of Eq. (4.55) as a function of temperature T **(a)** for a bulk fluid of size $L = 7.0$ (\square), $L = 10.0$ (\circ), $L = 14.0$ (Δ), $L = 17.5$ (\diamond) and **(b)** for a fluid between (quasi-) rigid walls with $\kappa = 10^4$ and $s_{z0} = 6.8$ of system size $L = 9.525$ (\square), $L = 12.7$ (\circ), $L = 15.875$ (Δ). Filled symbols of the insets mark the extrapolated critical densities at critical temperatures, respectively, which are given by Fig. 4.10a,b.

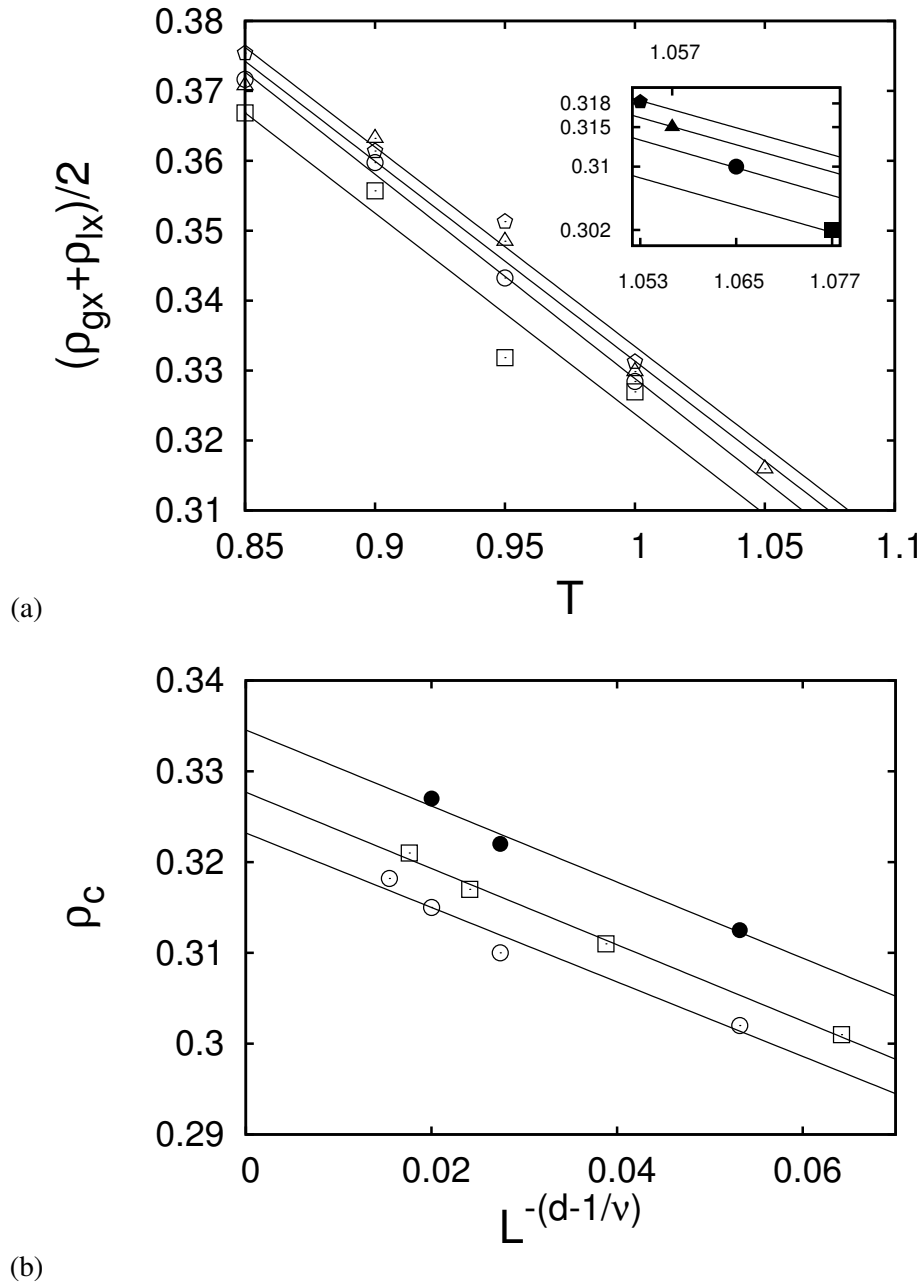


FIG. 4.13: (a) Binodal of Eq. (4.55) as a function of temperature T for a fluid between flexible walls with $\kappa = 30$ and $s_{z0} = 6.8$ of system size $L = 9.525$ (\square), $L = 12.7$ (\odot), $L = 15.875$ (\triangle), and $L = 19.05$ (\diamond). Filled symbols mark ρ_c at T_c , respectively, where latter are taken from Fig. 4.11a. (b) The critical density ρ_c as a function of $L^{-(d-1/\nu)}$ for the bulk fluid (\square , from Fig. 4.12a), the fluid confined in a rigid pore (\bullet , $\kappa = 10^4$, from Fig. 4.12b) as well as a fluid in a flexible pore (\odot , $\kappa = 30$, from Fig. 4.13a). In case of the latter two systems the confinement belongs to $s_{z0} = 6.8$. The dimension $d = 3$ and $\nu = 0.629$ have been utilised, according to Wilding [131].

4.5 | Coexisting Phases

walls in Fig. 4.11a. The linear dependence of the plots for the bulk as well as for the confined systems confirms the critical exponent $\beta = 1/3$ and therefore the critical temperature $T_c(L)$ can be extrapolated at $\Delta\rho_x^3 = 0$ which is shown in more detail in the inset, respectively. The obtained data of $T_c(L)$ are plotted in Fig. 4.11b according to the predicted scaling behaviour of Eq. (4.52) which is again verified by the linear behaviour in bulk (\square) as in confinement (\bullet, \circ). The critical temperature $T_c(L)$ decreases with system size L which agrees with the finding of Panagiotopoulos (cf. Figs. 4 and 5 in [141]). The deformability of the wall seems to have no impact on the critical temperature and, consequently, $T_c(\infty)$ is derived for bulk $T_{cb}(\infty)$ and confinement $T_c(\infty)$ at $L^{-(\theta+1)/\nu} \rightarrow 0$ as

$$T_{cb}(\infty) \simeq 1.161 \quad \text{in bulk} \quad (4.53)$$

$$T_c(\infty) \simeq 1.053 \quad \text{in confinement} \quad (4.54)$$

where the extrapolated value of Eq. (4.54) is based on data of the (quasi-) rigid pore *plus* data of the flexible pore, irrespective of κ .

A similar procedure is applied to determine the critical density ρ_c . Since coexistence densities meet one another at T_c , the so-called binodal $\bar{\rho}$ given by

$$\bar{\rho}(T) = \frac{1}{2}(\rho_{gx}(T) + \rho_{lx}(T)) \quad (4.55)$$

tends to the critical density $\bar{\rho} \rightarrow \rho_c$ as $T \rightarrow T_c$. The binodal usually shows a linear dependence on T and is a measure for the asymmetry of the phase diagram. The plots of $\bar{\rho}$ versus T for the bulk fluid in Fig. 4.12a as well as for the fluid between (quasi-) rigid walls in Fig. 4.12b and between deformable walls in Fig. 4.13a confirm the linear dependence. Although the statistical spread of the data suggests a rather large range of error, nevertheless the data gives reasonable linear fits if some outliers in the near-critical regime are ignored.

With regard to the critical temperatures $T_c(L)$ from Figs. 4.10a,b and 4.11a, the associated critical density $\rho_c(L)$ of a given system size L is determined from Figs. 4.12a, 4.12b and 4.13a which is marked by filled symbols in the insets, respectively. Contrary to the scaling behaviour of T_c , the field-mixing finite size scaling theory predicts that the critical density scales with system size L as [131]

$$\rho_c(L) - \rho_c(\infty) \propto L^{-(d-1/\nu)} \quad (4.56)$$

where d is the dimension of the system, i.e. $d = 3$ in the present three-dimensional model system. Again, the linear dependence shown in Fig. 4.13b confirms the scaling behaviour according to Eq. (4.56) for bulk (\square) as for confinement (\bullet, \circ). In the latter case, the flexibility of confinement has an impact on the critical density where a

deformable wall ($\kappa = 30$, \ominus) significantly decreases ρ_c in relation to a (quasi-) rigid wall ($\kappa = 10^4$, \bullet). The extrapolated critical density in the limit $L \rightarrow \infty$ for a bulk fluid $\rho_{cb}(\infty)$ and a fluid in confinement $\rho_c(\infty)$ are derived from Fig. 4.13b at $L^{-(d-1/\nu)} \rightarrow 0$ as

$$\rho_{cb}(\infty) \simeq 0.328 \quad \text{in bulk} \quad (4.57)$$

$$\rho_{cr}(\infty) \simeq 0.335 \quad \text{in confinement with } \kappa = 10^4 \quad (4.58)$$

$$\rho_{cf}(\infty) \simeq 0.323 \quad \text{in confinement with } \kappa = 30 \quad (4.59)$$

where the additional subscript ‘*r*’ denotes (quasi-) rigid confinement with $\kappa = 10^4$ and ‘*f*’ refers to flexible confinement with $\kappa = 30$.

In case of confined fluids, there is no comparable data available (to the author’s knowledge), but the critical parameters of the bulk fluid are in good agreement with previous studies of Lennard–Jones bulk systems. Since the critical temperature T_c marks the limit at which the kinetic energy of particles overcomes intermolecular attractions, it is expected that T_c increases if the cut-off radius r_c of the Lennard–Jones potential is increased (see Section 3.4) and, thus, the attraction becomes more long-ranged.

The studies by Smit [142] and Lotfi et al. [143] are consistent with this consideration because they yield a larger critical temperature $T_{cb}(\infty) = 1.316$ (Smit) respectively $T_{cb}(\infty) = 1.310$ (Lotfi) for a full (i.e. untruncated) Lennard–Jones bulk fluid, compared to $T_{cb}(\infty) \simeq 1.161$ of Eq. (4.53). The values of the critical density $\rho_{cb}(\infty) = 0.304$ (Smit) respectively $\rho_{cb}(\infty) = 0.314$ (Lotfi) are smaller in relation to Eq. (4.57). Panagiotopoulos [141] as well as Wilding [131] determine the critical parameters of a 3D Lennard–Jones bulk fluid with a truncated (but unshifted) potential at $r_c = 2.5$. Although the smaller r_c should lead to a decrease of T_c , the unshifted character of the potential results in a stronger attraction compared to a shifted one and, therefore, has an opposing effect. However, both studies yield a slightly larger critical temperature $T_{cb}(\infty) = 1.176$ (Panagiotopoulos) and $T_{cb}(\infty) = 1.1876$ (Wilding) respectively, while the critical density of Eq. (4.57) lies between the data given as $\rho_{cb}(\infty) = 0.33$ (Panagiotopoulos) and $\rho_{cb}(\infty) = 0.3197$ (Wilding).

Since the critical parameters of the bulk fluid agree with previous studies, the obtained critical parameters in confinement should be trustworthy as well. To summarise this section, the advantage of the finite size scaling analysis is two-fold: On the one hand, the critical parameters of a macroscopically large system are extrapolated which are essential for a reliable phase diagram. On the other hand, the critical

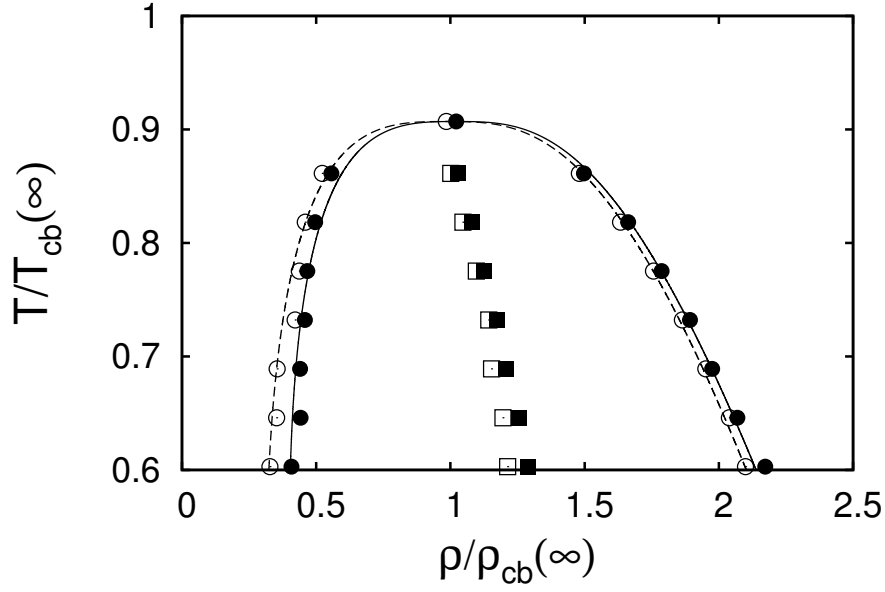


FIG. 4.14: Phase diagram $T/T_{cb}(\infty)$ as a function of $\rho/\rho_{cb}(\infty)$ for a fluid between (quasi-) rigid walls (\bullet , $\kappa = 10^4$) and between flexible walls (\circ , $\kappa = 30$) with $s_{z0} = 6.8$ and $L = 12.7$. Data of the near critical regime are replaced by the critical parameters $T_c(\infty)$ and $\rho_c(\infty)$ obtained from the finite size scaling analysis and therefore the phase diagram represents the behaviour of an infinite system. Data is normalised to the (infinite) bulk critical temperature $T_{cb}(\infty) = 1.161$ and density $\rho_{cb}(\infty) = 0.328$. Moreover, the binodal of Eq. (4.55) for the fluid in the (quasi-) rigid pore (\blacksquare , $\kappa = 10^4$) and in the flexible pore (\square , $\kappa = 30$) is shown, which is a measure of asymmetry of the phase diagram.

point

$$T_c(12.7) \simeq 1.060 \quad (4.60)$$

$$\rho_c(12.7) \simeq 0.316 \quad (4.61)$$

for a confined system of size $L = 12.7$ is obtained from Fig. 4.11b at $L^{-(\theta+1)/\nu} \simeq 0.002$ with high accuracy which is important for the remainder of this work.

4.5.5 Phase Diagram of a Fluid in Flexible Confinement

Now we can combine the data of phase coexistence (see Section 4.5.2) with the finite size scaling analysis of the previous section to construct reliable phase diagrams of confined fluids. In Fig. 4.14 the coexistence densities $\rho_{gx}(T)$ and $\rho_{lx}(T)$ at different temperatures are shown for a fluid between (quasi-) rigid walls (\bullet , $\kappa = 10^4$) and

between deformable walls (\odot , $\kappa = 30$). Both data sets are taken from systems of $s_{z0} = 6.8$ and size $L = 12.7$ for temperatures $T/T_c(12.7) \lesssim 0.94$ where finite size effects are assumed to be negligible (see Fig. 4.9). To represent the critical regime, critical parameters of the extrapolated infinite systems given by Eqs. (4.54) and (4.58) respectively (4.59) are incorporated. The lines are fits according to Eq. (4.44) for the (quasi-) rigid system (straight line, $\kappa = 10^4$) with $\rho_c = 0.335$, $a = 0.23$, $b = 0.4$ and for the deformable system (dashed line, $\kappa = 30$) with $\rho_c = 0.323$, $a = 0.21$, $b = 0.41$. In both cases $T_c = 1.053$ and $\beta = 0.33$ are utilised. Temperature and density are normalised to the critical parameters $T_{cb}(\infty) = 1.161$ and $\rho_{cb}(\infty) = 0.328$ of the (infinite) bulk system specified by Eqs. (4.53) and (4.57).

The phase diagram of the fluid in the (quasi-) rigid pore shows well known confinement effects, that is, the shift to smaller critical temperature and to higher critical density as well as a general narrower course compared to the bulk system. [55, 144] The last feature becomes apparent from Fig. 4.2 which yields $\rho_{gx}/\rho_{cb}(\infty) \approx 0.18$ and $\rho_{lx}/\rho_{cb}(\infty) \approx 1.93$ for the bulk fluid at $T/T_{cb}(\infty) \approx 0.86$, whereas the coexistence densities of the confined fluid are $\rho_{gx}/\rho_{cb}(\infty) \approx 0.5$ and $\rho_{lx}/\rho_{cb}(\infty) \approx 1.5$ at the same temperature. Since T and ρ are normalised to the critical parameters of the bulk system, confinement effects result in $T_c/T_{cb}(\infty) < 1$ and $\rho_c/\rho_{cb}(\infty) > 1$.

If the confining walls become deformable, i.e. $\kappa = 10^4 \rightarrow 30$, the phase diagram is shifted to lower densities. This shift affects the gas-like branch, the liquid-like branch and the critical point. While the discrepancy in coexistence densities is rather little in the critical regime, it becomes more pronounced with decreasing temperature where the discrepancy is larger for the gas-like phase than for the liquid-like phase. At the lowest temperature in Fig. 4.14, $T/T_{cb}(\infty) \approx 0.6$, the discrepancy due to the walls flexibility amounts for the gas-like phase 20% whereas coexistence densities in the liquid-like phase differ only by 1.4%.

The shift of the critical density due to the wall flexibility is confirmed by the (slightly) shifted binodal according to Eq. (4.55) of the flexible pore (\square , $\kappa = 30$) compared to the (quasi-) rigid pore (\blacksquare , $\kappa = 10^4$). Contrary to the (quasi-) rigid wall, the shift to lower values leads to $\rho_c/\rho_{cb}(\infty) < 1$, see also Fig. 4.13b. This is a consequence of the weak attraction of the walls whose particles are of the same type as the fluid. Thus, the fluid–wall attraction comes about merely by the larger density of the wall, a quite minute effect, which is obvious from the only slight increase of ρ_c in the case of the (quasi-) rigid wall. An increase in fluid–wall attraction is expected to overwhelm the wall flexibility-induced shift to result in a total shift of $\rho_c > \rho_{cb}(\infty)$ for flexible pores.

4.6 Fluid Structure between Flexible Walls

The macroscopically observable change in phase behaviour on account of wall flexibility is expected to be the consequence of a different organisation of matter at the molecular level.

4.6.1 Local Density

To address the structural changes of the fluid and the substrate that occur on account of the substrate softness and the thermodynamic state of the fluid, we consider the local density $\rho^{f,s}(z)$ given by

$$\rho^{f,s}(z) \equiv \frac{\langle N_{f,s}(z) \rangle}{A_0 \delta s_z} \quad (4.62)$$

where subscripts ‘ f ’ and ‘ s ’ refer to the local density of the fluid and the substrate particles, respectively. According to this notation, $N_{f,s}(z)$ is the number of fluid or wall particles in a parallelepiped of dimensions $A_0 \times \delta s_z$ centred on z where $\delta s_z = 0.01$ is used (see Table 3.1).

In Fig. 4.15a the local density of fluid particles (full lines) and wall particles (dashed lines) across the pore is shown as a function of the normalised pore width z/s_{z0} for a fluid in a liquid-like state. With regard to the (quasi-) rigid character of the wall, for $\kappa = 10^4$ the local density of wall particles $\rho^s(z)$ (- - -) is given by

$$\rho^s(z) = \delta(z^{[1]} - s_{z0}/2) + \delta(z^{[2]} + s_{z0}/2) \quad (4.63)$$

where δ denotes the Dirac δ -function (see Section B.6.1 of [32]). Consequently, the (quasi-) rigid wall represents a static external field imposed on the confined fluid. As a reaction, the fluid (—) stratifies in layers along the pore walls, that is the centres of mass of fluid particles arrange themselves at preferred regions of z where $\rho^f(z)$ is a maximum while other regions, the minima of $\rho^f(z)$, are disfavoured. Thus, the fluid particles conglomerate in layers parallel to the walls where the layers are less pronounced the larger is the distance to the wall, according to the lesser fluid–substrate interaction.

Stratification is a well known feature of confined fluids and has been noted for a wide range of systems. Among these systems are simple models which consider only repulsive forces such as hard spheres between hard walls, i.e. impenetrable spheres between impenetrable planar parallel regions, to more sophisticated models that involve attractive potentials such as LJ-particles between smooth walls. [145] Stratification has even been reported for nonspherical fluids, ranging from nonspherical

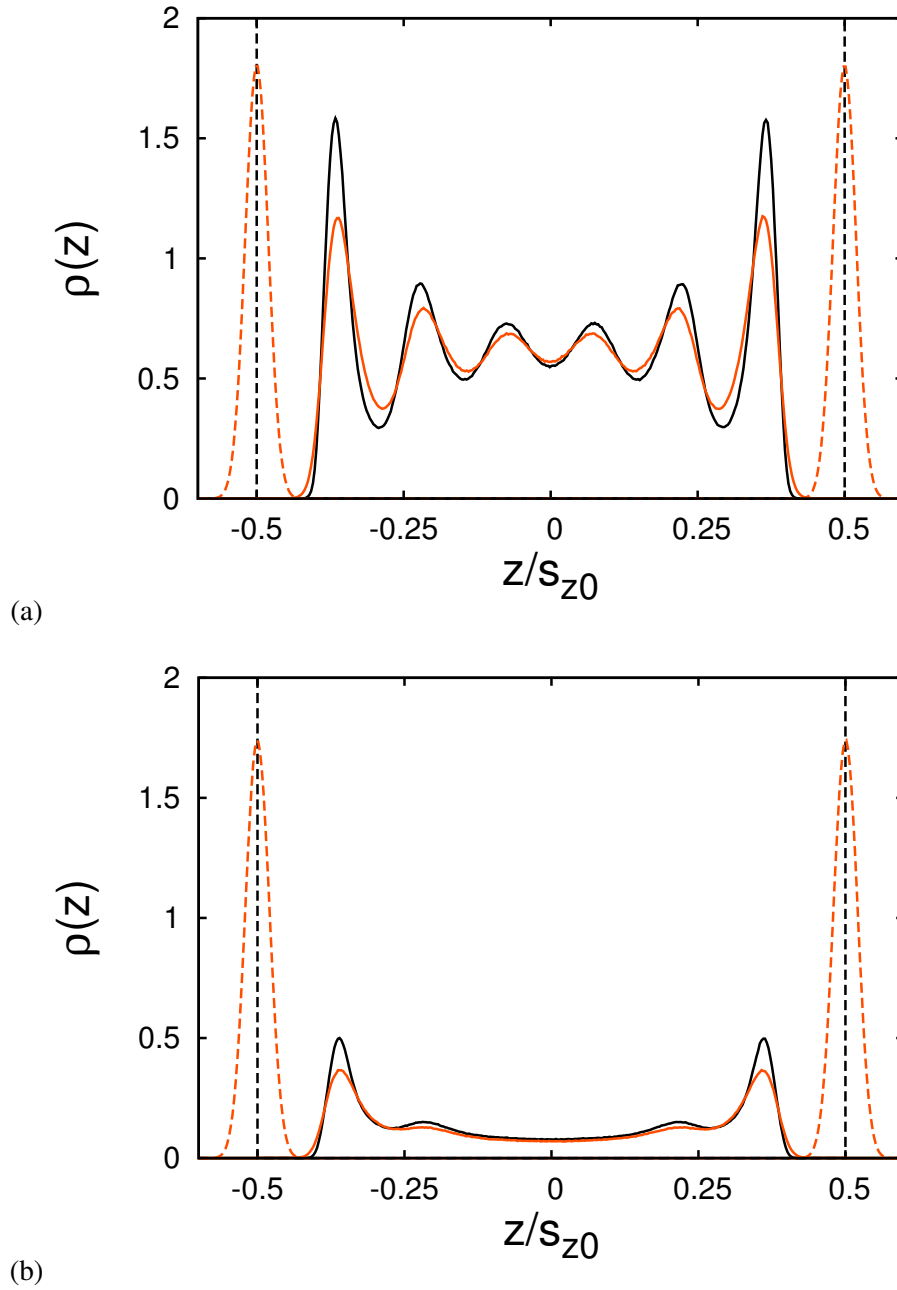


FIG. 4.15: Local density profile $\rho^{f,s}(z)$ across the pore with (quasi-) rigid walls ($\kappa = 10^4$, black) and with deformable walls ($\kappa = 30$, orange) for fluid particles (full lines) and wall particles (dashed lines) at $T = 1.0$ and $s_{z0} = 6.8$. Plot **(a)** shows the fluid in a liquid-like phase at $\mu = -11.3 \leftrightarrow P/P_0 \approx 0.85$ whereas in **(b)** the fluid is in a gas-like phase at $\mu = -11.6 \leftrightarrow P/P_0 \approx 0.55$ both at $T = 1.0$, see Fig. 4.6b.

4.6 | Fluid Structure between Flexible Walls

LJ-particles [146] to alkane-like [147] or water-like molecules [148], as well as for more complex confining geometries, where the walls are e.g. structured [149, 150], chemically patterned [38, 151] or nonplanar [152–154].

If the walls become deformable, that is, if the harmonic force constant is decreased to $\kappa = 30$, the wall particles depart from their lattice sites to some extent which is reflected by the broader $\rho^s(z)$ (---) around $z/s_{z0} = \pm 0.5$ in Fig. 4.15a. The associated thermal roughness of the wall is imparted to the fluid structure through a template effect and therefore the stratification of the fluid diminishes. The fluid appears less ordered because the extrema of $\rho^f(z)$ (—) are less pronounced, i.e. maxima are lower and minima are less shallow. A similar situation is found in the gas-like phase, as plotted in Fig. 4.15b, where stratification is less pronounced and therefore the impact of the substrate softness is rather weak, being virtually restricted to the adsorbed fluid layer. Since the discrepancy is larger for the maxima than for the minima, the overall average density reduces in liquid-like and gas-like phases if the wall flexibility is increased, according to the lower adsorption of Fig. 4.6b.

At least if κ of the present model system would be further decreased, the situation of a fluid at a flexible wall may relate to the interface of two immiscible fluids as described in [155, 156]. In these studies Bresme et al. use molecular dynamics to simulate alkane–water interfaces where priority is given to structural aspects. From the perspective of the alkane, the alkane fluid is in contact with a highly flexible, thermal rough wall composed of water particles along the interface whose rigidity correlates to the surface tension of the alkane–water interface. On account of the high flexibility of the interface, the *intrinsic sampling method* is used to compute *intrinsic density profiles*, that are density profiles of a fluid where thermal fluctuations of the boundary (i.e., of the other fluid) are eliminated. The intrinsic density profile reveals a layering structure of the alkane fluid at the alkane–water interface for a hexane–water system as well as for a dodecane–water system where both systems differ in the surface tension of the interface. The study presented in [156] finds that stratification of the alkane fluid is more pronounced the larger the surface tension, i.e. the rigidity, of the interface, in analogy to the result in Fig. 4.15.

4.6.2 In-Plane Pair Correlation

Because of the arrangement of fluid particles into layers, the molecular structure transverse to the walls within a particular layer is characterised by the in-plane pair

correlation function $g_{\parallel}(r)$ given through [105]

$$g_{\parallel}(r) = \frac{\langle N(r) \rangle}{2\pi r \Delta r \Delta z \rho(z_i)} \quad (4.64)$$

in analogy to $g(r)$ (see Section 2.4). In Eq. (4.64), $N(r)$ is the number of particles in a cylindrical annulus of radius r , thickness Δr and height Δz centred on a reference particle, sketched in Fig. 4.16a. Consequently, the in-plane pair correlation function relates to the probability of finding another particle at distance r within the same layer if a reference particle is located at $r = 0$. The mean local density $\rho(z_i)$ of the i -th layer centred on z_i is given by

$$\rho(z_i) = \frac{1}{\Delta z} \int_{z_i - \Delta z/2}^{z_i + \Delta z/2} \rho(z) dz \quad (4.65)$$

where the boundaries of the layer with respect to the z -direction are determined by the minima accompanying each maximum. Because the volume of the cylindrical annulus increases with increasing r , in Eq. (4.64) the term $\langle N(r) \rangle / 2\pi r \Delta r \Delta z \rightarrow \rho(z_i)$ and therefore $g_{\parallel}(r) \rightarrow 1$, if the limiting case of $r \rightarrow \infty$ is concerned.

Unlike $g(r)$, the in-plane pair correlation function $g_{\parallel}(r)$ of a single fluid layer cannot be extracted directly from experiment because in confinement additional effects must be considered such as ‘cross correlation’ and ‘excluded volume effects’ which may dominate $S(\mathbf{k})$ [see Eq. (2.56)]. [157, 158] The cross correlation is that part of scattering which involves the interaction between the confining matrix and the fluid, while excluded volume effects account for the space in confinement that is unavailable to the fluid due to packing effects and blocked pore regions. To approximate both effects computer simulations are needed [157] and therefore $g_{\parallel}(r)$ can only be extracted *indirectly* if at all.

Nevertheless the in-plane pair correlation function is useful for determining structural aspects of the confined fluid. The function $g_{\parallel}(r)$ is plotted in Fig. 4.16b for the adsorbed fluid layers next to the pore wall of Fig. 4.15a. The black line corresponds to the fluid confined by (quasi-) rigid walls and shows the typical near-order behaviour of liquid-like phases characterised by pronounced but rapidly decreasing extrema which vanish within a few molecule diameters. The near-order behaviour arises mainly on account of repulsive forces between particles at medium and high densities since it is even observable in hard sphere systems. [59, 159] The impact of the substrate softness on the structure of the adsorbed fluid layer parallel to the walls is rather minute as reflected by the orange line corresponding to the fluid between deformable walls with $\kappa = 30$. The (slightly) lower maxima and the faster convergence

4.6 | Fluid Structure between Flexible Walls

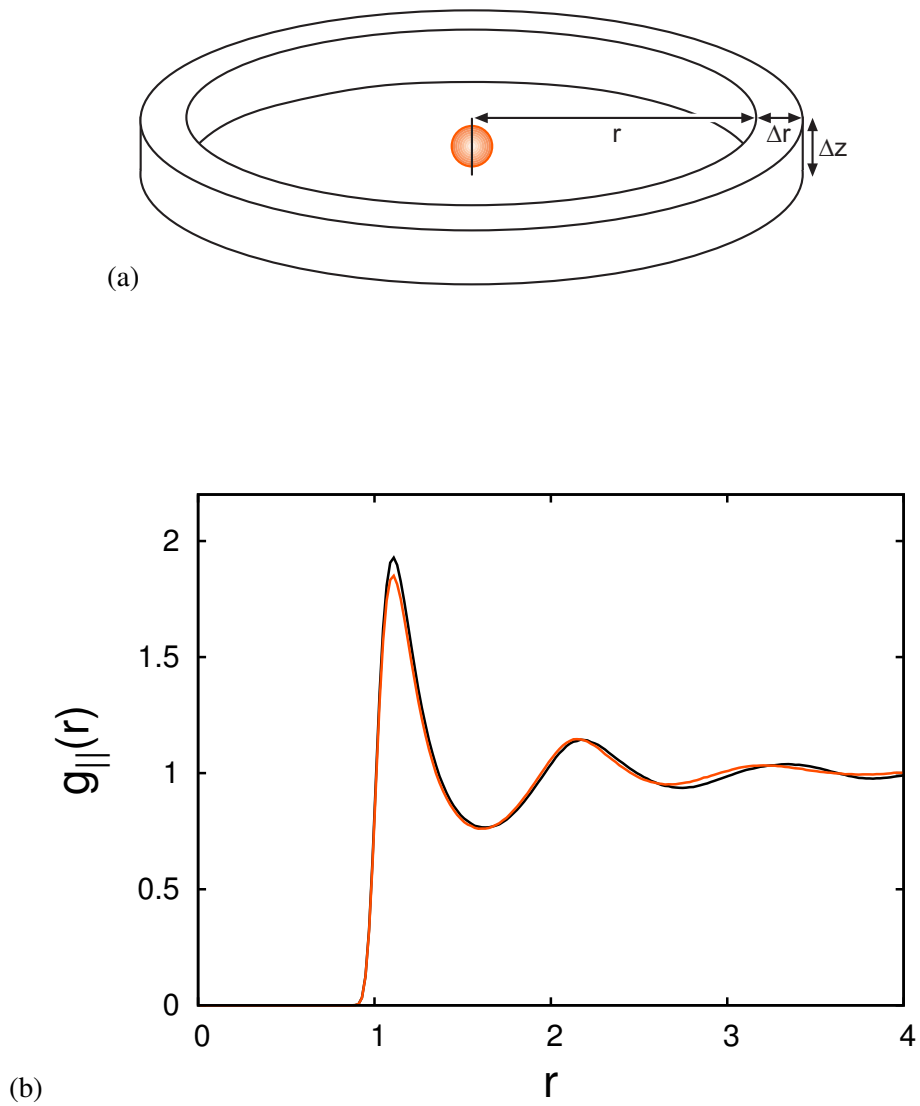


FIG. 4.16: (a) Sketch of the geometry centred on a reference particle (orange) used in Eq. (4.64) to calculate the in-plane pair correlation function $g_{||}(r)$ which is shown in (b) for the adsorbed fluid layer along a (quasi-) rigid pore wall ($\kappa = 10^4$, black) and a deformable pore wall ($\kappa = 30$, orange) where the fluid is in a liquid-like phase at $\mu = -11.3 \leftrightarrow P/P_0 \approx 0.85$ and $T = 1.0$, corresponding to Fig. 4.15a.

$g_{\parallel}(r) \rightarrow 1$ point to a (slightly) more disordered structure of the adsorbed layer along the pore wall. The shift of the extrema to shorter distances for the fluid, adsorbed at the flexible wall, points to a (slightly) denser structure compared to the fluid at the (quasi-) rigid fcc wall. On account of the generally lower density of the adsorbed layer (cf. Fig. 4.15a) the fluid structure along the flexible wall must contain more defects, i.e. spaces along the wall where fluid particles are absent.

In Fig. 8 of [160] a similar shift of the in-plane pair correlation function has been observed for an adsorbed fluid layer at an fcc structured wall in comparison to the adsorbed fluid layer along an unstructured (smooth) wall. Taking this finding into account, the density of an adsorbed fluid layer in the directions parallel to the walls increases (slightly) in density in the progression unstructured \rightarrow structured \rightarrow flexible (structured) wall.

However, changes in the fluid's structure induced by the wall's flexibility are marginal in the directions parallel to the walls, unlike the changes arising perpendicular to the walls.

5

Pore Deformation

At this point we change the perspective and focus on the wall which represents the confining media of the present model system. On account of the thermodynamic state of the confined fluid which was the subject of the previous chapter, the behaviour of the substrate is investigated.

Since particles of the wall may depart from their equilibrium sites, the substrate is able to deform under the given stress which can be written according to Eq. (2.7) as follows:

$$\boldsymbol{\tau} = \begin{pmatrix} \tau_{\parallel} & 0 & 0 \\ 0 & \tau_{\parallel} & 0 \\ 0 & 0 & \tau_{zz} \end{pmatrix} \quad (5.1)$$

where we exploit slit-pore symmetry $\tau_{\parallel} = \tau_{xx} = \tau_{yy}$. Since periodic boundary conditions are applied in the x - and y -directions (see Section 3.6), *net* deformations of the wall along its plane do not occur. In other words, irrespective of the stress τ_{\parallel} acting in the x - and y -directions, momentary deformations σ_{xx} and σ_{yy} vanish *on average* in the present slit pore model due to its symmetry. Consequently, the system may only deform in the z -direction given through Eq. (2.8) as

$$\sigma_{zz} = \frac{s_z - s_{z0}}{s_{z0}} \quad (5.2)$$

where σ_{zz} is the strain tensor element in the direction normal to the walls. This approach coincides with the experimental finding that deformations in MCM-41 silicas

are isotropic in the plane perpendicular to the axis of the cylindrical pores and can be described by a scalar quantity (see Section 5.3.2).

5.1 Strain of Ideal Pores

It is then convenient to introduce general aspects of pore deformation on the basis of an *ideal* model in which the coupling between neighbouring wall particles is switched off, i.e. Eq. (3.23) satisfies $U_w(\mathbf{R}_s) = 0$. Furthermore, we start with the discussion of an empty pore, that is, a system of two parallel plane walls in which fluid particles are absent. Consequently, the contributions given by Eqs. (3.20) and (3.21) vanish according to $U_{ff}(\mathbf{R}) = U_{fs}(\mathbf{R}, \mathbf{R}_s) = 0$ and therefore the total potential energy of Eq. (3.27) reduces to

$$U(\mathbf{R}, \mathbf{R}_s, \kappa) \rightarrow \sum_{k=1}^2 U_h^{[k]}(\mathbf{R}_s, \kappa) = \kappa \sum_{k=1}^2 \sum_{i=1}^{N_s} (\mathbf{r}_i^{[k]} - \mathbf{r}_{i0}^{[k]})^2 \quad (5.3)$$

where $U_h^{[k]}(\mathbf{R}_s, \kappa)$ is given by Eq. (3.22). With respect to the z -direction perpendicular to the walls, Eq. (5.3) can be written as

$$\sum_{k=1}^2 U_h^{[k]}(z, \kappa) = \kappa \sum_{k=1}^2 \sum_{i=1}^{N_s} (z_i^{[k]} - z_{i0}^{[k]})^2 \quad (5.4)$$

where $z_i^{[k]}$ is the z -coordinate of wall particle i in wall k and $z_{i0}^{[k]}$ is the z -coordinate of its lattice site.

We adapt Eq. (2.46) with $N = 1$ and combine it with Eq. (5.4) to write the probability $P^{[k]}(z)$ of finding a single wall particle of wall k at position z as

$$P^{[k]}(z) = C e^{-\beta\kappa(z \pm s_{z0}/2)^2} \quad (5.5)$$

where ‘+’ refer to the lower wall $k = 1$ at $z = -s_{z0}/2$ and ‘-’ denote the upper wall $k = 2$ at $z = s_{z0}/2$. Combining Eqs. (5.5) and (2.24), the normalisation constant C is determined such that

$$P^{[k]}(z) = \sqrt{\frac{\beta\kappa}{\pi}} e^{-\beta\kappa(z \pm s_{z0}/2)^2} \quad (5.6)$$

Consequently, the distribution $P^{[k]}(z)$ of finding *any* wall particle of wall $k = 1$ or $k = 2$ at position z can be written as

$$P^{[k]}(z) \equiv P^{[1]}(z) + P^{[2]}(z) = \frac{1}{2} \sqrt{\frac{\beta\kappa}{\pi}} \left(e^{-\beta\kappa(z - s_{z0}/2)^2} e^{-\beta\kappa(z + s_{z0}/2)^2} \right) \quad (5.7)$$

5.1 | Strain of Ideal Pores

which represents two Gaussian distributions centred at $z = \pm s_{z0}/2$ provided that $\beta\kappa$ is sufficiently large. In the limit of $T\kappa^{-1} \rightarrow 0$ the two distributions of Eq. (5.7), which are analytical expressions of the local density $\rho^s(z)$, converge to Dirac δ -functions as stated before in Eq. (4.63).

On the other hand, for sufficiently small values of $\beta\kappa$, Eq. (5.7) becomes a rather broad function where the average position $\langle z^{[k]} \rangle$ of wall $k = 1$ or $k = 2$ is given by

$$\langle z^{[k]} \rangle \equiv \int z P^{[k]}(z) dz \quad (5.8)$$

where $P^{[k]}(z)$ is defined through Eq. (5.6). Thus, an *effective* slit-pore width s_z according to Eq. (5.2) may be defined as

$$s_z \equiv \langle z^{[2]} \rangle - \langle z^{[1]} \rangle \quad (5.9)$$

where $\langle z^{[k]} \rangle$ is given by Eq. (5.8).

Because wall particles do not interact with one another, the probability of finding a particle at position $z^{[1]}$ in the lower wall and simultaneously another particle at position $z^{[2]}$ in the upper wall is given by

$$P_h(z^{[1]}, z^{[2]}) = P^{[1]}(z^{[1]})P^{[2]}(z^{[2]}) = \frac{\beta\kappa}{\pi} e^{-\beta\kappa[(z^{[1]} - s_{z0}/2)^2 + (z^{[2]} + s_{z0}/2)^2]} \quad (5.10)$$

Introducing $s_z = z^{[2]} - z^{[1]}$ according to Eq. (5.9), the exponent in the far right side of Eq. (5.10) can be written as

$$\begin{aligned} \left(z^{[1]} - \frac{s_{z0}}{2}\right)^2 + \left(z^{[2]} + \frac{s_{z0}}{2}\right)^2 &= (z^{[1]})^2 + (z^{[2]})^2 + (z^{[2]} - z^{[1]})s_{z0} + \frac{s_{z0}^2}{2} \\ &= 2(z^{[1]})^2 - 2z^{[1]}s_z + s_z^2 - s_z s_{z0} + \frac{s_{z0}^2}{2} \\ &= 2 \left[\left(z^{[1]} - \frac{s_z}{2}\right)^2 + \frac{1}{4}(s_z - s_{z0})^2 \right] \end{aligned} \quad (5.11)$$

and therefore Eq. (5.10) can be expressed as

$$P_h(z^{[1]}, s_z) = \frac{\beta\kappa}{\pi} e^{-2\beta\kappa(z^{[1]} + s_z/2)^2} e^{-\frac{\beta\kappa}{2}(s_z - s_{z0})^2} \quad (5.12)$$

Since we are interested in the separation s_z of two opposing wall particles *irrespective* of the position $z^{[1]}$ of the reference atom in the lower wall, we integrate the last equation with respect to $z^{[1]}$ given by

$$P_h(s_z) = \frac{\beta\kappa}{\pi} e^{-\frac{\beta\kappa}{2}(s_z - s_{z0})^2} \int_{-\infty}^{\infty} e^{-2\beta\kappa(z^{[1]} - s_z/2)^2} dz^{[1]} \quad (5.13)$$

$$= \sqrt{\frac{\beta\kappa}{2\pi}} e^{-\frac{\beta\kappa}{2}(s_z - s_{z0})^2} \quad (5.14)$$

In Eq. (5.13) the limits of z -coordinates of the wall particles are set to infinity *formally* although the binding potential restricts the available space, depending on κ . With the transformation of the variables $s_z \rightarrow \sigma_{zz} = s_z - s_{z0}/s_{z0}$ according to Eq. (5.2) we arrive at the strain distribution $P_h(\sigma_{zz})$ of two opposing wall particles in the empty, ideal pore case as

$$P_h(\sigma_{zz}) = C \sqrt{\frac{\beta\kappa}{2\pi}} e^{-\beta\kappa s_{z0}^2 \sigma_{zz}^2 / 2} \quad (5.15)$$

where the normalisation constant C is again determined from combining Eq. (5.15) and (2.24) to result in

$$P_h(\sigma_{zz}) = s_{z0} \sqrt{\frac{\beta\kappa}{2\pi}} e^{-\beta\kappa s_{z0}^2 \sigma_{zz}^2 / 2} \quad (5.16)$$

From the latter equation it becomes apparent that in the limits $s_{z0} \rightarrow \infty$ or $\kappa \rightarrow \infty$ the strain distribution becomes

$$P_h(\sigma_{zz}) = \delta(\sigma_{zz}) \quad (5.17)$$

where $\delta(\sigma_{zz})$ is the Dirac δ -function (see Section B.6.1 of [32]).

However, for finite values of s_{z0} and κ , Eq. (5.16) is Gaussian, as shown in Fig. 5.1a (---) for $s_{z0} = 6.8$ and $\kappa = 30$ at $T = 1.0$. On account of its Gaussian character, the rather broad strain distribution $P_h(\sigma_{zz})$ reveals a vanishing *net* strain $\langle \sigma_{zz} \rangle$ according to

$$\langle \sigma_{zz} \rangle = \int \sigma_{zz} P_h(\sigma_{zz}) d\sigma_{zz} = 0 \quad (5.18)$$

As a consequence of this symmetry, any deformation of the pore, i.e. a non-vanishing net strain, must be connected with a non-Gaussian strain distribution.

5.2 Sorption Strain

In the system of interest, that is, the model of thermally coupled walls, the interaction between wall particles $U_w(\mathbf{R}_s) \neq 0$ is expected to lead to a slightly different strain distribution $P(\sigma_{zz})$ that deviates from the ideal Gaussian distribution $P_h(\sigma_{zz})$. Taking the additional interaction $U_w(\mathbf{R}_s) \neq 0$ into account makes an analytical treatment of the present model system quite cumbersome and therefore $P(\sigma_{zz})$ is computed numerically as a histogram in the semi-grand canonical ensemble. According to Eq. (5.2) the ensemble average of σ_{zz} can be written as

$$\langle \sigma_{zz} \rangle = \frac{\langle s_z \rangle - s_{z0}}{s_{z0}} \quad (5.19)$$

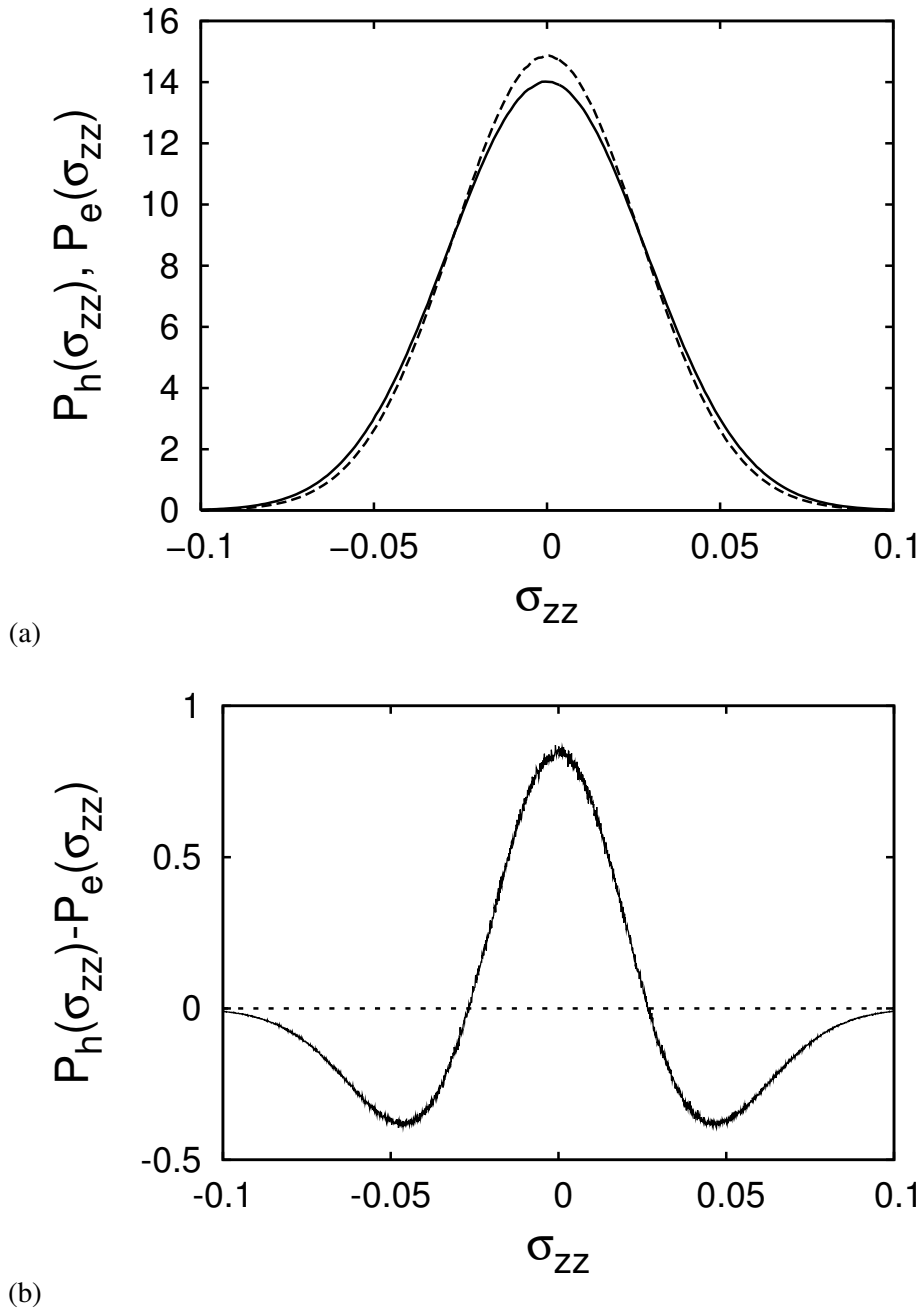


FIG. 5.1: (a) Distributions $P_h(\sigma_{zz})$ (- - -) and $P_e(\sigma_{zz})$ (—) as functions of strain σ_{zz} for an empty slit pore of width $s_{z0} = 6.8$ and $\kappa = 30$ at $T = 1.0$. The distribution $P_e(\sigma_{zz})$ with direct interaction between wall particles according to Eq. (3.23) is slightly broader and has a lower maximum than $P_h(\sigma_{zz})$ of the ideal model which lacks an interaction between wall particles. The rather small deviation between both distributions becomes obvious through the difference $P_h(\sigma_{zz}) - P_e(\sigma_{zz})$ shown in part (b) which is positive at the centre and negative at both sides.

where the effective pore width $\langle s_z \rangle$ is defined according to Eq. (5.9) as the (ensemble averaged) distance of two opposing wall particles i given through

$$\langle s_z \rangle \equiv \frac{1}{N_s} \left\langle \sum_{i=1}^{N_s} z_i^{[2]} - z_i^{[1]} \right\rangle \quad (5.20)$$

As usual, brackets $\langle \dots \rangle$ denote averages in the semi-grand canonical ensemble and $z_i^{[1]}$ as well as $z_i^{[2]}$ refer to the z -position of wall particles in the lower and upper wall whose lattice points share the same x - and y -positions.

The plot of $P_e(\sigma_{zz})$ versus σ_{zz} in Fig. 5.1a (—) of an empty pore reveals indeed a deviation from $P_h(\sigma_{zz})$ under the same conditions $s_{z0} = 6.8$, $\kappa = 30$, $T = 1.0$ and shows a slightly broader distribution compared with $P_h(\sigma_{zz})$. The broader distribution $P_e(\sigma_{zz})$ indicates that the additional potential $U_w(\mathbf{R}_s)$ causes wall particles to move farther from their equilibrium positions and, thus, gives rise to an increased incidence of smaller and larger strains at the expense of mid-sized strains. To test whether $P_e(\sigma_{zz})$ remains Gaussian we calculate its n -th moments $\langle \sigma_{zz}^n \rangle$ using

$$\langle \sigma_{zz}^n \rangle \equiv \int \sigma_{zz}^n P(\sigma_{zz}) d\sigma_{zz} \quad (5.21)$$

for $n = 2$ and $n = 4$. In general, a Gaussian distribution has vanishing odd moments

$$\langle \sigma_{zz}^{2n+1} \rangle = 0 \quad \forall n \quad (5.22)$$

due to its symmetry and in this case the skewness parameter U obeys [161]

$$U \equiv \frac{\langle \sigma_{zz}^2 \rangle^2}{\langle \sigma_{zz}^4 \rangle} = \frac{1}{3} \quad (5.23)$$

For the empty pore of $s_{z0} = 6.8$ and $\kappa = 30$ at $T = 1.0$, the numerical calculation of the skewness parameter yields $U \simeq 0.341$ which indicates that $P_e(\sigma_{zz})$ is not precisely Gaussian in nature. However, $P_e(\sigma_{zz})$ is symmetric and therefore bears no net strain, which is confirmed by computing $\sigma_{zz} \simeq 10^{-6}$ using Eq. (5.19). This symmetry is also obvious from Fig. 5.1b which shows that the (symmetric) Gaussian distribution $P_h(\sigma_{zz})$ deviates symmetrically from $P_e(\sigma_{zz})$. In other words, the interaction between wall particles introduces an anharmonicity into the spatial distribution of the wall particles and to the resulting strain distribution which nevertheless remains symmetric as long as the pore is empty.

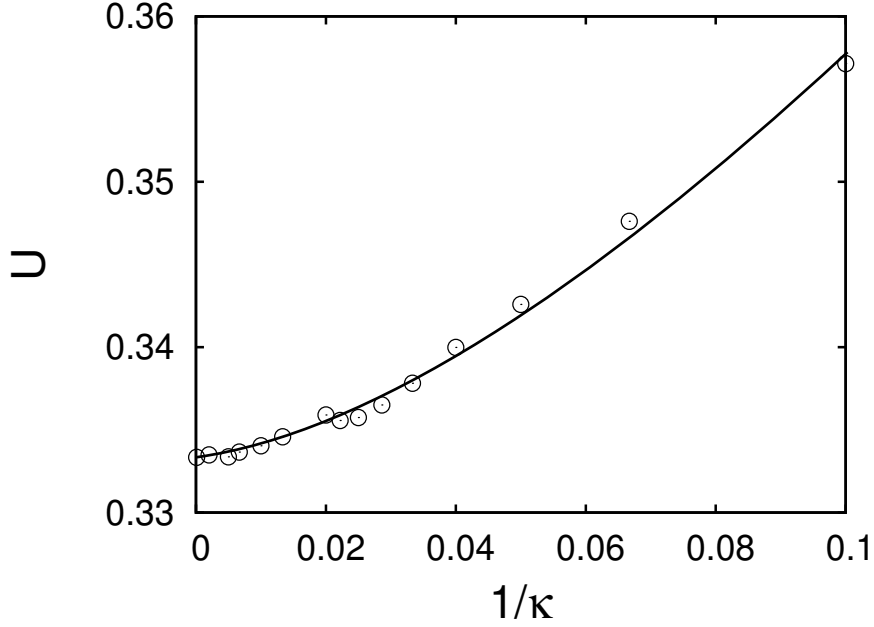


FIG. 5.2: The skewness parameter U of Eq. (5.23) versus inverse force constant $1/\kappa$ for a fluid filled pore under the same conditions $s_{z0} = 6.8$, $\mu = -11.4$, and $T = 1.0$. The skewness parameter U can be considered as a measure for the anharmonicity of a function.

5.2.1 Strain Distributions

Upon filling the empty pore with fluid matter, the presence of fluid particles at one side disturb the symmetric spatial distribution of wall particles and may lead to an asymmetric strain distribution, giving rise to a non-vanishing net strain. The impact of fluid matter on the strain distribution should increase with decreasing rigidity of the wall which is confirmed by the plot in Fig. 5.2. According to Eq. (5.23), the skewness parameter U deviates for a fluid filled pore from the ideal Gaussian value of $1/3$ with increasing deformability of the wall $1/\kappa$. In other words, the filling of the pore with fluid particles impose an anharmonicity on the substrate structure which is the more pronounced the more deformable the wall.

To evaluate the impact of the fluid on the strain distribution, we define the distribution function $\Delta P(\sigma_{zz})$ by

$$\Delta P(\sigma_{zz}) = P(\sigma_{zz}) - P_e(\sigma_{zz}) \quad (5.24)$$

in analogy to the distribution of Fig. 5.1b. In Eq. (5.24) $P(\sigma_{zz})$ is the strain distribution under consideration and $P_e(\sigma_{zz})$ is the strain distribution of an (identical but) empty pore shown in Fig. 5.1a. Consequently, $\Delta P(\sigma_{zz})$ is a measure for the deviation

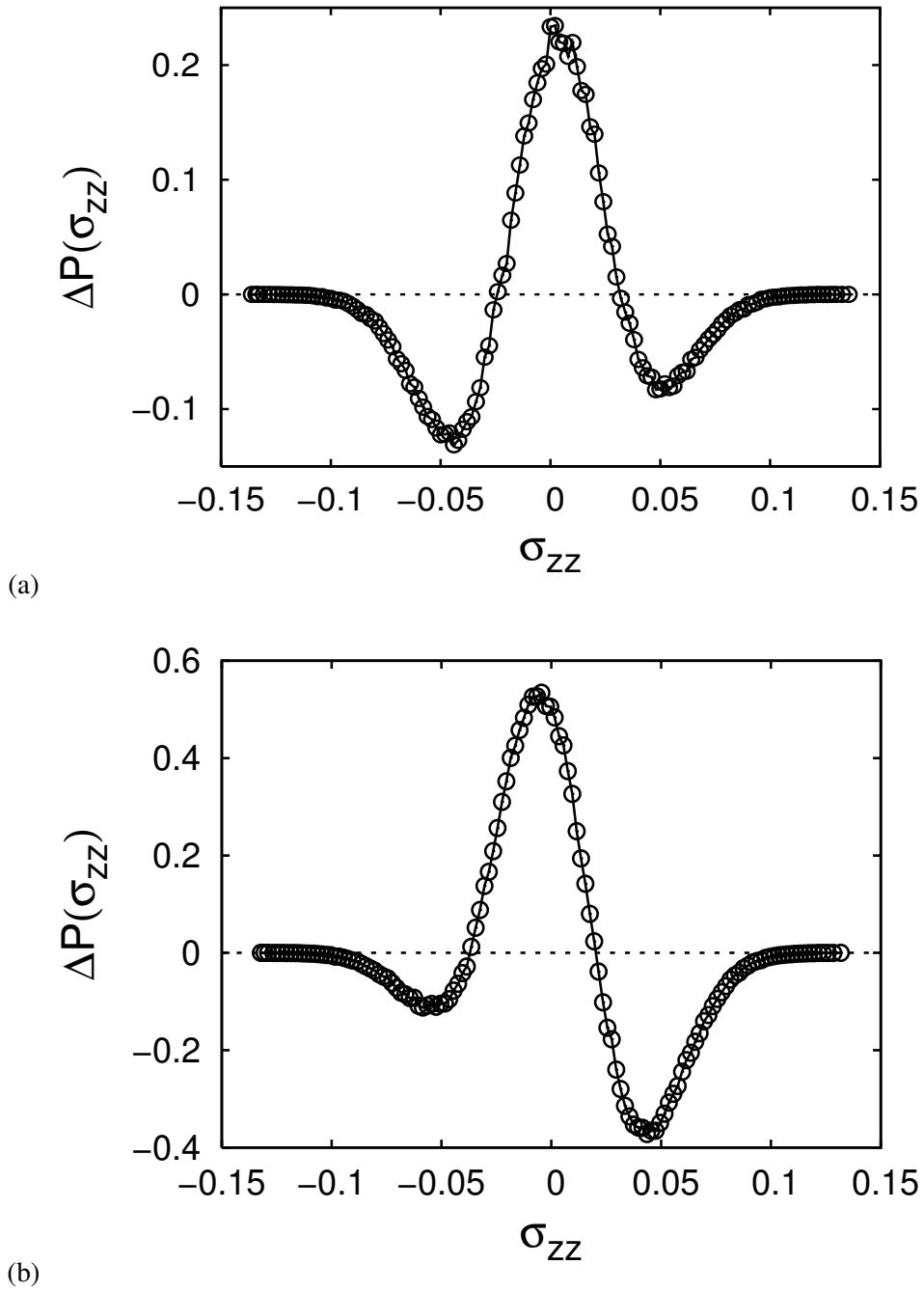


FIG. 5.3: Distributions $\Delta P(\sigma_{zz})$ of Eq. (5.24) versus strain σ_{zz} for a pore with $\kappa = 30$, $s_{z0} = 6.8$ at $T = 1.0$ before and after capillary condensation. The asymmetry of distributions gives rise to net strains **(a)** $\sigma_{zz} = 1.2 \times 10^{-4}$ where the confined fluid is in a gas-like state of $\rho \simeq 0.16$ at $\mu = -11.455 \leftrightarrow P/P_0 \simeq 0.7$ and **(b)** $\sigma_{zz} \simeq -6.2 \times 10^{-4}$ for a fluid in liquid-like state of $\rho \simeq 0.46$ at $\mu = -11.42 \leftrightarrow P/P_0 \simeq 0.73$.

5.2 | Sorption Strain

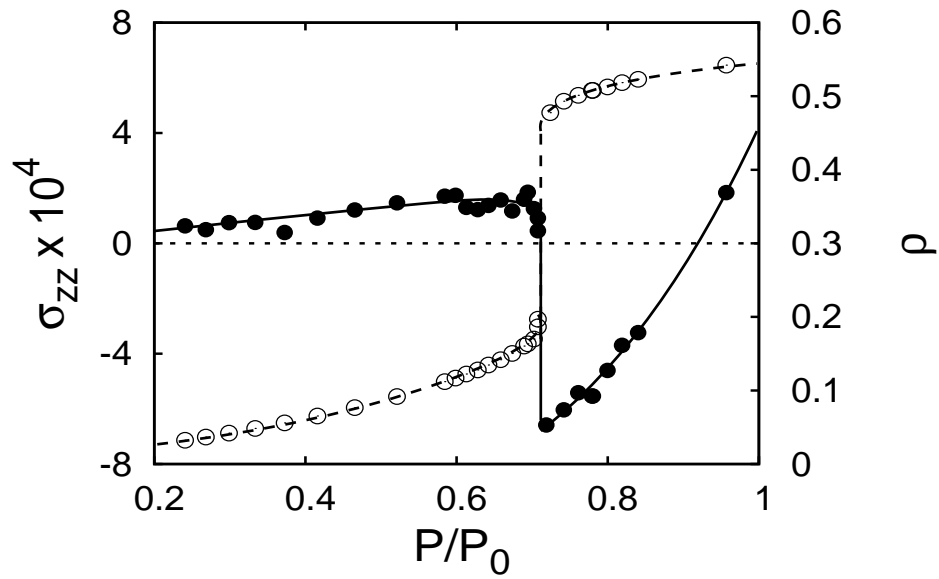
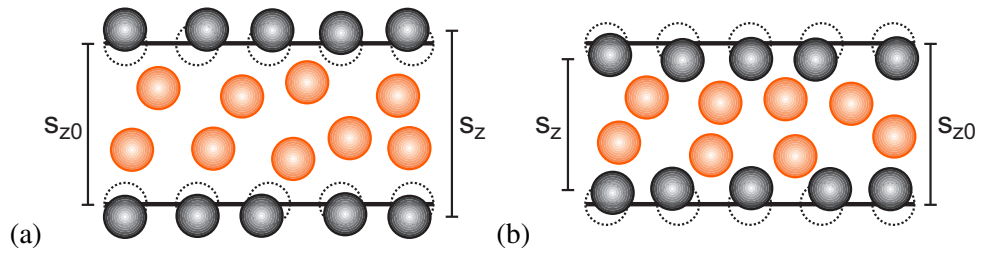
of $P(\sigma_{zz})$ from the strain distribution $P_e(\sigma_{zz})$ of an empty reference system.

Fig. 5.3a shows $\Delta P(\sigma_{zz})$ for flexible walls with $\kappa = 30$ and $s_{z0} = 6.8$ at $T = 1.0$ confining fluid in gas-like state. The plot reveals that the presence of a gas-like fluid favours moderate strains, characterised by positive $\Delta P(\sigma_{zz})$ around zero whose maximum is slightly shifted to positive strains, at the expense of larger and smaller strains where $\Delta P(\sigma_{zz})$ drops to negative values. The minimum of $\Delta P(\sigma_{zz})$ at negative strains $\sigma_{zz} < 0$ is deeper than the one at positive strains indicating that negative strains are more disfavoured and, thus, gives rise to (an albeit small) positive net strain $\sigma_{zz} \simeq 1.2 \times 10^{-4}$. After capillary condensation the now liquid-like fluid causes a reverse strain distribution as shown in Fig. 5.3b which has a deeper minimum at positive strains than the one at negative strains, demonstrating that the $\sigma_{zz} > 0$ are disfavoured. The maximum at moderate strains is slightly shifted to negative values $\sigma_{zz} < 0$, resulting in a negative net strain $\sigma_{zz} \simeq -6.2 \times 10^{-4}$.

Consequently, on account of the current thermodynamic state of the fluid, the induced anharmonicity may prefer negative or positive strains and, thus, may result in positive or negative net strains, i.e. an expansion or contraction of the pore as illustrated in Fig. 5.4a,b. It is noteworthy that the small net strains σ_{zz} of the order $O(10^{-4})$ are connected with rather broad strain distributions $P(\sigma_{zz})$ which exceed σ_{zz} by up to three orders of magnitude. The broad strain distributions up to a few percent accompanying the minute net strains are responsible for the modified phase behaviour of the confined fluid presented in Chapter 4 when confining walls become deformable. Since the discrepancy between the strain distributions confining gas-like and liquid-like fluid is negligible in comparison with the appearing strains, branches of sorption isotherms before and after capillary condensation are affected to the same extent as shown in Fig. 4.6b. The thermal roughness of the present model system also explains the disagreement with the theoretical studies discussed in Sections 4.4.2 and 4.4.3, in which the mobility of wall particles is not explicitly considered.

5.2.2 Strain Upon Pore Filling

Fig. 5.4c shows the net strain σ_{zz} (●) as a function of the (reduced) bulk fluid pressure P/P_0 for a deformable substrate with $s_{z0} = 6.8$ and $\kappa = 30$ at $T = 1.0$. This plot exhibits the reaction of the substrate while fluid matter is adsorbed, that is, ρ (⊙) of the confined fluid phase increases. During the gas-like phase characterised by $\rho \lesssim 0.2$, σ_{zz} increases slightly with increasing P/P_0 . At capillary condensation, indicated by a sharp increase of ρ , the strain suddenly drops to negative values. If P/P_0 is further increased, σ_{zz} rises again and reaches positive values for $P/P_0 \gtrsim 0.92$. Fig.



(c)

FIG. 5.4: Sketches of deformable pores with fluid particles (orange) and wall particles (grey) which are able to depart from their equilibrium positions (dashed circles) on account of substrate flexibility. Thus, the effective pore width s_z may differ from s_{z0} and indicate **(a)** an expansion if $s_z > s_{z0}$ that results in $\sigma_{zz} > 0$, or **(b)** a contraction of the pore which is characterised by $s_z < s_{z0}$ respectively $\sigma_{zz} < 0$. **(c)** Substrate strain σ_{zz} (●) and density ρ (○) of the confined fluid as functions of (reduced) bulk fluid pressure P/P_0 for a flexible pore with $\kappa = 30$ and $s_{z0} = 6.8$ at $T = 1.0$.

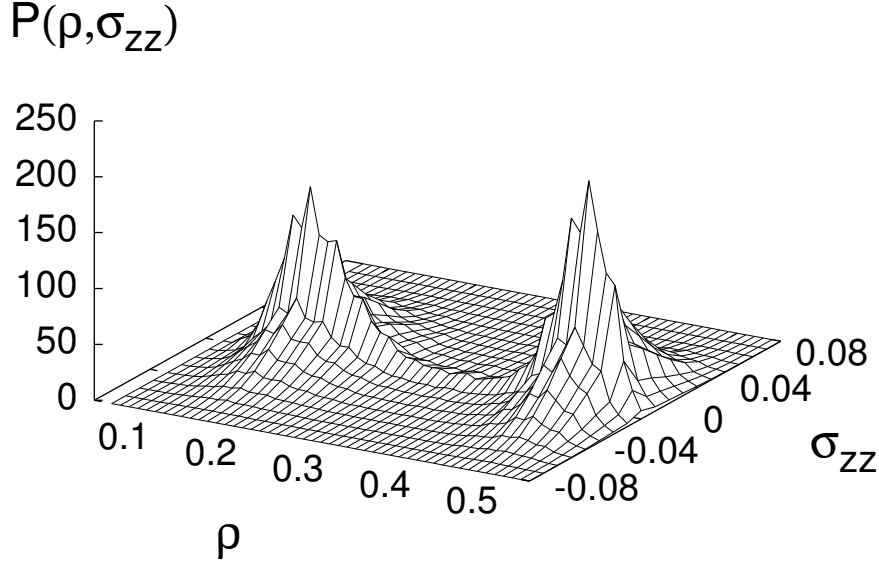
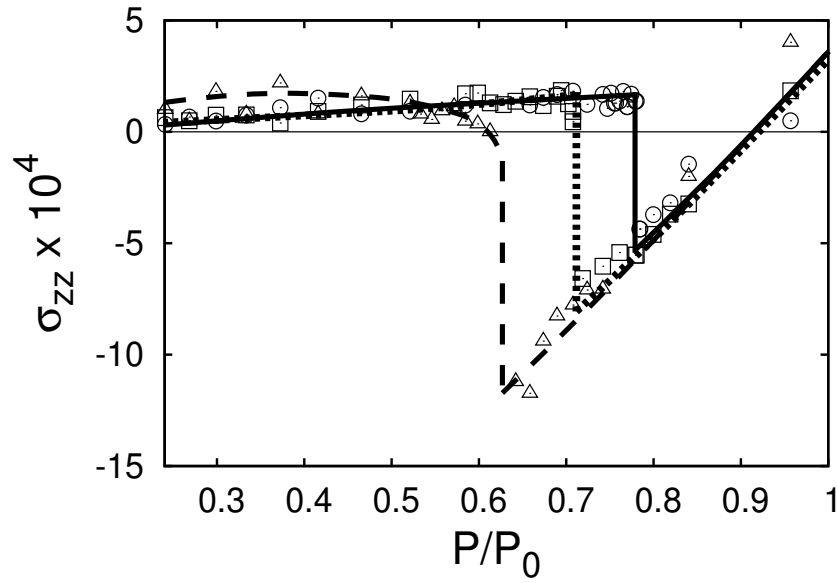


FIG. 5.5: Distribution $P(\rho, \sigma_{zz})$ as a function of density ρ of the confined fluid and the substrate strain σ_{zz} for a flexible pore with $s_{z0} = 6.8$ and $\kappa = 30$ at $T = 1.0$ and $\mu_x = -11.431$ at which gas-like phase and liquid-like phase coexist. Individual peaks of the distribution $P(\rho, \sigma_{zz})$, which resemble coexisting phases, comprise *net* strains of $\sigma_{zz}^{gx} \simeq 1.7 \times 10^{-4}$ for the gas-like phase with $\rho \simeq 0.17$ and $\sigma_{zz}^{lx} \simeq -4.8 \times 10^{-4}$ for the liquid-like phase with $\rho \simeq 0.48$.

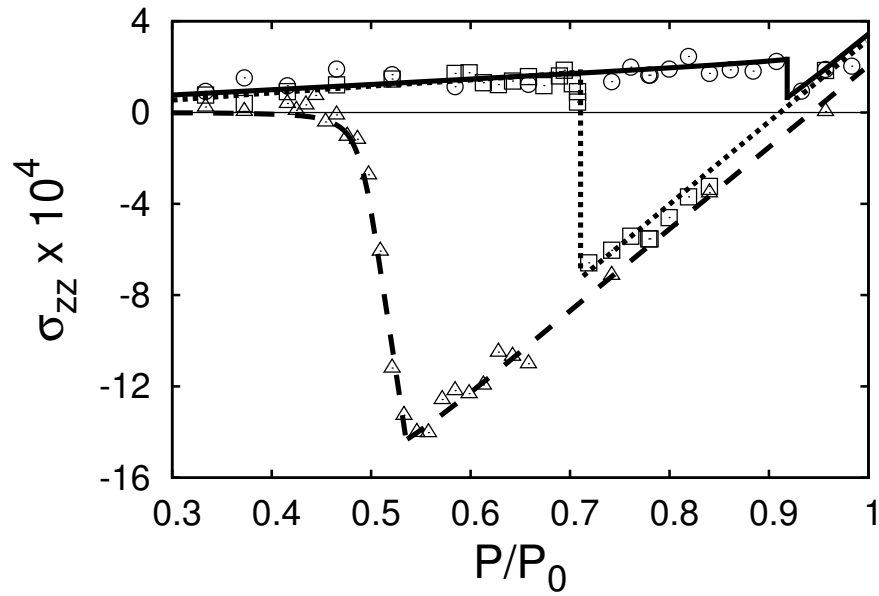
5.5 provides an insight into the strain distribution at phase coexistence under these conditions. Individual peaks $\mathcal{P}_\alpha(\rho, \sigma_{zz})$ of the distribution $P(\rho, \sigma_{zz})$ belong to the gas-like and liquid-like phase whose net strains are computed via

$$\sigma_{zz}^{\alpha x} = \frac{2}{\Omega} \int_0^\infty \int_0^\infty \sigma_{zz}(\rho) \mathcal{P}_\alpha(\rho, \sigma_{zz}) d\rho d\sigma_{zz} \quad (5.25)$$

where Eq. (4.42) is adapted. In Eq. (5.25), $\sigma_{zz}(\rho)$ is the strain appearing at a given density ρ and $\mathcal{P}_\alpha(\rho, \sigma_{zz})$ is the unnormalised probability of finding the system in a state of ρ and σ_{zz} . With this procedure, we obtain a positive strain $\sigma_{zz}^{gx} \simeq 1.7 \times 10^{-4}$ of the gas-like phase and a negative strain $\sigma_{zz}^{lx} \simeq -4.8 \times 10^{-4}$ of the liquid-like phase, confirming the discontinuous drop at the gas–liquid phase transition. Summing up the adsorption process, the confining substrate first expands, contracts discontinuously at capillary condensation and then expands again while the bulk fluid pressure is subsequently increased.



(a)



(b)

FIG. 5.6: Strain σ_{zz} as function of (reduced) bulk fluid pressure P/P_0 for various pores which **(a)** differ in width $s_{z0} = 5.6$ (Δ), $s_{z0} = 6.8$ (same data as Fig. 5.4c) (\square), $s_{z0} = 8.0$ (\odot) and which **(b)** differ in fluid–substrate interaction $\epsilon_{fs} = 0.75$ (\odot), $\epsilon_{fs} = 1.0$ (same data as Fig. 5.4c) (\square), $\epsilon_{fs} = 1.5$ (Δ) [see Eq. (3.21)]. $T = 1.0$ and $\kappa = 30$ for all data sets.

5.2 | Sorption Strain

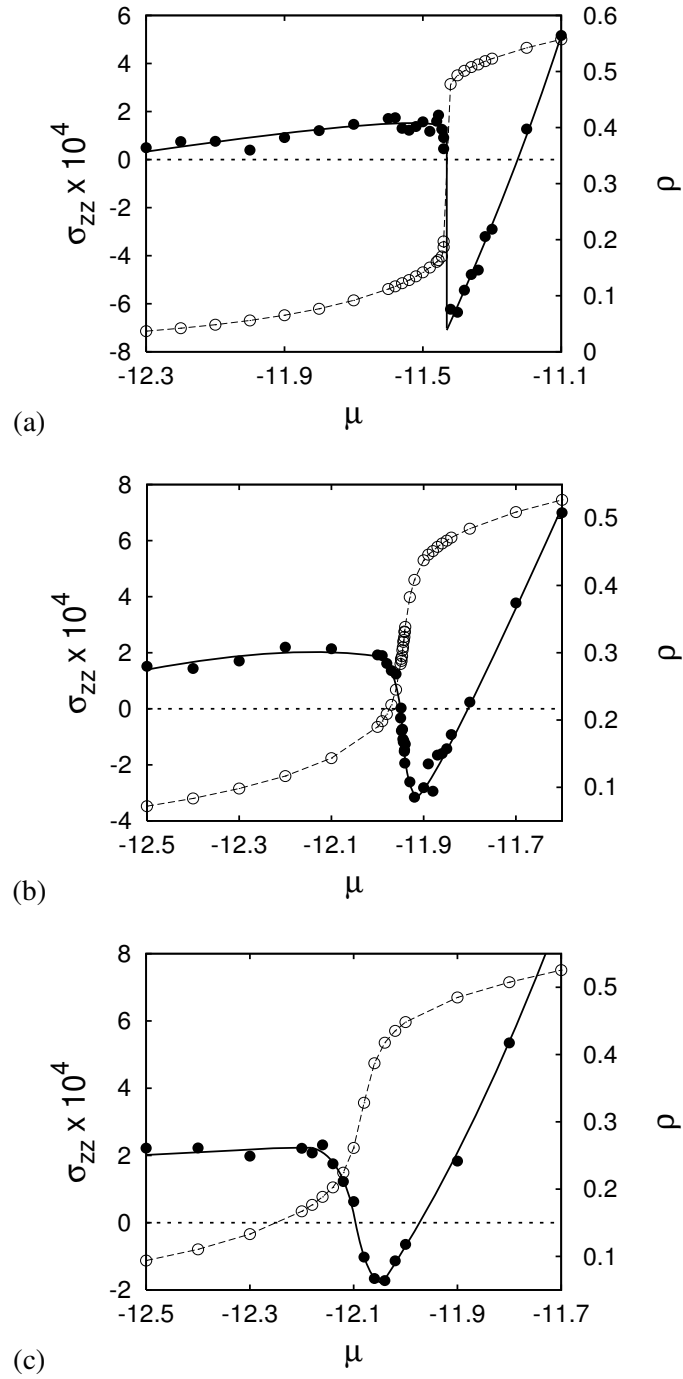
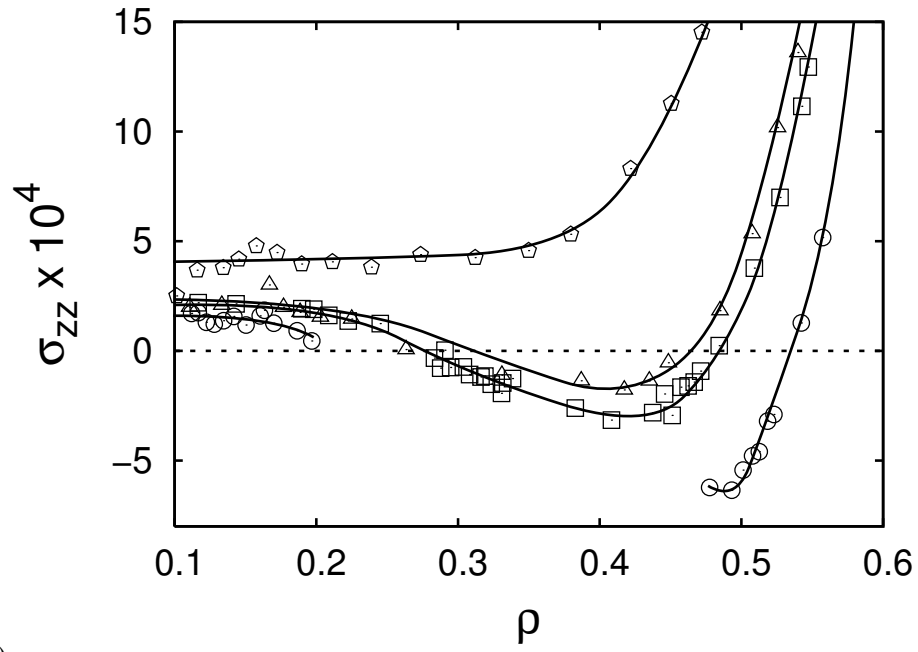
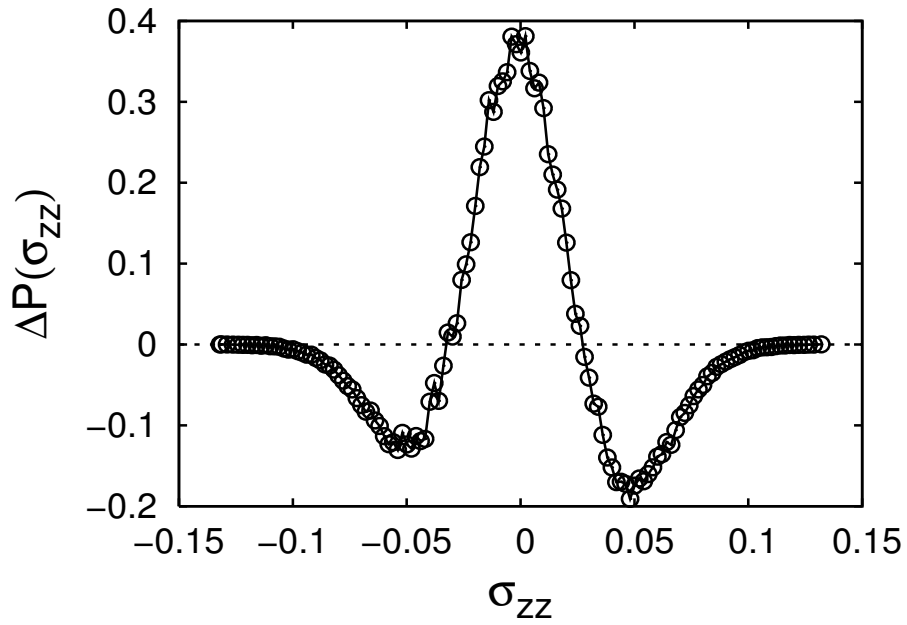


FIG. 5.7: Substrate strain σ_{zz} (●) and fluid density ρ (○) as functions of chemical potential μ . All data sets share pore width $s_{z0} = 6.8$ and substrate flexibility $\kappa = 30$ but differ in temperature T . Plots correspond to (a) subcritical regime at $T = 1.0$ (same data as Fig. 5.4c), (b) critical temperature $T = 1.06 \approx T_c(12.7)$ according to Eq. (4.60), and (c) supercritical regime at $T = 1.08$.



(a)



(b)

FIG. 5.8: (a) Strain σ_{zz} versus density ρ of the fluid confined in a flexible pore of $s_{z0} = 6.8$ and $\kappa = 30$ at different temperatures $T = 1.0$ (\odot), $T = 1.06 \simeq T_c(12.7)$ (\square), $T = 1.08$ (\triangle), and $T = 1.2$ (\diamond). (b) Strain distribution $\Delta P(\sigma_{zz})$ of Eq. (5.24) for a fluid in a flexible pore of $s_{z0} = 6.8$ and $\kappa = 30$ at the critical point $T = 1.06 \simeq T_c(12.7)$ [see Eq. (4.60)], $\rho = 0.316 \simeq \rho_c(12.7)$ [see Eq. (4.61)], $\mu = -11.918$ [see Fig. 4.8b].

5.2 | Sorption Strain

The same behaviour of the strain is observed if the pore width is changed to $s_{z0} = 5.6$ or $s_{z0} = 8.0$, as shown in Fig. 5.6a. The pressure P/P_0 at which capillary condensation occurs, indicated by a sharp drop of σ_{zz} , decreases with smaller pore size, i.e. with a larger degree of confinement ψ (see Section 3.2), as expected. Additionally, the contraction at capillary condensation is more pronounced the smaller is s_{z0} , that is, σ_{zz} drops to smaller values for larger ψ .

Reckoning the situation where s_{z0} is fixed but the fluid–wall attraction ϵ_{fs} , see Eq. (3.21), is modified to $\epsilon_{fs} = 0.75$ or $\epsilon_{fs} = 1.5$, the strain in the gas-like phase depends on ϵ_{fs} , plotted in Fig. 5.6b. In case $\epsilon_{fs} = 0.75$, the strain increases upon increasing P/P_0 contrary to $\epsilon_{fs} = 1.5$, where the substrate remains in an almost unstrained state up to $P/P_0 \approx 0.5$. Despite the difference in the gas-like phase, the strain isotherms show a similar course. As expected, with increasing ϵ_{fs} the point of capillary condensation shifts to lower bulk pressures P/P_0 and the substrate reacts to this phenomenon with a more pronounced contraction.

Even if we leave the subcritical temperature regime, the strain shows a similar behaviour, which is evident from the plots of σ_{zz} versus chemical potential μ in Fig. 5.7a–c. Particularly Fig. 5.7b and c with $T \geq T_c$ indicate that the contraction of the pore is not necessarily connected with the phenomenon of phase transition but is rather a reaction to a medium density ρ (\odot) of the confined fluid. Since in the critical and supercritical regime the density changes continuously, also the strain sequence ‘expansion–contraction–expansion’ becomes a continuous course. In fact, only the sharp discontinuous drop of the strain in Fig. 5.7a remains as a characteristic for capillary condensation, reflecting the discontinuous increase of fluid density. It can be explained if one recalls that the gas–liquid phase transition accounts for attractive forces that act between fluid particles. From the perspective of the substrate, at capillary condensation the field exerted by the confined fluid changes from repulsive to attractive in nature and results in a contraction of the confining medium.

Fig. 5.8a shows the strain σ_{zz} as a function of the density ρ of the confined fluid for different temperatures. The subcritical isotherm (\odot) lacks data points for $0.2 \lesssim \rho \lesssim 0.48$ as a result of the liquid–gas phase transition which omits this regime. The critical isotherm at $T = 1.06 \approx T_c$ (\square) and even the supercritical isotherm at $T = 1.08$ (\triangle) shows a continuous course with a contraction within the range $0.3 \lesssim \rho \lesssim 0.5$. The strain distribution $\Delta P(\sigma_{zz})$ according to Eq. (5.24) at the critical point, given in Fig. 5.8b, confirms this notion since it bears a resemblance to the distribution of the liquid-like phase in Fig. 5.3b. Although its maximum is centred at $\sigma_{zz} \approx 0$, the asymmetric distribution gives rise to a negative net strain $\sigma_{zz} \approx -1.5 \times 10^{-4}$ at the critical point.

At sufficiently high temperatures $T = 1.2$ (\diamond) the strain isotherm shown in Fig. 5.8a lacks any contraction and becomes a monotonically increasing function of ρ . The absence of contraction at $T = 1.2$ is a consequence of the shift of the strain isotherm to higher values with increasing temperature $\odot \rightarrow \square \rightarrow \triangle \rightarrow \diamond$ which goes along with a less pronounced contraction regime indicating that repulsive interactions overwhelm attractive ones.

5.3 Pentane in MCM-41: Theory and Experiment

Contrary to the phase behaviour, which is difficult to compare with experimental data for reasons discussed in Section 4.4.1, we are able to make contact with strain measurement experiments during the sorption process carried out by Paris et al. [27, 28]. They use *in-situ* small angle X-ray diffraction (SAXD) to measure deformations of mesoporous materials in dependence on the bulk fluid pressure of a connected reservoir. We focus on the experimental system of n-pentane in MCM-41(16), characterised in [34], on which our choice of model parameters are based (see Section 3.2).

5.3.1 Small-Angle X-Ray Diffraction

The experimental setup used by Paris et al. in their diffraction experiments is adumbrated in Fig. 5.9a. The thermostatted sorption cell with X-ray transparent windows contains grains of MCM-41(16) of roughly $1 \mu\text{m}$ in size bathed in n-pentane. The sorption cell is connected with a gas dosing system which essentially consists of a pentane (super-) reservoir and a valve. Upon opening or closing the valve the pentane pressure of the sorption cell is controlled and sorption of pentane inside the MCM-type silica takes place. The volume of the supersystem V_s exceeds the volume of the sorption cell V_c by far which itself is much larger than the pore volume V_p of the mesoporous probe, so that $V_p \ll V_c \ll V_s$.

The X-ray transparent windows of the sorption cell allow scattering experiments at different bulk fluid pressures P/P_0 . The beam of wavelength λ interacts with electrons that surround the atomic cores and results in a diffraction of the incident beam by angle θ according to Bragg's law [163]

$$\lambda = 2d \sin \theta \quad (5.26)$$

where d is the length scale by which regions of significant electron density are separated, i.e. the so-called lattice parameter. Since the wavelength of X-rays is of the

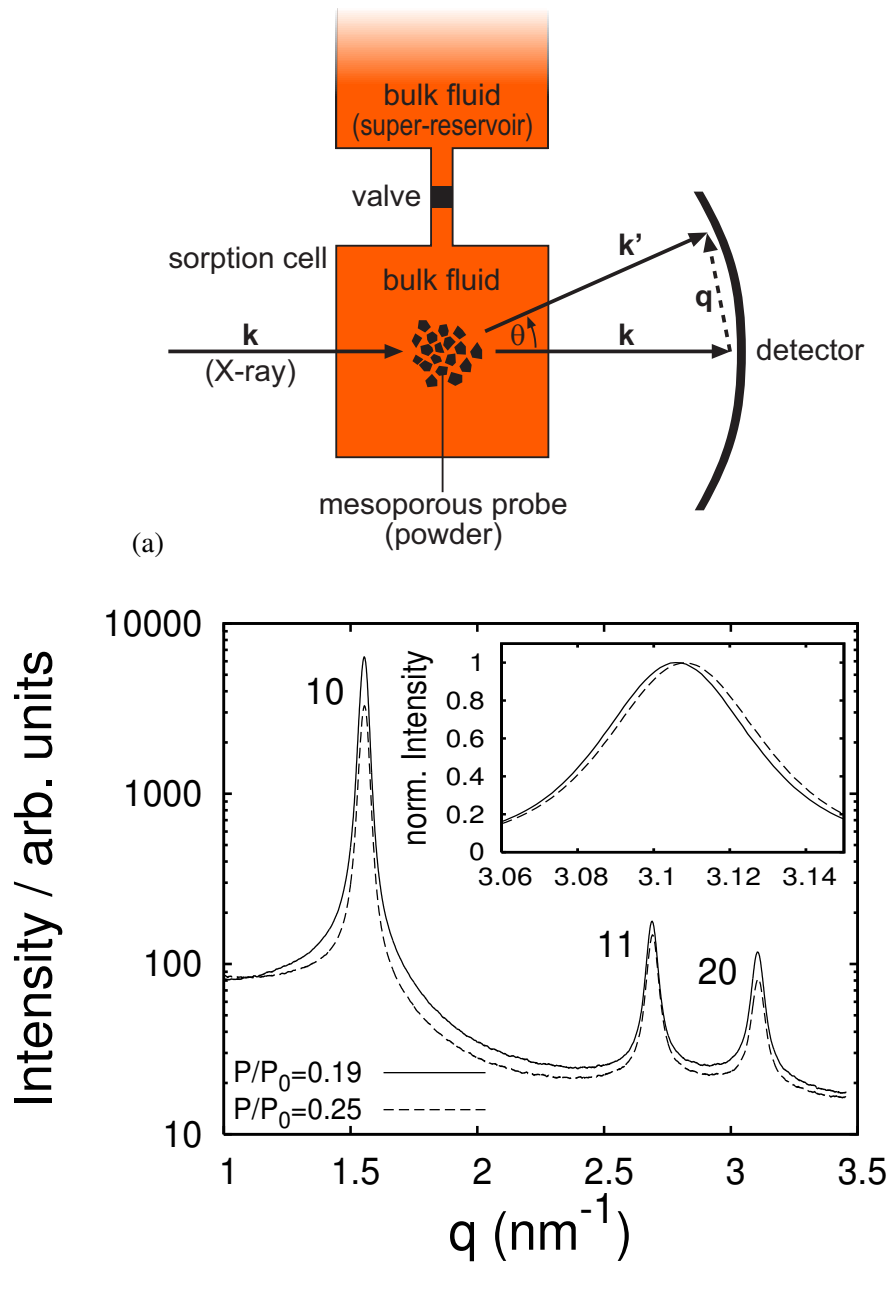


FIG. 5.9: (a) Sketch of experimental setup: The sorption cell is connected to a bulk fluid super-reservoir via a valve which is used to control the bulk fluid pressure of the sorption cell. The X-ray beam of wave vector \mathbf{k} is scattered by the mesoporous probe according to Bragg's law to result in a diffracted wave of vector \mathbf{k}' . The diffraction pattern is detected in dependence on the magnitude of the scattering vector $|\mathbf{q}| = q = (4\pi/\lambda) \sin \theta$. (b) Experimental data from [162]: X-ray diffraction pattern (intensity versus q) of n-pentane in MCM-41(16) for two bulk fluid pressures before ($P/P_0 = 0.19$, full line) and after ($P/P_0 = 0.25$, dashed line) capillary condensation. The inset shows the (20) peaks at an enhanced scale.

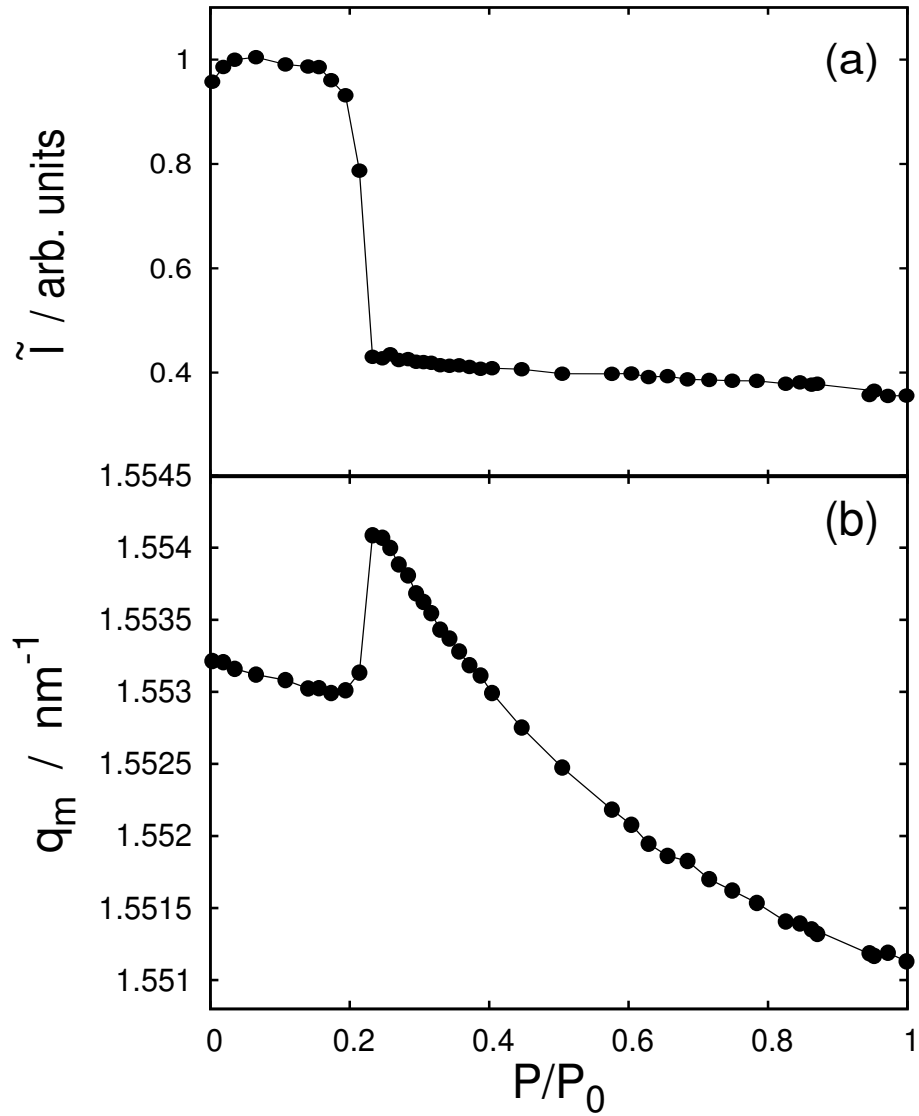


FIG. 5.10: Experimental data from [162]: (a) Integrated intensity \tilde{I} and (b) position q_m of the (10) Bragg peak (see Fig. 5.9b) as functions of the (reduced) bulk fluid pressure P/P_0 during adsorption of n-pentane in MCM-41 at standard conditions.

order $\lambda \approx 0.1\text{nm}$, at small angles θ the diffraction pattern reveals information about structures at the nanometre scale, that is, about the pores of MCM-41(16) of diameter $\sim 4\text{ nm}$.

Instead of the diffraction angle θ , SAXD data are usually presented in terms of the magnitude of the wave vector $q = |\mathbf{q}|$, which is advantageous because it is independent of λ contrary to θ . The scattering vector $\mathbf{q} = \mathbf{k}' - \mathbf{k}$ is a measure for the diffraction of the scattered beam of wave vector \mathbf{k}' in relation to the transmitted beam of wave vector \mathbf{k} (see Fig. 5.9a). The magnitude of \mathbf{k} is given by $|\mathbf{k}| = 2\pi/\lambda$ and q is related to the diffraction angle θ via $q = (4\pi/\lambda) \sin \theta$ where we assume elastic scattering $|\mathbf{k}| = |\mathbf{k}'|$. Since the powder probe consists of many small grains which are statistically oriented, a diffracted beam forms a cone resulting in a point symmetric pattern, a so-called Debye–Scherrer ring of radius q .

Pores in MCM-41(16) are arranged in a two-dimensional lattice of hexagonal order (see Fig. 3.1a on p. 32) whereas the pore length exceeds its width by far and, thus, remains unseen within the range of small-angle diffraction. According to the two-dimensional lattice, each signal of the diffraction pattern relates to a length scale d within the plane and is characterised by two Miller indices (hk) according to the direction of d . With regard to the symmetry of the hexagonal pore lattice [109], Bragg scattering is assigned to (10), (11), (20), (22) and so on, but not to (01), (02), (03) because they coincide with their counterparts in which h and k interchange.

Fig. 5.9b shows the diffraction pattern of n-pentane in MCM-41(16) for two different bulk pentane pressures at which the confined pentane is in a gas-like state (—) and in a liquid-like state (- - -). Despite a background noise which vanishes with increasing q , three signals in the form of peaks arise which assign to the (10), (11) and (20) direction of the lattice. The width of the peaks accounts mainly for imperfections of the mesoporous material and also reflects the (finite) grain size of the probe. [164] Apart from a general decrease in intensity, the peaks are slightly shifted to larger q for the mesopores containing liquid-like pentane compared with the ones confining gas-like pentane. The peak shift is symmetric without an appreciable change in peak width and accounts for all three peaks, signifying a purely radial change of the pore lattice. The mean peak position q_m of the (10) peak as a function of the bulk fluid pressure P/P_0 is shown in Fig. 5.10b revealing that q_m decreases with increasing P/P_0 interrupted by a sharp increase at $P/P_0 \simeq 0.22$. That the sharp increase occurs at capillary condensation becomes obvious from the parallel plot of the integrated intensity \tilde{I} in Fig. 5.10a. Because X-ray diffraction relies on the discrepancy in electron density which vanishes upon pore filling, \tilde{I} signifies the formation of the liquid phase by a sharp drop.

5.3.2 Lattice Strain vs. Pore Strain

The finding, that lattice deformations are purely radial and isotropic within the plane perpendicular to the pore axis, permits one to define the homogeneous lattice strain ε as a scalar through

$$\varepsilon = \frac{d(P) - d(0)}{d(0)} = \frac{q_m(0) - q_m(P)}{q_m(P)} \quad (5.27)$$

where $d(0)$ is the lattice parameter at $P/P_0 = 0$ and $q_m(0)$ the associated mean peak position, contrary to $d(P)$ and $q_m(P)$ which denote the respective quantities at arbitrary P/P_0 . In Eq. (5.27) the relation $q_m \propto 1/d$ is utilised.

Although the strain σ_{zz} of the present model system, cf. Eq. (5.2), is a scalar quantity as the experimental lattice strain ε , they are not directly comparable with one another since σ_{zz} refers to the deformation of a *single* pore in which a pore lattice is not meaningful. Nevertheless, one may assume that lattice deformations reflect mainly the reaction of that part of the mesoporous medium that is not filled with solid matter, i.e. the pores. The isotropy of the lattice strain implies that individual pores are deformed isotropically such that the pore geometry remains unaffected. Consequently, one may assume that both kinds of strain are proportional to one another

$$\varepsilon \propto \sigma_{zz} \quad (5.28)$$

The plots in Fig. 5.11a of σ_{zz} (\odot) and ε (\bullet) as functions of P/P_0^+ confirms this expectation where P_0^+ marks the respective bulk fluid pressure at which capillary condensation occurs. Both data show the sequence 'expansion–contraction–expansion', as sketched in Fig. 5.11b where the abrupt contraction coincides with capillary condensation as reflected by the fluid density (Δ) of the simulation. On account of the crudeness of the model system, the point of capillary condensation differs for the experimental systems with $P/P_0 \simeq 0.22$ and the simulation with $P/P_0 \simeq 0.71$ by a factor of approximately three.

Nevertheless, the semi-quantitative agreement between σ_{zz} and ε lets one conclude that the present model system is sufficiently realistic to capture key features of the experimental system and, thus, is able to reveal molecular details about the fluid and substrate during the sorption process.

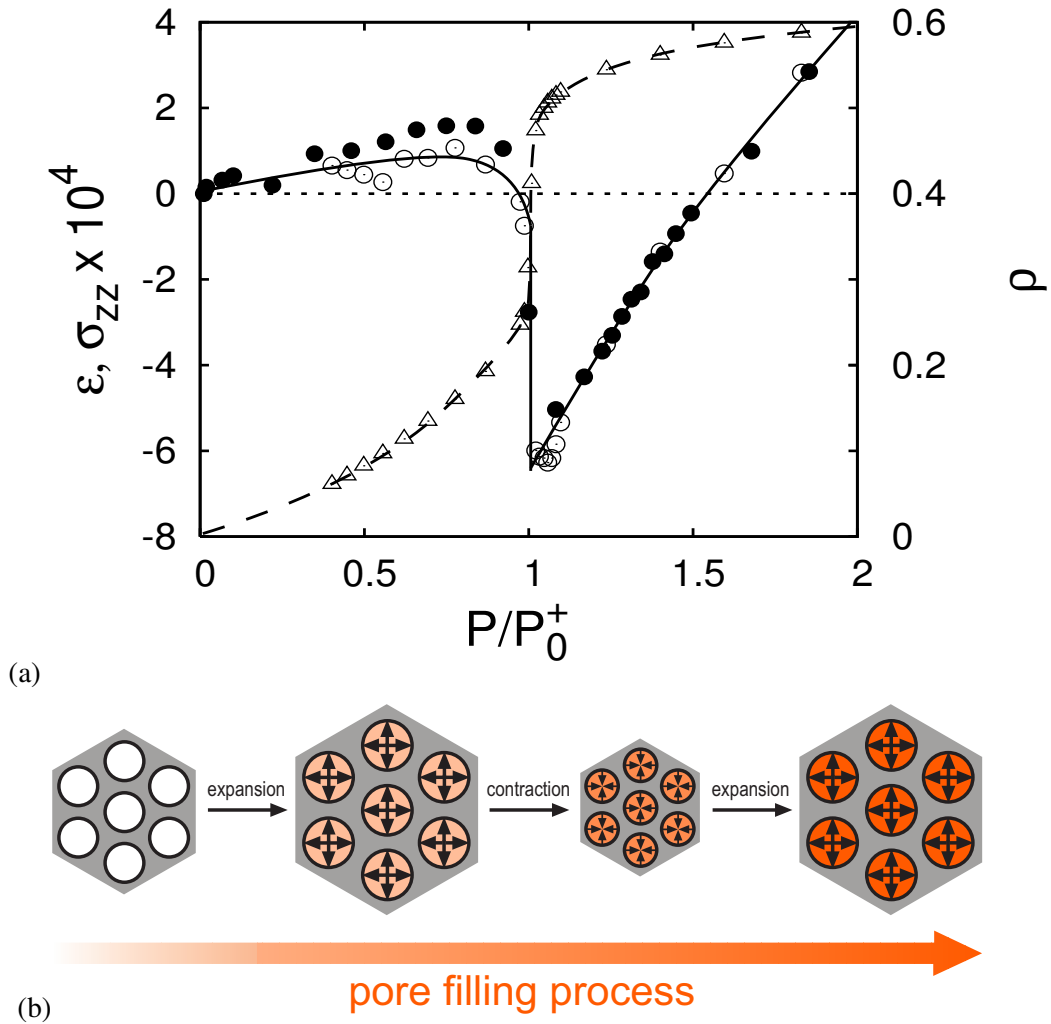


FIG. 5.11: (a) Experimental data from [165]: Experimental lattice strain ε (●) obtained from data of Fig. 5.10b according to Eq. (5.27) in comparison with pore strain σ_{zz} (○) of the simulation with optimised parameters $s_{z0} = 6.8$, $\kappa = 50$, $\epsilon_{fs} = 1.2$ and $T = 1.0$. Both quantities are plotted as functions of the (reduced) bulk fluid pressure P/P_0^+ where P_0^+ is the respective bulk fluid pressure at which capillary condensation sets in. The factor 10^4 applies to both quantities. Additionally, the density ρ (Δ) of the confined fluid is shown for the simulation. (b) Exaggerated sketch of sorption strain sequence which experiment and simulation share during pore filling.

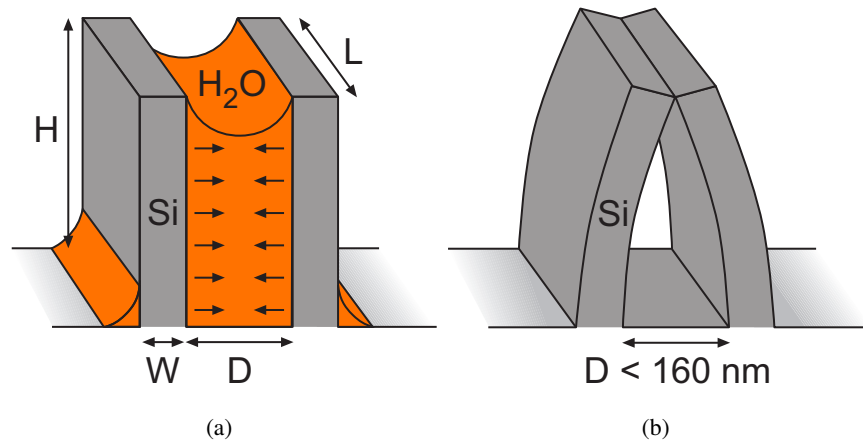


FIG. 5.12: Sketch of silicon structures of dimensions $W = 24 \text{ nm}$, $H = 640 \text{ nm}$, $L = 8000 \text{ nm}$, and $D < 160 \text{ nm}$ as synthesised by H. Namatsu et al. [166] before (a) and after (b) the drying of water. If the separation of plates is sufficiently large $D \geq 220 \text{ nm}$, silicon structures remain unaffected by the drying process.

5.4 Comparison With Other Studies

At the moment, highly flexible Sol-Gel derivatives such as aerogels or xerogels are the best explored family of porous materials in the sense of substrate deformation during the sorption process. [167–174] These derivatives feature an amorphous network of (mainly) mesopores with a high porosity, i.e. a large pore volume to total volume ratio (up to 99.9%), and as a result a large deformability so that volume shrinkage up to 40% may arise during sorption. [169, 175] Since synthesis yields macroscopic grains of a few mm in size [170], deformations of Sol-Gel derivatives on account of sorption are macroscopic phenomena apparent to the unaided eye. Nitrogen adsorption of aerogels reveals a similar behaviour to the findings of the present model system since aerogels contract severely at capillary condensation and then expand again with increasing bulk fluid pressure (see Fig. 4 of [169] and Fig. 5 of [170]). The equivalence to simulation data with a strong fluid–wall interaction $\epsilon_{fs} = 1.5$ presented in Fig. 5.6b (Δ) is suggested. However, on account of their large deformability, aerogels deform plastically during adsorption which becomes apparent from subsequent desorption which ends in a contracted state compared to the initial state of the adsorption–desorption cycle. In agreement with Fig. 5.8a, the synthesis of aerogels requires *supercritical* drying of the (confined) solvent [176] to prevent the highly porous (substrate) structure from contracting irreversibly during the transition from liquid-like to gas-like state.

A similar phenomenon is observed by Namatsu et al. [166] during the synthesis

5.4 | Comparison With Other Studies

of silicon nanostructures. Namatsu et al. synthesise plane-parallel thin silicon walls separated by a few nanometres, sketched in Fig. 5.12a. Here, the final drying process of water turns out to be a limiting factor since structures separated by less than 160 nm collapse and are permanently connected, as sketched in Fig. 5.12b. At larger separations $D \geq 220$ nm the contraction seems to be less pronounced and the silicon structures remain unaffected, in agreement with Fig. 5.6a of the present model system.

Dolino et al. [177] present pentane adsorption data for two types of porous silicon which differ in pore morphology. So-called p^+ -type porous silicon consists of more or less ordered cylindrical pores of approximately 10 nm diameter whereas p -type porous silicon comprises interconnected roughly spherical pores of about 3 nm diameter. Upon pentane sorption the lattice parameter of the silicon (*not* the pore lattice) is observed through X-ray scattering. Concerning the adsorption process in the range $0.2 \leq P/P_0 \leq 1$ (see Fig. 2b of [177])¹, p^+ -type porous silicon shows a sequence of 'expansion–contraction–expansion' similar to the findings of the present model system where the contraction is a minimum at capillary condensation. But p -type porous silicon reveals first a decrease of the lattice parameter until capillary condensation sets in and then an expansion with increasing bulk fluid pressure.

Experimental investigations of mesopore deformation spurs theoretical approaches ranging from continuum elasticity [178] and phenomenological thermodynamics [177, 179, 180] to computer aided calculations such as density functional theory [181, 182] and Monte Carlo simulations [95, 175]. To explain deformations of porous glasses which consist of a network of almost cylindrical mesopores, Scherrer argues with the Kelvin equation (see the Appendix C on p. 171) and refers to the specific surface energy γ as the driving force behind sorption strains. [178] Because the specific surface energy changes upon sorption, the pore radius should change to counteract energetic changes. For example, if γ increases, cylindrical pores should contract to decrease their surface area and therewith the surface energy. However, the good agreement between the present slit pore model and the experimental cylindrical pores (see Section 5.3.2) suggests that curvature effects have minor impact on deformations of porous materials because the surface area of slit pores remains fixed regardless of the strain.

Ash et al. [179] attribute mesopore deformations to the dispersion forces of the confined fluid which may represent a repulsive field as well as an attractive field to the pore walls. The study of Balbuena et al. [181] confirms this explanation because the presented solvation pressures, i.e. the pressure perpendicular to the pore

¹The lattice mismatch $\Delta a/a$ in [177] is related to the lattice parameter a of bulk silicon, so that empty porous silicon bears $\Delta a/a \neq 0$ at $P/P_0 = 0$, contrary to the definition of strain used throughout the present work.

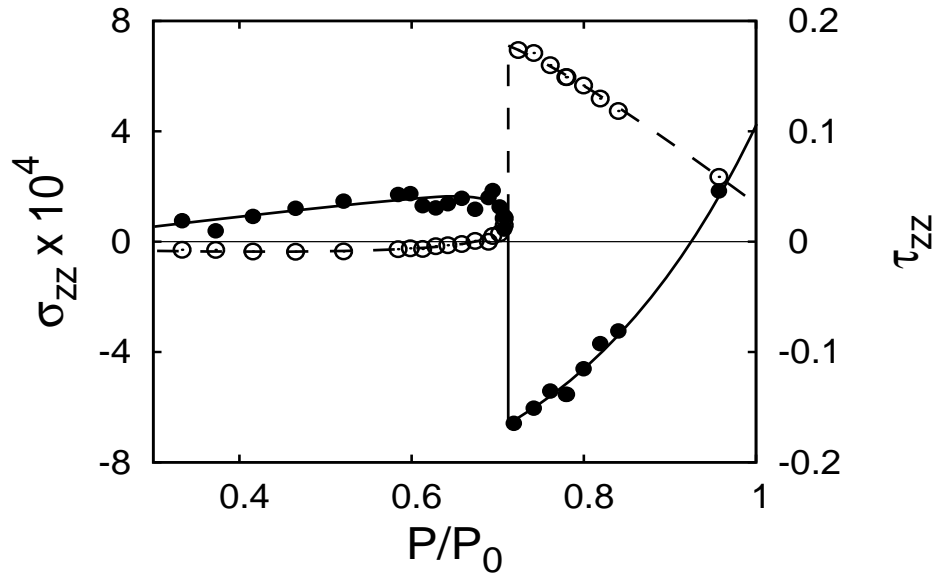


FIG. 5.13: Strain σ_{zz} (●) and stress tensor element τ_{zz} (○) as functions of the (reduced) bulk fluid pressure P/P_0 for a fluid between flexible walls with $s_{c0} = 6.8$ and $\kappa = 30$ at $T = 1.0$. Data from same simulation run as Fig. 5.4c is utilised.

walls, show a similar dependence on the bulk fluid pressure as the strain considered in [179]. Assuming that pore walls deform according to Hooke's law, i.e. the strain is proportional to the solvation pressure, the work of [179] corroborates the findings of [181].

A study of Neimark et al. presents experimental data in connection with Monte Carlo calculations of argon adsorption in carbide-derived activated carbon which can be considered to consist of slit-like micropores (i.e. pores of width ≤ 2 nm). [95] The experimental adsorption process is well reproduced by simulation where both show first a contraction followed by a monotonic expansion. However, in this study no relation between strain minimum and capillary condensation is established.

Despite the theoretical approach of [178], the above studies are consistent with the results of the present model system, although different definitions of strain are used throughout these works.

5.5 | Stress–Strain Relation

s_{z0}	τ_{zz}^{ff}	τ_{zz}^{fs}	Eq. (5.33)	Eq. (5.32)	$\sigma_{zz} \times 10^4$
			τ_{zz}	τ_{zz}	
1.5	-0.502	-3.235	-3.737	-3.739	1076.4
1.6	-0.481	-2.061	-2.542	-2.544	683.8
1.7	-0.455	-1.011	-1.466	-1.467	371.8
1.8	-0.432	-0.128	-0.560	-0.561	139.1
1.9	-0.411	0.555	0.144	0.142	-24.4
2.0	-0.396	1.047	0.651	0.649	-131.3
2.1	-0.390	1.357	0.967	0.965	-186.0
2.2	-0.400	1.476	1.076	1.072	-204.7
2.3	-0.441	1.421	0.980	0.975	-177.9
2.4	-0.542	1.171	0.629	0.622	-105.0
2.5	-0.721	0.769	0.048	0.038	-1.3
3.0	-0.580	0.695	0.115	0.109	-6.6
3.5	-0.615	0.638	0.023	0.017	6.8
4.0	-0.421	0.616	0.195	0.196	-12.5
5.0	-0.351	0.469	0.118	0.135	-5.0

TABLE 5.1: Comparison of virial and force expressions of τ_{zz} for a fluid in a flexible pore of various pore widths s_{z0} with $\kappa = 30$ at $\mu = -11.3$, $T = 1.0$ (cf. Fig. 5.14a). Additionally, the strain σ_{zz} is listed.

5.5 Stress–Strain Relation

We already suggested in Section 5.2.2 that the sharp drop of the strain at capillary condensation reflects the fundamental reorder of fluid matter from an almost disordered gaseous state to a denser organisation of matter in which attractive forces cause a near-order of fluid particles as well as wall particles. In other words, at capillary condensation, the substrate is affected in the same manner as the confined fluid and, thus, contracts. The plot in Fig. 5.13 confirms the suggestion that variations in strain σ_{zz} are correlated with those of the stress tensor element perpendicular to the walls τ_{zz} exerted by the fluid. To explore this relationship more closely we turn to the calculation of stress tensor elements in the present model system.

5.5.1 Force and Virial Expression of Stress

On account of the symmetry of the stress tensor due to the slit pore geometry given in Eq. (5.1), one may rewrite Eq. (3.29) in the form of

$$d\Omega = -SdT - Nd\mu + 2\mu_s dN_s + s_{z0}\tau_{||}dA + A_0\tau_{zz}ds_z \quad (5.29)$$

Here, $A_0 = s_{x0}s_{y0}$ is the area of the pore wall considered in an unstrained state whereas $A = s_x s_y$ specify this area in an arbitrary (maybe strained) state. For a certain pore with fixed N_s in a given thermodynamic state of fixed A , μ and T , Eq. (5.29) can be rewritten as

$$\tau_{zz} = A_0^{-1} \left(\frac{\partial \Omega}{\partial s_z} \right)_{N_s, A, \mu, T} \quad (5.30)$$

which combined with Eqs. (2.41) and (3.31) leads to

$$\begin{aligned} \tau_{zz} &= \frac{-k_B T}{A_0 \Xi} \left(\frac{\partial \Xi}{\partial s_z} \right)_{N_s, A, \mu, T} \\ &= \frac{-k_B T}{A_0 \Xi} \sum_N e^{\gamma N} \frac{1}{N! \Lambda^{3(N+2N_s)}} \left(\frac{\partial Z}{\partial s_z} \right)_{N_s, A, T} \end{aligned} \quad (5.31)$$

Thus, the stress tensor element depends on the derivative of the configuration integral Z with respect to the slit pore width s_z . Depending on the way in which the derivative is calculated, one may end up with the ‘force’ expression of the stress written as

$$\tau_{zz} = -\frac{\epsilon_{fs}}{2A_0} \left\langle \sum_{k=1}^2 \sum_{i=1}^N \sum_{j=1}^{N_s} |u'(r_{ij}^{[k]}) (\hat{\mathbf{r}}_{ij}^{[k]} \cdot \hat{\mathbf{e}}_z)| \right\rangle \quad (5.32)$$

or one may arrive at the ‘virial’ expression given by

$$\tau_{zz} = \tau_{zz}^{ff} + \tau_{zz}^{fs} \quad (5.33)$$

$$\tau_{zz}^{ff} = -\frac{\langle N \rangle k_B T}{A_0 s_{z0}} + \frac{1}{A_0 s_{z0}} \left\langle \sum_{i=1}^N \sum_{j>i}^N u'(r_{ij}) r_{ij} (\hat{\mathbf{r}}_{ij} \cdot \hat{\mathbf{e}}_z)^2 \right\rangle \quad (5.34)$$

$$\tau_{zz}^{fs} = \frac{\epsilon_{fs}}{A_0 s_{z0}} \left\langle \sum_{k=1}^2 \sum_{i=1}^N \sum_{j=1}^{N_s} u'(r_{ij}^{[k]}) r_{ij}^{[k]} \left[(\hat{\mathbf{r}}_{ij}^{[k]} \cdot \hat{\mathbf{e}}_z) (\hat{\mathbf{r}}_{ij}^{[k]} + \Delta \hat{\mathbf{r}}_j^{[k]}) \cdot \hat{\mathbf{e}}_z \right] \right\rangle \quad (5.35)$$

where the latter is expressed in separate contributions of fluid–fluid interactions τ_{zz}^{ff} and fluid–wall interactions τ_{zz}^{fs} . In Eqs. (5.32), (5.34) and (5.35), $\hat{\mathbf{r}} = \mathbf{r}/r$ denotes an unit vector and $\hat{\mathbf{e}}_z$ is a unit vector which points along the z -coordinate of the Cartesian coordinate system. Both expressions for the stress are taken from the work of Diestler and Schoen [105] and their derivation is reproduced in detail in Appendix B

5.5 | Stress–Strain Relation

on page 163.

Since Eqs. (5.32) and (5.33) represent two different but equivalent molecular expressions for the normal stress τ_{zz} , they provide a consistency check for the reliability of Monte Carlo simulations. In Table 5.1, the computed values from the virial expression of Eq. (5.33) along with its separate contributions as well as the results from the force expression of Eq. (5.32) are listed for different pore sizes. The comparison of both data sets is gratifying, especially at smaller pore sizes. Even at larger pore sizes the agreement is quite good although contributions of τ_{zz}^{ff} and τ_{zz}^{fs} match each other in magnitude but with opposite sign so that the sum of both is expected to bear a larger error bar.

5.5.2 Strain as a Packing Phenomenon

In Table 5.1, the strain σ_{zz} is added as a separate entry to emphasise that σ_{zz} varies with the pore size in the same manner as τ_{zz} . Strain and stress tensor elements are explicitly correlated to one another which becomes evident from Fig. 5.14a where τ_{zz} and σ_{zz} are plotted as functions of the pore size s_{z0} . The oscillating course of the stress at smaller pore sizes is a well known phenomenon in confinement and is found in theory [32, 145, 181, 183, 184] and in experiment [185, 186].

A prominent realisation of an adjustable confinement, from which the force exerted by the fluid on the walls can be detached, is the atomic force microscope (AFM). [32, 185] In AFM experiments two surfaces immersed in a fluid are subsequently approached or removed in relation to one another in (predetermined) steps of approximately 0.1 nm where the force acting between the surfaces is measured. It is observed that the period of the oscillation depends on the particle diameter of the confined fluid. [185]

Evans et al. demonstrate that the oscillating behaviour of the stress is based on repulsive forces since it occurs even for hard spheres confined between hard walls where attraction is absent. [187] The study also shows that stress oscillations reflect the stratification of the confined fluid along the walls (see Section 4.6.1). The damped oscillatory character of the local density (shown e.g. in Fig. 4.15a) near the wall results in a damped oscillation of the stress if the distance between the walls is changed. As long as the wall separation is of the order of a few particle diameters, the stress is dominated by packing effects where each stress period reflects the formation of a new fluid layer.

Fig. 5.14a reveals that the period of stress oscillations is indeed approximately 1σ . In Fig. 5.15a–h the local density profiles across the pore are shown for different wall

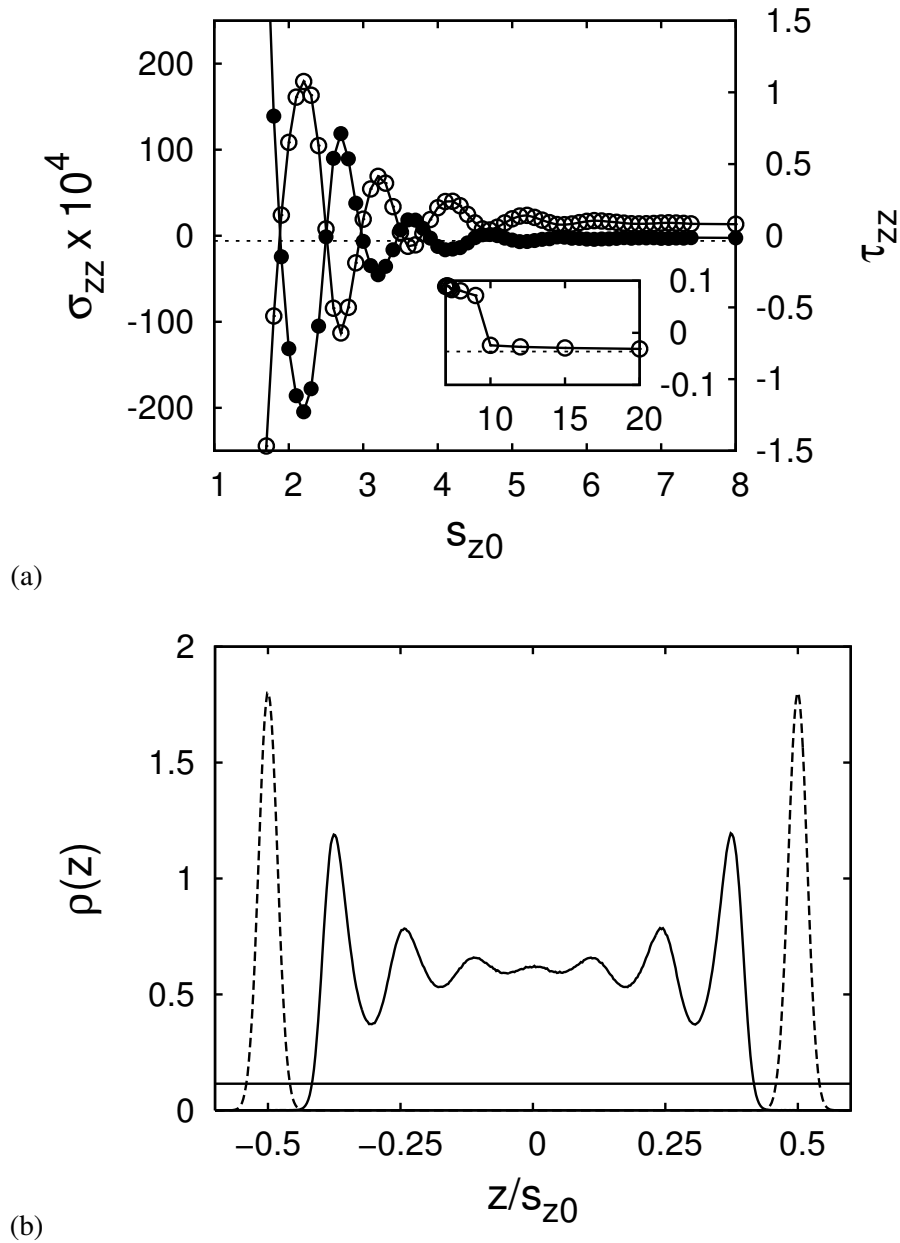


FIG. 5.14: (a) Strain σ_{zz} (●) and stress tensor element τ_{zz} (○) as functions of the pore width s_{z0} for a flexible pore. For $s_{z0} < 10$ the fluid is in a liquid-like state whereas for pores of width $s_{z0} \gtrsim 10$ the fluid is in a gas-like state. The liquid-gas phase transition is characterised by the drop of τ_{zz} from positive to negative values as shown in the inset. With increasing pore width, τ_{zz} converges to the stress of the corresponding bulk fluid system $\tau_b \approx -0.036$ (- - -). (b) Local density $\rho(z)$ versus z/s_{z0} for fluid (—) and wall particles (- - -) for a flexible pore with $s_{z0} = 7.5$. The horizontal line corresponds to the average density $\rho_b \approx 0.115$ of a bulk fluid system under the same thermodynamic conditions. $T = 1.0$, $\mu = -11.3$ and $\kappa = 30$ for all data sets.

5.5 | Stress–Strain Relation

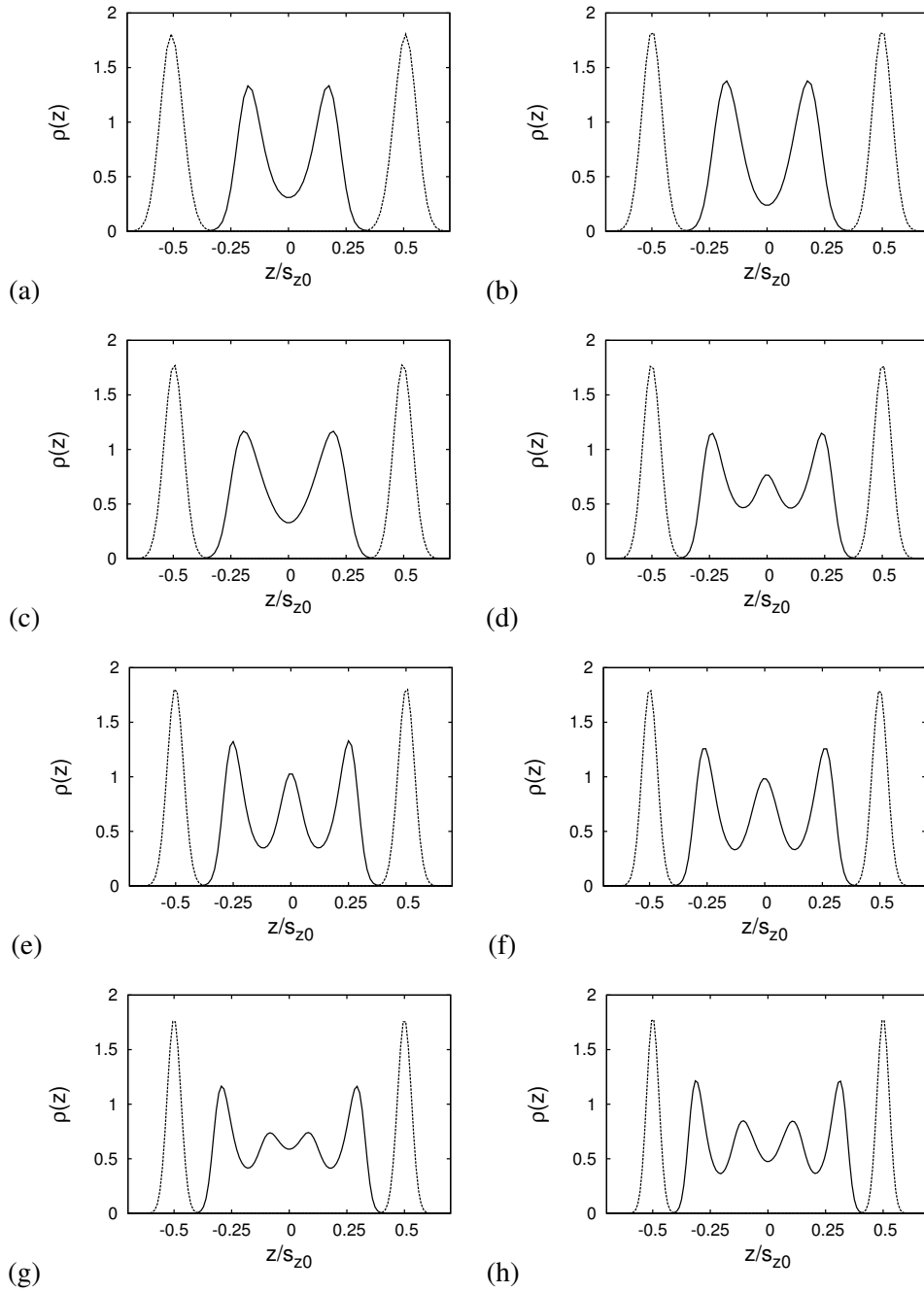


FIG. 5.15: Local density profiles $\rho(z)$ of fluid (—) and wall particles (---) across the pore with $\kappa = 30$ and different pore widths: **(a)** $s_{z0} = 2.7$, **(b)** $s_{z0} = 3.0$, **(c)** $s_{z0} = 3.2$, **(d)** $s_{z0} = 3.5$, **(e)** $s_{z0} = 3.7$, **(f)** $s_{z0} = 4.0$, **(g)** $s_{z0} = 4.5$ and **(h)** $s_{z0} = 5.0$. Data sets correspond to situations of Fig. 5.14a where the fluid is in a liquid-like state at $\mu = -11.3$ and $T = 1.0$.

separations s_{z0} of Fig. 5.14a, demonstrating the formation of new fluid layers. The density profile of Fig. 5.15a represents a situation with $s_{z0} = 2.7$ where two fluid layers fit well between the walls which is reflected by a local minimum of the normal stress τ_{zz} (see Fig. 5.14a). A further comparison between Fig. 5.15a–c and Fig. 5.14a indicates that with increasing wall separation s_{z0} the normal stress increases until reaching a local maximum at $s_{z0} \approx 3.2$, cf. Fig. 5.15c. From this point a new fluid layer arises as shown in Fig. 5.15d and the stress releases. After a full period of 1σ the stress drops again to a local minimum at $s_{z0} \approx 3.7$ reflecting that three layers meet the packing requirements in confinement which is confirmed by the density profile in Fig. 5.15e.

In general, Fig. 5.14a reflects that the normal stress reaches local extrema after a period of $\frac{1}{2}\sigma$. At integer values $s_{z0} \approx n$ ($n \in \mathbb{N}$) $n-1$ fluid layers fit the packing constraints in confinement whereas at $s_{z0} \approx (2n + 1)/2$ half-finished layer formations appear.

For large wall separations s_{z0} , the stress should converge to the stress τ_b of the bulk fluid under the same thermodynamic conditions, marked by the dashed line in Fig. 5.14a. It is obvious that the stress deviates significantly from the value $\tau_b \approx -0.036$. Contrary to the gaseous state of the bulk fluid under the given thermodynamic conditions, the confined fluid is in a liquid-like state which the density profile in Fig. 5.14b for the pore size $s_{z0} = 7.5$ reveals. At the centre of the pore at $z/s_{z0} \approx 0$ the influence of the pore walls diminishes so that the confined fluid is almost homogeneously distributed in space with an average density $\rho \approx 0.62$ confirming the discrepancy from the bulk density $\rho_b \approx 0.115$ which is demarcated by the horizontal line. The inset of Fig. 5.14a focuses on larger wall separations at an enhanced scale and indicates the transition of the confined fluid from the liquid-like state to the gas-like state in which the stress almost coincide with the one of the bulk fluid.

However, the oscillatory behaviour of the stress causes oscillations of the strain as well, indicating that packing effects dominate σ_{zz} at smaller wall separations $s_{z0} \lesssim 5$. With regard to the focus of the present work, that is, the sorption strain of pore sizes $s_{z0} > 5$, packing effects seem to be of lesser influence.

5.6 Strain Caused by Gas-like Phases

To investigate the reaction of the substrate to the gas-like state of the confined fluid, we leave the more fluid-oriented stress τ_{zz} in favour of the more substrate-oriented pressure tensor element P_{zz} where both are simply related through $P_{zz} = -\tau_{zz}$. It is

5.6 | Strain Caused by Gas-like Phases

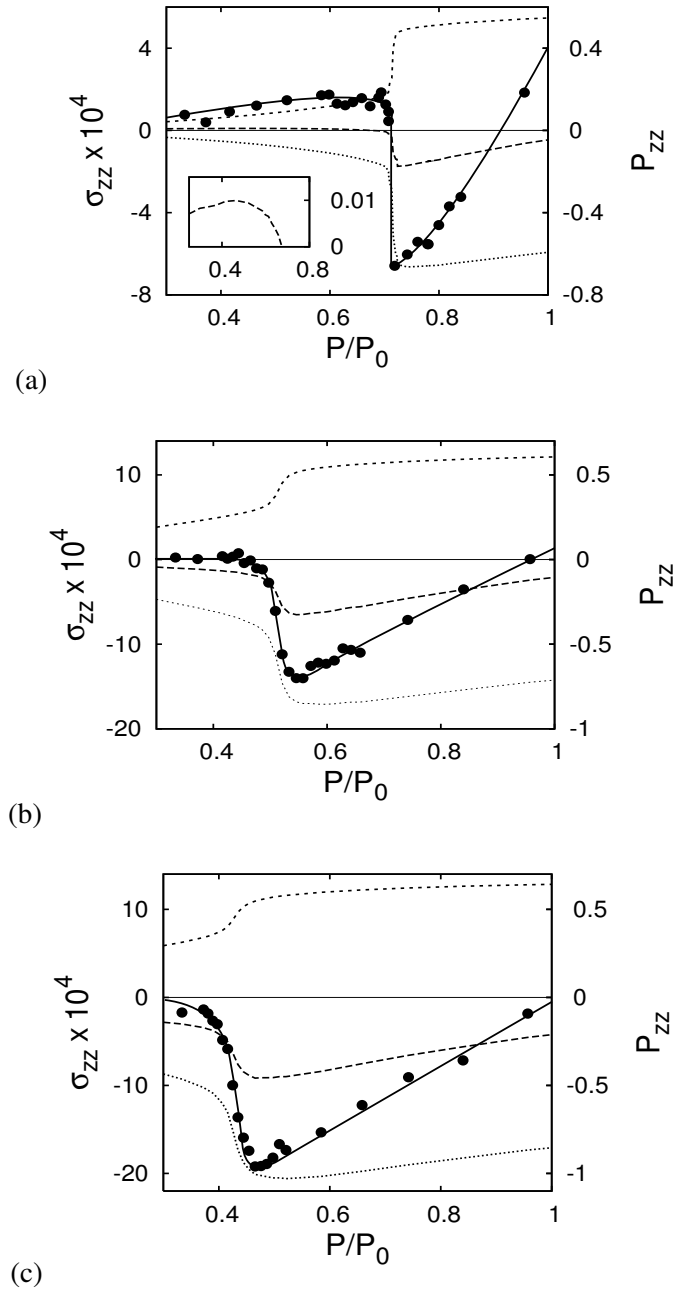


FIG. 5.16: Strain σ_{zz} (●) and pressure-tensor element P_{zz} (---) as functions of (reduced) bulk pressure P/P_0 . In addition, the two contributions to P_{zz} , namely P_{zz}^{id} (-·-) and P_{zz}^{pot} (···), are shown. All data sets share $s_{z0} = 6.8$, $\kappa = 30$, and $T = 1.0$ but differ in fluid–substrate interaction ϵ_{fs} [see Eq. (3.21)]: **(a)** $\epsilon_{fs} = 1.0$, **(b)** $\epsilon_{fs} = 1.5$, and **(c)** $\epsilon_{fs} = 2.0$. The inset in part (a) shows the variation of P_{zz} with P/P_0 on an enhanced scale.

convenient to separate the normal pressure derived via the virial expression of the stress, cf. Eq. (5.33), into separate contributions according to

$$-\tau_{zz} = P_{zz} = P_{zz}^{id} + P_{zz}^{pot} \quad (5.36)$$

where P_{zz}^{id} can be considered as the ideal gas part of the pressure, that is, the force exerted by non-interacting point-like particles on the wall, cast as

$$P_{zz}^{id} = \frac{\langle N \rangle k_B T}{A_0 s_{z0}} \quad (5.37)$$

and P_{zz}^{pot} contains the remaining parts, i.e. contributions that arise from intermolecular interactions of fluid–fluid and fluid–wall particles, given by

$$P_{zz}^{pot} = -\frac{1}{A_0 s_{z0}} \left\langle \sum_{i=1}^N \sum_{j>i}^N u'(r_{ij}) r_{ij} (\hat{\mathbf{r}}_{ij} \cdot \hat{\mathbf{e}}_z)^2 \right\rangle \quad (5.38)$$

$$-\frac{\epsilon_{fs}}{A_0 s_{z0}} \left\langle \sum_{k=1}^2 \sum_{i=1}^N \sum_{j=1}^{N_s} u'(r_{ij}^{[k]}) r_{ij}^{[k]} \left[(\hat{\mathbf{r}}_{ij}^{[k]} \cdot \hat{\mathbf{e}}_z) (\hat{\mathbf{r}}_{ij}^{[k]} + \Delta \hat{\mathbf{r}}_j^{[k]}) \cdot \hat{\mathbf{e}}_z \right] \right\rangle \quad (5.39)$$

The latter, non-ideal part depends on ϵ_{fs} which specifies the strength of the fluid–solid interaction in terms of the fluid–fluid interaction $\epsilon \equiv 1.0$. Fig. 5.16 shows the normal pressure together with its separate contributions and the strain for different ϵ_{fs} as functions of the bulk fluid pressure. According to Eq. (5.37) P_{zz}^{id} is a monotonically increasing positive function of the bulk fluid pressure P/P_0 because for a given temperature P_{zz}^{id} depends only on the average fluid density $\rho = \langle N \rangle / A_0 s_{z0}$. On the other hand P_{zz}^{pot} is a monotonically decreasing negative function of P/P_0 as long as the fluid is in a gas-like state.

It is obvious that in all three cases σ_{zz} correlates with P_{zz} in sign, that is, negative P_{zz} causes a contraction of the pore whereas positive P_{zz} results in an expansion of the confining medium. The comparison of the plots indicates that with increasing ϵ_{fs} the capillary condensation pressure, characterised by a strain minimum, shifts to lower bulk fluid pressures as expected. Concerning the pressure range before capillary condensation, i.e. the gas-like phase, the strain behaviour depends significantly on ϵ_{fs} .

If the strength of the fluid–solid interaction matches the one of the fluid–fluid interaction, shown in Fig. 5.16a, the pore expands with increasing P/P_0 following the minute positive pressure perpendicular to the walls emphasised on an enhanced scale in the inset. In this situation the ideal gas part P_{zz}^{id} exceeds the intermolecular interaction part P_{zz}^{pot} resulting in a slightly positive net pressure P_{zz} . By increasing the fluid–wall interaction strength to $\epsilon_{fs} = 1.5$, both pressure contributions P_{zz}^{id} and P_{zz}^{pot}

5.7 | Strain Caused by Liquid-like Phases

are almost of the same magnitude but opposite in sign so that P_{zz} nearly vanishes, see Fig. 5.16b. Consequently, the substrate remains in an almost unstrained state up to $P/P_0 \approx 0.5$. In Fig. 5.16c the fluid–solid interaction is further increased to $\epsilon_{fs} = 2.0$ and therefore P_{zz}^{pot} dominates P_{zz} so that σ_{zz} decreases monotonically during the gas-like phase of the confined fluid.

Thus, during the gas-like phase, the strain behaviour is dominated by ϵ_{fs} which is a measure for the wetting characteristics of the substrate, i.e. the ability to form a fluid layer along the substrate. In Fig. 5.17 the local density profiles for two wetting scenarios $\epsilon_{fs} = 1.0$ (—) and $\epsilon_{fs} = 2.0$ (- - -) are shown. To illustrate the difference in wetting characteristics, the thermodynamic states of the systems are selected in such a way that both share the same density $\rho \approx 0.028$ in the bulk-like centre of the pore at which the influence of the wall diminishes. Due to the difference in fluid–solid interaction strength, this approach requires that systems differ in chemical potential. As one moves from the bulk-like centre of the pore towards the walls at $z/s_{z0} = \pm 0.5$ the local density of both systems increases which signifies that pore walls are wetted by the fluid. In the case of $\epsilon_{fs} = 1.0$, the density profile reveals only a slight increase near the wall which denotes that wetting is not much pronounced. As expected, the wetting characteristics of the system with $\epsilon_{fs} = 2.0$ is much better indicated by a pronounced wetting layer next to the pore wall and an additional secondary layer located at larger distance to the substrate.

5.7 Strain Caused by Liquid-like Phases

Upon significant imbibition of fluid matter at capillary condensation the strain behaviour becomes independent of the fluid’s wetting characteristics, contrary to the confinement of gas-like phases. Fig. 5.18 shows the substrate strain σ_{zz} as a function of P/P_0 on a logarithmic scale for liquid-like states of different wetting characteristics, i.e., for different ϵ_{fs} . Although ϵ_{fs} varies between 0.75 and 1.5, the strain isotherms of liquid-like phases coincide, that is, they show the same dependence on the bulk fluid pressure irrespective of ϵ_{fs} .

5.7.1 Quasi-Kelvin Equation

To explain the logarithmic dependence of the substrate strain on the bulk fluid pressure, we turn to the thermodynamic analysis of the liquid-like fluid in confinement. For this purpose we slightly change our point of view and determine the thermody-

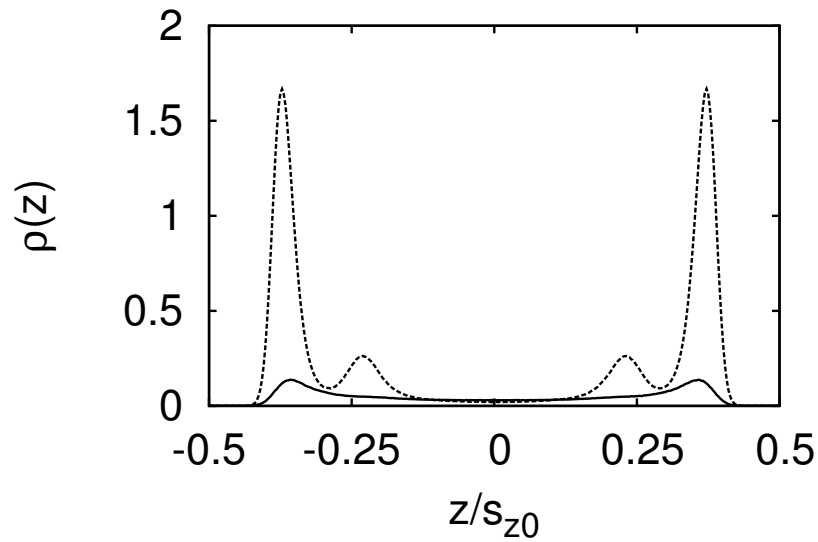


FIG. 5.17: Local density $\rho(z)$ of fluid particles as a function of z/s_{z0} between lower ($z/s_{z0} = -0.5$) and upper substrate ($z/s_{z0} = +0.5$) for different fluid–wall interactions: (—) $\epsilon_{fs} = 1.0$ at $\mu = -12.15$ and (---) $\epsilon_{fs} = 2.0$ at $\mu = -13.00$. $T = 1.0$ and $\kappa = 30$ applies to both data sets.

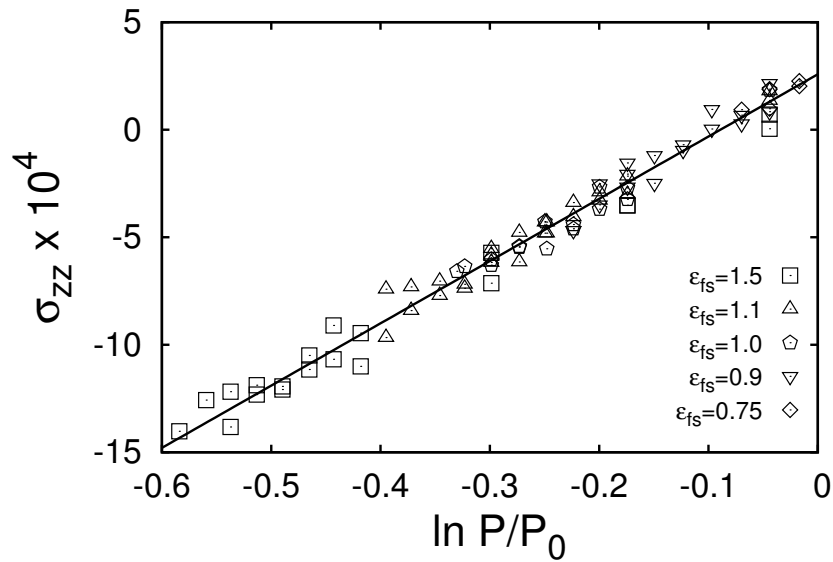


FIG. 5.18: Substrate strain σ_{zz} of liquid-like phases as a function of P/P_0 on a logarithmic scale for different fluid–wall interaction strengths ϵ_{fs} as indicated in the figure. $T = 1.0$, $s_{z0} = 6.8$ and $\kappa = 30$ for all data sets. The solid line is a linear fit through all data points.

5.7 | Strain Caused by Liquid-like Phases

dynamic state of the system through N , T and \mathbf{P} where the Gibbs potential \mathcal{G} turns out to be the relevant thermodynamic potential. \mathcal{G} is related to the grand potential Ω through a Legendre transformation of the form

$$\mathcal{G} \equiv \Omega + A_0 s_z P_{zz} \quad (5.40)$$

which combined with Eq. (5.29) yields

$$d\mathcal{G} = d(\Omega + A_0 s_z P_{zz}) = -SdT - Nd\mu - P_{\parallel} s_{z0} dA + A_0 s_{z0} dP_{zz} \quad (5.41)$$

where a fixed number of wall particles is incorporated, i.e. we consider a *certain* slit-pore with fixed N_s .

As discussed in Section 4.3, the discrete structure of the wall prevents the relevant thermodynamic potential from being translationally invariant. Since in the present model the potential energy U of a fluid particle depends on the distance to the walls (i.e. on z) and changes periodically as it moves parallel to the walls, in general the displacement of a fluid particle is connected with a change in U which relates to \mathcal{G} via Eqs. (2.41), (3.31), (3.32) and (5.40). In other words, \mathcal{G} is not a homogeneous function of degree one which is a prerequisite to apply Euler's Theorem and to derive a Gibbs–Duhem equation.

Nevertheless \mathcal{G} can be considered to be approximately a homogeneous function of degree one following the argument of Schoen [188]: with regard to the limit of rigid substrates ($\kappa \rightarrow \infty$), wall particles are arranged in the x - and y -direction according to an ideal lattice characterised by the lattice parameter $\ell = \ell_x = \ell_y$, see Fig. 3.3 on p. 40. If one allows fluid particles to move only in units of ℓ , their potential energy remains constant with regard to displacements parallel to the walls. If we consider that displacements in directions parallel to the walls occur in an integer number n of unit cell lengths ℓ , \mathcal{G} does not change for fluid particles moving in the x - and y -directions. This means that the system is coarse-grained within the x - y plane on the length scale of ℓ . As long as n is sufficiently large (or ℓ sufficiently small), changes in n become approximately continuous and \mathcal{G} becomes approximately a homogeneous function of degree one in τ_{\parallel} . This notion is further corroborated, if one reduces κ , that is, if the walls become deformable, because the motion of wall particles reduces the periodicity of the wall structure. Thus, a given configuration of fluid particles ‘feel’ the field of an fcc wall which is spatially smeared to some extent, depending on the binding strength κ of the wall particles.

Following the argument of Section 4.2, cf. Eqs. (4.3)–(4.7), under conditions of fixed T , μ and P_{zz} , one may write

$$\mathcal{G} \approx -A s_{z0} P_{\parallel} \quad (5.42)$$

where s_{z0} is a constant and, therefore, the exact differential of \mathcal{G} is

$$d\mathcal{G} \approx d(-As_{z0}P_{\parallel}) = -As_{z0}dP_{\parallel} - P_{\parallel}s_{z0}dA \quad (5.43)$$

Combining the last equation with Eq. (5.41) gives the Gibbs–Duhem equation:

$$0 = -SdT - Nd\mu + As_{z0}dP_{\parallel} + A_0s_{z0}dP_{zz} \quad (5.44)$$

which states that an equation of state of the form $P_{zz} = P_{zz}(T, \mu, P_{\parallel})$ exists *in principle*. In Eq. (5.44) the last two terms account for the mechanical work that is done by the system where its anisotropy compels one to express the mechanical work through pressure tensor elements parallel to the walls P_{\parallel} and perpendicular to the walls P_{zz} .

Now following a *gedankenexperiment*, we consider only a part of the pore as the system in the thermodynamic sense, whereas the remainder of the pore *plus* the bulk fluid represent the surroundings. Thus, the boundary of the system follows not necessarily a ‘natural’ interface, but is a lamella of height s_z and finite extent $A = s_x s_y$ in the directions parallel to the walls. While the boundary in the z -direction is determined by the fluid–wall interface, the boundary within the x - y plane can be considered as imaginary and immaterial pistons through which system and surroundings may exchange mechanical work. With the Gibbs potential as the relevant thermodynamic potential, we always adjust A in such a way that the system is at constant P_{\parallel} . In other words, any change in the pressure of the system is counteracted through a rearrangement of the imaginary boundaries to prevent the system from doing work in the x - and y -directions. Consequently, mechanical work may only occur in the direction normal to the pore walls. This approach is consistent with the present model in which the periodic boundary conditions prevent the system from doing work in the directions parallel to the walls (see p. 93). Moreover, it reflects the fact that the deformation of the experimental system is reproduced by a scalar quantity, as discussed in Section 5.3.2.

According to the above consideration, we drop the term $As_{z0}dP_{\parallel}$ in Eq. (5.44) and write

$$0 = -SdT - Nd\mu + A_0s_{z0}dP_{zz} \quad (5.45)$$

Now we consider two states $P_{zz}(P)$ and $P_{zz}(P_0)$ of the sorption isotherm where P and P_0 are bulk fluid pressures: the former is an arbitrary pressure $P < P_0$ while the latter demarcates the bulk condensation pressure at which the sorption experiment naturally ceases, for reasons discussed in Section 4.1. Consequently, we may integrate Eq. (5.45) under the constraint of fixed T written as

$$A_0s_{z0} \int_{P_{zz}(P)}^{P_{zz}(P_0)} dP_{zz} = \int_{\mu(P)}^{\mu(P_0)} Nd\mu \quad (5.46)$$

5.7 | Strain Caused by Liquid-like Phases

Up to this point, the *ansatz* applies to gas-like phases as well as to liquid-like phases, but to proceed we restrict ourselves to the part of the sorption isotherm after capillary condensation, i.e. to liquid-like phases, in which N can be considered to be approximately constant. Thus, assuming a fixed particle number N the integrals in Eq. (5.46) are performed such that

$$\mu_l [P_{zz}(P_0), T] = \mu_l [P_{zz}(P), T] + \frac{1}{\rho_l} [P_{zz}(P_0) - P_{zz}(P)] \quad (5.47)$$

where $\rho_l = N/A_0 s_{z0} = \text{const.}$ is the density of the (incompressible) liquid-like phase and the subscript ' l ' denotes that we solely focus on liquid-like phases.

We already suggested that the confined fluid is in thermodynamic equilibrium with a gaseous bulk fluid reservoir, which can be considered to be ideal, so that we may write [66]

$$\mu_l [P_{zz}(P), T] = \mu_{bg}(P, T) = \mu_0 + k_B T \ln P \quad (5.48)$$

$$\mu_l [P_{zz}(P_0), T] = \mu_{bg}(P_0, T) = \mu_0 + k_B T \ln P_0 \quad (5.49)$$

where μ_{bg} is the chemical potential of the gaseous bulk fluid reservoir and μ_0 is the chemical potential of the ideal gas in its standard state. Combining the last two equations with Eq. (5.47) yields the quasi-Kelvin equation

$$P_{zz}(P) = \rho_l k_B T \ln \frac{P}{P_0} + P_{zz}(P_0) \quad (5.50)$$

Unlike the Kelvin equation [189] which is based upon the assumption of a meniscus, i.e. a curved liquid–gas interface, and force balance consideration (see Appendix C), the quasi-Kelvin equation states an equivalent relation just from the notion of a liquid-like phase in thermodynamic equilibrium with an ideal gas reservoir, irrespective of any geometric constraint.

5.7.2 Nanomechanical Substrate Properties

The plot of substrate strain σ_{zz} versus the normal pressure component P_{zz} in Fig. 5.19 shows a Hookean relationship, that is, $\sigma_{zz} \propto P_{zz}$, as long as small deformations respectively small pressures are concerned. Thus, focussing on small deformations, the substrate responds to the confined fluid as a Hookean solid which obeys

$$P_{zz} = M \sigma_{zz} \quad (5.51)$$

where we refer to M as the *pore-load modulus*. Because of its definition through Eq. (5.51) and the strain as a dimensionless quantity, M is a nanomechanical substrate

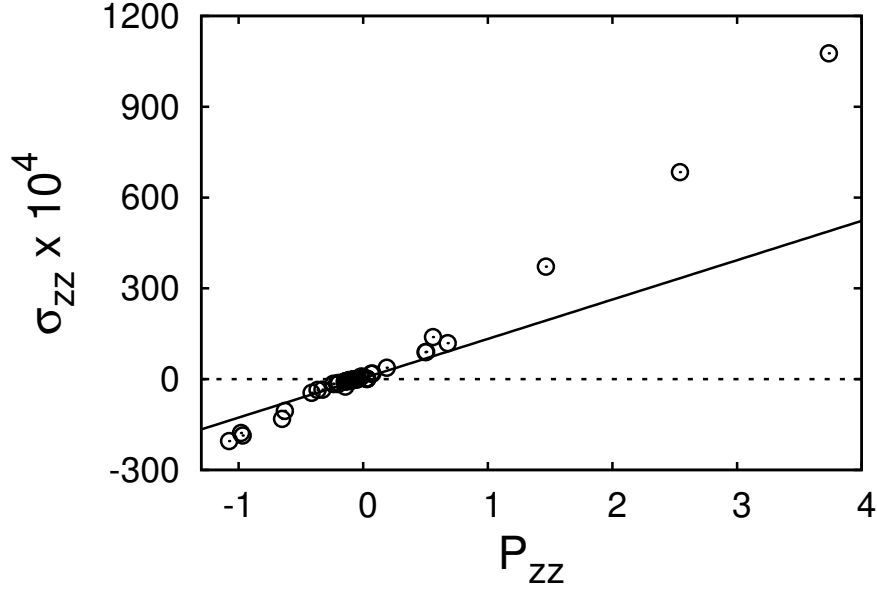


FIG. 5.19: Substrate strain σ_{zz} as a function of the pressure tensor element P_{zz} for a confined fluid between flexible walls with $\kappa = 30$ at $\mu = -11.3$, $T = 1.0$ and at various pore sizes s_{z0} , obtained from Fig. 5.14a. The solid line is a linear fit through the regime of moderate strains $-50 \lesssim \sigma_{zz} \times 10^4 \lesssim 50$, in which the stress–strain relation is approximately Hookean in character.

property of the same dimension as pressure, i.e. a directed force per area. In other words, M is a quantitative measure for the pressure needed to cause a specific deformation.

Combining Eqs. (5.50) and (5.51), one may write

$$\sigma_{zz} \propto \frac{\rho_l k_B T}{M} \ln \frac{P}{P_0} \quad (5.52)$$

which explains the relationship found in Fig. (5.18). That M exhibits a nanomechanical property of the substrate is further confirmed by the plots in Fig. 5.20. Part (a) of this figure shows σ_{zz} versus $\ln P/P_0$ for a fluid in the liquid-like state confined by substrates of different rigidities κ . As expected, the slope m of the best linear fit through individual data sets is a measure for the substrate deformability since

$$m \equiv \frac{\rho_l k_B T}{M} \propto \frac{1}{\kappa} \quad (5.53)$$

holds, which can be seen from part (b) of Fig. 5.20 (straight line). Because the liquid-like phase is assumed to be incompressible ($\rho_l = \text{const.}$), M is proportional to κ . To corroborate that M depends only on the substrate *irrespective* of the fluid, the slopes

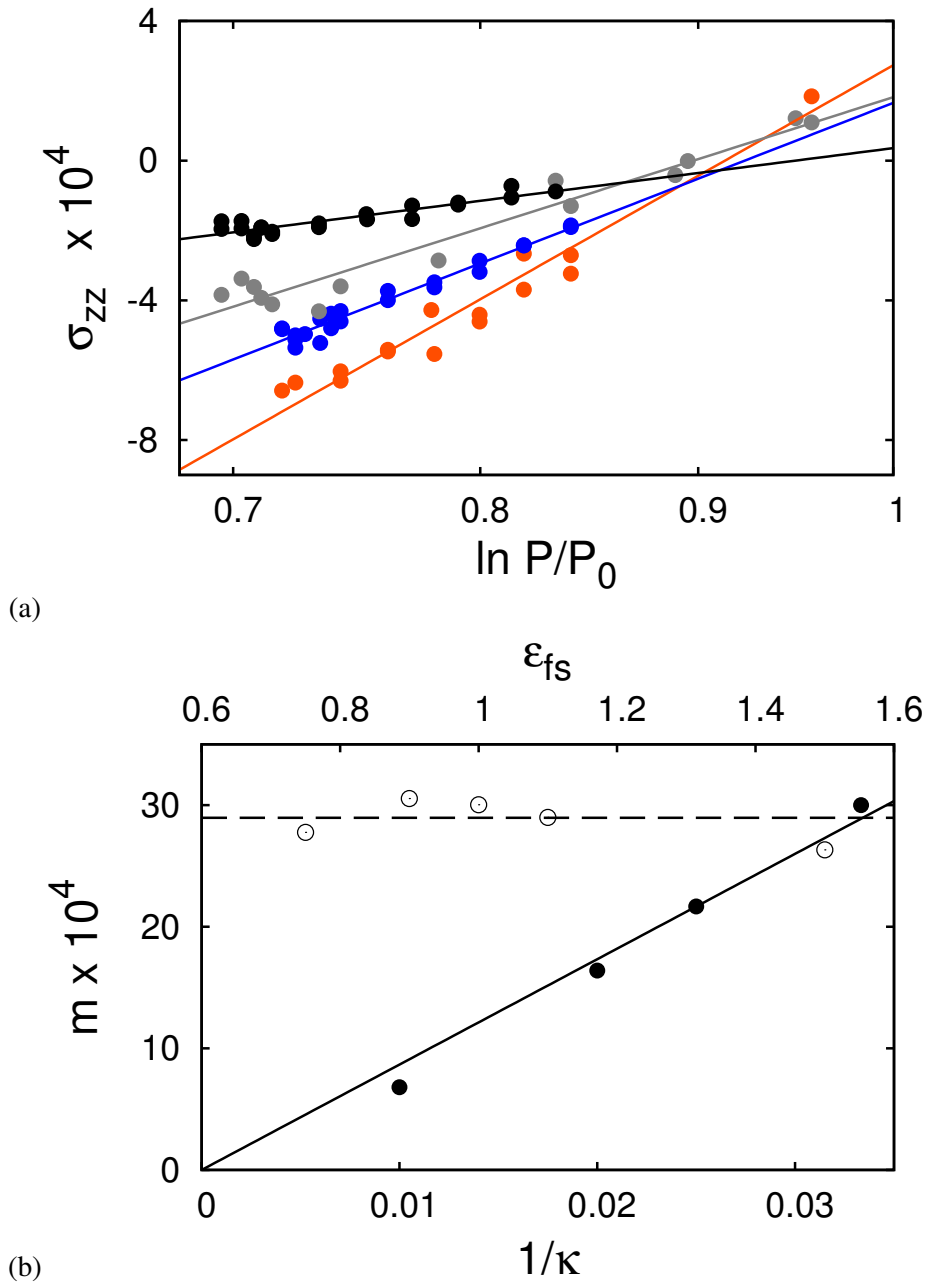


FIG. 5.20: (a) Substrate strain σ_{zz} as a function of P/P_0 on a logarithmic scale for a fluid in the liquid-like phase at $T = 1.0$ in pores of different rigidity: $\kappa = 30$ (●), $\kappa = 40$ (●), $\kappa = 50$ (●), and $\kappa = 100$ (●). The limiting case of perfectly rigid substrates ($\kappa \rightarrow \infty$) would be represented by a horizontal line $\sigma_{zz} = 0$. (b) The slopes m (●) of linear fits through individual data sets, shown in part (a), as a function of $1/\kappa$ (lower abscissa). The fit incorporates the limiting case of a perfectly rigid substrate with $m(\kappa^{-1} \rightarrow 0) = 0$. Additionally, the slopes m (○) of linear fits through individual data sets of Fig. 5.18 are plotted as a function of the fluid–substrate interaction strength ϵ_{fs} (upper abscissa).

of the best linear fits through individual data sets of Fig. 5.18 are also shown in Fig. 5.20b as a function of the fluid–substrate interaction strength ϵ_{fs} . The data sets of Fig. 5.18 correspond to the situation in which different fluids are confined by pores of the same rigidity ($\kappa = 30$), nevertheless the slopes (\odot) coincide with $m \simeq 29 \times 10^{-4}$ (dashed line) within a reasonable margin of error.

5.7.3 Comparison with Experiment

Prass et al. [26] present experimental sorption strain isotherms for n-pentane, perfluoropentane and water in MCM-41(16). The strain of the liquid-like branches of the isotherms show a logarithmic dependence on the bulk fluid pressure, as predicted by Eq. (5.52), while their slopes coincide and, thus, are independent of the fluid properties which agrees with the results shown in Fig. 5.18. Moreover, a reasonable value for the *pore-load modulus* could be extracted, that is further used as an input parameter in finite element calculations. The calculations reproduce the strain behaviour of a porous matrix of the MCM-type fairly well.

Fig. 9 of [165] presents the experimentally measured strain of liquid-like n-pentane as a function of the bulk fluid pressure on a logarithmic scale for four different MCM-type silicas. Here, the slope decreases with the wall thickness of the silica matrix, that is, with the assumed rigidity of the porous medium. This finding is consistent with the results of Fig. 5.20a.

6

Summary

Several experiments [26, 28, 51–53] point at deformations of nanopores due to the sorption of confined fluids where even rigid substrates, such as metals and silicas of the MCM-type, deform. To investigate the sorption strains of the confining matrix and their influence on the phase behaviour of the confined fluid, we employ a semi-grand canonical ensemble Monte Carlo method, according to sorption experiments in which the system of interest exchanges heat and matter with a bulk fluid reservoir.

We consider a *single* slit-pore where a simple fluid is confined between two parallel plane walls which consist of one *explicitly* treated layer of wall particles. Wall and fluid particles are of the same type, that is, they share the same size and interact via Lennard–Jones(12,6) potentials. The wall particles are not fixed to their lattice sites but bound to them by harmonic potentials. This harmonic potential prevents the wall from melting and mimics the remainder of the solid matrix in an average manner.

By changing the force constant of the harmonic potential, we are able to control the deformability of the wall from an almost rigid structure to more flexible walls. Flexible means that the wall particles can move farther from their lattice sites to react to the fluid to a greater extent. Depending on the deformability of the wall and the fluid–wall interaction, the average pore-size may differ from the distance that lattice sites of opposite walls are separated. Thus, the pore may be in a strained state and the pore strain is calculated as an ensemble average of the positions of the wall particles.

We make contact with sorption experiments of n-pentane in MCM-type silica by

introducing a *degree of confinement*, that is, the ratio of pore volume to wall area, to adjust the slit-pore size of the model according to the experimental system of (nearly) cylindrical pores. With this, we obtain a strain isotherm which is in semi-quantitative agreement with experimental data (cf. Fig. 5.11a), despite the crudeness of the model. In general, the strain is found to be a reaction to the pressure tensor element perpendicular to the walls. It is a well known packing phenomenon [32, 185] that the pressure oscillates if the pore-size is changed within the length scale of a few particle diameters. Consequently, in narrow pores the correlated sorption strain is also dominated by packing effects (cf. Fig. 5.14a), that is, by the exact interplay of fluid and confining geometry.

The strain behaviour is different in larger pores where packing effects are less important: the strain originates from properties of either the fluid or the substrate, depending on the thermodynamic state of the fluid. Changing the fluid–wall interaction strength suggests that the strain course *before* capillary condensation (during the gas-like state of the fluid) is dominated by wetting phenomena: upon fluid adsorption strong wetting leads to a contraction (cf. Fig. 5.16a), unlike the situation in which the substrate is poorly wetted by the fluid which leads to an expansion of the pore (cf. Fig. 5.16c). At capillary condensation the pore contracts discontinuously, which is accompanied by a discontinuous increase in fluid density. This contraction is a reaction to the medium density of the confined fluid, where attraction dominates the interaction of particles, because a similar behaviour is observed in the critical and even in the supercritical temperature regime (cf. Figs. 5.7a–c).

Once the pore is filled with a liquid-like phase, the strain behaviour is qualitatively different: regardless of the fluid properties the strain increases with increasing bulk fluid pressure P/P_0 where a linear dependence on $\ln P/P_0$ is observed (cf. Fig. 5.18). We explain this linear relationship through a simple thermodynamic analysis which results in the quasi-Kelvin equation [cf. Eq. (5.50)]. This equation is almost identical with the celebrated Kelvin equation but it is free of geometrical constraints, such as the existence of a meniscus. The logarithmic pressure dependence is achieved simply by assuming that a confined liquid-like phase is in thermodynamic equilibrium with a bulk reservoir of an ideal gas. Provided that the substrate is Hookean in character, the slope of the strain depends on the stiffness of the substrate and exhibits a nanomechanical property of the porous matrix, i.e., the pore-load modulus (cf. Fig. 5.20a,b). This notion is corroborated by experimental data. [26, 165]

Although the model used is rather crude, the good agreement of the strain behaviour with sorption experiments lets us conclude that it is sufficiently realistic to capture the key features governing the physics of such systems. Unlike the average

net strain of the order 10^{-4} , the *actual* strains appearing during the course of the simulations are much larger, by up to 2–3 orders of magnitude, approximately. These large momentary strains of deformable pores have an impact on the phase behaviour of the confined fluid. To determine the conditions at which capillary condensation occurs, we use the (semi-) grand potential to indicate the phase transition. Since the (semi-) grand potential is not accessible *directly* in the system of interest, we use a perturbational approach for its calculation: we compute the (semi-) grand potential for a reference model of smooth walls and establish a thermodynamic connection between the reference model and the model of interest through a λ -expansion. With the parameter λ the model of interest is (continuously) switched on in the form of a perturbation. The results of this procedure show that the deformability of the walls causes a shift of capillary condensation toward the bulk fluid condensation pressure, i.e. to larger P/P_0 , compared with a rigid pore (cf. Fig. 4.6a,b). This shift is of a few percent and should be experimentally observable *in principle*, although the experimental realisation would be cumbersome.

By using a finite size scaling analysis, the phase diagram of a fluid confined in a flexible pore and in a rigid pore are investigated. Additionally, the critical temperature and the critical density of the bulk fluid are determined: their values are in good agreement with previous studies. In confinement, it is found that the densities of coexisting gas-like and liquid-like phases are smaller if the walls are deformable than when the walls are rigid. This shift to lower densities applies also to the critical point, so that the critical density of the fluid decreases if the confining walls become deformable, whereas the critical temperature remains unaffected (cf. Fig. 4.14).

The discrepancy in phase behaviour reflects the structural changes of the fluid at the molecular level: the structure of the confined fluid is more ordered, that is, the stratification is more pronounced, the more rigid is the confining wall (cf. Fig. 4.15). On the other hand, a wall's rigidity increases with the imbibition of fluid matter which is evident from the Lindemann ratio (cf. Fig. A.4a) and from the strain distribution which becomes narrower and more sharply peaked if fluid is adsorbed (compare Figs. 5.3a and b). Thus, there is a synergistic coupling between the fluid and solid phase where some kind of order and rigidity is mutually induced.

In this context, further theoretical studies would be interesting, in which the fluid–substrate interaction is significantly increased so that the net strain is of the order of the actual strain, i.e., the fluid dominates the strain distribution. A realisation of such a system may be water in MCM-type silicas [26] or water in porous glass [180] whose net strains are of the order 10^{-2} – 10^{-1} .

Bibliography

- [1] W. Nolting. *Grundkurs Theoretische Physik: 6. Statistische Physik* (Springer, 2002), 4th edition. ISBN 3-540-41918-7.
- [2] L. Pusztai. *Reverse Monte Carlo analyses of diffraction data on molecular liquids*. *Novel Approaches to the Structure and Dynamics of Liquids: Experiments, Theories and Simulations* 129–142 (2002). ISBN 1-4020-1846-0.
- [3] Y. G. J. Lau, R. M. Richardson, and R. Cubitt. *Smectic order induced at homeotropically aligned nematic surfaces: A neutron reflection study*. *J. Chem. Phys.* **124**: 234 910–234 919 (2006).
- [4] M. J. Sammon and J. A. N. Zasadzinski. *Electron-microscope observation of the smectic–nematic transition in a lyotropic liquid crystal*. *Phys. Rev. Lett.* **57**(22): 2834–2837 (1986).
- [5] H. Steuer, S. Hess, and M. Schoen. *Phase behavior of liquid crystals confined by smooth walls*. *Phys. Rev. E* **69**: 031 708 (2004).
- [6] A. P. Jephcoat, H. k. Mao, L. W. Finger, D. E. Cox, R. J. Hemley, and C. s. Zha. *Pressure-induced structural phase transitions in solid xenon*. *Phys. Rev. Lett.* **59**(23): 2670–2673 (1986).
- [7] W. W. Wood and J. D. Jacobson. *Preliminary results from a recalculation of the Monte Carlo equation of state of hard spheres*. *J. Chem. Phys.* **27**: 1207–1208 (1957).
- [8] B. J. Alder and T. E. Wainwright. *Phase transition for a hard sphere system*. *J. Chem. Phys.* **27**: 1208–1209 (1957).
- [9] H. Reiss and A. D. Hammerich. *Hard spheres: Scaled particle theory and exact relations on the existence and structure of the fluid/solid phase transition*. *J. Phys. Chem.* **90**: 6252–6260 (1986).

- [10] P. A. Monson and D. A. Kofke. *Solid–fluid equilibrium: Insights from simple molecular models*. *Advances in Chemical Physics* **115**: 113 (2000).
- [11] A. Hinchliffe. *Molecular Modelling for Beginners* (John Wiley and Sons, West Sussex, 2003).
- [12] L. D. Landau and E. M. Lifschitz. *Lehrbuch der Theoretischen Physik V: Statistische Physik, Teil 1* (Verlag Harri Deutsch, Frankfurt am Main, 2008). ISBN 978-3-8171-1330-9.
- [13] T.-W. Kim, I.-S. Park, and R. Ryoo. *A synthetic route to ordered mesoporous carbon materials with graphitic pore walls*. *Angew. Chem. Int. Ed.* **42**: 4375–4379 (2003).
- [14] R. Tenne. *Fortschritte bei der Synthese anorganischer Nanoröhren und Fulleren-artiger Nanopartikel*. *Angew. Chem.* **115**: 5280–5289 (2003).
- [15] B. L. Newalkar, S. Komarneni, and H. Katsuki. *Rapid synthesis of mesoporous SBA-15 molecular sieve by a microwave-hydrothermal process*. *Chem. Commun.* **23**: 2389–2390 (2000).
- [16] M. E. Davis. *Ordered porous materials for emerging applications*. *Nature* **417**: 813–821 (2002).
- [17] J. Weissmüller, R. C. Newman, H.-J. Jin, A. M. Hodge, and J. W. Kysar. *Nanoporous metals by alloy corrosion: Formation and mechanical properties*. *MRS Bull.* **34**(8): 577–586 (2009).
- [18] Z. Hu and A. M. Jonas. *Control of crystal orientation in soft nanostructures by nanoimprint lithography*. *Soft Matter* **6**: 21–28 (2010).
- [19] M. Thommes, R. Köhn, and M. Fröba. *Sorption and pore condensation behavior of pure fluids in mesoporous MCM-48 silica, MCM-41 silica, SBA-15 silica and controlled-pore glass at temperatures above and below the bulk triple point*. *Applied Surface Science* **196**: 239–249 (2002).
- [20] A. Sayari and Y. Yang. *SBA-15 templated mesoporous carbon: New insights into the SBA-15 pore structure*. *Chem. Mater.* **17**: 6108–6113 (2005).
- [21] D. Zhao, J. Feng, Q. Huo, N. Melosh, G. H. Fredrickson, B. F. Chmelka, and G. D. Stucky. *Triblock copolymer syntheses of mesoporous silica with periodic 50 to 300 Angstrom pores*. *Science* **279**: 548–552 (1998).

Bibliography

- [22] D. Zhao, Q. Huo, J. Feng, B. F. Chmelka, and G. D. Stucky. *Nonionic triblock and star diblock copolymer and oligomeric surfactant syntheses of highly ordered, hydrothermally stable, mesoporous silica structures*. *J. Am. Chem. Soc.* **120**(24): 6024–6036 (1998).
- [23] T. Hofmann, D. Wallacher, P. Huber, R. Birringer, K. Knorr, A. Schreiber, and G. H. Findenegg. *Small-angle X-ray diffraction of Kr in mesoporous silica: Effects of microporosity and surface roughness*. *Physical Review B* **72**: 064 122 (2005).
- [24] M. Kruk, M. Jaroniec, Y. Sakamoto, O. Terasaki, R. Ryoo, and C. H. Ko. *Determination of pore size and pore wall structure of MCM-41 by using nitrogen adsorption, transmission electron microscopy, and X-ray diffraction*. *J. Phys. Chem. B* **104**: 292–301 (2000).
- [25] R. Ryoo, C. H. Ko, M. Kruk, V. Antochshuk, and M. Jaroniec. *Block-copolymer-templated ordered mesoporous silica: Array of uniform mesopores or mesopore-micropore network?*. *J. Phys. Chem. B* **104**: 11 465–11 471 (2000).
- [26] J. Prass, D. Mütter, P. Fratzl, and O. Paris. *Capillarity-driven deformation of ordered nanoporous silica*. *Appl. Phys. Lett.* **95**: 083 121 (2009).
- [27] G. Zickler, S. Jaehnert, W. Wagermaier, S. Funari, G. Findenegg, and O. Paris. *Physisorbed films in periodic mesoporous silica studied by in situ synchrotron small-angle diffraction*. *Physical Review B* **73**: 184 109 (2006).
- [28] G. Zickler, S. Jaehnert, S. Funari, G. Findenegg, and O. Paris. *Pore lattice deformation in ordered mesoporous silica studied by in situ small-angle X-ray diffraction*. *J. Appl. Cryst.* **40**: s522–s526 (2007).
- [29] H.-Y. Kim, S. M. Gatica, G. Stan, and M. Cole. *Effects of substrate relaxation on adsorption in pores*. *J. Low Temp. Phys.* **156**(1-2): 1–8 (2009).
- [30] S. M. Gatica and H.-Y. Kim. *Condensation of fluids confined in non-rigid nanopores: With a little help from the substrate*. *J. Low Temp. Phys.* **157**(3-4): 382–394 (2009).
- [31] L. D. Gelb, K. E. Gubbins, R. Radhakrishnan, and M. Sliwinska-Bartkowiak. *Phase separation in confined systems*. *Rep. Prog. Phys.* **62**: 1573–1659 (1999).
- [32] M. Schoen and S. H. L. Klapp. *Nanoconfined fluids. Soft matter between two and three dimensions* (John Wiley and Sons, New York, 2007).

- [33] G. H. Findenegg, S. Jähnert, D. Akcakayiran, and A. Schreiber. *Freezing and melting of water confined in silica nanopores*. ChemPhysChem **9**: 2651–2659 (2008).
- [34] S. Jähnert, F. V. Chávez, G. E. Schaumann, A. Schreiber, M. Schönhoff, and G. H. Findenegg. *Melting and freezing of water in cylindrical silica nanopores*. Phys. Chem. Chem. Phys. **10**: 6039–6051 (2008).
- [35] K. B. Jinesh and J. W. M. Frenken. *Capillary condensation in atomic scale friction: How water acts like a glue*. Phys. Rev. Lett. **96**: 166 103 (2006).
- [36] J. Dore, B. Webber, D. Montague, and T. Hansen. *Structural change and nucleation characteristics of water/ice in confined geometry*. Novel Approaches to the Structure and Dynamics of Liquids: Experiments, Theories and Simulations 143–156 (2002). ISBN 1-4020-1846-0.
- [37] K. Binder, J. Horbach, A. Milchev, M. Müller, and R. Vink. *Monte Carlo simulations of phase transitions of systems in nanoscopic confinement*. Computer Physics Communications **177**(1-2): 140–145 (2007).
- [38] M. Schoen. *Fluid bridges confined between chemically nanopatterned solid substrates*. Phys. Chem. Chem. Phys. **10**: 223–256 (2008).
- [39] B. S. Liu, D. F. Xu, J. X. Chu, W. Liu, and C. T. Au. *Deep desulfurization by the adsorption process of fluidized catalytic cracking (FCC) diesel over mesoporous Al-MCM-41 materials*. Energy & Fuels **21**: 250–255 (2007).
- [40] R. Rockmann, G. Kalies, and O. Klepel. *Liquid-phase adsorption experiments on ordered mesoporous silicas*. Adsorption **13**(5-6): 515–522 (2007).
- [41] M. Vallet-Regí, F. Balas, M. Colilla, and M. Manzano. *Bioceramics and pharmaceuticals: A remarkable synergy*. Solid State Sciences **9**: 768–776 (2007).
- [42] D. M. Ford, E. E. Simanek, and D. F. Shantz. *Engineering nanospaces: Ordered mesoporous silicas as model substrates for building complex hybrid materials*. Nanotechnology **16**: 458–475 (2005).
- [43] D. Brunel, A. C. Blanc, A. Galarneau, and F. Fajula. *New trends in the design of supported catalysts on mesoporous silicas and their applications in fine chemicals*. Catalysis Today **73**: 139–152 (2002).

Bibliography

- [44] I. Gerlach, M. Kawase, and K. Miura. *In-Situ preparation of supported precious metal and metal oxide nanoparticles by nanoreactor flash pyrolysis*. *Microporous and Mesoporous Materials* **122**(1-3): 79–86 (2009).
- [45] G. S. Chai, S. B. Yoon, J.-S. Yu, J.-H. Choi, and Y.-E. Sung. *Ordered porous carbons with tunable pore sizes as catalyst supports in direct methanol fuel cell*. *J. Phys. Chem. B* **108**(22): 7074–7079 (2004).
- [46] J. C. T. Eijkel and A. van den Berg. *Nanotechnology for membranes, filters and sieves*. *Lab Chip* **6**: 19–23 (2006). DOI: 10.1093/b516903h.
- [47] S. Kuiper, C. van Rijn, W. Nijdam, O. Raspe, H. van Wolferen, G. Krijnen, and M. Elwenspoek. *Filtration of lager beer with microsieves: flux, permeate haze and in-line microscope observations*. *Journal of Membrane Science* **196**(2): 159–170 (2002).
- [48] A. Calvo, B. Yameen, F. J. Williams, G. J. A. A. Soler-Illia, and O. Azzaroni. *Mesoporous films and polymer brushes helping each other to modulate ionic transport in nanoconfined environments. An interesting example of synergism in functional hybrid assemblies*. *J. Am. Chem. Soc.* **131**: 10 866–10 868 (2009).
- [49] D. K. Dysthe and R. A. Wogelius. *Confined fluids in the earth's crust—Properties and processes*. *Chemical Geology* **230**: 175–181 (2006).
- [50] R. Evans and A. O. Parry. *Liquids at interfaces: What can a theorist contribute?*. *J. Phys.: Condens. Matter* **2**: SA15–SA32 (1990). DOI: 10.1088/0953-8984/2/S/003.
- [51] J. Biener, A. Wittstock, L. A. Zepeda-Ruiz, M. M. Biener, V. Zielasek, D. Kramer, R. N. Viswanath, J. Weissmüller, M. Bäumer, and A. V. Hamza. *Surface-chemistry-driven actuation in nanoporous gold*. *Nature Materials* **8**: 47–51 (2009).
- [52] J. Weissmüller, R. N. Viswanath, D. Kramer, P. Zimmer, R. Würschum, and H. Gleiter. *Charge-induced reversible strain in a metal*. *Science* **300**: 312–315 (2003).
- [53] E. Hoinkis. *Small-angle scattering studies of adsorption and of capillary condensation in porous solids*. *Part. Part. Syst. Charact.* **21**: 80–100 (2004).
- [54] N. Mitarai and F. Nori. *Wet granular materials*. *Advances in Physics* **55**(1-2): 1–45 (2006).

- [55] M. Thommes, G. H. Findenegg, and M. Schoen. *Critical depletion of a pure fluid in controlled-pore glass. Experimental results and grand canonical ensemble Monte Carlo simulation*. *Langmuir* **11**(6): 2137 (1995).
- [56] H. B. Callen. *Thermodynamics* (John Wiley and Sons, New York, 1966). ISBN-13: 978-0471130352.
- [57] J. W. Gibbs. *Elementary principles in statistical mechanics* (Charles Scribener's sons, New York, 1902).
- [58] M. Plischke and B. Bergersen. *Equilibrium statistical physics* (World Scientific, 1994), 2nd edition. ISBN 9810216424.
- [59] D. A. McQuarrie. *Statistical Mechanics* (University Science Books, 2000), 2nd edition. ISBN 1891389157.
- [60] R. K. Pathria. *Statistical Mechanics* (Elsevier, Oxford, 1996), 2nd edition. ISBN 0 7506 2469 8.
- [61] W. Heisenberg. *Über den anschaulichen Inhalt der quantentheoretischen Kinematik und Mechanik*. *Z. Phys.* **43**: 172–198 (1927).
- [62] D. Henderson. *Fundamentals of inhomogeneous fluids* (Marcel Dekker, New York, 1992).
- [63] J. M. Ziman. *Models of disorder: The theoretical physics of homogeneously disordered systems* (Cambridge University Press, Cambridge, 1979). ISBN 0 521 21784 9.
- [64] A. K. Soper. *On the determination of the pair correlation function from liquid structure factor measurements*. *Chemical Physics* **107**(1): 61–74 (1986).
- [65] R. J. Baxter. *Exactly Solved Models in Statistical Mechanics* (Academic Press, London, 1982). ISBN 0 12 083180 5.
- [66] T. L. Hill. *An Introduction to statistical Thermodynamics* (Dover, New York, 1960).
- [67] J. D. van der Waals. *Die Continuitaet des gasfoermigen und fluessigen Zustandes* (Verlag von J. A. Barth, Leipzig, 1899). 2nd edition.
- [68] J. M. Seminario. *Recent Developments and Applications of Modern Density Functional Theory* (Elsevier, Amsterdam, 1996). ISBN 0 444 82404 9.

Bibliography

- [69] M. P. Allen and D. J. Tildesley. *Computer Simulation of Liquids* (Oxford Science Publications, Oxford, 2001). ISBN 0 19 855645 4.
- [70] N. Metropolis, A. W. Rosenbluth, M. N. Rosenbluth, A. H. Teller, and E. Teller. *Equation of state calculations by fast computing machines*. J. Chem. Phys. **21**(6): 1087–1092 (1953).
- [71] J. von Neumann and R. Richtmyer. *LAMS-551: Statistical methods in neutron diffusion*. Analogies Between Analogies: The Mathematical Reports of S. M. Ulam and his Los Alamos Collaborators (1947).
- [72] N. Metropolis and S. Ulam. *The Monte Carlo method*. Journal of the American Statistical Association **44**(247): 335–341 (1949).
- [73] A. A. Markov. *An example of statistical investigation of the text Eugene Onegin concerning the connection of samples in chains*. Science in Context **19**(4): 591–600 (2006). Translation of a lecture in 1913.
- [74] R. C. Tolman. *The Principles of statistical mechanics* (Dover, New York, 1978). ISBN 0-486-63896-0.
- [75] M. Schoen, D. J. Diestler, and J. H. Cushman. *Fluids in mesopores. I. Structure of a simple classical fluid in a slit-pore*. J. Chem. Phys. **87**(9): 5464–5476 (1987).
- [76] D. Frenkel and B. Smit. *Understanding Molecular Simulation. From Algorithms to Applications* (Academic Press, London, 2002). 2nd edition.
- [77] W. K. Hastings. *Monte Carlo sampling methods using Markov chains and their applications*. Biometrika **57**(1): 97–109 (1970).
- [78] P. G. Bolhuis, D. Chandler, C. Dellago, and P. L. Geissler. *Transition path sampling: Throwing ropes over rough mountain passes, in the dark*. Annu. Rev. Phys. Chem. **53**: 291–318 (2002).
- [79] N. Muroyama, T. Ohsuna, R. Ryoo, Y. Kubota, and O. Terasaki. *An analytical approach to determine the pore shape and size of MCM-41 materials from X-ray diffraction data*. J. Phys. Chem. B **110**: 10 630–10 635 (2006).
- [80] B. Coasne, A. Grosman, C. Ortega, and M. Simon. *Adsorption in noninterconnected pores open at one or at both ends: A reconsideration of the origin of the hysteresis phenomenon*. Phys. Rev. Lett. **88**(25): 256 102 (2002).

- [81] A. Grosman and C. Ortega. *Nature of capillary condensation and evaporation processes in ordered porous materials*. *Langmuir* **21**(23): 10 515–10 521 (2005).
- [82] A. Grosman and C. Ortega. *Capillary condensation in porous materials. Hysteresis and interaction mechanism without pore blocking/percolation process*. *Langmuir* **24**: 3977–3986 (2008).
- [83] A. Grosman and C. Ortega. *Influence of elastic strains on the adsorption process in porous materials. Thermodynamics and experiment*. *Applied Surface Science* **25** (2010). In press, doi:10.1016/j.apsusc.2009.12.098.
- [84] M. Erko, D. Wallacher, A. Brandt, and O. Paris. *In-situ small-angle neutron scattering study of pore filling and pore emptying in ordered mesoporous silica*. *J. Appl. Cryst.* **43**: 1–7 (2010). DOI: 10.1107/S0021889809044112.
- [85] Z. Bochyński and H. Drozdowski. *X-ray scattering in liquid pentane*. *Physics and Chemistry of Liquids* **39**(2): 189–199 (2001).
- [86] H. Haken and H. C. Wolf. *The Physics of Atoms and Quanta* (Springer Verlag, Berlin, 2004), 6th edition.
- [87] M. Jaroniec and L. A. Solovyov. *Improvement of the Kruk-Jaroniec-Sayari method for pore size analysis of ordered silicas with cylindrical mesopores*. *Langmuir* **22**(16): 6757–6760 (2006).
- [88] M. Kruk, M. Jaroniec, and A. Sayari. *Application of large pore MCM-41 molecular sieves to improve pore size analysis using nitrogen adsorption measurements*. *Langmuir* **13**(23): 6267–6273 (1997).
- [89] T. K. Wei. *Nanoporous Materials: Science and Engineering* (Imperial College Press, London, 2004). Chapter 11.
- [90] P. C. Ball and R. Evans. *Temperature dependence of gas adsorption on a mesoporous solid: Capillary criticality and hysteresis*. *Langmuir* **5**(3): 714–723 (1989).
- [91] W. L. Jorgensen, J. D. Madura, and C. J. Swenson. *Optimized intermolecular potential functions for liquid hydrocarbons*. *J. Am. Chem. Soc.* **106**: 6638–6646 (1984).
- [92] J. E. Lennard-Jones. *Cohesion*. *Proc. Phys. Soc.* **43**(5): 31 (1931).

Bibliography

- [93] F. London. *Zur Theorie und Systematik der Molekularkräfte*. *Zeitschrift für Physik* **63**: 245–279 (1930).
- [94] A. Vishnyakov and A. V. Neimark. *Studies of liquid-vapor equilibria, criticality, and spinodal transition in nanopores by the Gauge Cell Monte Carlo simulation method*. *J. Phys. Chem. B* **105**: 7009–7020 (2001).
- [95] P. Kowalczyk, A. Ciach, and A. V. Neimark. *Adsorption-induced deformation of microporous carbons: Pore size distribution effect*. *Langmuir* **24**: 6603–6608 (2008).
- [96] P. Demontis and G. B. Suffritti. *Structure and dynamics of zeolites investigated by molecular dynamics*. *Chem. Rev.* **97**: 2845–2878 (1997).
- [97] W. L. Jorgensen. *Optimized intermolecular potential functions for liquid alcohols*. *J. Phys. Chem.* **90**: 1276–1284 (1986).
- [98] W. L. Jorgensen and J. Tirado-Rives. *The OPLS potential functions for proteins. Energy minimizations for crystals of cyclic peptides and crambin*. *J. Am. Chem. Soc.* **110**(6): 1657–1666 (1988).
- [99] W. Song, P. J. Rossky, and M. Maroncelli. *Modeling alkane+perfluoralkane interactions using all-atom potentials: Failure of the usual combining rules*. *J. Chem. Phys.* **119**(17): 9145–9162 (2003).
- [100] A. Loiruangsinsin, S. Fritzsche, and S. Hannongbua. *Newly developed ab initio potentials for molecular dynamics simulations of n-pentane in the zeolite silicate-I*. *Chemical Physics Letters* **390**: 485–490 (2004).
- [101] F. Cuadros, I. Cachadina, and W. Ahumada. *Determination of Lennard–Jones interaction parameters using a new procedure*. *Molecular Engineering* **6**: 319–325 (1996).
- [102] D. Janssen, R. D. Palma, S. Verlaak, P. Heremans, and W. Dehaen. *Static solvent contact angle measurements, surface free energy and wettability determination of various self-assembled monolayers on silicon dioxide*. *Thin Solid Films* **515**(4): 1433–1438 (2006).
- [103] I. Wong and C.-M. Ho. *Surface molecular property modifications for poly(dimethylsiloxane)(PDMS) based microfluidic devices*. *Physical Review E* **7**: 291–306 (2009).

- [104] A.-S. Duwez. *Exploiting electron spectroscopies to probe the structure and organization of self-assembled monolayers: A review*. Journal of Electron Spectroscopy and Related Phenomena **134**(2-3): 97–138 (2004).
- [105] D. J. Diestler and M. Schoen. *Fluids in micropores. V. Effects of thermal motion in the walls of a slit-micropore*. J. Chem. Phys. **104**(17): 6784–6795 (1996).
- [106] D. Berthelot. *Sur le melange des gaz*. C. R. Hebd. Seances Acad. Sci. **126**: 1857–1858 (1898).
- [107] J.-L. Barrat and J.-P. Hansen. *Basic concepts for simple and complex liquids* (Cambridge University Press, Cambridge, 2003). ISBN 0-521-78344-5.
- [108] O. Pizio, A. Patrykiewicz, and S. Sokolowski. *Phase behavior of Lennard–Jones fluids in slit-like pores with walls modified by preadsorbed molecules: A density functional approach*. J. Phys. Chem. C **111**(43): 15 743–15 751 (2007).
- [109] S. Jähnert. *Untersuchung von reinen Stoffen in periodisch mesoporösen Silikamaterialien mit thermophysikalischen Methoden und in-situ Röntgenkleinwinkelstreuung* (2008). <http://opus.kobv.de/tuberlin/volltexte/2008/1869/>.
- [110] L. D. Gelb. *The ins and outs of capillary condensation in cylindrical pores*. Mol. Phys. **100**(13): 2049–2057 (2002).
- [111] V. Krakoviack, E. Kierlik, M.-L. Rosinberg, and G. Tarjus. *Adsorption of a fluid in an aerogel: Integral equation approach*. J. Chem. Phys. **115**(24): 11 289–11 298 (2001).
- [112] B. Coasne, F. R. Hung, R. J.-M. Pellenq, F. R. Siperstein, and K. E. Gubbins. *Adsorption of simple gases in MCM-41 materials: The role of surface roughness*. Langmuir **22**: 194–202 (2006).
- [113] B. Coasne, A. Galarneau, F. D. Renzo, and R. J. M. Pellenq. *Gas adsorption in mesoporous micelle-templated silicas: MCM-41, MCM-48, and SBA-15*. Langmuir **22**: 194–202 (2006).
- [114] C. G. Sonwane, C. W. Jones, and P. J. Ludovice. *A model for the structure of MCM-41 incorporating surface roughness*. J. Phys. Chem. B **109**(49): 23 395–23 404 (2005).
- [115] J. Keller and R. Staudt. *Gas adsorption equilibria: Experimental methods and adsorptive isotherms* (Springer Science, New York, 2005).

Bibliography

- [116] K. W. Kolasinski. *Surface Science: Foundations of catalysis and nanoscience* (John Wiley & Sons, West Sussex, England, 2008), 2nd edition.
- [117] P. I. Ravikovitch, S. C. Ó Domhnaill, A. V. Neimark, F. Schüth, and K. K. Unger. *Capillary hysteresis in nanopores: Theoretical and experimental studies of nitrogen adsorption on MCM-41*. *Langmuir* **11**: 4765–4772 (1995).
- [118] M. Schoen, C. Rhykerd, J. Cushman, and D. Diestler. *Slit-pore sorption isotherms by the grand-canonical Monte Carlo method—Manifestations of hysteresis*. *Mol. Phys.* **66**(6): 1171–1182 (1989).
- [119] R. W. Zwanzig. *High-temperature equation of state by a perturbation method. I. Nonpolar gases*. *J. Chem. Phys.* **22**(8): 1420–1426 (1954).
- [120] S. Sacquin-Mora, A. H. Fuchs, and M. Schoen. *Torsion-induced phase transitions in fluids confined between chemically decorated substrates*. *J. Chem. Phys.* **121**(18): 9077–9086 (2004).
- [121] M. Schoen, J. H. Cushman, and D. J. Diestler. *Anomalous diffusion in confined monolayer films*. *Mol. Phys.* **81**(2): 475–490 (1994).
- [122] W. A. Steele. *The physical interaction of gases with crystalline solids*. *Surface Science* **36**: 317 (1973).
- [123] F. F. Abraham. *The interfacial density profile of a Lennard–Jones fluid in contact with a (100) Lennard–Jones wall and its relationship to idealized fluid/wall systems: A Monte Carlo simulation*. *J. Chem. Phys.* **68**(8): 3713–3716 (1978).
- [124] J. P. Hansen and I. R. McDonald. *Theory of simple liquids* (Academic Press, London, 1986).
- [125] W. H. Press, B. P. Flannery, S. A. Teukolsky, and W. T. Vetterling. *Numerical recipes. The art of scientific computing (FORTRAN version)* (1996).
- [126] R. Mokaya. *Improving the stability of mesoporous MCM-41 silica via thicker more highly condensed pore walls*. *J. Phys. Chem. B* **103**(46): 10 204–10 208 (1999).
- [127] A. Grosman and C. Ortega. *Influence of elastic strains on the adsorption process in porous materials: An experimental approach*. *Langmuir* **25**: 8083 (2009).

- [128] P. Röcken and P. Tarazona. *Capillary condensation in structured pores*. J. Chem. Phys. **105**(5): 2034–2043 (1996).
- [129] E. A. Ustinov and D. D. Do. *Effect of adsorption deformation on thermodynamic characteristics of a fluid in slit pores at sub-critical conditions*. Carbon **44**(13): 2652–2663 (2006).
- [130] D. P. Landau and K. Binder. *A Guide to Monte Carlo Simulations in Statistical Physics* (Cambridge University Press, Cambridge, 2000). ISBN 0 521 65366 5.
- [131] N. B. Wilding. *Critical-point and coexistence-curve properties of the Lennard–Jones fluid: A finite-size scaling study*. Physical Review E **52**(1): 602–610 (1995).
- [132] J. E. Hunt and W. P. Reinhardt. *Finite-size scaling behaviour of the free energy barrier between coexisting phases: Determination of the critical temperature and interfacial tension of the Lennard–Jones fluid*. J. Chem. Phys. **103**: 8627–8637 (1995).
- [133] P. Christe and M. Henkel. *Introduction to Conformal Invariance and Its Applications to Critical Phenomena* (Springer-Verlag, Berlin, 1993). ISBN: 3-540-56504-3.
- [134] J. M. Yeomans. *Statistical Mechanics of Phase Transitions* (Oxford Science Publications, Oxford, 1992). ISBN 0-19-851730-0.
- [135] N. B. Wilding and A. D. Bruce. *Density fluctuations and field mixing in the critical fluid*. J. Phys.: Condens. Matter **4**: 3087–3108 (1992).
- [136] M. Rovere, D. W. Heermann, and K. Binder. *The gas–liquid transition of the two-dimensional Lennard–Jones fluid*. J. Phys.: Condens. Matter **2**: 7009–7032 (1990).
- [137] W. Rzysko, J. J. de Pablo, and S. Sokolowski. *Critical behaviour of simple fluids confined by microporous materials*. J. Chem. Phys. **113**(21): 9772–9777 (2000).
- [138] N. R. Council. *Condensed-Matter Physics* (National Academy Press, Washington, D.C., 1986).
- [139] D. I. Uzunov. *Theory of Critical Phenomena* (World Scientific, Singapore, 1993). ISBN-13: 981-02-0389-6.

Bibliography

- [140] N. B. Wilding. *Simulation studies of fluid critical behaviour*. J. Phys.: Condens. Matter **9**: 585–612 (1997).
- [141] A. Z. Panagiotopoulos. *Molecular simulation of phase coexistence: Finite-size effects and determination of critical parameters for two- and three-dimensional Lennard–Jones fluids*. International Journal of Thermophysics **15**(6): 1057–1072 (1994).
- [142] B. Smit. *Phase diagrams of Lennard–Jones fluids*. J. Chem. Phys. **96**(11): 8639–8640 (1992).
- [143] A. Lotfi, J. Vrabec, and J. Fischer. *Vapour liquid equilibria of the Lennard–Jones fluid from the NpT plus test particle method*. J. Mol. Phys. **76**(6): 1319–1333 (1992).
- [144] E. V. Votyakov and Y. K. Tovbin. *A theoretical study of the phase diagrams of simple fluids confined within narrow pores*. Langmuir **15**(18): 5713–5721 (1999).
- [145] I. K. Snook and W. van Megen. *Solvation forces in simple dense fluids. I*. J. Chem. Phys. **72**(5): 2907–2913 (1980).
- [146] A. Huerta, O. Pizio, and S. Sokolowski. *Phase transitions in an associating, network-forming, Lennard–Jones fluid in slit-like pores. II. Extension of the density functional method*. J. Chem. Phys. **112**: 4286–4295 (2000).
- [147] S. T. Cui, P. T. Cummings, and H. D. Cochran. *Structural transition and solid-like behaviour of alkane films confined in nano-spacing*. Fluid Phase Equilib. **183**: 381–387 (2001).
- [148] T. M. Truskett, P. G. Debenedetti, and S. Torquato. *Thermodynamic implications of confinement for a waterlike fluid*. J. Chem. Phys. **114**: 2401–2418 (2001).
- [149] M. Schoen, J. H. Cushman, D. J. Diestler, and C. L. Rhykerd. *Fluids in micropores. II. Self-diffusion in a simple classical fluid in a slit pore*. J. Chem. Phys. **88**(2): 1394–1406 (1988).
- [150] D. P. Cao, X. R. Zhang, Z. G. Shen, J. F. Chen, and J. Yun. *Density functional theory of adsorption and phase behavior of the Lennard–Jones fluids confined in MCM-41 with a finite thickness*. Colloids. Surf. A Physicochem. Eng. Aspects **247**: 91–98 (2004).

- [151] A. Valencia and R. Lipowsky. *Nucleation through a double barrier on a chemically patterned substrate*. *Langmuir* **20**: 1986–1996 (2004).
- [152] M. Schoen and S. Dietrich. *Structure of a hard-sphere fluid in hard wedges*. *Phys. Rev. E* **56**: 499–510 (1997).
- [153] A. O. Parry, C. Rascón, N. B. Wilding, and R. Evans. *Condensation in a capped capillary is a continuous critical phenomenon*. *Phys. Rev. Lett* **98**: 226 101 (2007).
- [154] H. Bohlen, A. O. Parry, E. Díaz-Herrera, and M. Schoen. *Intrusion of fluids into nanogrooves—How geometry determines the shape of the gas–liquid interface*. *Eur. Phys. J. E* **25**: 103–115 (2008).
- [155] F. Bresme, E. Chacón, P. Tarazona, and K. Tay. *Intrinsic structure of hydrophobic surfaces: The oil–water interface*. *Phys. Rev. Lett.* **101**: 056 102 (2008).
- [156] F. Bresme, E. Chacón, and P. Tarazona. *Molecular dynamics investigation of the intrinsic structure of water–fluid interfaces via the intrinsic sampling method*. *Phys. Chem. Chem. Phys.* **10**: 4704–4715 (2008).
- [157] D. Morineau and C. Alba-Simionesco. *Liquids in confined geometry: How to connect changes in the structure factor to modifications of local order*. *J. Chem. Phys.* **118**(20): 9389 (2003).
- [158] M. Sliwinska-Bartkowiak, R. Sikorski, R. Gras, R. Radhakrishnan, and K. E. Gubbins. *Melting/freezing behavior of a fluid confined in porous glasses and MCM-41: Dielectric spectroscopy and molecular simulation*. *J. Chem. Phys.* **114**(2): 950 (2001).
- [159] X. Guo and U. Riebel. *Theoretical direct correlation function for two-dimensional fluids of monodisperse hard spheres*. *J. Chem. Phys.* **125**: 144 504 (2006).
- [160] S. Toxvaerd. *The structure and thermodynamics of a solid–fluid interface*. *J. Chem. Phys.* **74**(3): 1998–2005 (1981).
- [161] R. Lupton. *Statistics in Theory and Practice* (Princeton University Press, Princeton, 1993). ISBN 0 691 07429 1.

Bibliography

- [162] G. Günther, J. Prass, O. Paris, and M. Schoen. *Novel insights into nanopore deformation caused by capillary condensation*. Phys. Rev. Lett. **101**: 086 104 (2008).
- [163] D. A. Skoog and J. J. Leary. *Instrumentelle Analytik* (Springer-Verlag, Berlin, 1996).
- [164] C. Koch, I. Ovid'ko, S. Seal, and S. Veprek. *Structural Nanocrystalline Materials: Fundamentals and Applications* (Cambridge University Press, Cambridge, 2007).
- [165] M. Schoen, O. Paris, G. Günther, D. Mütter, and J. Prass. *Pore-lattice deformations in ordered mesoporous matrices: Experimental studies and theoretical analysis*. Phys. Chem. Chem. Phys. (2010). DOI: 10.1039/C000782J.
- [166] H. Namatsu, K. Kurihara, M. Nagase, K. Iwadate, and K. Murase. *Dimensional limitations of silicon nanolines resulting from pattern distortion due to surface tension of rinse water*. Appl. Phys. Lett. **66**(20): 2655 (1995).
- [167] T. Herman, J. Day, and J. Beamish. *Deformation of silica aerogel during fluid adsorption*. Physical Review B **73**: 094 127 (2006).
- [168] G. Reichenauer. *New insights and characterization methods through sol-gel derived porous solids*. Part. Part. Syst. Charact. **21**: 117–127 (2004).
- [169] G. Reichenauer and G. W. Scherer. *Nitrogen sorption in aerogels*. Journal of Non-Crystalline Solids **285**: 167–174 (2001).
- [170] G. Reichenauer and G. W. Scherer. *Nitrogen adsorption in compliant materials*. Journal of Non-Crystalline Solids **277**: 162–172 (2000).
- [171] R. Pirard and J.-P. Pirard. *Aerogel compression theoretical analysis*. Journal of Non-Crystalline Solids **212**: 262–267 (1997).
- [172] L. Duffours, T. Woignier, and J. Phalippou. *Irreversible volume shrinkage of silica aerogels under isostatic pressure*. Journal of Non-Crystalline Solids **194**: 283–290 (1996).
- [173] G. W. Scherer, D. M. Smith, and D. Stein. *Deformation of aerogels during characterization*. Journal of Non-Crystalline Solids **186**: 309–315 (1995).
- [174] D. M. Smith, G. W. Scherer, and J. M. Anderson. *Shrinkage during drying of silica gel*. Journal of Non-Crystalline Solids **188**: 191–206 (1995).

- [175] J. Shen and P. Monson. *A molecular model of adsorption in a dilute semiflexible porous network*. *Mol. Phys.* **100**(13): 2031–2039 (2002).
- [176] G. B. (Editor). *Supercritical Fluids as Solvents and Reaction Media* (Elsevier B.V., Amsterdam, 2004). Chapter 3.1.
- [177] G. Dolino, D. Bellet, and C. Faivre. *Adsorption strains in porous silicon*. *Phys. Rev. B* **54**(24): 17 919–17 929 (1996).
- [178] G. W. Scherer. *Dilatation of porous glass*. *J. Am. Ceram. Soc.* **69**(6): 473–480 (1986).
- [179] S. G. Ash, D. H. Everett, and C. Radke. *Thermodynamics of the effects of adsorption on interparticle forces*. *J. Chem. Soc., Faraday Trans. 2* **69**: 1256–1277 (1973).
- [180] G. Y. Gor and A. V. Neimark. *Adsorption-induced deformation of mesoporous solids*. *Langmuir* **26**(16): 13 021–13 027 (2010).
- [181] P. B. Balbuena, D. Berry, and K. E. Gubbins. *Solvation pressures for simple fluids in micropores*. *J. Phys. Chem.* **97**: 937–943 (1993).
- [182] P. I. Ravikovitch and A. V. Neimark. *Density functional theory model of adsorption deformation*. *Langmuir* **22**(26): 10 864–10 868 (2006).
- [183] S. H. L. Klapp, Y. Zeng, D. Qu, and R. von Klitzing. *Surviving structure in colloidal suspensions squeezed from 3d to 2d*. *PRL* **100**: 118 303 (2008).
- [184] S. Grandner and S. H. L. Klapp. *Freezing of charged colloids in slit pores*. *J. Chem. Phys.* **129**: 244 703 (2008).
- [185] J. Israelachvili. *Solvation force and liquid structure, as probed by direct force measurement*. *Acc. Chem. Res.* **20**: 415–421 (1987).
- [186] M. L. Gee, P. M. McGuiggan, and J. N. Israelachvili. *Liquid to solidlike transitions of molecularly thin films under shear*. *J. Chem. Phys.* **93**(3): 1895–1906 (1990).
- [187] R. Evans, J. R. Henderson, D. C. Hoyle, A. O. Parry, and Z. A. Sabeur. *Asymptotic decay of liquid structure: Oscillatory liquid–vapour density profiles and the Fisher–Widom line*. *Mol. Phys.* **80**(4): 755–775 (1993).

Bibliography

- [188] M. Schoen. *On the uniqueness of stratification-induced structural transformations in confined films*. Ber. Bunsenges. Phys. Chem. **100**(8): 1355–1362 (1996).
- [189] W. Thomson (Lord Kelvin). *On the equilibrium of vapour at a curved surface of liquid*. Proceedings of the Royal Society of Edinburgh **7**: 63–68 (1870).
- [190] L. Smart and E. Moore. *Solid state chemistry: An introduction* (Taylor & Francis, Boca Raton, 2005).
- [191] D. J. Diestler, M. Schoen, A. W. Hertzner, and J. H. Cushman. *Fluids in micropores. III. Self-diffusion in a slit-pore with rough hard walls*. J. Chem. Phys. **95**(7): 5432–5436 (1991).
- [192] M. Schoen, D. J. Diestler, and J. H. Cushman. *Fluids in micropores. IV. The behavior of molecularly thin films in the grand isostress ensemble*. J. Chem. Phys. **100**(10): 7707–7717 (1994).
- [193] H. J. Raveché, R. D. Mountain, and W. B. Streett. *Freezing and melting properties of the Lennard–Jones system*. J. Chem. Phys. **61**(5): 1970 (1974).
- [194] J.-P. Hansen and L. Verlet. *Phase transitions of the Lennard–Jones system*. Phys. Rev. **184**: 151–161 (1969).
- [195] P. V. Giaquinta and G. Giunta. *About entropy and correlations in a fluid of hard spheres*. Physica A **187**(1-2): 145–158 (1992).
- [196] F. A. Lindemann. *The calculation of molecular vibration frequencies*. Z. Phys. **11**: 609–612 (1910).
- [197] F. Saija, S. Prestipino, and P. V. Giaquinta. *Evaluation of phenomenological one-phase criteria for the melting and freezing of softly repulsive particles*. J. Chem. Phys. **124**: 244 504 (2006).
- [198] E. J. Meijer and D. Frenkel. *Melting line of Yukawa system by computer simulation*. J. Chem. Phys. **94**(3): 2269 (1991).
- [199] Z. H. Jin, P. Gumbsch, K. Lu, and E. Ma. *Melting mechanisms at the limit of superheating*. Phys. Rev. Lett. **87**: 055 703 (2001).
- [200] J. Zhengming, Y. Genqing, C. Zhaonian, L. Xianghuai, and Z. Shichang. *The two-dimensional pair correlation function for the Si(001) surface: Computer simulation results*. J. Phys.: Condens. Matter **6**: 1083–1088 (1994).

- [201] R. W. Cahn. *Material science: Melting from within*. *Nature* **413**: 582–583 (2001).
- [202] C. Chakravarty, P. G. Debenedetti, and F. H. Stillinger. *Lindemann measures for the solid–liquid phase transition*. *J. Chem. Phys.* **126**(20): 204 508 (2007).
- [203] H. Wayland. *Differential Equations Applied in Science and Engineering* (Van Nostrand, Lancaster, 1957).
- [204] M. Fogiel. *The essentials of physical chemistry II* (Research and Education Association, 1988).
- [205] T. Young. *An essay on the cohesion of fluids*. *Phil. Trans. R. Soc.* **95**: 65–87 (1805).



Substrate Details

A.1 Choice of Unit Cell in a 2-Dimensional Lattice

Structures of a high degree of molecular order, such as crystals, can often be described by a unit cell, that is a small (idealised) fragment of the system reflecting the order and symmetry of the structure. [190] Consequently, the unit cell repeated in each principal direction reproduces the infinite (ideal) structure. In general, there are many ways to choose a unit cell, even e.g. in the simple two-dimensional arrangement shown in Fig. A.1a. Here, the structure can be represented by the unit cell of the square lattice as well as by a unit cell according to the (100) plane of a face centred cubic lattice. Since the unit cell of the fcc lattice is $\sqrt{2}$ -times larger than the one of the square lattice, usually the smaller unit cell of the square lattice is chosen by convention.

Nevertheless we choose the description according to the fcc lattice to make contact with [75, 105, 149, 191, 192] which can be regarded as predecessors of the present study. In [75] Schoen et al. showed that under certain conditions the first and second adsorbed fluid layers freeze in a way that fluid and wall form an fcc-like lattice, illustrated in Fig. A.1b and c. Thus, to take into account the symmetry of adsorbed fluid particles, we keep the description of the wall structure in terms of the fcc lattice.

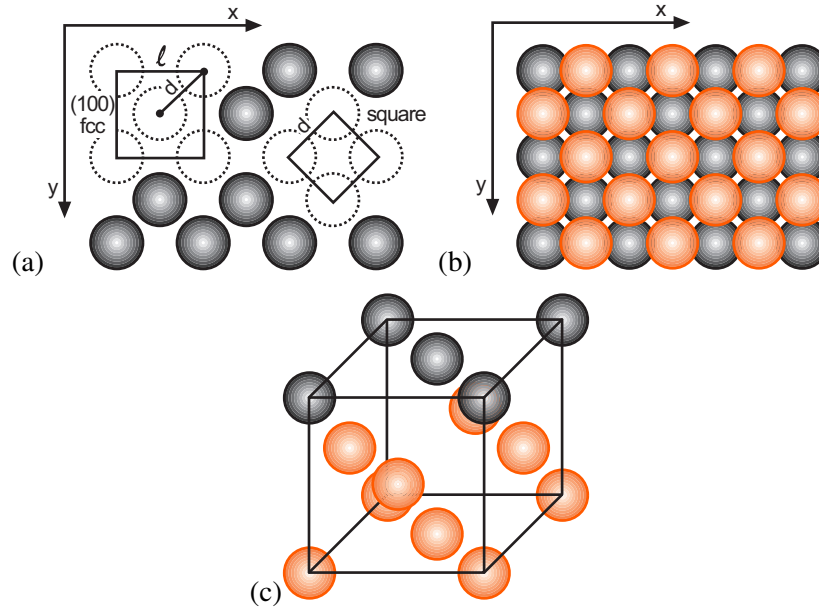


FIG. A.1: (a) The arrangement of wall particles according to the (100) layer of a fcc unit cell (with lattice parameter $\ell = \sqrt{2}d$) can alternatively be represented by the simpler unit cell of the square lattice (with lattice parameter $\ell' = d$). The former description takes the symmetry of adsorbed fluid layers into account where (b) an adsorbed fluid particle (orange) prefers to locate above the hole between wall particles (grey). The second fluid layer is adsorbed in the same way, i.e. filling the holes of the first fluid layer, so that (c) the arrangement of wall particles *plus* adsorbed fluid particles corresponds to the fcc lattice structure.

A.2 Mobility of Wall Particles

In the present study we modify the original model system of Diestler and Schoen [105] by introducing an LJ-interaction potential [see Eq. (3.23)] between the wall particles. Since in the original model, wall particles do not interact with one another, their configuration is only determined through the harmonic potential of Eq. (3.22), apart from their interaction with fluid particles. As long as the harmonic force constant κ is large, there is no need for an additional interaction potential between wall particles, because wall particles can only depart from their lattice sites to a certain extent. But the smaller is κ , the farther wall particles may depart from their lattice site and may come closer to one another.

In Fig. A.2 the in-plane pair correlation functions [cf. Eq. (4.64) on p. 90] $g_{\parallel}(r)$ of wall particles of a substrate with $\kappa = 50$ are plotted for both model systems under the same conditions. The wall particles of the original model (black line), which lack a direct interaction, come unrealistic close to each other characterised by $g_{\parallel}(r)$ that

A.3 | Substrate Structure

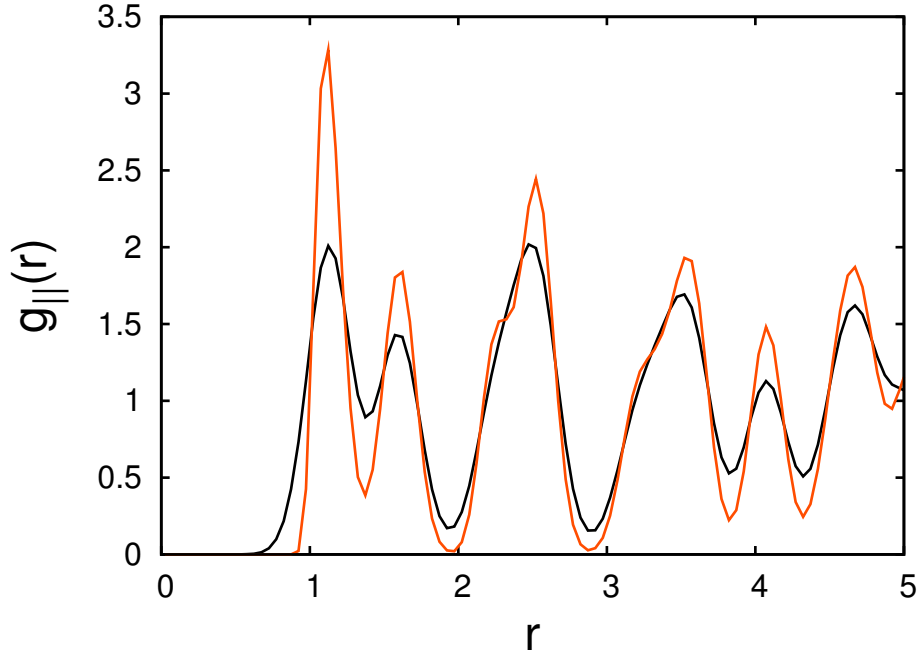


FIG. A.2: In-plane pair correlation function $g_{||}(r)$ of wall particles, depending on the distance r between two wall particles, for substrates with force constant $\kappa = 50$. The black line represents the original model of [105] without the LJ-interaction potential of Eq. (3.23) between the wall particles where wall particles come unrealistically close to each other at $r < 1$. The orange graph corresponds to the model of this study with a more realistic behaviour. Data are obtained from two separate simulation runs with different κ under the same conditions in which substrates are separated by $s_{z0} = 8.0$ and confine a liquid-like phase with $\rho \approx 0.53$ at $\mu = -11.3$ and $T = 1.0$, respectively.

takes on significant values for $r < 1$. In the present study the additional LJ potential of Eq. (3.23) prevents that wall particles approach each other unrealistic close. This is reflected by the associated in-plane pair correlation function $g_{||}(r)$ (orange) which has no significant values for $r < 1$.

A.3 Substrate Structure

Since wall particles are able to move from their lattice sites to some extent, we have to verify that the substrates considered throughout this work represent solid bodies and do not melt.

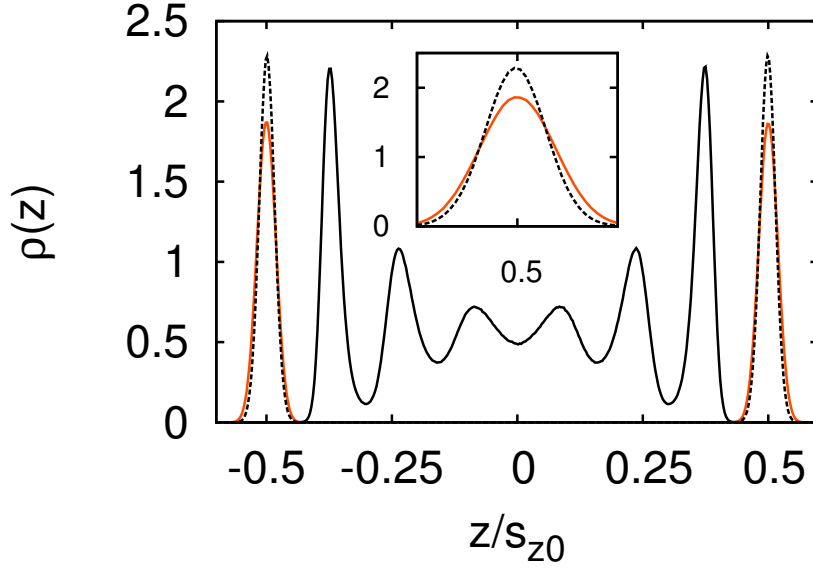


FIG. A.3: Local density profile $\rho(z)$ of fluid (—) and wall (---) across a flexible pore of $s_{z0} = 6.8$ and $\kappa = 30$ at $T = 1.0$ and $\mu = -11.8 \leftrightarrow P/P_0 \approx 0.47$ for a fluid-wall interaction $\epsilon_{fs} = 2.0$ (cf. Fig. 5.16c). Additionally, the local density of wall particles of the empty pore is given (—) which emphasises the impact of the confined fluid with $\rho \approx 0.55$ on the wall resulting in $\sigma_{zz} = -19.8 \times 10^{-4}$. Compared with the empty pore with $L_s = 0.139$, the Lindemann ratio decreases for the fluid-filled pore to $L_s = 0.118$ which signifies a more rigid wall structure. The inset shows the wall around $z_0 = 0.5$ of the fluid-filled and empty pore on an enhanced scale.

A.3.1 Solid vs. Liquid

As discussed in Chapter 1, a solid represents a highly ordered state of matter, compared with a liquid or gas, and, therefore, the mobility of its wall particles should be within physically reasonable limits. There are different methods to distinguish solids from liquids, that is, to distinguish a long-ranged order from a near-order of matter. For example, the empirical Raveché–Mountain–Streett method [193] uses the radial (bulk) pair correlation function (cf. Section 2.4) as an indicator where a pronounced ratio between the first maximum and the first non-zero minimum is crucial for identifying solid states. The Hansen–Verlet freezing rule [194] is a phenomenological method to determine the freezing of a simple liquid, and relies on a related criterion: the height of the first peak of the structure factor (cf. Section 4.6.2) is larger for solids than for liquids. Another approach uses the entropy to identify the liquid–solid phase transition: the so-called residual multiparticle entropy [195] has been found to vanish whenever a disordered structure transforms into a more structured one and, thus, may

be used to detect the melting of solid substrates. However, in this work we use the Lindemann criterion to ensure that the confining walls remain solid-like in character.

A.3.2 Lindemann Criterion

The Lindemann ratio L_s [196] is defined as the (average) root-mean-square displacement of wall particles from their lattice sites divided by the nearest-neighbour distance d given by [197]

$$L_s = \frac{1}{d} \left\langle \frac{1}{2N_s} \sum_{k=1}^2 \sum_{i=1}^{N_s} (\Delta r_i^{[k]})^2 \right\rangle^{\frac{1}{2}} \quad \text{with } \Delta r_i^{[k]} = |\mathbf{r}_i^{[k]} - \mathbf{r}_{i0}^{[k]}| \quad (\text{A.1})$$

where $d = 2^{1/6}$ for the present model (cf. Fig. 3.3a) and brackets $\langle \dots \rangle$ denote ensemble averages. In Eq. (A.1), $\mathbf{r}_i^{[k]}$ is the position of the i -th wall particle of wall k and $\Delta r_i^{[k]}$ determines the absolute departure from its lattice site $\mathbf{r}_{i0}^{[k]}$. The Lindemann ratio is a measure for the thermally driven disorder of wall particles in relation to the nearest-neighbour distance and depends on T and κ through the root-mean-square displacement, as stated for the one-dimensional case in Eq. (3.16).

Upon increasing T or decreasing κ , the Lindemann ratio may reach a *critical* value L_c at which the disorder of the wall particles and, therefore, L_s increase sharply, indicating that the solid melts. The critical value L_c depends on the lattice structure and the particle interaction potential. [197] For example, particles interacting via a so-called Yukawa potential [198] or modified Buckingham potential [197] melt at $L_c \simeq 0.15$ – 0.16 if they are arranged in a face centred cubic lattice (fcc), whereas in a body centred cubic lattice melting occurs at $L_c \simeq 0.19$. On the other hand, the critical Lindemann ratio for an fcc¹ Lennard–Jones crystal is reported as $L_c \simeq 0.12$ – 0.13 [199], if the point is considered at which solid and liquid coexist. This value applies to a (surface-free) bulk situation, but in the present model we are dealing with the surface of a solid body as the confining medium where particles are expected to be more mobile than in inner layers. Indeed, Zhengming et al. [200] found that the surface layer of solids reveals a more disordered structure than inner layers, suggesting that L_c further increases toward the solid surface. Jin et al. [199] show that an fcc Lennard–Jones crystal is thermodynamically stable up to $L_c \simeq 0.22$ if *mechanical* melting is considered, that is, the point at which a solid body loses its rigidity due to a vanishing elastic shear modulus. [201] The L_c of mechanical melting is proposed as a local

¹Note that although the substrate structure of the present model is referred to as an fcc lattice, it applies equally to any cubic arrangement of particles, as discussed in Appendix A.1 on p. 155.

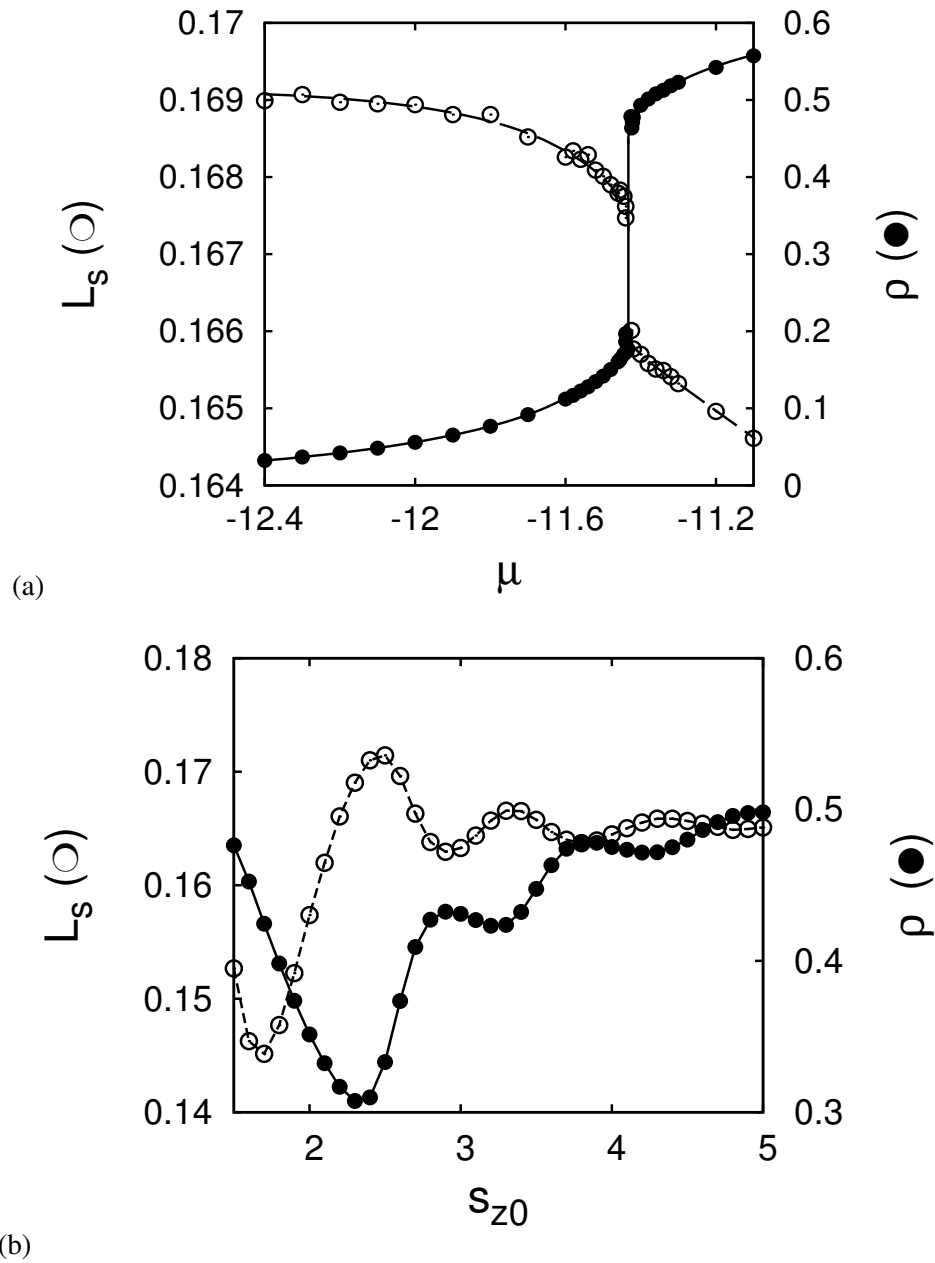


FIG. A.4: Variation of Lindemann ratio L_s (\odot) of the substrate and density ρ (\bullet) of the confined fluid **(a)** as functions of μ for a fluid in a flexible pore with $\kappa = 30$ and $s_{z0} = 6.8$ at $T = 1.0$ (cf. Fig. 5.7a), or **(b)** as functions of pore size s_{z0} for a fluid-filled pore with $\kappa = 30$ at $T = 1.0$ and $\mu = -11.3$ (cf. Fig. 5.14a).

A.3 | Substrate Structure

threshold value [202] and, therefore, is suggested to apply to particles of the surface at the liquid–solid coexistence melting point. [199, 201] Hence, the confining walls should resemble a realistic surface layer of a solid, as long as $L_s \lesssim 0.22$.

Since the Lindemann ratio increases with decreasing κ , we restrict the discussion to situations with the smallest κ used in this work, that is, $\kappa = 30$. As discussed in chapter 5, the presence of fluid particles affects the substrate structure and, therefore, also has an impact on the Lindemann ratio, as shown in Fig. A.3. Unlike the empty pore with $L_s \approx 0.139$, the imbibition of fluid matter decreases the mobility of wall particles, indicated by $L_s \approx 0.118$. The value of L_s depends on the adsorbed amount of fluid matter, as shown, for example, in Figs. A.4a and b, in which the Lindemann ratio is plotted as functions of the chemical potential (a) and pore size (b). Throughout this work, the walls have a Lindemann ratio smaller than 0.19 and, thus, we conclude that the substrates correspond to a realistic solidlike situation, with regard to the assumed threshold value of 0.22.

B

Stress in Deformable Pores

Despite the interaction between wall particles, cf. Eq. (3.23), the present model system of thermally coupled walls coincides with the model of Diestler and Schoen reported in [105]. Since stress can only be applied to the walls due to the interaction with fluid particles, interactions between wall particles have not to be considered in stress calculations. The interaction between wall particles as well as their harmonic binding potential which binds them spatially dominates the *reaction* of the wall to the stress but exerts no stress on the system. This fact becomes obvious from an empty pore in which the wall particles remain *in average* at their equilibrium positions. In other words, for stress considerations only those energy contributions have to be accounted for which depend on the fluid particles. Consequently, the derivation of the normal stress τ_{zz} given in [105] also holds for the present model system of thermally coupled walls. The following text reproduces the work of Diestler and Schoen in detail.

We start by rewriting Eq. (3.29) according to symmetry considerations given in Eq. (5.1) in the form of

$$d\Omega = -SdT - Nd\mu + 2\mu_s dN_s + s_{z0}\tau_{||}dA + A_0\tau_{zz}ds_z \quad (\text{B.1})$$

where $A = s_x s_y$ is the area of the wall considered and $A_0 = s_{x0} s_{y0}$ denotes its value in the unstrained state. For a certain pore, N_s is fixed and A keeps constant in the present model system for reasons discussed on p. 93. Consequently, the normal stress τ_{zz} at

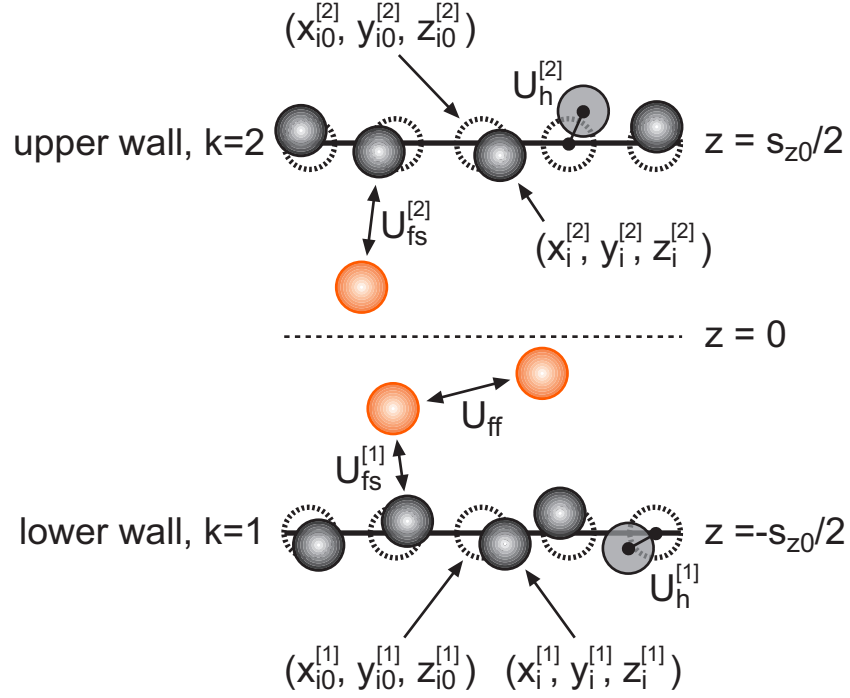


FIG. B.1: Sketch of the model system with terminology used in the derivation of the normal stress tensor element. Fluid particles are orange whereas wall particles are grey. Equilibrium lattice sites of wall particles are represented by dashed circles.

fixed μ and T is given through

$$\tau_{zz} = A_0^{-1} \left(\frac{\partial \Omega}{\partial s_z} \right)_{N_s, A, \mu, T} \quad (\text{B.2})$$

Combining the last equation with those of (2.41) and (3.31) one obtains

$$\begin{aligned} \tau_{zz} &= \frac{-k_B T}{A_0 \Xi} \left(\frac{\partial \Xi}{\partial s_z} \right)_{N_s, A, \mu, T} \\ &= \frac{-k_B T}{A_0} \sum_N e^{\gamma N} \frac{1}{N! \Lambda^{3(N+2N_s)} \Xi} \left(\frac{\partial Z}{\partial s_z} \right)_{N_s, A, T} \end{aligned} \quad (\text{B.3})$$

Depending upon how the partial derivative of Z with respect to s_z is calculated, we may get different expressions for τ_{zz} . Here, we follow two different routes which result in the ‘force’ expression and the ‘virial’ expression of τ_{zz} (see Sections E.3.1 and E.3.2 of [32]). The terminology and coordinates used throughout the following considerations are illustrated in Fig. B.1.

B.1 Stress via the Force Route

Using Eq. (3.32) we write the partial derivative given on the far right side of Eq. (B.3) more explicitly as

$$\frac{\partial Z}{\partial s_z} = \frac{\partial}{\partial s_z} \int_{-s_{z0}/2}^{s_{z0}/2} \int_{-s_{y0}/2}^{s_{y0}/2} \int_{-s_{x0}/2}^{s_{x0}/2} \int_{-\infty}^{\infty} e^{-\beta U} d^{6N_s} \mathbf{R}_s d^N \mathbf{x} d^N \mathbf{y} d^N \mathbf{z} \quad (\text{B.4})$$

where $\alpha \equiv (\alpha_1, \alpha_2, \alpha_3 \dots \alpha_N)$ with $\alpha = \mathbf{x}, \mathbf{y}, \mathbf{z}$. We employ Cartesian coordinates for the fluid particles to emphasise that the integral of Eq. (B.4) depends on s_z . In Eq. (B.4) the limits of wall particle coordinates \mathbf{R}_s are set to infinity formally, although the binding potential (whose strength is defined through κ) restricts the space which is effectively available to wall particles.

According to Leibnitz's rule for the differentiation of an integral [203] the last equation can be written as

$$\frac{\partial Z}{\partial s_z} = -\beta \int \int e^{-\beta U} \left(\frac{\partial U}{\partial s_z} \right) d^{3N} \mathbf{R} d^{6N_s} \mathbf{R}_s \quad (\text{B.5})$$

where we incorporate $U \rightarrow \infty$ at the limits of z -coordinates on account of wall repulsion so that the integrand vanishes at $z = \pm s_{z0}/2$ (see Section E.3.2 of [32]). Combining the latter equation with Eq. (B.3) and comparing the result with Eq. (3.30), one finds that the stress

$$\tau_{zz} = A_0^{-1} \left\langle \frac{\partial U}{\partial s_z} \right\rangle \quad (\text{B.6})$$

is computed from the average force $\langle \partial U / \partial s_z \rangle$ acting to the walls with respect to the z -direction where $\langle \dots \rangle$ refers to the ensemble average.

With regard to Eqs. (3.26) and (3.27) the potential energy U of the system under consideration can be expressed as

$$U = U_{ff} + U_{fs} + \sum_{k=1}^2 U_w^{[k]} + U_h^{[k]} \quad (\text{B.7})$$

Assuming that the distance between opposite walls is sufficiently large, the only way to apply force directly to the substrates is using the interaction between wall particles and fluid particles, that is, due to U_{fs} . Thus, in the case of Eq. (B.6) we have to consider only U_{fs} and we can write

$$\frac{\partial U}{\partial s_z} = \frac{\partial U_{fs}}{\partial s_z} = \epsilon_{fs} \sum_{k=1}^2 \sum_{i=1}^N \sum_{j=1}^{N_s} \frac{du(r_{ij}^{[k]})}{dr_{ij}^{[k]}} \frac{\partial r_{ij}^{[k]}}{\partial s_z} \quad \text{with } r_{ij}^{[k]} = |\mathbf{r}_i - \mathbf{r}_j^{[k]}| \quad (\text{B.8})$$

where we use Eq. (3.21). The distance of a fluid particle i to a wall particle j is given by

$$r_{ij}^{[k]} = |\mathbf{r}_i - \mathbf{r}_j^{[k]}| = \sqrt{(x_i - x_j^{[k]})^2 + (y_i - y_j^{[k]})^2 + (z_i - z_j^{[k]})^2} \quad (\text{B.9})$$

Consequently, concerning the upper wall $k = 2$ the derivation of $r_{ij}^{[2]}$ with respect to s_z leads to

$$\frac{\partial r_{ij}^{[2]}}{\partial s_z} = -\frac{1}{2} \frac{z_{ij}^{[2]}}{r_{ij}^{[2]}} = -\frac{1}{2} (\hat{\mathbf{r}}_{ij}^{[2]} \cdot \hat{\mathbf{e}}_z) \quad \text{with } z_{ij}^{[2]} = z_i - z_j^{[2]} \quad (\text{B.10})$$

whereas in the case of the lower wall $k = 1$ the result just changes its sign. In Eq. (B.10) $\hat{\mathbf{r}}_{ij} = \mathbf{r}_{ij}/r_{ij}$ applies and $\hat{\mathbf{e}}_z$ is a unit vector pointing along the z -axis of the Cartesian coordinate system. Combining Eqs. (B.6), (B.8) and (B.10) the force expression of the stress is

$$\tau_{zz} = -\frac{\epsilon_{fs}}{2A_0} \left\langle \sum_{k=1}^2 \sum_{i=1}^N \sum_{j=1}^{N_s} |u'(r_{ij}^{[k]})| (\hat{\mathbf{r}}_{ij}^{[k]} \cdot \hat{\mathbf{e}}_z) \right\rangle \quad (\text{B.11})$$

where $u'(r_{ij}^{[k]})$ is the derivative of $u(r_{ij}^{[k]})$ with respect to $r_{ij}^{[k]}$.

B.2 Stress via the Virial Route

Taking another approach, we introduce the transformation of z -coordinates of fluid particles according to Fig. B.1 expressed as

$$z_i = \frac{s_{z0}}{2} z'_i \quad (\text{B.12})$$

In terms of the new variable z'_i the configuration integral of Eq. (3.32) is written as

$$Z = \left(\frac{s_{z0}}{2}\right)^N \prod_{i=1}^N \int_{-1}^1 \int_{-s_{y0}/2}^{s_{y0}/2} \int_{-s_{x0}/2}^{s_{x0}/2} \int_{-\infty}^{\infty} e^{-\beta U} d^{6N_s} \mathbf{R}_s \, dx_i \, dy_i \, dz'_i \quad (\text{B.13})$$

where again the wall particle coordinates are *formally* not restricted in space, cf. Eq. (B.4). With regard to Eq. (B.3) we take the derivative of Z with respect to s_z resulting

B.2 | Stress via the Virial Route

in

$$\begin{aligned}
\frac{\partial Z}{\partial s_z} &= \frac{N}{s_{z0}} \left(\frac{s_{z0}}{2}\right)^{N-1} \times \frac{s_{z0}}{2} \prod_{i=1}^N \int_{-1}^1 \int_{-s_{y0}/2}^{s_{y0}/2} \int_{-s_{x0}/2}^{s_{x0}/2} \int_{-\infty}^{\infty} e^{-\beta U} d^{6N_s} \mathbf{R}_s dx_i dy_i dz'_i \\
&\quad - \beta \left(\frac{s_{z0}}{2}\right)^N \prod_{i=1}^N \int_{-1}^1 \int_{-s_{y0}/2}^{s_{y0}/2} \int_{-s_{x0}/2}^{s_{x0}/2} \int_{-\infty}^{\infty} e^{-\beta U} \left(\frac{\partial U}{\partial s_z}\right) d^{6N_s} \mathbf{R}_s dx_i dy_i dz'_i \\
&= \frac{N}{s_{z0}} Z - \beta \int \int e^{-\beta U} \left(\frac{\partial U}{\partial s_z}\right) d^{6N_s} \mathbf{R}_s d^{3N} \mathbf{R}
\end{aligned} \tag{B.14}$$

Now z'_i appears also in U where only the contributions U_{ff} , cf. Eq. (3.20), and U_{fs} , cf. Eq. (3.21), which depend on the fluid particle coordinates, have to be considered for stress calculations as discussed in the beginning of this chapter. For this purpose U can be expressed as

$$\begin{aligned}
\frac{\partial U}{\partial s_z} &= \frac{\partial U_{ff}}{\partial s_z} + \frac{\partial U_{fs}}{\partial s_z} \\
&= \sum_{i=1}^N \sum_{j>i}^N \frac{du(r_{ij})}{dr_{ij}} \frac{\partial r_{ij}}{\partial s_z} + \epsilon_{fs} \sum_{k=1}^2 \sum_{i=1}^N \sum_{j=1}^{N_s} \frac{du(r_{ij}^{[k]})}{dr_{ij}^{[k]}} \frac{\partial r_{ij}^{[k]}}{\partial s_z}
\end{aligned} \tag{B.15}$$

The distance r_{ij} between two fluid particles i and j is given by

$$r_{ij} = \sqrt{(x_i - x_j)^2 + (y_i - y_j)^2 + \frac{s_{z0}^2}{4} (z'_i - z'_j)^2} \tag{B.16}$$

and, consequently, its derivative with respect to s_z yields

$$\begin{aligned}
\frac{\partial r_{ij}}{\partial s_z} &= \frac{1}{2s_{z0}} \left[(x_i - x_j)^2 + (y_i - y_j)^2 + \frac{s_{z0}^2}{4} (z'_i - z'_j)^2 \right]^{-\frac{1}{2}} \times \frac{2s_{z0}}{4} (z'_i - z'_j)^2 s_{z0} \\
&= \frac{z_{ij}^2}{s_{z0} r_{ij}} \\
&= r_{ij} (\hat{\mathbf{r}}_{ij} \cdot \hat{\mathbf{e}}_z)^2
\end{aligned} \tag{B.17}$$

where $\hat{\mathbf{r}}_{ij} = \mathbf{r}_{ij}/r_{ij}$ and $\hat{\mathbf{e}}_z$ denotes a unit vector along the z -direction of the Cartesian coordinate system.

To express the distance between fluid particles and wall particles, we make a transformation of wall particle coordinates: In the model system a wall particle may depart from its lattice site $\mathbf{r}_{j0}^{[k]}$ to another location $\mathbf{r}_j^{[k]}$ where the new position is separated from the lattice site by $\Delta \mathbf{r}_j^{[k]}$ expressed as

$$\Delta \mathbf{r}_j^{[k]} = \mathbf{r}_j^{[k]} - \mathbf{r}_{j0}^{[k]} \tag{B.18}$$

Thus, we can change the notation and express the location $\mathbf{r}_j^{[k]}$ of wall particle j in wall k through its deviation $\Delta\mathbf{r}_j^{[k]}$ from its equilibrium position $\mathbf{r}_{j0}^{[k]}$ as

$$\mathbf{r}_j^{[k]} = \mathbf{r}_{j0}^{[k]} + \Delta\mathbf{r}_j^{[k]} \quad (\text{B.19})$$

Combining Eqs. (B.9) and (B.19), the distance $r_{ij}^{[k]}$ between a fluid particle i and a wall particle j of wall k can be expressed as

$$r_{ij}^{[k]} = \sqrt{(x_i - x_{j0}^{[k]} - \Delta x_j^{[k]})^2 + (y_i - y_{j0}^{[k]} - \Delta y_j^{[k]})^2 + \left(\frac{s_{z0}}{2} z'_i \pm \frac{s_{z0}}{2} - \Delta z_j^{[k]}\right)^2} \quad (\text{B.20})$$

where ‘+’ corresponds to the lower wall $k = 1$ and ‘-’ corresponds to the upper wall $k = 2$. The derivative of $r_{ij}^{[k]}$ with respect to s_z is

$$\begin{aligned} \frac{\partial r_{ij}^{[k]}}{\partial s_z} &= \frac{1}{2s_{z0}} \left[(x_i - x_{j0}^{[k]} - \Delta x_j^{[k]})^2 + (y_i - y_{j0}^{[k]} - \Delta y_j^{[k]})^2 \right. \\ &\quad \left. + \left(\frac{s_{z0}}{2} z'_i \pm \frac{s_{z0}}{2} - \Delta z_j^{[k]}\right)^2 \right]^{-\frac{1}{2}} \times 2z'_{ij} \left(\frac{z'_i}{2} \pm \frac{1}{2}\right) s_{z0} \\ &= \frac{1}{s_{z0} r_{ij}^{[k]}} z_{ij}^{[k]} \left(z_i \pm \frac{s_{z0}}{2} - \Delta z_j^{[k]} + \Delta z_j^{[k]} \right) \\ &= \frac{1}{s_{z0}} \frac{z_{ij}^{[k]} (z_{ij}^{[k]} + \Delta z_j^{[k]})}{r_{ij}^{[k]}} \\ &= \frac{1}{s_{z0}} \left(\frac{(z_{ij}^{[k]})^2}{r_{ij}^{[k]}} + \frac{z_{ij}^{[k]} \Delta z_j^{[k]}}{r_{ij}^{[k]}} \right) \\ &= \frac{1}{s_{z0}} r_{ij}^{[k]} (\hat{\mathbf{r}}_{ij}^{[k]} \cdot \hat{\mathbf{e}}_z) (\hat{\mathbf{r}}_{ij}^{[k]} + \Delta\hat{\mathbf{r}}_j^{[k]}) \cdot \hat{\mathbf{e}}_z \end{aligned} \quad (\text{B.21})$$

where $\hat{\mathbf{r}}_{ij} = \mathbf{r}_{ij}/r_{ij}$ and $\Delta\hat{\mathbf{r}}_{ij} = \Delta\mathbf{r}_{ij}/\Delta r_{ij}$.

Combining Eqs. (B.3), (B.14), (B.15), (B.17) and (B.21) leads to the virial expression in the form of

$$\tau_{zz} = \tau_{zz}^{ff} + \tau_{zz}^{fs} \quad (\text{B.22})$$

where the contribution of the fluid–fluid interaction is

$$\tau_{zz}^{ff} = -\frac{\langle N \rangle k_B T}{A_0 s_{z0}} + \frac{1}{A_0 s_{z0}} \left\langle \sum_{i=1}^N \sum_{j>i}^N u'(r_{ij}) r_{ij} (\hat{\mathbf{r}}_{ij} \cdot \hat{\mathbf{e}}_z)^2 \right\rangle \quad (\text{B.23})$$

and the contribution of the fluid–wall interaction is given by

$$\tau_{zz}^{fs} = \frac{\epsilon_{fs}}{A_0 s_{z0}} \left\langle \sum_{k=1}^2 \sum_{i=1}^N \sum_{j=1}^{N_s} u'(r_{ij}^{[k]}) r_{ij}^{[k]} (\hat{\mathbf{r}}_{ij}^{[k]} \cdot \hat{\mathbf{e}}_z) (\hat{\mathbf{r}}_{ij}^{[k]} + \Delta\hat{\mathbf{r}}_j^{[k]}) \cdot \hat{\mathbf{e}}_z \right\rangle \quad (\text{B.24})$$

B.2 | Stress via the Virial Route

In Eqs. (B.23) and (B.24), u' is the derivative of u with respect to r_{ij} or $r_{ij}^{[k]}$, respectively.



Kelvin Equation

In this chapter we derive the celebrated Kelvin equation [189] in order to recall and analyse the assumptions on which it is based. We mainly follow [204] and start with a spherical droplet of liquid of radius r which is surrounded by a gas, as shown in Fig. C.1a. The liquid and gas phase are separated by the surface of the liquid where the surface tension γ , i.e. the force per unit length directed perpendicularly to the surface, maintains the shape of the droplet. The creation of a liquid surface of area $A = 4\pi r^2$ requires work dW_s to be done, expressed as

$$dW_s = \frac{dW_s}{dr} dr = F_s dr = \left(\frac{A\gamma}{dr} \right) dr = 8\pi r \gamma dr \quad (\text{C.1})$$

where $F_s = 8\pi r \gamma$ is the surface force. Supposing mechanical equilibrium between liquid and gas, the pressure inside the droplet P_l equals the pressure outside the droplet P_g plus the surface force F_s , written as [204]

$$\begin{aligned} P_l 4\pi r^2 &= P_g 4\pi r^2 + 8\pi r \gamma \\ \Leftrightarrow P_l - P_g &= \frac{2\gamma}{r} \end{aligned} \quad (\text{C.2})$$

which is known as the Laplace equation. Since this *ansatz* is based on simple force considerations, it holds also for the case in which a liquid phase inside a cylinder is in equilibrium with a surrounding gas phase, as sketched in Fig. C.1b. Thus, a prerequisite for applying Eq. (C.2) to this situation is the existence of a meniscus, i.e.

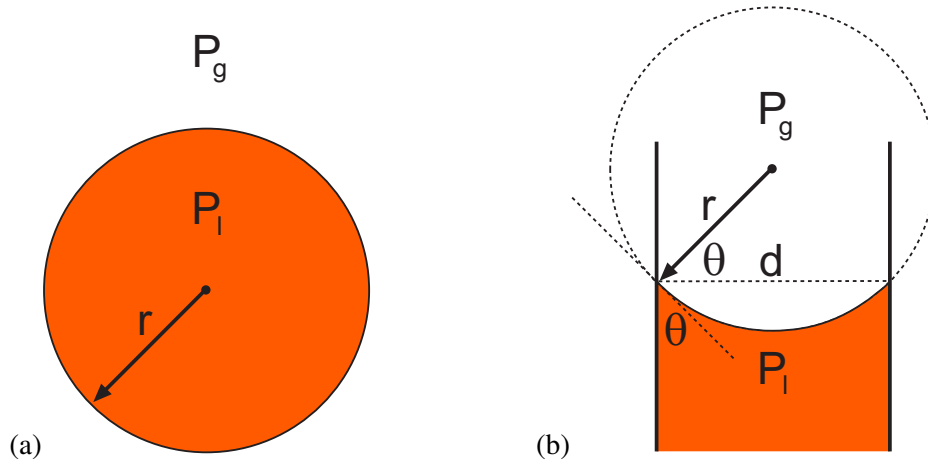


FIG. C.1: (a) Liquid droplet of radius r and (b) liquid inside a (macroscopic) cylinder of diameter d . In both cases, the liquid phase of pressure P_l is in contact with a gas phase of pressure P_g , where the liquid–gas interface is assumed to be of strictly spherical shape.

a liquid–gas interface in the shape of a segment of a circle. In mechanical equilibrium, Eq. (C.2) can be rewritten in the following form

$$dP_l - dP_g = d \left(\frac{2\gamma}{r} \right) \quad (\text{C.3})$$

and chemical equilibrium between liquid and gas requires

$$\mu_l = \mu_g \quad (\text{C.4})$$

On account of the symmetric geometry of the liquid-phase in form of a droplet, mechanical work can be expressed via $W_{mech} = PdV$ (as in bulk) whereas the Gibbs potential is given through the Legendre transformation $\mathcal{G} = \Omega + VP$ in analogy to Eq. (5.40). Combining these findings with Eqs. (2.11), (2.12), (2.17) and (3.28), under conditions of fixed T and N_s the chemical potential can be expressed as

$$\mu = \left(\frac{\partial \mathcal{G}}{\partial N} \right) = VdP \quad (\text{C.5})$$

and combined with Eq. (C.4) yields

$$V_l dP_l = V_g dP_g \quad (\text{C.6})$$

where V_l and V_g are the molar volumes of the liquid and the gas. Eqs. (C.3) and (C.6) can be written as

$$d \left(\frac{2\gamma}{r} \right) = \frac{V_g - V_l}{V_l} dP_g \approx \frac{V_g}{V_l} dP_g \quad (\text{C.7})$$

where the molar volume of the liquid is neglected compared to the molar volume of the gas. Assuming the gas to be ideal, we can express V_g as

$$V_g = \frac{RT}{P_g} \quad (\text{C.8})$$

where R is the ideal gas constant. Combining Eqs. (C.7) and (C.8) gives

$$d\left(\frac{2\gamma}{r}\right) = \frac{RT}{V_l} \frac{dP_g}{P_g} \quad (\text{C.9})$$

The isotherm from the state with $1/r = 0$ and P_0 , at which the surrounding gas phase condenses, to an arbitrary state with $1/r$ and P is obtained through integrating the last equation in the form

$$\int_0^{1/r} d\left(\frac{2\gamma}{r}\right) = \frac{RT}{V_l} \int_{P_0}^P \frac{dP_g}{P_g}$$

$$\ln \frac{P}{P_0} = \frac{2\gamma}{r} \frac{V_l}{RT} \quad (\text{C.10})$$

which is referred to as the Kelvin equation. In the last equation we can express $r = d/2 \cos \theta$ through the diameter d of the cylindrical pore and the contact angle θ [205] between the liquid–gas interface and the substrate, see Fig. C.1b, written as

$$\ln \frac{P}{P_0} = \frac{4\gamma \cos \theta}{d} \frac{V_l}{RT} \quad (\text{C.11})$$

In retrospect, the most serious assumption in the derivation of the Kelvin equation is the existence of a meniscus in the shape of a circle segment. This *ansatz* is dubious at least if the pore size enters the nanometre scale where macroscopic concepts, such as the meniscus, are expected to be meaningless because the associated dimensions would be of the same order of magnitude as the interparticle correlation, cf. Section 4.6.2.

Acknowledgement

I am deeply grateful to Martin Schoen for his supervision of and his continuous provision of support for the work on this thesis. This work would not have been possible without him. My warm thanks to Oskar Paris, Johannes Prass and Dirk Müter for their excellent cooperation and fruitful discussions, and to Sabine Klapp for her constructive comments and advice during my entire time as a doctoral student.

I warmly thank Marco Mazza who reviewed parts of the manuscript and made helpful comments. I would like to thank my colleagues Holger Bohlen, Jörg Silbermann, Jelena Jordanowic, Manuel Greschek and Timo Poppmann for the pleasant working environment.

Financial support from the Deutsche Forschungsgemeinschaft through its Collaborative Research Area 448 'Mesoscopically Structured Composites' is gratefully acknowledged.